Assessing primary versus secondary features in two pegmatite swarms with implications for the nature of pegmatitic systems

by

Jérémie Damien Pfister

A thesis submitted in partial fulfillment
of the requirements for the degree of
Doctor of Philosophy (PhD) in Mineral Deposits and Precambrian Geology

The Office of Graduate Studies
Laurentian University
Sudbury, Ontario, Canada

THESIS DEFENCE COMMITTEE/COMITÉ DE SOUTENANCE DE THÈSE
Laurentian Université/Université Laurentienne
Office of Graduate Studies/Bureau des études supérieures

Title of Thesis Titre de la thèse	Assessing primary versus secondary features in two pegmatite swarms with implications for the nature of pegmatitic systems
Name of Candidate Nom du candidat	Pfister, Jeremie
Degree Diplôme	Doctor of Philosophy
Program Programme	Mineral Deposits and Precambrian Geology
Date of Defence Date de la soutenance	March 24, 2023

APPROVED/APPROUVÉ

Thesis Examiners/Examinateurs de thèse:

Dr. Dan Kontak
(Supervisor/Directeur(trice) de thèse)

Dr. Lee Groat
(Committee member/Membre du comité)

Dr. Mostafa Fayek
(Committee member/Membre du comité)

Dr. John Hanchar
(External Examiner/Examinateur externe)

Dr. Julie Selway
(Internal Examiner/Examinateur interne)

Approved for the Office of Graduate Studies
Approuvé pour le Bureau des études supérieures
Tammy Eger, PhD
Vice-President Research (Office of Graduate Studies)
Vice-rectrice à la recherche (Bureau des études supérieures)
Laurentian University / Université Laurentienne

ACCESSIBILITY CLAUSE AND PERMISSION TO USE

I, **Jeremie Pfister**, hereby grant to Laurentian University and/or its agents the non-exclusive license to archive and make accessible my thesis, dissertation, or project report in whole or in part in all forms of media, now or for the duration of my copyright ownership. I retain all other ownership rights to the copyright of the thesis, dissertation or project report. I also reserve the right to use in future works (such as articles or books) all or part of this thesis, dissertation, or project report. I further agree that permission for copying of this thesis in any manner, in whole or in part, for scholarly purposes may be granted by the professor or professors who supervised my thesis work or, in their absence, by the Head of the Department in which my thesis work was done. It is understood that any copying or publication or use of this thesis or parts thereof for financial gain shall not be allowed without my written permission. It is also understood that this copy is being made available in this form by the authority of the copyright owner solely for the purpose of private study and research and may not be copied or reproduced except as permitted by the copyright laws without written authority from the copyright owner.

Abstract

Understanding the processes behind the formation and evolution of pegmatites, which host globally significant resources of strategic metals (*e.g.*, Li, Ta, Nb, Sn, Cs, Rb, Y, REE) critical to the global renewable energy transition, is paramount for their exploration and exploitation.

This study investigates the nature, origin and evolution of two distinct pegmatite swarms (*i.e.*, the LCT-type Little Nahanni Pegmatite Group, NWT, Canada, and the NYF-type Highway 69 Pegmatite Group, Ontario, Canada) in order to address several unresolved aspects of pegmatite genesis, such as the origin of pegmatite-forming melts (*i.e.*, anatexis *versus* fractional crystallization), nature of various pegmatitic textures (*i.e.*, primary *versus* secondary), metasomatism and re-mobilization of rare-metal mineralization, and influence of the host rocks on pegmatites (*i.e.*, open- *versus* closed systems).

This study integrates various aspects of field observations that include detailed mapping, field and petrographic observations (transmitted light, BSE, SEM-CL), bulk whole-rock and trace-elements geochemistry (ICP-AES, ICP-MS), *in situ* mineral analysis (SEM-EDS), *in situ* trace-elements analysis (LA-ICP-MS), bulk and *in situ* stable isotopes (O, H) geochemistry (DI-IRMS, SIMS), and *in situ* U-Pb geochronology (LA-ICP-MS). The principal findings suggest that: (1) both anatexis and fractional crystallization of a parental melt are viable processes of pegmatite formation; (2) most macroscopic pegmatitic textures are primary and are generally preserved during sub-solidus evolution of pegmatites; (3) late-stage, fine-grained albitic and micaceous units associated with significant rare-metal mineralization are secondary; (4) secondary micro-features related to coupled dissolution-precipitation processes in pegmatites are profuse, despite being rarely reported, and are frequently associated with accessory rare-metal mineralization; and (5)

pegmatites evolve as partially open systems during both magmatic and metasomatic stages with influence from the host rocks, and in some cases, external fluids.

Keywords

Pegmatites, LCT, NYF, lithium, tantalum, niobium, rare earth elements, undercooling, metasomatism, fluid:rock interaction, anatexis, geochemistry, mineralogy, pegmatitic textures, geochronology, LA-ICP-MS, SIMS, DI-IRMS, stable isotopes, *in-situ* analysis, SEM-CL, cathodoluminescence, trace elements, Cretaceous, Little Nahanni Pegmatite Group, LNPG, Selwyn, Northwest Territories, Neoproterozoic, Highway 69 Pegmatite Group, Grenville, Grenville Front Tectonic Zone, Sudbury, Ontario, Canada, economic geology.

Co-authorship statement

This thesis consists of four manuscripts (Chapters 2, 3, 4 and 5) that are formatted for separate journal requirements. Chapter 2, co-authored by D.J. Kontak and L.A. Groat (accepted and soon to be published in The Canadian Mineralogist), and chapter 3, co-authored by D.J. Kontak, L.A. Groat and M. Fayek (to be submitted to Geochimica et Cosmochimica Acta), focus on the Little Nahanni Pegmatite Group (NWT, Canada). Field work and sample collection for chapters 2 and 3 were completed by D.J. Kontak and L.A. Groat from 2003 to 2009, stable isotopic analyses (SIMS, DI-IRMS, respectively) were performed by M. Fayek and K. Kyser, while sample preparation, sample characterization, and all other analyses (SEM-EDS, SEM-CL, LA-ICP-MS) were completed by J.D. Pfister. Chapter 4, co-authored by D.J. Kontak and J.H. Marsh (accepted in Precambrian Research), and Chapter 5, co-authored by D.J. Kontak, R. Lorenzo and M. Fayek (to be further divided into two separate publications), focus on the Highway 69 Pegmatite Group (Ontario, Canada). The LA-ICP-MS analysis of trace elements in quartz was performed by R. Lorenzo, stable isotopic analysis (SIMS) of quartz was performed by M. Fayek, and ICP-AES analysis of whole-rock and K-feldspar samples were completed by ALS laboratories. Field work, mapping, sample collection, sample preparation, and all other analyses (SEM-EDS, SEM-CL, LA-ICP-MS) were completed by J.D. Pfister, with consultation from D.J. Kontak. J.D. Pfister is also responsible for all interpretations presented in the manuscripts and thesis with consultation from D. J. Kontak. Manuscript preparation benefited from suggestions and revisions by co-authors.

Acknowledgements

First and foremost, the most heartfelt thanks to my supervisor, Dr. Daniel Kontak, for his unwavering guidance, support, encouragement and patience throughout this project. His mentorship helped me grow both as a person and student, and will remain a highlight of my graduate studies.

Special thanks are offered to Drs. Jeffrey Marsh and Joe Petrus for their assistance with LA-ICP-MS analysis and interpretation, and to Drs. William Zhe and Kirk Ross for their assistance with SEM-EDS/CL analysis and interpretation. I am most appreciative of the constructive discussions that have benefited my understanding of pegmatites with many researchers in this field, including but not limited to, Drs. Lee Groat, Andy McDonald, Skip Simmons, Al Falster, Karen Webber, Alan Anderson and Axel Müller. The close friendship, support and assistance from fellow students Drake Hyden, Keaton Strongman and Ben Mark is much appreciated.

I am most grateful to my parents, Jean-Pierre and Catherine Pfister, as well as my partner, Sophie Michel, for their constant support and encouragement along the way. The help provided by Roxane Bourgouin-Mehes, Dr. Elizabeth Turner and Gabrielle Dufresne when needed the most, are greatly appreciated.

Finally, I would like to thank Caroline Ferrara, Cédric Schnyder and Dr. Michel Meyer, who have helped nurture and develop my curiosity for minerals into a career in geology.

This study was supported by an NSERC discovery grant to Dr. Daniel Kontak and a GTA fellowship to Jérémie Pfister from the Laurentian University.

Table of Contents

List of Tables

List of Figures

List of Appendices

Chapter 1

1. General introduction

Granitic pegmatites are a globally important source of strategic metals (*i.e.,* Li, Be, Rb, Cs, Ta, Nb, Sn, REE, U) (*e.g.,* Jahns 1955, Černý 1982, 1989, London, 2008, 2018; Linnen et al., 2012; London & Kontak, 2012), which are now critical to the global renewable energy transition. Therefore, understanding the nature, origin and evolution, both magmatic and subsolidus, of granitic pegmatites is paramount for both the exploration and exploitation of such deposits. Additionally, pegmatites represent the most evolved of the natural magmatic rocks and therefore such work also contributes to the fundamentals of igneous petrology.

The exotic composition of many pegmatite-forming melts (*i.e.,* highly enriched in incompatible elements and fluxing components) raises the question of their origin. Experimental and empirical studies have demonstrated several possible mechanisms for the formation of such melts. Fractional crystallization of a parental melt of granitic composition is usually a preferred explanation (*e.g*., Černý, 1991; London 2008, 2018) and is supported by many studies documenting the basic field relationships between pegmatites and their progenitors (*e.g.*, Černý, 1991 and references therein; Mulja & Williams-Jones, 2018). More recently, anatexis of appropriate source-rocks has been proposed as a viable mechanism of pegmatite formation (*e.g.,* Nabalek *et al*., 1992; Simmons *et al*., 2016; Knoll *et al*., 2018; Vignola *et al*., 2018; Webber *et al*., 2019). Alternatively, some authors have argued for the generation of pegmatite-forming melt *via* melt immisicibility on the basis of fluid and melt inclusions studies (*e.g.,* Thomas et *al.,* 2012).Thus, there is a clear need for further work to clarify this simple but fundamental aspect of pegmatite genesis.

Pegmatites, *sensu stricto*, are defined by their textural features rather than chemistry (London, 2008), which range from highly-evolved felsic to ultramafic compositions (*e.g.,* the famous Merensky and JM reefs of the Bushveld (S. Africa) and Stillwater (USA) complexes respectively, which host globally significant PGE resources), as well as more uncommon compositions (*e.g.,* alkaline melts, carbonatites, nelsonites, etc.). Thus, petrologic studies have historically been focused on resolving the processes behind the formation of the complex macroscopic pegmatitic textures and spatial heterogeneity that distinguish pegmatites from their finer-grained counterparts (*e.g.*, London, 2018). Recent experimental studies have shown that most of the common, but highly unusual, pegmatitic textures (*e.g.*, graphic texture, high aspect-ratios, skeletal, dendritic and plumose mineral morphologies, rhythmic aplitic layering) are formed under disequilibrium conditions promoted by significant undercooling (ΔT) of the pegmatite-forming melt (*e.g*., London, 2005, 2008; Maneta & Baker, 2014; Maneta *et al.,* 2015; London & Morgan, 2017; Sirbescu *et al.,* 2017).

There are, however, multiple textures, such as well-documented but controversial late-stage fine-grained albitic and micaceous units, whose origin remain enigmatic. These are variably interpreted as the products of purely magmatic (*e.g*., Norton, 1983; London & Morgan, 2017, London, 2018) or metasomatic (*e.g.,* Černý, 1989; Foord & Cook, 1989; Kontak *et al.,* 2002; Sweetapple & Collin, 2002; Kontak, 2006; Pfister *et al.*, 2023) processes, but are of particular, if not paramount importance today due to their intimate spatial relationship with rare-metal mineralization (*e.g*., Černý 1989, Suwimonprecha *et al.* 1995, Fuertes-Fuente & Martin-Izard 1998, Lumpkin 1998, Sweetapple & Collins 2002, Kontak 2006, Kontak & Kyser 2009, Wise & Brown 2011, Kaeter *et al.* 2018, Fuchsloch *et al.* 2019).

Additionally, a myriad of commonly-overlooked secondary micro-features are observed in pegmatites, such as: (1) pervasive recrystallization of quartz, only visible under cathodoluminescence (CL) imagery (*e.g.*, London, 2014; Pfister *et al*., 2023); (2) profusion of secondary fluid inclusions (*e.g.*, London, 1986; Kontak *et al.*, 2002; Thomas *et al.*, 2012; London, 2018; Burns, 2019); (3) porosity development associated with the coarsening of perthitic textures (*i.e*., film through flame to patchy; see Parsons & Lee, 2005), a fundamental feature of coupled dissolution-precipitation (Worden *et al.,* 1990; Putnis, 2002; Parsons & Lee, 2005; Plumper & Putnis, 2009; Maneta & Anderson, 2018); and (4) pseudomorphism (e.g., Černý, 1989; London, 2008; Martin & De Vito, 2014; Pfister et al., 2023). Collectively, these commonly-overlooked features indicate that pegmatites undergo pervasive sub-solidus fluid:rock interactions, despite the preservation of primary macroscopic pegmatitic textures.

Relevant to these controversies is that despite an increasing amount of textural, mineralogical, geochemical, isotopic and fluid inclusion evidence suggestive of pegmatite-wall rock interactions (*e.g.*, Taylor *et al.,* 1979; London *et al.,* 1996; Dyar *et al.,* 1999; Kontak & Kyser, 2009; Martin & De Vito, 2014; Burns, 2019; Pieczka *et al.,* 2019), popular models for pegmatite formation and evolution treat these systems as entirely closed systems (Jahns 1955, Jahns & Burnham, 1969; Černý, 1991; London, 2008; 2018), which is largely based on the scarcity, or perhaps poorly studied, metasomatic aureoles surrounding pegmatites and experiments under controlled conditions (*e.g.,* London, 2008; London & Morgan, 2017).

The aforementioned discussion provides the foundation for the main objectives of this thesis, which is to understand, and then compare elsewhere, the formation and evolution of two well-exposed pegmatite systems hosted in very contrasting temporal and spatial geological settings: (1) the Cretaceous (*ca.* 85 Ma), highly-evolved, Li-Cs-Ta (LCT)-type Little Nahanni

pegmatite group of the NWT (Canada) (Mauthner, 1996; Groat *et al*., 2003) that is hosted in low-grade metasedimentary rocks (*i.e*., thus unlikely anatectic); and (2) the Neoproterozoic, relatively primitive Nb-Y-F (NYF)-type Highway 69 pegmatite group (Sudbury, ON) (Van Walraven, 2011; Lorenzo, 2017), hosted in high-grade metamorphic rocks. More specifically, the objectives of the thesis are to address: (1) origin of the pegmatite-forming melts; (2) formation of primary *versus* secondary pegmatitic textures; (3) chemical, textural and mineralogical evolution of the pegmatites; (4) role of metasomatism, particularly in respect to rare-metal mineralization; (5) assess open- *versus* closed-system evolution of pegmatite systems; and (6) characterize and date the poorly documented Highway 69 pegmatite swarm. In order to address these topics, the thesis presented four papers which collectively integrate various aspects of field observations that includes detailed mapping, petrographic observations (transmitted light, BSE, SEM-CL), bulk whole-rock and trace-elements geochemistry (ICP-AES, ICP-MS), *in situ* mineral analysis (SEM-EDS), *in situ* trace-elements analysis (LA-ICP-MS), bulk and *in situ* stable isotopes (O, H) geochemistry (DI-IRMS, SIMS), and *in situ* U-Pb geochronology (LA-ICP-MS).

1.1 References

Burns M. G. (2019) A fluid inclusion study of the Little Nahanni LCT-type pegmatite group, NWT Canada: Implications for the nature and origin of fluids in LCT-type pegmatites and pegmatite evolution. Laurentian University.

Černý P. (1989) Characteristics of pegmatite deposits of tantalum. In *Lanthanides, Tantalum and Niobium* Berlin. pp. 195–239.

Černý P. (1982) Anatomy and classification of granitic pegmatites. *Mineral. Assoc. Canada, Short Course Handb.* **8**, 1–39.

Dyar M. D., Guidotti C. V., Core D. P., Wearn K. M., Wise M. A., Francis C. A., Johnson K., Brady J. B., Robertson J. D. and Cross L. R. (1999) Stable isotope and crystal chemistry of tourmaline across pegmatite - country rock boundaries at Black Mountain and Mount Mica, southwestern Maine, USA. *Eur. J. Mineral.* **11**, 281–294.

Foord E. E. and Cook R. B. (1989) Mineralogy and paragenesis of the McAllister Sn-Ta-bearing pegmatite, Coosa County, Alabama. *Can. Mineral.* **27** pt **1**, 93–105.

Fuchsloch W. C., Nex P. A. M. and Kinnaird J. A. (2019) The geochemical evolution of Nb–Ta–Sn oxides from pegmatites of the Cape Cross–Uis pegmatite belt, Namibia. *Mineral. Mag.* **83**, 161–179.

Fuertes-Fuente M. and Martin-Izard A. (1998) The Forcarei Sur rare-element granitic pegmatite field and associated mineralization, Galicia, Spain. *Can. Mineral.* **36**, 303–325.

Groat L. A., Mulja T., Mauthner M. H. F., Ercit T. S., Raudsepp M., Gault R. A. and Rollo H. A. (2003) Geology and mineralogy of the Little Nahanni rare-element granitic pegmatites, Northwest Territories. *Can. Mineral.* **41**, 139–160.

Jahns R. H. (1955) The study of pegmatites. *Econ. Geol.* **50th Anniv**, 1025–1130.

Jahns R. H. and Burnham C. W. (1969) Experimental studies of pegmatite genesis: I. A model for the derivation and crystallization of granitic pegmatites. *Econ. Geol.* **64**, 843–864.

Kaeter D., Barros R., Menuge J. F. and Chew D. M. (2018) The magmatic–hydrothermal transition in rare-element pegmatites from southeast Ireland: LA-ICP-MS chemical mapping of muscovite and columbite–tantalite. *Geochim. Cosmochim. Acta* **240**, 98–130.

Knoll T., Schuster R., Huet B., Mali H., Onuk P., Horschinegg M., Ertl A. and Giester G. (2018) Spodumene pegmatites and related leucogranites from the austroalpine unit (eastern alps, central europe): Field relations, petrography, geochemistry, and geochronology. *Can. Mineral.* **56**, 489–528.

Kontak D. J. (2006) Nature and origin of an LCT-suite pegmatite with late-stage sodium enrichment, Brazil Lake, Yarmouth County, Nova Scotia. I. Geological setting and petrology. *Can. Mineral.* **44**, 563–598.

Kontak D. J., Dostal J., Kyser K. and Archibald D. A. (2002) A petrological, geochemical, isotopic and fluid-inclusion study of 370Ma pegmatite-aplite sheets, Peggys Cive, Nova Scotia, Canada. *Can. Mineral.* **40**, 1249–1286.

Kontak D. J. and Kyser T. K. (2009) Nature and origin of an LCT-suite pegmatite with late-stage sodium enrichment, Brazil Lake, yarmouth county, Nova Scotia. II. Implications of stable isotopes (δ18o, δd) for magma source, internal crystallization and nature of sodium metasomatism. *Can. Mineral.* **47**, 745–764.

Linnen R., McNeil A. and Flemming R. (2019) Some Thoughts On Metasomatism in Pegmatites. *Can. Mineral.* **57**, 765–766.

London D. (2014) A petrologic assessment of internal zonation in granitic pegmatites. *Lithos* **184**–**187**, 74–104.

London D. (2005) Granitic pegmatites: An assessment of current concepts and directions for the future. *Lithos* **80**, 281–303.

London D. (1986) Magmatic-hydrothermal transition in the Tanco rare-element pegmatite: evidence from fluid inclusions and phase-equilibrium experiments. *Am. Mineral.* **71**, 376–395.

London D. (2018) Ore-forming processes within granitic pegmatites. *Ore Geol. Rev.* **101**, 349–383.

London D. (2008) *Pegmatites*., The Canadian Mineralogist, Special Publication 10, Quebec.

London D. and Kontak D. J. (2012) Granitic pegmatites: Scientific wonders and economic bonanzas. *Elements* **8**, 257–261.

London D. and Morgan G. B. (2017) Experimental crystallization of the Macusani Obsidian, with applications to lithium-rich granitic pegmatites. *J. Petrol.* **58**, 1005–1030.

London D., Morgan G. B. and Wolf M. B. (1996) Boron in granitic rocks and their contact aureoles. *Rev. Mineral. Geochemistry* **33**, 299–330.

Lorenzo R. I. (2017) Relevance of fluid:rock interaction in Proterozoic pegmatites near Sudbury, Ontario to mineralization in rare-metal pegmatite settings. Laurentian University.

Lumpkin G. R. (1998) Rare-element mineralogy and internal evolution of the Rutherford #2 pegmatite, Amelia County, Virginia:A classic locality revisited. *Can. Mineral.* **36**, 339–353.

Maneta V. and Anderson A. J. (2018) Monitoring the crystallization of water-saturated granitic melts in real time using the hydrothermal diamond anvil cell. *Contrib. to Mineral. Petrol.* **173**, 1–18.

Maneta V. and Baker D. R. (2014) Exploring the effect of lithium on pegmatitic textures: An experimental study. *Am. Mineral.* **99**, 1383–1403.

Maneta V., Baker D. R. and Minarik W. (2015) Evidence for lithium-aluminosilicate supersaturation of pegmatite-forming melts. *Contrib. to Mineral. Petrol.* **170**, 1–16.

Martin R. F. and De Vito C. (2014) The late-stage miniflood of Ca in granitic pegmatites: An open-system acid-reflux model involving plagioclase in the exocontact. *Can. Mineral.* **52**, 165–181.

Mauthner M. H. F. (1996) Mineralogy, geochemistry, and geochronology of the Little Nahanni Pegmatite Group, Logan Mountains, Southwestern Northwest Territories. University of British Columbia.

Mulja T. and Williams-Jones A. E. (2018) The physical and chemical evolution of fluids in rare-element granitic pegmatites associated with the Lacorne pluton, Québec, Canada. *Chem. Geol.* **493**, 281–297.

Nabelek P. I., Russ-Nabelek C. and Denison J. R. (1992a) The generation and crystallization conditions of the Proterozoic Harney Peak Leucogranite, Black Hills, South Dakota, USA: Petrologic and geochemical constraints. *Contrib. to Mineral. Petrol.* **110**, 173–191.

Nabelek P. I., Russ-Nabelek C. and Haeussler G. T. (1992b) Stable isotope evidence for the petrogenesis and fluid evolution in the Proterozoic Harney Peak leucogranite, Black Hills, South Dakota. *Geochim. Cosmochim. Acta* **56**, 403–417.

Norton J. J. (1983) Sequence of mineral assemblages in differentiated granitic pegmatites. *Econ. Geol.* **78**, 854–874.

Parsons I. and Lee M. R. (2005) Minerals are not just chemical compounds. *Can. Mineral.* **43**, 1959–1992.

Pfister J. D., Kontak D. J. and Groat L. (2023) Textural and mineralogical evolution of the Little Nahanni Pegmatite Group (NWT, Canada) with implications for metasomatism, rare-metal mineralization and pegmatite-wall rock interaction. *Can. Mineral.* Accepted with revisions.

Pieczka A., Szuszkiewicz A., Szełęg E. and Nejbert K. (2019) Calcium Minerals and Late-stage Ca-metasomatism in the Julianna Pegmatitic System, the GÓry Sowie Block, Sw Poland. *Can. Mineral.* **57**, 775–777.

Plümper O. and Putnis A. (2009) The complex hydrothermal history of granitic rocks: Multiple feldspar replacement reactions under subsolidus conditions. *J. Petrol.* **50**, 967–987.

Putnis A. (2002) Mineral replacement reactions: from macroscopic observations to microscopic mechanisms. *Mineral. Mag.* **66**, 689–708.

Simmons W., Falster A., Webber K., Roda-Robles E., Boudreaux A. P., Grassi L. R. and Freeman G. (2016) Bulk composition of MT. Mica Pegmatite, Maine, USA: Implications for the Origin of An LCT Type Pegmatite by Anatexis. *Can. Mineral.* **54**, 1053–1070.

Sirbescu M. L. C., Schmidt C., Veksler I. V., Whittington A. G. and Wilke M. (2017) Experimental crystallization of undercooled felsic liquids: Generation of pegmatitic texture. *J. Petrol.* **58**, 539–568.

Suwimonprecha P., Cerny P. and Friedrich G. (1995) Rare metal mineralization related to granites and pegmatites, Phuket, Thailand. *Econ. Geol.* **90**, 603–615.

Sweetapple M. T. and Collins P. L. F. (2002) Genetic framework for the classification and distribution of Archean rare metal pegmatites in the North Pilbara Craton, Western Australia. *Econ. Geol.* **97**, 873–895.

Taylor B. E., Foord E. E. and Friedrichsen H. (1979) Stable isotope and fluid inclusion studies of gem-bearing granitic pegmatite-aplite dikes, San Diego Co., California. *Contrib. to Mineral. Petrol.* **68**, 187–205.

Thomas R., Davidson P. and Beurlen H. (2012) The competing models for the origin and internal evolution of granitic pegmatites in the light of melt and fluid inclusion research. *Mineral. Petrol.* **106**, 55–73.

Van Walraven P. (2011) A textural and mineralogical study of pegmatites on Highway 69, Sudbury, Ontario, with implications for the London model. Laurentian University.

Vignola, P., Zucali, M., Rotiroti, N., Marotta, G., Risplendente, A., Pavese, A., & Bertoldi, G. (2018) The chrysoberyl-and phosphate-bearing albite pegmatite of Malga Garbella, Val Di Rabbi, Trento province, Italy. *The Canadian Mineralogist*, **56**, 411-424.

Webber K. L., Simmons W. B., Falster A. U. and Hanson S. L. (2019) Anatectic pegmatites of the Oxford County pegmatite field, Maine, USA. *Can. Mineral.* **57**, 811–815.

Wise M. A. and Brown C. D. (2011) Chemical composition of coexisting columbite-group minerals and cassiterite from the Black Mountain pegmatite, Maine. *Eur. J. Mineral.* **23**, 817–828.

Worden R. H., Walker F. D. L., Parsons I. and Brown W. L. (1990) Development of microporosity, diffusion channels and deuteric coarsening in perthitic alkali feldspars. *Contrib. to Mineral. Petrol.* **104**, 507–515.

Chapter 2

TEXTURAL AND MINERALOGICAL EVOLUTION OF THE LITTLE NAHANNI PEGMATITE GROUP (NWT, CANADA) WITH IMPLICATIONS FOR METASOMATISM, RARE-METAL MINERALIZATION AND PEGMATITE-WALL ROCK INTERACTION

JÉRÉMIE D. PFISTER[§] AND DANIEL J. KONTAK

Harquail School of Earth Sciences, 935 Ramsey Lake Rd, Sudbury, Ontario P3E 2C6, Canada

LEE A. GROAT

Department of Earth, Ocean and Atmospheric Sciences, University of British Columbia,

Vancouver, British Columbia V6T 1Z4, Canada

Accepted and soon to be published in the Canadian Mineralogist.

2.1 Abstract

Situated in the Northwest Territories (Canada), the Cretaceous (*ca*. 85 Ma) Little Nahanni Pegmatite Group (LNPG) is an LCT-type pegmatite swarm enriched in Li, Sn and Ta. Displaying intensive albitization associated with Rare-Metal (RM) mineralization (*i.e.,* Nb, Ta, Sn), a notably high surface-area-to-volume ratio (*i.e.*, hundreds of thin dikes) and being particularly well exposed in a suite of thirteen glacial cirques, the LNPG provides an ideal opportunity to investigate some unresolved aspects of pegmatite formation and evolution, such as metasomatism, pegmatite-wall rock interaction, and nature and origin of RM mineralization (*i.e.*, magmatic *versus* metasomatic).

Using an integrated approach combining field observations with detailed textural and mineralogical studies, two different stages of pegmatite evolution are documented: primary magmatic followed by intense metasomatism. Preservation of primary magmatic features, such as coarse oriented high-aspect ratio crystals (spodumene, K-feldspar), banded aplites, anisotropic fabrics, and skeletal textures, highlight the importance of undercooling (ΔT) the melt with consequent disequilibrium crystallization and boundary-layer effects. The metasomatic stage is dominated by domains of secondary albite and is attributed to interaction with a residual highly-fluxed sodic melt and is responsible for most of the RM mineralization; less abundant micaceous units and cafemic domains reflect incursion of acidic magmatic-sourced and alkaline wall-rock derived fluids.

Our findings are significant and have widespread application to all pegmatite types. Significant is the finding that the RM mineralization mostly localized to zones of metasomatism.

2.2 Introduction

Pegmatites, which have the same general bulk composition as their more common and voluminous finer-grained plutonic counterparts, are defined by their textural features rather than their chemistry (*i.e.* pegmatites can be granitic, mafic, carbonatitic, etc., but share the same textures; London 2008). Some of the more common textures in pegmatites include: exceptionally coarse grain size, disequilibrium-related mineral intergrowths (*e.g.* graphic granite), strong zoning, masses of fine-grained albitic and/or micaceous units often enriched in incompatible elements, replacement textures (*e.g*. pseudomorphism, dissolution cavities), and an overall strong textural anisotropy. Whereas some of these textures are unequivocally magmatic (*e.g*. graphic granite; London 2009) or secondary (*e.g*. pseudomorphism, dissolution cavities; Černý 1991), the nature and origin of others, such as fine-grained masses of albite and micas with their exotic mineralogy, is more ambiguous. Chemical alteration and replacement of previous phases is usually a preferred explanation (*e.g*., Černý 1982a, Černý 1989, Foord & Cook 1989, Kontak *et al.* 2002, Sweetapple & Collin 2002, Kontak 2006), but many consider such units to be primary (*e.g*., Norton 1983, London & Morgan 2017). The origin of these domains is particularly relevant due to the intimate spatial association of such late-stage units with RM (*i.e.* Ta-Nb-Sn) mineralization, as documented in many Li-Cs-Ta (LCT) pegmatites (Černý 1982a, Černý 1989, Suwimonprecha *et al.* 1995, Fuertes-Fuente & Martin-Izard 1998, Lumpkin 1998, Sweetapple & Collins 2002, Kontak 2006, Kontak & Kyser 2009, Wise & Brown 2011, Kaeter *et al.* 2018, Fuchsloch *et al.* 2019).

Thus, the varied interpretations noted above reveal a wider disagreement about the role of metasomatism in pegmatites. On one side, the apparent lack of replacement textures in primitive pegmatites (London 2008) and experimental data suggesting most textures are primary (London *et al.* 1989, London 2005, 2009, Maneta & Baker 2014, London & Morgan 2017, Sirbescu *et al.*

2017), including late-stage albitic and micaceous units (London & Morgan 2017), suggest metasomatism plays a minimal role in pegmatite formation (London 2008, 2018, London & Morgan 2017). In contrast, empirical and experimental evidence supporting a secondary origin for the aforementioned textures and mineral assemblages (Jahns 1955, 1982, Stewart 1978, Černý 1982a, 1982b, Foord and Cook 1989, Kontak *et al.* 2002, Kontak 2006, Alfonso & Melgarejo 2008, Martin & De Vito 2014, Pieczka *et al.* 2019), including videos of sub-solidus formation of saccharoidal albite after K-feldspar (Maneta and Anderson 2018), suggest that metasomatism plays a significant role in the evolution of pegmatites.

Relevant to this controversy is, that despite an increasingly large amount of textural, mineralogical, geochemical, isotopic, and fluid inclusion evidence suggestive of pegmatite-wall rock interactions (Taylor *et al.* 1979, London *et al.* 1996, Dyar *et al.* 1999, Kontak & Kyser 2009, Martin & De Vito 2014, Burns 2019, Pieczka *et al.* 2019), the commonly cited models for pegmatite formation and evolution treat these magmatic vessels as entirely closed systems (Jahns 1955, London & Morgan 2017).

In order to address the aforementioned issues, we build on previous mineralogical and geochemical studies of a swarm of LCT-type pegmatite dikes referred to as the Little Nahanni Pegmatite Group (LNPG; Groat *et al.* 2003, Kontak *et al*. 2004, Barnes 2010, Barnes *et al.* 2012, Burns 2019). Using numerous field observations of these exceptionally exposed pegmatites and an extensive sample suite selected from about 200 exposed dikes used for detailed petrographic and SEM-EDS (Scanning Electron Microscopy coupled with Energy Dispersive Spectroscopy) analysis, this study addresses the following aspects of pegmatite formation at the LNPG: 1) primary versus secondary mineralogical and textural features; 2) role of metasomatism; 3) nature

of RM mineralization; and 4) pegmatite-wall rock interaction. The results are used to formulate a model for evolution of the LNPG which we suggest is applicable to other rare-element pegmatites.

2.3 Regional geological setting

The LNPG is exposed in a series of thirteen cirques in the Selwyn Mountains (62˚12'N, 128˚50'W) about 45 km NW of the variably active mining community of Tungsten (CanTung Mine), itself ≈10 km from the Yukon-Northwest Territories border (Fig. 1A). It lies in the former Selwyn Basin, a passive margin zone that formed in the Neoproterozoic due to rifting of Rodinia until its closure in the late Devonian (Gordey & Anderson 1993). Starting in the Jurassic, the area was affected by regional-scale deformation due to NE-SW compression and subsequent uplift. This deformation resulted in decollement-style folds on both small- and large scales, in addition to numerous low-angle thrust faults; all such structures trend NW-SE (Gordey 2013). This deformation resulted in a regional metamorphic grade of subgreenschist facies (Gordey & Anderson 1993, Gordey 2013). Maximum regional metamorphic grade is estimated at about 300˚C (Gordey 2013), although andalusite-, sillimanite-, staurolite- and garnet-bearing hornfels (e.g. Fig. 1C, D) are found in the immediate vicinity of felsic intrusions (*i.e.,* aureoles).

The main felsic intrusive event regionally relates to mid-Cretaceous magmatism, the Selwyn Plutonic Suite (SPS), which covers over 8% of the Selwyn Basin at surface (Gordey 2013). This magmatism is associated with numerous important metal deposits, including the CanTung (*ca.* 95 Ma; Hart *et al.* 2004) and MacTung (*ca.* 97 Ma; Selby *et al.* 2003) W-Cu skarns and varied pegmatite systems, such as at O'Grady (Ercit *et al.* 2003) and the LNPG. The LNPG is constrained to *ca.* 85 Ma based on U-Pb TIMS (Thermal Ionization Mass Spectrometry) dating of columbite

(81.6 ± 0.5 Ma; Mauthner *et al.* 1995), zircon (87.3 ± 1.2 Ma; Kontak *et al.* 2016) and cassiterite (87.3 ± 1.7 Ma; Kontak, unpublished data). Thus the LNPG is the youngest known felsic magmatic event in this part of the Selwyn Plutonic Suite. However, despite good bedrock exposure in the area, a possible progenitor granite for the LNPG remains elusive. The closest plutons are the Lened (*ca.* 93 Ma), Cac (age unknown), and Rudi (*ca.* 84-87 Ma) (Groat et al. 2003, Rasmussen 2013) which are all within 30 kms of the LNPG (Fig. 1A).

2.4 Setting and previous studies of the LNPG suite

The LNPG, consisting of more than 200 dikes covering an area of about 15 km by 5 km, occurs on the northeast limb of the Fork Anticline and SW of the regional March Fault (Fig. 1B). The dikes are subparallel to this anticlinal hinge and local folding that trends NW. They are exceptionally well exposed in the faces of numerous cirques which cut into the mixed metasedimentary rocks of the Yusezyu and Narchilla formations, both part of the Proterozoic Hyland Group (Gordey & Anderson 1993). Locally, these metasedimentary rocks consist of coarse- to fine-grained siliciclastic units with variable amounts of carbonate matrix (Barnes 2010). The widest dikes measure about 10 m, although most are ≤2 m. The dikes are particularly enriched in Li and Ta with sub-economic to economic Li and RM mineralization (*i.e.*, Sn, Ta, Nb) (Liverton 2017).

Previous studies of the pegmatites, which are variably incorporated into the model presented below, include general aspects of their setting, textural features, and whole-rock geochemistry (Kontak *et al.* 2004, Barnes 2010), mineralogy and chemistry of the feldspars, micas and oxide phases (Mauthner 1996, Rollo 1999, Pemberton 2002, Groat *et al.* 2003), stable isotopes

(Li, O, D, Fe; Barnes *et al.* 2012, Telus *et al.* 2012, Pfister *et al.* 2019), geochronology (Mauthner *et al.* 1995, Kontak *et al*. 2016) and fluid inclusions (Burns *et al.* 2012, Burns 2019).

2.5 Analytical methods

Field work and collection of samples used in this study were done during three field seasons - 2004, 2007 and 2008 – which was supplemented by additional material collected in the 1990s (Groat *et al*. 2003). From this material, 96 petrographic polished sections were studied in detail using an Olympus BX51 microscope with select samples used for subsequent detailed mineralogical analysis. The latter employed a JEOL 6400 scanning electron microscope (SEM) housed in the Micro-analytical Centre (MAC), Laurentian University which is coupled to a solid-state Oxford-Sight energy dispersive spectrometer (EDS) detector. Analyses were done using a 20 kV accelerating voltage, 1 nA beam current, working distance of 15 mm and acquisition times ranging from 5 to 15 seconds. Data were processed using a combination of Oxford Instrumentation softwares AZtec and INCA. Data were normalized to the non-volatile and non-light (*i.e*. excluding H to F) components of the idealized mineral formulas (*e.g*. 100% for feldspars, 96% for muscovite, 92% for spodumene, etc.).

2.6 Results

The pegmatites are poorly zoned to unzoned at both the local (*i.e.,* outcrop of single dike) and regional (*i.e.,* LNPG dike swarm) scales in the traditional sense (*e.g*., London 2008), yet they exhibit a great degree of textural and mineralogical heterogeneity on both of these scales. In this

study, the term “domain”, which is defined by a distinctive mineral assemblage and textural features, is used instead of the traditional pegmatite “zones”, which imply spatial restrictions (*e.g.,* border zone, outer zone, inner zone, core zone; London 2008). For the LNPG dikes, these various domains are not spatially restricted (other than the pegmatite-wall rock domain) and are commonly superimposed on each other. These domains, which are schematically summarized in Figure 2, are described separately below and referred to throughout.

2.6.1 General observations

As noted previously, the more than 200 dikes are thin (commonly <2 m) and long (up to 100s of meters) (Fig. 3A, B, C), which translates to a very large pegmatite-wall rock contact surface area. Faults crosscutting the dikes (Fig. 3C) and boudinaging (Fig. 3D) indicate post-emplacement brittle-ductile deformation, while dike curvature (Fig. 3E), *en echelon* dikes (Fig. 3F), branching (Fig. 3G, H), and evidence of dextral motion during pegmatite crystallization (Fig. 3I) suggest that overall the pegmatites were emplaced into extensional zones related to bounding shears, such as expected in a Riedel shear-type model, although the aforementioned structures have not been verified.

Regional metamorphism did not exceed sub-greenschist facies (Anderson and Gordey 1993, Gordey 2013), thus the presence of locally abundant cordierite, garnet and andalusite ± staurolite, indicative of higher PT conditions in the wall rock (Fig. 1C, D) at the northernmost part of the pegmatite field (see star in Fig. 1B), suggests contact metamorphism as observed around contemporaneous plutons of the SPS. Local wall-rock brecciation (Fig. 3J) associated with fine-grained quartz-albite dikes suggest a high fluid pressure during the evolution of the LNPG. Additional relevant general observations include: (1) lack of graphic texture and quartz cores, both

noted as common features in pegmatites in general (*e.g.,* London 2008, 2009, 2017); (2) scarcity of mariolitic cavities (i.e., one good locality observed) and boron-bearing phases; and (3) crosscutting relationships within pegmatites dikes (Fig. 3K, L, M).

Observations related to individual domains are summarized in Table 1, illustrated in Figures 4 to 12, and representative EDS analyses of various phases from the LNPG are given in Table 2. The following general features are noted (see Fig. 2 for schematic summary): 1) narrow (<1-2 cm) wall zones of fine-grained equigranular leucogranite material border some pegmatites; 2) the latter gives way to either coarse domains of K-feldspar and spodumene (±quartz, albite and rarely muscovite) with minerals aligned perpendicular to the wall rock contacts, or laminated domains of variable texture and mineralogy; 3) domains of albitization whereby fine-grained saccharoidal type albite or coarse cleavelandite replace earlier domains. Importantly, RM mineralization is common in such areas; 4) dissolution features are lined by zeolite phases with and associated phases; and 5) at the microscopic scale there is abundant textural evidence for replacement reactions *via* coupled dissolution precipitation (CDP) mechanisms.

2.7 Discussion

The following discussion aims to address aspects of the LNPG: (1) its magmatic evolution and in particular various textures (*e.g.*, banded aplites, acicular spodumene); (2) its subsolidus (*i.e.,* metasomatic) stage, including the nature and origin of the metasomatizing agent(s); (3) the nature of RM mineralization and its relationship to metasomatism; and (4) internally- *versus* externally-sourced chemical components and the importance of pegmatite-wall rock interaction. Prior to this, we briefly address the source of pegmatitic melts.

2.7.1 Source of the LNPG melt

The LNPG is an expansive network of dikes extending for 15 km without apparent regional fractionation based on whole-rock (Barnes 2010) and K-feldspar (Kontak *et al.* 2016) chemistry, thus lacking direct petrochemical indices for a potential source of the melts (*i.e.,* progenitor granite). As noted, peak regional metamorphism at the time of dike emplacement (*ca.* 85 Ma) did not exceed sub-greenschist facies which therefore precludes a proximal anatexis model for these LCT-type pegmatites, as suggested for other pegmatite fields (*e.g*., Nabalek et al. 1992, Simmons *et al*. 2016, Knoll *et al*. 2018, Vignola *et al*. 2018, Webber *et al*. 2019), and instead favours melt extraction from an evolved felsic magma (London 2008, Simmons & Webber 2008), such as the regional, contemporaneous, S-type granitic Selwyn Plutonic Suite. An extensive stable isotopic study of the LNPG, which is to be presented independently, also supports a pluton-related origin. That the northern part of the LNPG spatially overlaps with an extensive area of cordierite-andalusite-staurolite-garnet hornfels (Fig. 1C, D), otherwise only observed in aureoles surrounding granitic plutons in the area, offers a solution to the conundrum of a source for the dike and supports a plausible fertile felsic intrusive body. The apparent absence of the inferred progenitor granite is, we suggest, adequately resolved by the presence of the nearby March Fault (Fig. 1B) which may have transported eastwards the pegmatites and their host rocks from their structural footwall wherein would be located the source of the pegmatites (Fig. 13A).

2.7.2 Paragenetic stages

The aforementioned textural and mineralogical information (Table 1) has been used to construct a detailed paragenetic history for the LNPG (Fig. 14) which forms in part the basis of the following discussion. As seen, the evolution of the LNPG is broken into magmatic and metasomatic stages that incorporate the different domains referred to previously, in addition to the pegmatite - wall-rock interaction. An important departure from how other mineral paragenesis are presented for pegmatites in general is that the dominance of melt *versus* fluid does not correlate 1:1 with magmatic *versus* metasomatic. Below is discussed in detailed the nature, evolution and implications of these different stages, which is summarized schematically in Figure 13.

2.7.3 Magmatic stage

The KFD and SAQD: The scarcity of miarolitic cavities, narrow exomorphic aureoles, as well as relatively low abundance of early primary hydrated phases (*i.e*., micas, tourmaline), suggest an initial volatile-undersaturated melt, which concurs with the London model (*e.g.,* London 2008). In addition, the paucity of tourmaline and other B-bearing phases in both the pegmatite dikes and wall rock halo suggests undersaturation in boron. On the other hand, abundant early spodumene crystals (Fig. 5A, B, D, E), disseminated early F-bearing apatite (Fig. 4J), and occasional F-bearing montebrasite (Fig. 11F) indicates the melt was enriched in some fluxing elements (*i.e*., Li, P, F), which is further supported by whole-rock analysis (Barnes 2010). The presence of these fluxes reduces: (1) the viscosity of the melt (Dingwell *et al.* 1996), facilitating its migration away from the parental pluton (Baker 1998); (2) the solidus temperature of the melt (London 2018), allowing a larger degree of undercooling; and (3) the nucleation rate (London 1987), which further promotes undercooling.

The lack of graphic texture, but presence of extremely elongated crystals with high aspect-ratio (up to 1:45; *i.e*., acicular), and sometime skeletal crystal habits, as well as other disequilibrium growth-related textures (*e.g*. plumose micas, various disequilibrium intergrowths; see Fig. 5W; also Barnes 2010), indicates the LNPG collectively underwent substantial undercooling (Lofgren 1974, Maneta & Baker 2014, London & Morgan 2017, Sirbescu *et al.* 2017). In particular, the high aspect-ratio morphology of the early spodumene (Fig. 5A, B, D) and K-feldspar (Fig. 4C) indicates a rapid growth rate coupled to fast cooling rates (Kostov & Kostov 1999), both related to disequilibrium conditions promoted by undercooling. This is consistent with the thin morphology of the dikes (*i.e.,* high aspect ratios and large surface areas) and cooler wall-rock temperatures (*i.e*., ≤250°C), hence rapid heat loss, based on PT conditions constrained from fluid inclusion studies (Burns 2019). This is congruous with both empirical evidence and theoretical conductive thermal modelling of pegmatites (Webber *et al.* 1999, London 2008, 2018, Simmons & Webber 2008, Sirbescu *et al.* 2008). The thermal gradients developed during heat loss resulted in the preferred orientation of the megacrystic phases, spodumene and K-feldspar perpendicular to the pegmatite - wall-rock contact (Fig. 4C, 5A, D).

Commencing with an undercooled melt enriched in some fluxes (*i.e*., Li, P, F) and undersaturated in others (*i.e*., H_2O, B), crystallization started with sanidine ($Or_{86}Ab_{14}$) megacrysts, now represented by perthitic microcline, accompanied by minor quartz (Fig. 4B), albite (Fig. 4I), muscovite, and occasional accessory phases such as apatite (Fig. 4J) and zircon (Fig. 4M). This continued until the activity of Li increased to saturate spodumene, at which point spodumene nucleated at or near the pegmatite margins and grew rapidly perpendicular to the ambient thermal gradient in the dikes. Rare occurrences of dikes locally quenched at this stage preserve acicular spodumene growing into the melt (Fig. 5E). Such rapid crystallization of the spodumene likely

promoted a boundary layer effect and concomitant accumulation of excluded components (*e.g.,* H_2O, Si, Be, Sn, Nb, Ta) at this interface, which resulted in local saturation of quartz (Fig. 5J), muscovite (Fig. 5R), beryl (Fig. 5R, U), cassiterite (Fig. 5S) and CGM (Fig. 5U), all of which are found at the edges of elongate spodumene crystals.

SQUI has been reported from the LNPG (*e.g.* Groat *et al.* 2003, Barnes 2010), but its occurrence rimming earlier spodumene (Fig. 5P, Q) is a new observation. Such domains having an Al:Si ratio of 1:3.96 confirms the isochemical replacement of petalite ($LiAlSi_4O_{10}$), hence a legitimate pseudomorphic SQUI texture. Formation of petalite around earlier magmatic spodumene crystals implies either a temperature increase or a pressure drop (Fig. 15A; London 1984). The latter model, which is considered more plausible for LNPG, thus reflects a change in pressure (*i.e.,* from lithostatic to partially hydrostatic) and is supported by the density variation of secondary fluid inclusions (Burns 2019; isochores in Fig. 15A) which evidently continued post crystallization. Similar pressure changes are reported in other pegmatite districts, such as Covas de Barroso, Portugal (Charoy *et al.* 2001), Forcarei Sur, Spain (Fuertes-Fuente & Martin-Izard 1998), and Preissac-Lacorne, Canada (Mulja & Williams-Jones 2018).

Post spodumene crystallization, a matrix assemblage dominated by albite and quartz with minor muscovite crystalized between the early spodumene and K-feldspar megacrysts (Fig. 4B, C). This matrix exhibits disequilibrium textures, such as plumose muscovite growing on earlier K-feldspar and apatite-muscovite intergrowth (Fig. 5W). This primary albite-quartz assemblage reflects a compositional evolution of the melt towards a more sodic nature, as expected, due to crystallization of abundant K-feldspar and spodumene.

2.7.4 Nature and origin of banded aplite units

Despite a fundamentally different texture with monomineralic layers, the banded aplites consist of the same magmatic minerals as the SAQD but with the important addition of lepidolite. In addition, these aplitic layers often alternate with pegmatite zones (Fig. 6B, C, D) and are sometimes crosscut by the same magmatic material (Fig. 3K, L, M), thus constraining their formation to the magmatic stage. The progressive zoning of CGM seen in these layers, that is Ta enrichment from core to rim (Fig. 6J, K, L), which is a common phenomenon for magmatic CGM (Lathi 1987, Van Lichtervelde *et al.* 2007), further supports a magmatic origin for this domain. The presence of occasional coarse K-feldspar and spodumene pre-dating the aplitic layers (Fig. 6F) is further evidence of a mid- or late magmatic stage for the aplitic layers.

Several models are proposed for the origin of the banded aplites, such as: (1) replacement of layered country rock (Schaller 1925, McLaughlin 1940, also discussed in Jahns 1955); (2) multiple magma injections (Rose 1981, Kleck & Foord 1999); (3) fluctuating pressure or loss of volatiles promoting a change in nucleation and crystal growth kinematics (*i.e.,* quenching) in addition to migration of the quartz-alkali feldspar cotectic (Jahns and Tuttle 1963, also discussed in London 2005); and (4) local saturation in a boundary layer liquid (Rockhold *et al.* 1987, Webber *et al.* 1997, London 1992, 2005, 2014, London *et al.* 2012, London & Morgan 2017). Aplites at the LNPG are clearly magmatic based on both textures and compositions (Barnes 2010), thus hydrothermal mediated replacement of layered wall rock is not considered viable. As for multiple injections, there is some evidence (Fig. 3K, L, M), but even within what would be considered individual pulses, fine-scale banding occurs which demands an alternative model. Although fluctuating pressure is documented in the LNPG (Burns 2019), the lack of petalite and/or SQUI in spodumene-bearing aplites and lack of aplitic texture near the SQUI texture preclude pressure drops. Instead, local saturation of excluded components in the boundary layer is considered more

likely. In this model, components excluded from the crystallization front accumulate in the boundary layer to the point of mineral saturation, which is followed by subsequent and repeated saturation events giving rise to fine-scale banding of quasi-monomineralic composition. Thus, such layers represent episodic advances of the crystallization front in an undercooled melt, as demonstrated experimentally (London 2005, London & Morgan 2017). This model also explains the formation of primary lepidolite layers, which is made possible by the accumulation of volatile component ($H_2O \pm Li, F$) in the boundary layer in an otherwise volatile-undersaturated melt. The banding at the LNPG is thus interpreted as being the product of boundary layer effects along the crystallization front, with sporadic subsequent melt injections responsible for the crosscutting banding (Fig. 3K, L, M) and occasional razor-sharp transitions.

2.7.5 Metasomatic evolution of the LNPG

Much as changes in the melt resulted in forming distinct mineral assemblages in the magmatic stage, evolution of a metasomatizing agent formed metasomatic domains which can partially overlap: (1) saccharoidal albite (±quartz) and associated RM mineralization; (2) mica-rich assemblages; and (3) late-stage Ca-rich assemblages. Textural modification of K-feldspar megacrysts, which record extended subsolidus processes, is discussed separately.

2.7.5.1 Albitization

This is the most widespread post-magmatic feature seen in all dikes where primary K-feldspar is albitized. A secondary origin for the albite is supported by: (1) unequivocal textures showing replacement of K-feldspar (Fig. 10A, C); and (2) relict fragments of earlier phases (Fig. 4B, 10B) which retain primary magmatic features (*i.e.*, glassy K-feldspar with film perthite;

igneous growth zoning in relict CGM (Fig. 10H)), thus predating the saccharoidal albite. Similar albitization is extensively documented in granitic rocks (*e.g*., Lee & Parsons 1997, Parsons & Lee 2005, Plumper & Putnis 2009) and pegmatites (*e.g*., Černý 1989, Kontak *et al*. 2002, Kontak 2006, Kontak & Kyser 2009) and has long been considered a fundamental metasomatic process in mineralized felsic intrusive centres (*e.g.,* Taylor 1979). The occurrence of fine-grained albite (saccharoidal and cleavelanditic) is particularly important given its association with significant RM mineralization (Fig. 4B, 10B, D to G), a feature observed globally in other LCT pegmatites (Černý 1982a, Černý 1989, Suwimonprecha *et al.* 1995, Fuertes-Fuente & Martin-Izard 1998, Lumpkin 1998, Sweetapple & Collins 2002, Kontak 2006, Kontak & Kyser 2009, Wise & Brown 2011, Kaeter *et al.* 2018, Fuchsloch *et al.* 2019).

The metasomatizing agent, sodic in nature, must have contained significant Nb, Ta, Sn ± P in order to form the high concentration of CGM (Fig. 10B, D, E, F), cassiterite (Fig. 10I, J) and phosphates (Fig. 10I, J, K). The abundance of CGM (Fig. 10B), whose constituents (*i.e*., Ta, Nb) are traditionally considered immobile in aqueous fluids (Wood 2005), and paucity of hydrated phases suggests a late Na- and RM-enriched melt as the likely metasomatizing agent versus a hydrothermal fluid (*cf.* Kontak 2006). The evolutionary trend of the melt towards a sodic composition is indicated by formation of albite-quartz as the last primary assemblage in SAQD (Fig. 5B). Such a melt would eventually cause chemical disequilibrium among the residual melt and earlier phases (*i.e*., K-feldspar; *e.g*., Černý 1989), thus causing dissolution and subsequent precipitation of the secondary albite-rich assemblage. We propose therefore a melt-mediated coupled dissolution-precipitation (CDP) model versus alkali ion exchange as the main albitization process. This is further supported by widespread porosity in relict K-feldspar (Fig. 10B, D), a characteristic feature of CDP (Parsons & Lee 2005, Putnis 2002, Putnis *et al*. 2007, Plumper &

Putnis 2009), and the formation of exotic accessory phases (*e.g*., CGM, cassiterite, apatite) in this assemblage, which cannot be explained by simple alkali-exchange.

The H_2O content of this residual melt can only be conjectured, but melt inclusions containing upwards of 50 wt. % H_2O are documented in pegmatites (Thomas & Davidson 2012, Thomas *et al.* 2012), although such evidence is not without debate (*e.g*., Anderson 2016). Furthermore, complete miscibility between pegmatitic melt and H_2O has been verified experimentally (Thomas *et al.* 2000), albeit at PT conditions (>720°C, 1 kbar) a bit unlikely for the LNPG. London (2008, 2014) also reports elevated H_2O in the boundary layer at the crystal-melt interface. Significantly, volatile enrichment (±fluxes) reduces both the viscosity and density of melts thus enhancing migration which would therefore enabled evolved, here sodic melts to migrate through the partially crystallized dikes and facilitate development of widespread albitization herein documented at the LNPG. Additionally, local deviatoric stresses present pegmatite evolution (*e.g.*, *en echelon* (Fig. 3F) and boudinaged (Fig. 3D) dikes) could have played a role in "squeezing" such residual sodic melts upward. Whether the late Na-RM-H_2O-enriched melt formed *via* immiscibility (Thomas *et al*. 2000, Thomas *et al*. 2012), coalescence of boundary layers (London 2008), or fractional crystallization of the parental melt at depth, as suggested for other similar systems (*cf.* Kontak 2006, Kontak & Kyser 2009), remains unanswered in the case of the LNPG.

2.7.5.2 Mica-quartz assemblages

Two types of secondary fine-grained mica-quartz assemblages are observed, muscovite-quartz and lepidolite±quartz. As these are spatially distinct, they are discussed separately. The muscovite-quartz assemblage is less abundant than the saccharoidal albite domain and is

commonly observed as a direct replacement of K-feldspar along fractures and intergranular boundaries (Fig. 11 A to F) or associated with saccharoidal albite (Fig. 10). In the latter, muscovite formation provides a local sink for K released by albitization of K-feldspar. As for replacement of K-feldspar by muscovite-quartz, this suggests hydrolysis of K-feldspar *via* an acidic fluid, as is common in many magmatic-hydrothermal settings where the following reaction (*e.g.*, Plumper & Putnis 2009 and reference therein) applies:

$$3KAlSi_3O_8 + 2H^+ \rightarrow KAlSi_3O_{10}(OH)_2 + 6SiO_2 + 2K^+ \quad (1)$$

Additionally, the scarcity of RM oxides and other HSFE-bearing phases in this assemblage further supports a hydrothermal origin, as such elements (*e.g.*, Ta, Nb, Zr) are traditionally considered immobile in aqueous fluids (Wood 2005). These observations suggest the muscovite-quartz assemblage relates to reaction of crystalized pegmatite with a relatively acidic hydrothermal fluid with low HSFE and RM content. Additionally, the muscovite-quartz assemblage occasionally fills fractures in secondary albite (Fig. 11F), suggesting it post-dates albitization. The presence of Ca-bearing phases (*i.e.*, apatite) in the assemblage (Fig. 11C, E) suggests an external contribution from the wall rock (Fig. 13C). The latter exchange may thus couple with the excess K generated from reaction (1) above causing formation of biotite-rich exomorphic aureoles (Fig. 7A, B), K-feldspathization of plagioclase in the proximal wall rock (Fig. 7G), and formation of muscovite/biotite-rich veins extending from pegmatites into wall rocks (Fig. 7C).

The lepidolite(±quartz) assemblage is also likely related to an acidic hydrothermal fluid, as suggested by: (1) presence of cleavelanditic albite (a low-temperature hydrothermal variety of albite); and (2) breakdown of spodumene to a fine-grained mix of hydrated phases (*e.g.*, illite-montmorillonite, kaolinite, lepidolite, muscovite (Groat *et al.* 2003); Fig. 11G) typical of H- and

F-rich environments (Munoz 1971, London & Burt 1982). The fundamental differences between the two fluids (*i.e*., muscovite-quartz *versus* lepidolite-quartz) are: (1) lower pH allowing the breakdown of spodumene (relatively unaltered in the vicinity of muscovite-quartz (Fig. 5F)], which provided the Li necessary for the formation of lepidolite; and (2) higher fluoride activity, as indicated by significant F in the lepidolite (up to 6.6 wt. %; Groat *et al*. 2003), which explains the presence of many HSFE-bearing phases (*e.g*., CGM, cassiterite, zircon) in the lepidolite(±quartz) assemblages (Fig. 11I, J, K, L) but few in the muscovite-quartz assemblages, as such elements become mobile in F-bearing fluids (Timofeev *et al.* 2015, 2017, Anderson *et al.* 2019). Additionally, acidic fluoride-bearing fluids promote the stability of a trilithionite-quartz (*i.e*., lepidolite-quartz) assemblage over anhydrous K- and Li-aluminosilicates (K-feldspar + spodumene + HF → trilithionite + quartz; see Munoz 1971). The presence of significant F and some HSFE suggests that most of the components of this fluid were internally derived, although some external contribution is reflected by the high Ca- (*i.e*., abundant apatite; Fig. 11H) and Sr- (up to 13 wt. % SrO in apatite) contents of this assemblage.

2.7.5.3 Late stage Ca-metasomatism

The latest stage in the evolution of LNPG is recorded by formation and filling of irregular shaped cavities attributed to fracture-controlled fluid focused dissolution. The lining reflects intense CDP of the wall rock to produce zeolites, micas, clays, quartz, Ca-bearing albite, apatite and carbonates (Fig. 8B, C, D). Examples include: (1) oligoclase ($\leq An_{15}$; Table 2) replacing end-member albite (An_0) (Fig. 12F, G) as indicated by pitting (Fig. 12F, H); (2) Na-dominant (Na>K>Ca) zeolites near albite-rich primary assemblages (Fig. 8I, 12B, C, L); (3) muscovite altered to paragonite and cookeite (Fig. 12D, E); (4) fine-grained muscovite and apatite replacing lepidolite (Fig. 12N); and (5) calcite in partially dissolved (Na, Ca)-bearing zeolites (Fig. 12L, M).

The chemistry of these assemblages reflects the progenitor material being altered, but overall there is significantly more Ca than in the earlier assemblages (Table 2), as commonly observed in pegmatites and referred to as the late-stage Ca-miniflood (Martin & De Vito 2014; also see Moiana (2017) and Pieczka *et al.* (2019)). The elevated Ca-content, an element depleted in the magmatic stage of LNPG and LCT pegmatites in general, necessitates the late-stage fluid to be externally derived, as noted by Burns (2019) based on the chemistry of fluid inclusions and further discussed below. The presence of disseminated Sn- and Ta-bearing phases, such as cassiterite (Fig. 12H), wodginite (Fig. 12K), wickmanite (Fig. 12J) and calcio-microlite (Fig. 12I), in dissolution features in this assemblage indicates the fluid was able to re-mobilize some of the RM, likely facilitated by residual fluoride (*i.e.*, presence of fluorapatite and fluorite).

2.7.5.4. Textural modification of K-feldspar megacrysts

The K-feldspar megacrysts record extended sub-solidus modification facilitated by a fluid, as evidence by the presence of fluid inclusions in the neomorphic phase (Fig. 4O; see also Burns 2019). Originally crystallized as homogeneous sanidine ($Or_{86}Ab_{14}$; Table 2), the K-feldspar is now perthitic microcline (*i.e.*, intermediate to ordered low microcline; Groat *et al.* 2003) with near end-member domains (*i.e.*, Ab_{100} and $Or_{95\text{-}100}$). The perthitic textures reflect an overall coarsening or maturation from film through string, flame, and patchy/bleb types (Fig. 4D to G) and is intimately related to development of micropores (Fig. 4D to H), a well-known and fundamental feature of CDP indicative of fluid-mediated reactions (Worden *et al.* 1990, Putnis 2002, Parsons & Lee 2005, Plumper & Putnis 2009, Maneta & Anderson 2018). That domains of variable perthites co-exist on the mm scale (Fig. 4H) indicates the heterogeneous nature of the crystal-fluid interactions (*e.g.*, Worden *et al*. 1990, Parsons & Lee 2005).

2.7.5.5 Summary of the metasomatic evolution

The LNPG records the imprint of a compositionally evolving metasomatizing agent. It started with a corrosive sodic- and volatile-enriched residual melt that infiltrated, likely in an upward direction related to its density, through the sub-vertical dikes (Fig. 13C). This medium caused widespread albitization with associated RM mineralization. Subsequently a residual acidic fluid effected hydrolysis of earlier aluminosilicates (*i.e.*, K-feldspar, spodumene) to mica-quartz assemblages. Variations in the pH and fluoride activity of the fluid related to fluid-rock interactions and contributions of an external fluid resulted in formation of either HSFE-poor muscovite-quartz assemblage after K-feldspar (*i.e.*, low pH, low-F activity) in some dikes or HSFE-bearing lepidolite(±quartz) assemblage after K-feldspar and spodumene (*i.e.*, very low pH, high-F activity) in other dikes. Collapse of the orthomagmatic dominated alteration allowed infiltration of an external fluid (Fig. 13C) which resulted in the paragenetic evolution towards a late Ca-rich stage culminated by a zeolite-apatite-calcite assemblage that occluded dissolution features.

2.7.6. Rare-metal mineralization

As described above, RM mineralization, whether hosted in magmatic or metasomatic stages, is more abundant where sodic-rich metasomatic domains prevail. Notably this feature is common to LCT pegmatites globally (see references below). Given their distinct features and implications, the magmatic and metasomatic RM formation are discussed separately below.

2.7.6.1 Magmatic RM mineralization

These RM oxides are found in the KFD and SAQD and are characterized by having either fluctuating (Fig. 4K, 9F) or progressive (Fig. 6J, K, L, 10H) zoning. Fluctuating growth zoning of HFSE phases, particularly in CGM, is common in granitic pegmatites and generally attributed to a magmatic origin (Lahti 1987, Van Lichtervelde *et al.* 2007). As network-forming elements Nb and Ta have slow diffusivities in highly polymerized peraluminous melts (*e.g.,* Nb^{5+} present as NbO_6 moeities share corners with SiO_4 and AlO_4 tetrahedra; Piilonen *et al.* (2006)), fluctuating growth zoning in CGM is commonly attributed to slow diffusion of these elements relative to their crystal growth rate (Van Lichtervelde *et al.* 2007), as well as disequilibrium crystallization (Van Lichtervelde *et al.* 2018). An alternative explanation for the development of fluctuating or oscillatory zoning in HSFE-bearing phases (*e.g*., CGM, zircon) consists of fluctuating PT during crystal growth, as supported by experiments suggesting temperature fluctuations of 3-10˚C can produce oscillatory zoning in zircon (Melnik & Bindeman 2018). The same experiments suggest ΔP_{fluid} of 50 bars, such as documented at LNPG (Burns 2019), does not produce oscillatory zoning. Considering that most of the fluctuatingly-zoned CGM formed during the early magmatic stage at LNPG (*i.e*., KFD and SAQD) the diffusion-controlled processes is favoured.

RM oxides in the banded aplite-pegmatite dikes tend to be concentrated along specific layers (Fig. 6F). The CGM grains exhibit progressive zoning (increase of Ta from core to rims; Fig 6J, K L), which is considered a magmatic feature (Lahti 1987), and are commonly accompanied by cassiterite (Fig 6G, H, I). As the banding in these dikes is attributed to boundary layer effects at the crystallization front (see above), it is not surprising that CGM and cassiterite saturation regularly occurred in the advancing boundary layer. For this reason, the aplitic layers contain higher RM mineralization than other magmatic domains (Fig. 6F).

2.7.6.2 Metasomatic rare-metal mineralization

Most of the RM oxide mineralization at the LNPG are associated with the metasomatic stage and particularly in the saccharoidal albite masses (Fig. 4B, 10B), with notable occurrences in the fine-grained lepidolite±quartz assemblage (Fig. 11, I, J, K) and locally in the late Ca-rich assemblages (Fig. 12H, I, J, K). For the association of RM with saccharoidal albite, we noted that it is also reported for many LCT pegmatites (Černý 1982, 1989, Suwimonprecha *et al.* 1995, Fuertes-Fuente and Martin-Izard 1998, Lumpkin 1998, Sweetapple & Collins 2002, Kontak 2006, Kontak & Kyser 2009, Wise & Brown 2011, Keater *et al.* 2018). For LNPG, the CGM consist of small (≤2 mm; Fig. 11B), chemically homogeneous (Fig 9G) and commonly elongate (Fig. 10B, G) crystals. These grains are almost invariably Nb- and Mn-dominant, which contrasts with fluctuatingly-zoned and occasional Ta-rich CGM in the earlier magmatic stage. Rare relic CGM grains exhibiting fluctuating zoning and corrosion rims (Fig. 10H) are occasionally in this domain, but the homogeneous columbite-(Mn) grains are clearly contemporaneous with albitization as they are absent in relict K-feldspar, as noted in other settings (*e.g.*, Kontak 2006). The presence of significant Li, F, and P in the melt during its earlier stages would have enhanced the solubility of Nb and Ta (Keppler 1993, Wolf & London 1993, Linnen & Keppler 1997, Linnen 1998, Bartels *et al*. 2010), thus delaying CGM crystallization and promoting Nb- and Ta-enrichment in the residual melt. Decreasing temperature and crystallization of abundant spodumene, which consumed large amounts of Li, considerably reduced Nb and Ta solubility (Linnen 1998) which likely triggered CGM precipitation during SAQD formation. However, the evolution of the melt from strongly peraluminous to sodic- and volatile-enriched indicates depolymerization and increased alkalinity, which allowed the residual melt to retain Nb and Ta until albitization commenced. The increase of Nb and Ta solubility in melts with a lower Aluminium Saturation Index (ASI; molar (Na+K)/Al)>1), that is increasing alkalinity, is well documented (*e.g.,* Linnen

& Keppler 1997, Van Lichtervelde et al. 2010, Aseri *et al*. 2015). Importantly, lower ASI has a greater impact on Ta and Nb solubilities than the presence of volatiles and fluxing elements, such as Li, F, P (Aseri *et al*. 2015), and decreases the temperature-dependence of such solubilities (Linnen & Keppler 1997). Furthermore, Linnen & Keppler (1997) note that since the O-Na bond is weaker than the O-H bond, Nb^{5+} and Ta^{5+} will react much more easily with the (Si,Al)-ONa moieties than with (Si,Al)-OH. Piilonen *et al.* (2006) also suggest the presence of Na in the vicinity of Nb^{5+}, present as NbO_6 moieties in the melt, *via* non-bridging atoms of oxygen (NBO) to fulfil bond-valence requirements. Thus, it is the sodic nature of the residual melt rather than its enrichment in volatile and/or fluxes that allow elevated Nb and Ta contents despite its low temperature.

The RM mineralization related to the lepidolite±quartz assemblage, itself a function of an acidic F-bearing hydrothermal fluid, contains disseminated and unzoned CGM albeit in lesser concentrations than saccharoidal albite. It has been shown that such acidic F-bearing fluids can carry both Nb and Ta (Timofeev *et al.* 2015, 2017, Anderson *et al.* 2019). Additionally, Harlaux *et al.* (2017) and Fredriksson (2017) recently documented Ta- and Nb-enrichment in fluid inclusions from pegmatites. Relevant here is that formation of lepidolite and other hydrated phases, which consumed F and OH, can destabilize the fluoride and hydroxide complexes carrying Nb and Ta which therefore trigger CGM precipitation (Timofeev *et al.* 2017, Anderson *et al.* 2019).

Finally, the presence of cassiterite, wodginite, (tetra-?)wickmanite, and calciomicrolite in the latest Ca-rich assemblage suggests that the late-stage fluid was able to re-mobilize small amounts of Ta and Sn. Cassiterite and calcio-microlite are clearly associated with replacement of earlier phases *via* CDP (Fig. 12H, I) while wodginite and wickmanite occur along fractures (Fig 12J, K). The restricted distribution of calcio-microlite in apatite (Fig. 12I) and wickmanite along

fractures in Mn-bearing apatite (Fig. 12J) suggests that fluid-mineral interaction triggered this mineralization. More specifically, the interaction between a Ta-bearing fluid and a Ca-bearing phase triggered the precipitation of calico-microlite and the interaction between a Sn-bearing fluid and Mn-bearing apatite triggered the precipitation of (tetra-?)wickmanite.

2.7.6.3 RM mineralization in the greisen-like domain

Although only restricted to a few dikes, the greisen-like domain includes some of the highest RM oxide concentration in the LNPG and exhibits textures unique to this domain. Figure 9 shows three different generations of RM mineralization: 1) relict fragments of early magmatic fluctuatingly-zoned CGM (Fig. 9E, F); 2) large (Ta, Nb)-bearing cassiterite (Fig 9A, D, G) intergrown with quartz and pencil muscovite; and 3) homogeneous manganocolumbite in late fluorapatite veinlet (Fig 9G).

The cassiterite, which represents most of the RM mineralization in this domain, exhibits micro-strings and patches of stoichiometric SnO_2 (*i.e.,* > 99.9% SnO_2) (Fig. 9E) suggestive of an exsolution texture. Curiously, most fragments of fluctuatingly-zoned CGM, which only occur in the cassiterite, are found in areas of pure SnO_2 (Fig. 9E). Suwimonprecha *et al.* (1995) suggested that CGM can exsolve from Nb-Ta(±Mn,Fe)-bearing cassiterite. In such cases, the cassiterite becomes depleted in Nb, Ta and Mn(±Fe) (*i.e.,* stoichiometric SnO_2; > 99.9% SnO_2), such as the strings and patches observed here. However, the presence of fluctuating zoning in those CGM inclusions and their fragmental morphologies (Fig. 9F) suggests that they are relict fragments of early magmatic CGM rather than the product of exsolution. The spatial relationship between the CGM fragments and the strings of pure cassiterite therefore remain enigmatic.

2.7.7 Pegmatite-wall rock interaction

Multiple lines of evidence support chemical exchange between pegmatite and wall-rock domains from the early magmatic to later hydrothermal stage of pegmatite evolution. Local enrichment in cafemic elements (*e.g.,* Ca, Fe, Mg) is divided in two main categories: (1) an early stage localized to the contact due to melt contamination by the wall rock attending its emplacement and crystallization; and (2) later fluid-mediated exchange during the metasomatic stage.

Early magmatic Ca-, Fe- and Mg-bearing phases such as apatite (Fig. 7D), tourmaline (Fig. 7E, F), and garnet (Fig. 7E) are common near the contact, yet rare elsewhere in the dikes. The latter elements were likely externally derived with melt-wall rock exchange triggering crystallization of the noted phases, as in other settings (*e.g*., London *et al.* 1996, Kontak 2006, Martin & De Vito 2014). Wall-rock inclusions in the dikes, as observed in other pegmatites (Van Lichtervelde *et al.* 2006), are absent at the LNPG, hence early pegmatite-wall rock exchange was likely fluid-mediated (rather than dissolution of wall-rock components at the contact), and the volatile-undersaturated nature of the melt suggests it may have been externally derived. The presence of impermeable shale units (Barnes 2010) in the pegmatite-hosting Fork anticline (Fig. 1B), which constitutes a structural trap for hydrothermal fluids, supports the presence of an ambient fluid in the wall rock (Fig. 13A). We suggest that the volatile-undersaturated melt facilitated dissolving some of this external fluid (London & Morgan 2017), perhaps under periods of pressure cycling, and the elements it carried (Ca, Fe, Mg) which combined with melt components (*e.g.,* P, Al, Si, B) to saturate it in apatite, garnet, and tourmaline (Fig. 13B). Saturation of pegmatitic phases due to wall-rock derived components *via* an external fluid has been previously suggested by others (London *et al.* 1996, Linnen *et al.* 2019).

Pegmatite-wall rock exchange during the metasomatic stage is recorded by late stage Ca-metasomatism, as seen by replacement of end-member albite by oligoclase (An_{15}) *via* CDP (Fig. 12F, G, H), and abundance of Ca-bearing phases such as zeolites (Fig. 8G, I, 12A), apatite (Fig. 8F, G, 9L, M, 10M, 12N), calcite (Fig. 8A, 12K-M) and fluorite (Fig. 8B-D) lining dissolution cavities and fractures. Enrichment of Ca, an element depleted in LCT pegmatites in general (*e.g.* London 2008), suggests the late-stage fluid was significantly influenced by the metasedimentary wall rock. A small degree of potassic alteration in the proximal wall rock (Fig. 7A, B, G) and phosphoric alteration of allanite to monazite in the exomorphic aureole (Fig. 7K) further support fluid-mediated pegmatite-wall rock exchange. Similar features, particularly the late stage Ca "miniflood", are commonly observed in other pegmatites (Martin & De Vito 2014, Moiana 2017, Pieczka *et al.* 2019). Martin & De Vito (2014) proposed an open system acid-reflux model, where a pegmatite-derived orthomagmatic fluid leaches Ca from the proximal wall rocks and re-introduces it into the pegmatites *via* convection. However, the large amount of acidic orthomagmatic fluid required for this model, yet limited alteration of Ca-bearing phases in the wall rock and small size of the exomorphic aureoles, make this model difficulty to envisage at the LNPG. An alternative explanation, consisting of an incursion of externally derived fluid during the metasomatic stage, is therefore preferred. Fluid inclusions studies at the LNPG (Burns 2019) further support an external fluid based on the chemisry of secondary fluid inclusions: 1) their depleted $\delta^{13}C$ signature (*i.e.*, -25‰); 2) enrichment of the volatile component in N_2 and CH_4; and 3) enrichment of solute component in cafemic elements. We therefore propose that the evolution of the metasomatizing fluid from acidic and F-rich (mica-rich assemblages) to Ca-bearing aqueous-carbonic (late stage Ca-rich assemblages) represents a progressive fluid mixing between orthomagmatic derived and externally sourced fluids (Fig. 13C), rather than convection of an

orthomagmatic fluid redistributing elements between pegmatite and wall rock. Given the larger volume of external fluid available versus orthomagmatic fluid, such mixing inevitably resulted in a composition that approached that of the external fluid. This is further supported by stable isotopic data (Pfister *et al.* 2019; our unpublished data) indicating a contribution from external O- and D reservoirs during pegmatite evolution.

2.7.8 Implications for the internal evolution of LCT-type pegmatites

The results of the present study provide a basis to address several aspects of current models for the internal evolution of LCT-type pegmatites: 1) metasomatism; 2) RM mineralization; and 3) pegmatite-wall rock exchange.

The role of metasomatism in pegmatites remains contentious with some models advocating a minimal to non-existent role (*e.g.*, London 2008, 2018, London & Morgan 2017) while others argue it is crucial in pegmatite evolution (*e.g.*, Kontak 2006, Kontak & Kyser 2009, Martin & De Vito 2014). For example, the controversial nature of late-stage fine-grained albitic and micaceous units has been variably interpreted as either primary (*e.g.*, Norton 1983, London 2009, London & Morgan 2017) or secondary (*i.e.,* metasomatic; Černý 1989, Kontak *et al.* 2002, Kontak 2006, Kontak & Kyser 2009, Martin & De Vito 2014, Kaeter et *al.* 2018). The abundance of relict K-feldspar fragments (*e.g.*, Fig. 4B, 10B), replacement textures (*e.g.*, Fig. 10A, C, 11A, B, C), and dissolution features (*e.g.*, porosity development; Fig. 10B, D) associated with saccharoidal albite we argue are unequivocally supportive of CDP processes for such units.

While some authors interpret albitization as strictly hydrothermal (*e.g.,* Martin & De Vito 2014), others have argued for a late-stage corrosive sodic melt as metasomatizing agent (*e.g.*, Kontak 2006, Kontak & Kyser 2009). In the context of the LNPG, the albitizing agent is considered a highly-fluxed sodic residual melt in disequilibrium with earlier phases causing CDP as it migrates through the dikes. Melt-crystal disequilibrium is generally uncommon in most igneous rocks as it requires a significant change in melt composition (*e.g.*, magma mixing). However, pegmatites are a notable exception as sequential crystallization causes an evolutionary trend of the melt towards sodic, alkaline and silica-poor compositions (London 2008, 2014, London & Morgan 2017), which eventually becomes corrosive to earlier K-feldspar-rich assemblages (Černý 1989). In our model, the late sodic-rich melt must interact with earlier phases (*e.g.* K-feldspar) to cause albitization *via* CDP, which is dependent on its ability to migrate through the dikes. Such migration is facilitated by: (1) significant volatile- and flux enrichment, reducing both melt density and viscosity; (2) vertical geometry of the dikes facilitating the ascent of this melt; and (3) local shear stress. We recognize that such parameters differ among pegmatite systems, thus resulting in various degree of albitization. Pegmatites exhibiting poor internal zoning and widespread albitization, such as the LNPG, indicate significant migration of the late sodic melt, while concentrically zoned pegmatites where discrete saccharoidal albite units are spatially restricted to the inner zones indicate a low degree of residual melt migration.

In addition to melt-mediated Na metasomatism, this study provides abundant evidence for subsequent hydrothermal metasomatism: (1) intense porosity development, a characteristic feature of CDP processes (Parsons & Lee 2005, Plumper & Putnis 2009); (2) generation of irregular cavities, likely products of fracture-controlled fluid focused dissolution *via* CDP processes; (3) hydrolysis of K-feldspar to fine-grained mica-quartz assemblages; and (4) fluid-mediated textural

evolution of the K-feldspar. Although commonly overlooked, similar features are present in most LCT-type pegmatites (*e.g*., Tanco, MB and Aubrey, northern ON; our unpubl. observations) and suggest metasomatism *via* CDP is crucial to the evolution of LCT-type pegmatites to accommodate their present-day mineralogy.

RM mineralization is frequently associated with late-stage albitic and micaceous units in LCT-type pegmatites (Černý 1982a, Černý 1989, Suwimonprecha *et al.* 1995, Fuertes-Fuente & Martin-Izard 1998, Lumpkin 1998, Sweetapple & Collins 2002, Kontak 2006, Kontak & Kyser 2009, Wise & Brown 2011, Kaeter *et al.* 2018, Fuchsloch *et al.* 2019). Despite this intimate spatial relationship with replacement units, such RM mineralization is also interpreted as primary (*e.g*., Taylor *et al.* 2005, Van Lichtervelde *et al.* 2007) and preceding metasomatism. We argue that RM mineralization can be delayed until the metasomatic stage, originally caused by the presence of Li, F, ±P in the melt and followed by its subsequent evolution towards a more sodic (*i.e*., alkaline) composition (Linnen & Keppler 1997, Linnen 1998, Bartels *et al*. 2010, Van Lichtervelde *et al.* 2010, Aseri *et al*. 2015), promoting high Nb and Ta solubilities. Metasomatic RM mineralization is supported by our observations: (1) lack of magmatic features (*i.e*., fluctuating or progressive zoning) in CGM in saccharoidal albite and lepidolite±quartz units; and (2) scarcity of RM mineralization in early magmatic units (*e.g*., KFD, SAQD). Furthermore, we also document some late hydrothermal RM mineralization associated with lepidolite±quartz and Ca-rich assemblages. Controversial in the past, hydrothermal Ta-Nb mineralization is supported by recent experimental work by Timofeev *et al.* (2017) and Anderson *et al.* (2019) demonstrating Ta and Nb mobility in F-bearing fluids and has been documented in other types of RM deposits (*e.g*., Timofeev & Linnen 2015). These observations indicate that metasomatism is an ore-forming process in pegmatites, as

suggested by its abundance in the metasomatic domains of LCT-type pegmatites and noted by others (*e.g*., Kontak 2006, Martin & De Vito 2014).

Finally, Jahns (1955) and London & Morgan (2017) argued that pegmatites evolve as essentially closed systems. However, the formation of garnet, tourmaline, and apatite at the contact and the late stage Ca-miniflood indicate a protracted pegmatite-wall rock exchange through the LNPG evolution. This is further supported by fluid inclusion studies (Burns 2019) and our stable isotopic data (Pfister *et al.* 2019). Similar evidence for pegmatite-wall rock exchange is documented in other pegmatite settings (Taylor *et al*. 1979, London *et al.* 1996, Dyar *et al.* 1999, Kontak *et al*. 2002, Carruzzo *et al*., 2004, Kontak & Kyser 2009, Ashworth 2014, Martin & De Vito 2014, Burns 2019, Pieczka *et al.* 2019), suggesting that pegmatites evolve as partially open systems.

2.8 Conclusions

This study presents abundant evidence for the presence of two different stages, magmatic and metasomatic, in the evolution of a well-exposed LCT-type pegmatite setting at LNPG (NWT, Canada). The magmatic stage records many of the diagnostic textures widely recognized to reflect disequilibrium crystallization of felsic pegmatite melts (*e.g*., line-rock, coarse oriented crystals, skeletal textures, anisotropic fabrics). In particular for LNPG, we interpret the textures observed at the macro- and microscopic scales to reflect crystallization of a volatile undersaturated melt that experienced substantial undercooling (ΔT). Whereas the magmatic stage of pegmatite evolution has received much attention in the literature, we suggest the second, metasomatic stage so pervasive at LNPG is misrepresented and in fact is far more important and widespread a

phenomenon than historical literature suggests. The latter is represented by development of secondary albite-rich domains, both saccharoidal and cleavelanditic, muscovite/lepidolite domains, and calcic-rich domains. This textural modification of the magmatic assemblage is attributed to its interaction with a late-stage sodic-rich melt, an acidic hydrothermal fluid, and an alkaline cafemic-rich fluid, respectively; whereas the first two of these are cognate to the evolving pegmatite system the third is wall rock sourced. Importantly, whereas some RM mineralization occurs in the earlier magmatic stage at LNPG, most is distributed in the subsequent metasomatic stage.

Lastly, we suggest these findings have widespread application to LCT pegmatite settings globally, and in fact to all other pegmatite-types, and are particular relevant for the origin, nature and distribution of critical metals in pegmatites.

2.9 Acknowledgments

We would like to thank Dr. Andrew McDonald for multiple discussions which improved sections of this publication and William Zhe for his assistance regarding the calibration and usage of the SEM-EDS at the Laurentian University. Dr. R.F."Bob" Martin is acknowledged for his long-time contribution to furthering our understanding of pegmatites and his many discussions over the years, some aspects of which are contained in this contribution (*e.g.*, "Ca-miniflood"). The paper was substantially modified and much improved due to the constructive comments of journal reviewers for which we are most appreciative. This study was supported financially by an NSERC Discovery Grant to Dr. Daniel J. Kontak.

2.10 References

Alfonso P., & Melgarejo J.C. (2008) Fluid evolution in the zoned rare-element pegmatite field at Cap de Creus, Catalonia, Spain. *The Canadian Mineralogist* **46** 597–617.

Anderson A. J. (2016) Discreditation of diomignite and its petrologic implications. *American Mineralogist* **101**, 1700–1703.

Anderson A. J., Mayanovic R. A., & Lee T. (2019) The local structure of Ta(V) aqua ions in high temperature fluoride and chloride-bearing solutions: Implications for Ta transport in granite-related postmagmatic fluids. *The Canadian Mineralogist* **57**, 1–19.

Aseri A. A., Linnen R. L., Che X. D., Thibault Y., & Holtz, F. (2015) Effects of fluorine on the solubilities of Nb, Ta, Zr and Hf minerals in highly fluxed water-saturated haplogranitic melts. *Ore Geology Reviews* **64**, 736–746.

Ashworth, L. (2014) *Mineralised Pegmatites of the Damara Belt , Namibia : Fluid inclusion and geochemical characteristics with implications for post- collisional mineralisation*. Ph.D. thesis, University of the Witwatersrand, 299 pp.

Baker, D. R. (1998) The escape of pegmatite dikes from granitic plutons: Constraints from new models of viscosity and dike propagation. *The Canadian Mineralogist* **36(2)**, 255–263.

Bartels A., Holtz F., & Linnen R. L. (2010) Solubility of manganotantalite and manganocolumbite in pegmatitic melts. *American Mineralogist* **95(4)**, 537–544.

Barnes E.M. (2010) *Emplacement and geological setting of the Little Nahanni Pegmatite Group, Northwest Territories and its geochemical and lithium isotopic evolution*. Ph.D. thesis, University of British Columbia, 236 pp.

Barnes E.M., Weis D., & Groat L.A. (2012) Significant Li isotope fractionation in geochemically evolved rare element-bearing pegmatites from the Little Nahanni Pegmatite Group, NWT, Canada. *Lithos* **132–133**, 21–36.

Burns M.G. (2019) *A fluid inclusion study of the Little Nahanni LCT-type pegmatite group, NWT Canada: Implications for the nature and origin of fluids in LCT-type pegmatites and pegmatite evolution*. M.Sc. thesis, Laurentian University, 92 pp.

Burns M.G., Kontak D.J., and Groat L.A. (2012): The role of fluids during alteration and mineralization of the highly evolved Little Nahanni LCT-type Pegmatite Group: A fluid inclusion approach. *Program with Abstracts, 11th Pan-American Current Research on Fluid Inclusions Conference*, Windsor, ON, p. 11-12.

Carruzzo, S., Kontak, D.J., Clarke, D.B., & Kyser, T.K.. (2004) Stable isotope study of mineralization in the New Ross area, South Mountain Batholith, Nova Scotia: evidence for multiple source reservoirs. *Canadian Mineralogist* **42**, 1425-1442.

Černý P. (1982a) The Tanco pegmatite at Bernic Lake, southeastern Manitoba. *Mineral Assoc Canada*, Short Course Handbook **8**, 527–543.

Černý P. (1982b) Anatomy and classification of granitic pegmatites. *Mineral Assoc Canada*,

Short Course Handbook **8**, 1–39

Černý P. (1989) Characteristics of pegmatite deposits of tantalum. In: *Lanthanides, Tantalum and Niobium*. Berlin, 195–239.

Černý, P. (1991) Rare-element Granitic Pegmatites. Part I: Anatomy and Internal Evolution of Pegmatite Deposits. *Geoscience Canada* **18**, 49–67.

Černý P., & Ercit T.S. (2005) The classification of granitic pegmatites revisited. *The Canadian Mineralogist* **43**, 2005–2026.

Charoy B., Noronha F., & Lima A. (2001) Spodumene-petalite-eucryptite: mutual relationshops and pattern of alteration in Li-rich aplite-pegmatite dykes from northern Portugal. *The Canadian Mineralogist* **39**, 729–746.

Chevychelov V., Zaraisky G., Borisovsky S., & Borkov D. (2004) Partitioning of Ta and Nb between magmatic melt and aqueous (K,Na,H)F-containing fluid: Effects of temperature and chemical composition of the melt. In: *EMPG-X Symposium abstracts*

Dingwell D. B., Hess K. U., & Knoche R. (1996) Granite and granitic pegmatite melts: Volumes and viscosities. *Transactions of the Royal Society of Edinburgh, Earth Sciences*, **87(1–2)**, 65–72.

Dyar M.D., Guidotti C.V., Core D.P., Wearn K.M., Wise M.A., Francis C.A., Johnson K., Brady J.B., Robertson J.D., & Cross L.R. (1999) Stable isotope and crystal chemistry of tourmaline across pegmatite - country rock boundaries at Black Mountain and Mount Mica, southwestern Maine, USA. *European Journal of Mineralogy* **11**, 281–294.

Ercit T.S., Groat L.A., & Gault R.A. (2003) Granitic pegmatites of the O'Grady batholith, N.W.T., Canada: A case study of the evolution of the elbaite subtype of rare-element granitic pegmatite. *The Canadian Mineralogist* **41**, 117–137.

Foord E.E., & Cook R.B. (1989) Mineralogy and paragenesis of the McAllister Sn-Ta-bearing pegmatite, Coosa County, Alabama. *The Canadian Mineralogist* **27**, 93–105.

Fredriksson J. R. (2017) *Fluid inclusion and trace-element analysis of the rare- element pegmatite bodies Altim and Tamanduá from the Borborema Province, Brazil*. MSc thesis. University of Helsinki. 98 pp.

Fuchsloch W.C., Nex P.A.M., & Kinnaird J.A. (2019) The geochemical evolution of Nb–Ta–Sn oxides from pegmatites of the Cape Cross–Uis pegmatite belt, Namibia. *Mineralogical Magazine* **83**, 161–179.

Fuertes-Fuente M., & Martin-Izard A. (1998) The Forcarei Sur rare-element granitic pegmatite field and associated mineralization, Galicia, Spain. *The Canadian Mineralogist* **36**, 303–325.

Hart C. J. R., Goldfarb R. J., Lewis L. L., & Mair J. L. (2004) The northern Cordilleran mid-Cretaceous plutonic province: Ilmenite/magnetite-series granitoids and intrusion-related mineralisation. *Resource Geology* **54(3)**, 253–280.

Harlaux M., Mercadier J., Bonzi W. M. E., Kremer V., Marignac C., & Cuney, M. (2017)

Geochemical signature of magmatic-hydrothermal fluids exsolved from the Beauvoir rare-metal granite (Massif Central, France): Insights from LA-ICPMS analysis of primary fluid inclusions. *Geofluids*.

Gordey S.P. (2013) Evolution of the Selwyn Basin region, Sheldon Lake and Tay River map areas, central Yukon. *Geological Survey of Canada Bulletin* **599**.

Gordey S.P., & Anderson R.G. (1993) Evolution of the northern Cordilleran miogeocline, Nahanni map area (105I), Yukon and Northwestern Territories. *Geological Survey of Canada Memoir* **428**.

Groat L.A., Mulja T., Mauthner M.H.F., Ercit T.S., Raudsepp M., Gault R.A., & Rollo H.A. (2003) Geology and mineralogy of the Little Nahanni rare-element granitic pegmatites, Northwest Territories. *The Canadian Mineralogist* **41**, 139–160.

Iveson A.A., Webster J.D., Rowe M.C., & Neill O.K. (2019) Fluid-melt trace-element partitioning behaviour between evolved melts and aqueous fluids: Experimental constraints on the magmatic-hydrothermal transport of metals. *Chemical Geology* **516**, 18–41.

Jahns R.H. (1955) The study of pegmatites. *Economic Geology 50th Anniversary*:1025–1130.

Jahns R.H. (1982) Internal Evolution of Pegmatite Bodies. *Mineralogical Association of Canada*, Short Course Handb **8**, 293–327.

Jahns R.H., & Burnham C.W. (1969) Experimental studies of pegmatite genesis: I. A model for the derivation and crystallization of granitic pegmatites. *Economic Geology* **64**, 843–864.

Jahns R.H., & Tuttle O.F. (1963) Layered pegmatite-aplite intrusives. *Mineralogical Society of America Special Paper* **1**, 78–92.

Kaeter D., Barros R., Menuge J.F., & Chew D.M. (2018) The magmatic–hydrothermal transition in rare-element pegmatites from southeast Ireland: LA-ICP-MS chemical mapping of muscovite and columbite–tantalite. *Geochimica et Cosmochimica Acta* **240**, 98–130.

Keppler H. (1996) Constraints from partitioning experiments on the composition of subduction-zone fluids. *Nature* **380**, 237–240.

Kleck W.D., & Foord E.E. (1999) The chemistry, mineralogy, and petrology of the George Ashley Block pegmatite body. *American Mineralogist* **84**, 695–707.

Knoll T., Schuster R., Huet B., Mali H., Onuk P., Horschinegg M., Ertl A. and Giester G. (2018) Spodumene pegmatites and related leucogranites from the austroalpine unit (eastern Alps, central Europe): field relations, petrography, geochemistry, and geochronology. *Can. Mineral.* **56**, 489–528.

Kontak D.J. (2006) Nature and origin of an LCT-suite pegmatite with late-stage sodium enrichment, Brazil Lake, Yarmouth County, Nova Scotia. I. Geological setting and petrology. *The Canadian Mineralogist* **44**, 563–598.

Kontak D. J., Dostal J., Kyser K., & Archibald D. A. (2002) A petrological, geochemical, isotopic and fluid-inclusion study of 370Ma pegmatite-aplite sheets, Peggys Cive, Nova Scotia, Canada. *The Canadian Mineralogist* **40(5)**, 1249–1286.

Kontak D.J., Groat L., & Barnes E.M. (2004) A visit to the Little Nahanni rare-element pegmatites, N.W.T., and other curiosities along the way. *Newsletter of the Mineralogical Association of Canada* **42(5)**, p. 1, 4, 5, 20, 21.

Kontak D.J., Groat L., Burns M.G., Archibald D.A., & Creaser R. (2016) Documenting the complex evolution of a rare-metal pegmatite swarm: The Little Nahanni Pegmatite Group, NWT, Canada. *Geological Association of Canada, Mineralogical Association of Canada, Whitehorse, YK, Canada*, *Program with Abstracts,* v. **39**.

Kontak D.J., & Kyser T.K. (2009) Nature and origin of an LCT-suite pegmatite with late-stage sodium enrichment, Brazil Lake, yarmouth county, Nova Scotia. II. Implications of stable isotopes (δ18o, δd) for magma source, internal crystallization and nature of sodium metasomatism. *The Canadian Mineralogist* **47**, 745–764.

Kostov I., & Kostov R. I. (1999) *Crystal habits of minerals*. Bulgarian Academic Monographs 1, Sofia, Bulgaria.

Lahti S.I. (1987) Zoning in columbite-tantalite crystals from the granitic pegmatites of the Eräjärvi area, southern Finland. *Geochimica et Cosmochimica Acta* **51**, 509–517.

Lee M. R., & Parsons I. (1997) Dislocation formation and albitization in alkali feldspars from the Shap granite. *The Canadian Mineralogist* **82**, 557–570.

Linnen R. L. (1998) The solubility of Nb-Ta-Zr-Hf-W in granitic melts with Li and Li + F: Constraints for mineralization in rare metal granites and pegmatites. *Economic Geology* **93(7)**, 1013–1025.

Linnen R.L., & Cuney M. (2005) Granite-related rare-element deposits and experimental constraints on Ta-Nb-W-Sn-Zr-Hf mineralization. *Geological Association of Canada Short Course Notes* **17**, 45–63

Linnen R.L., & Keppler H. (1997) Columbite solubility in granitic melts: Consequences for the enrichment and fractionation of Nb and Ta in the Earth's crust. *Contributions to Mineralogy and Petrology* **128,** 213–227.

Linnen R.L., McNeil A., & Flemming R. (2019) Some Thoughts On Metasomatism in Pegmatites. *The Canadian Mineralogist* **57**, 765–766.

Liverton T. (2017) *Geology and summary report of the Little Nahanni Pegmatite prospect*

Lofgren G. (1974) An experimental study of plagioclase crystal morphology; isothermal crystallization. *American Journal of Science* **274**, 243–273

London D. (1984) Experimental phase equilibria in the system LiAlSiO4- SiO2-H2O: a petrogenetic grid for lithium-rich pegmatites. *American Mineralogist* **69**, 995–1004

London D. (1987) Internal differentiation of rare-element pegmatites: Effects of boron, phosphorus, and fluorine. *Geochimica et Cosmochimica Acta* **51(3)**, 403–420.

London D. (2005) Granitic pegmatites: An assessment of current concepts and directions for the future. *Lithos* **80**, 281–303.

London D. (2008) *Pegmatites*. The Canadian Mineralogist, Special Publication **10**, Quebec

London D. (2009) The origin of primary textures in granitic pegmatites. *The Canadian Mineralogist* **47**, 697–724.

London D. (2014) A petrologic assessment of internal zonation in granitic pegmatites. *Lithos* **184–187**, 74–104.

London D. (2018) Ore-forming processes within granitic pegmatites. *Ore Geology Reviews* **101**, 349–383.

London D., & Burt D.M. (1982) Chemical models for lithium aluminosilicate stabilities in pegmatites and granites. *American Mineralogist* **67**, 494–509.

London D., Hervig R.L., & Morgan G.B. (1988) Melt-vapor solubilities and elemental partitioning in peraluminous granite-pegmatite systems: experimental results with Macusani glass at 200 MPa. *Contributions to Mineralogy and Petrology* **99,** 360–373.

London D., & Morgan G.B. (2017) Experimental crystallization of the Macusani Obsidian, with applications to lithium-rich granitic pegmatites. *Journal of Petrology* **58**, 1005–1030.

London D., Morgan G.B., & Hervig R.L. (1989) Vapor-undersaturated experiments with Macusani glass+H2O at 200 MPa, and the internal differentiation of granitic pegmatites. *Contributions to Mineralogy and Petrology* **102**, 1–17.

London D, Morgan G. B., Paul K. A., & Guttery B. M. (2012) Internal evolution of miarolitic granitic pegmatites at the little three Mine, Ramona, California, USA. *The Canadian Mineralogist* **50(4)**, 1025–1054.

London D., Morgan G.B., & Wolf M.B. (1996) Boron in granitic rocks and their contact aureoles. *Reviews in Mineralogy and Geochemistry* **33**, 299–330.

Lumpkin G.R. (1998) Rare-element mineralogy and internal evolution of the Rutherford #2 pegmatite, Amelia County, Virginia: A classic locality revisited. *The Canadian Mineralogist* **36**, 339–353.

Maneta V., & Anderson A.J. (2018) Monitoring the crystallization of water-saturated granitic melts in real time using the hydrothermal diamond anvil cell. *Contributions to Mineralogy and Petrology* **173**, 1–18.

Maneta V., & Baker D.R. (2014) Exploring the effect of lithium on pegmatitic textures: An experimental study. *American Mineralogist* **99**, 1383–1403.

Martin R.F., & De Vito C. (2014) The late-stage miniflood of Ca in granitic pegmatites: An open-system acid-reflux model involving plagioclase in the exocontact. *The Canadian Mineralogist* **52**, 165–181.

Mauthner M.H.F. (1996) *Mineralogy, geochemistry, and geochronology of the Little Nahanni Pegmatite Group, Logan Mountains, Southwestern Northwest Territories*. University of British Columbia, 192 pp.

Mauthner M.H.F., Mortensen J.K., Groat L.A., & Ercit T.S. (1995) Geochronology of the Little Nahanni pegmatite group, Selwyn Mountains, southwestern Northwest Territories. *Canadian Journal of Earth Sciences* **32**, 2090–2097.

McLaughlin T.G. (1940) Pegmatite dikes of the Bridger Mountains, Wyoming. *American Mineralogist* **25**, 46–68

Melnik O.E., & Bindeman I.N. (2018) Modeling of trace elemental zoning patterns in accessory minerals with emphasis on the origin of micrometer-scale oscillatory zoning in zircon. *American Mineralogist* **103**, 355–368.

Moiana M. (2017) The expression of the late-stage calcium influx in the Licungo Pegmatite Field, Zambezia, Mozambique. In: *8th International Symposium on Granitic Pegmatites*. pp 80–83

Mulja T., & Williams-Jones A.E. (2018) The physical and chemical evolution of fluids in rare-element granitic pegmatites associated with the Lacorne pluton, Québec, Canada. *Chemical Geology* **493**, 281–297.

Munoz J.L. (1971) Hydrothermal stability relations of synthetic lepidolite. *American Mineralogist* **56**, 2069–2087

Nabelek P. I., Russ-Nabelek C., & Denison J. R. (1992). The generation and crystallization conditions of the Proterozoic Harney Peak Leucogranite, Black Hills, South Dakota, USA: Petrologic and geochemical constraints. *Contributions to Mineralogy and Petrology* **110(2–3)**, 173–191.

Norton J.J. (1983) Sequence of mineral assemblages in differentiated granitic pegmatites. *Economic Geology* **78**, 854–874.

Parsons I., & Lee M.R. (2005) Minerals are not just chemical compounds. *The Canadian Mineralogist* **43**, 1959–1992.

Pemberton B.C. (2002) *The origin of cassiterite at the Little Nahanni Pegmatite Group, Northwest Territories*. B.Sc.H. thesis, University of British Columbia, 64 pp.

Pfister J. D., Kontak D. J., Groat L., & Fayek M. (2019) Textural and isotopic studies of the Cretaceous Little Nahanni pegmatite Group (NWT, Canada) suggests mixed fluid reservoirs during its evolution. *The Canadian Mineralogist* **57(5)**, 771–773.

Pieczka A., Szuszkiewicz A., Szełęg E., & Nejbert K. (2019) Calcium Minerals and Late-stage Ca-metasomatism in the Julianna Pegmatitic System, the Góry Sowie Block, Sw Poland. *The Canadian Mineralogist* **57**, 775–777.

Piilonen P.C., Farges F., Linnen R.L., Brown G.E., Pawlak M., & Pratt A. (2006) Structural environment of Nb 5+ in dry and fluid-rich (H2O, F) silicate glasses: A combined xanes and exafs study. *The Canadian Mineralogist* **44**, 775–794.

Plümper O., & Putnis A. (2009) The complex hydrothermal history of granitic rocks: Multiple feldspar replacement reactions under subsolidus conditions. *Journal of Petrology* **50**, 967–987.

Putnis A. (2002) Mineral replacement reactions: from macroscopic observations to microscopic mechanisms. *Mineralogical Magazine* **66(5)**, 689–708.

Rasmussen K.L. (2013) *The timing, composition, and petrogenesis of syn- to post-accretionary*

magmatism in the northern Cordilleran miogeocline, eastern Yukon and southwestern Northwest Territories. Ph.D. thesis, University of British Columbia, 810 pp.

Rockhold J.R., Nabelek P.I., & Glascock M.D. (1987) Origin of rhythmic layering in the Calamity Peak satellite pluton of the Harney Peak Granite, South Dakota: The role of boron. *Geochimica et Cosmochimica Acta* **51,** 487–496.

Roda, E., Keller, P. Pesquera, A., & Fontan F. (2007) Micas of the muscovite–lepidolite series from Karibib pegmatites, Namibia. *Mineralogical Magazine* **71(1)**, 41–62.

Rollo H.A. (1999) *Mineralogy and geochemistry of mica minerals from the Little Nahanni Pegmatite Group, Northwest Territories*. B.Sc.H. thesis, University of British Columbia, 61 pp.

Rose D. (1981) Multi-step emplacement of a pegmatite vein - Brabant pegmatite, Namibia. *Neues Jahrbuch der Mineralogie* **8**, 355–373.

Schäfer B., Frischknecht R., Günther D., & Dingwell D.B. (1999) Determination of trace-element partitioning between fluid and melt using LA-ICP-MS analysis of synthetic fluid inclusions in glass. *European Journal of Mineralogy* **11**, 415–426.

Schaller W.T. (1925) The genesis of lithium pegmatites. *American Journal of Science* **10**, 269–279

Selby D., Creaser R. A., Heaman L. M., & Hart C. J. R. (2003) Re-Os and U-Pb geochronology of the Clear Creek, Dublin Gulch, and Mactung deposits, Tombstone Gold Belt, Yukon, Canada: Absolute timing relationships between plutonism and mineralization. *Canadian Journal of Earth Sciences* **40(12)**, 1839–1852.

Simmons W.B.S., & Webber K.L. (2008) Pegmatite genesis: state of the art. *European Journal of Mineralogy* **20**, 421–438.

Simmons W., Falster A., Webber K., Roda-Robles E., Boudreaux A. P., Grassi L. R. and Freeman G. (2016) Bulk composition of Mt. Mica Pegmatite, Maine, USA: Implications for the origin of an LCT type pegmatite by anatexis. *Can. Mineral.* **54**, 1053–1070.

Sirbescu M.L.C., Hartwick E.E., & Student J.J. (2008) Rapid crystallization of the Animikie Red Ace Pegmatite, Florence county, northeastern Wisconsin: Inclusion microthermometry and conductive-cooling modeling. *Contributions to Mineralogy and Petrology* **156**, 289–305.

Sirbescu M.L.C., Schmidt C., Veksler I.V., Whittington A.G., & Wilke M. (2017) Experimental crystallization of undercooled felsic liquids: Generation of pegmatitic texture. *Journal of Petrology* **58**, 539–568.

Stewart D.B. (1978) Petrogenesis of lithium-rich pegmatites. *American Mineralogist* **63**, 970–980

Suwimonprecha P., Černý P., & Friedrich G. (1995) Rare metal mineralization related to granites and pegmatites, Phuket, Thailand. *Economic Geology* **90**, 603–615.

Sweetapple M.T., & Collins P.L.F. (2002) Genetic framework for the classification and distribution of Archean rare metal pegmatites in the North Pilbara Craton, Western

Australia. *Economic Geology* **97**, 873–895.

Taylor B.E., Foord E.E., & Friedrichsen H. (1979) Stable isotope and fluid inclusion studies of gem-bearing granitic pegmatite-aplite dikes, San Diego Co., California. *Contributions to Mineralogy and Petrology* **68**, 187–205.

Taylor R. G. (1979) *Geology of tin deposits*. Textbook. Elsevier Scientific Publishing.

Taylor R.P., Pedersen J.C., Bubar D.S., Campbell I.C., Rees K., Morgan J.A., & Barclay W.A. (2005) The nature and distribution of tantalum mineralization in pegmatite dikes, Lilypad Lakes property, Fort Hope, Northwestern Ontario. *Exploration and Mining Geology* **14**, 31–44.

Telus M., Dauphas N., Moynier F., Tissot F. L. H., Teng F. Z., Nabelek P. I., Craddock P. R., & Groat L. A. (2012). Iron, zinc, magnesium and uranium isotopic fractionation during continental crust differentiation: The tale from migmatites, granitoids, and pegmatites. *Geochimica et Cosmochimica Acta* **97**, 247–265.

Thomas R., Davidson P., & Beurlen H. (2012) The competing models for the origin and internal evolution of granitic pegmatites in the light of melt and fluid inclusion research. *Mineralogy and Petrology* **106**, 55–73.

Thomas R., Webster J.D., & Heinrich W. (2000) Melt inclusions in pegmatite quartz: Complete miscibility between silicate melts and hydrous fluids at low pressure. *Contributions to Mineralogy and Petrology* **139**, 394–401.

Timofeev A., Migdisov A.A., & Williams-Jones A.E. (2015) An experimental study of the solubility and speciation of tantalum in fluoride-bearing aqueous solutions at elevated temperature. *Geochimica et Cosmochimica Acta* **158**, 103–111.

Timofeev A., Migdisov A.A., & Williams-Jones A.E. (2017) An experimental study of the solubility and speciation of tantalum in fluoride-bearing aqueous solutions at elevated temperature. *Geochimica et Cosmochimica Acta* **197**, 294–304.

Timofeev A., & Williams-Jones A.E. (2015) The origin of niobium and tantalum mineralization in the Nechalacho REE deposit, NWT, Canada. *Economic Geology* **110**, 1719-1735.

Van Lichtervelde M., Salvi S., Beziat D., & Linnen R.L. (2007) Textural features and chemical evolution in tantalum oxides: Magmatic versus hydrothermal origins for Ta mineralization in the Tanco Lower pegmatite, Manitoba, Canada. *Economic Geology* **102**, 257–276.

Van Lichtervelde M., Holtz F., & Hanchar J. M. (2010) Solubility of manganotantalite, zircon and hafnon in highly fluxed peralkaline to peraluminous pegmatitic melts. *Contributions to Mineralogy and Petrology* **160(1)**, 17–32.

Van Lichtervelde M., Holtz F., & Melcher F. (2018) The effect of disequilibrium crystallization on Nb-Ta fractionation in pegmatites: Constraints from crystallization experiments of tantalite-tapiolite. *American Mineralogist* **103**, 1401–1416.

Vignola, P., Zucali, M., Rotiroti, N., Marotta, G., Risplendente, A., Pavese, A., & Bertoldi, G. (2018) The chrysoberyl-and phosphate-bearing albite pegmatite of Malga Garbella, Val Di Rabbi, Trento province, Italy. *The Canadian Mineralogist*, **56**, 411-424.

Webber K.L., Falster A.U., Simmons W.B., & Foord E.E. (1997) The role of diffusion-controlled oscillatory nucleation in the formation of line rock in pegmatite-aplite dikes. *Journal of Petrology* **38**, 1777–1791.

Webber K.L., Simmons W.B., Falster A.U., & Foord E.E. (1999) Cooling rates and crystallization dynamics of shallow level pegmatite-aplite dikes, San Diego County, California. *American Mineralogist* **84**, 708–717.

Webber K. L., Simmons W. B., Falster A. U., & Hanson S. L. (2019). Anatectic pegmatites of the Oxford County pegmatite field, Maine, USA. *Canadian Mineralogist* **57(5)**, 811–815.

Webster J.D., Holloway J.R., & Hervig R.L. (1989) Partitioning of lithophile trace elements between H_2O and $H_2O + CO_2$ fluids and rhyolite melt. *Economic Geologic* **84**, 116–134.

Wise M.A., & Brown C.D. (2011) Chemical composition of coexisting columbite-group minerals and cassiterite from the Black Mountain pegmatite, Maine. *European Journal of Mineralogy* **23**, 817–828.

Worden R. H., Walker F. D. L., Parsons I., & Brow, W. L. (1990) Development of microporosity, diffusion channels and deuteric coarsening in perthitic alkali feldspars. *Contributions to Mineralogy and Petrology* **104(5)**, 507–515.

Wood S.A. (2005) The aqueous geochemistry of zirconium, hafnium, niobium and tantalum. In: Linnen RL, Samson IM (eds) Rare-element geochemistry and mineral deposits. *GAC Short Course Notes* **17**, Ontario, pp 217–268

Zajacz Z., Halter W.E., Pettke T., & Guillong M. (2008) Determination of fluid/melt partition coefficients by LA-ICPMS analysis of co-existing fluid and silicate melt inclusions: Controls on element partitioning. *Geochimica et Cosmochimica Acta* **72**:2169–2197.

2.11 Figures and tables

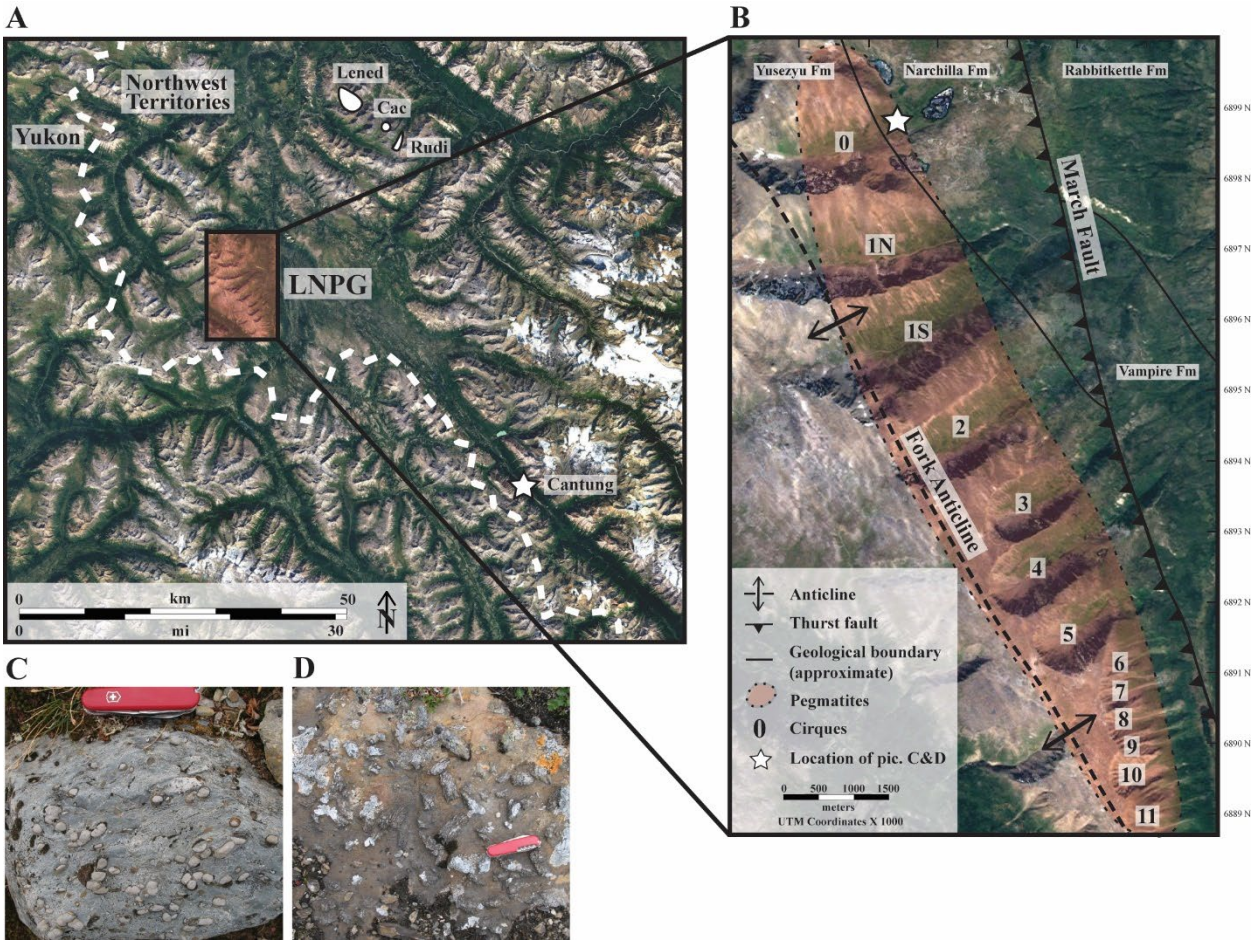

FIG. 1. A) Satellite image (Google Earth™) showing the location of: LNPG, Yukon-Northwest Territories border, local plutons of the Selwyn Plutonic Suite (Lened, Cac and Rudi) and Cantung mine (W-skarn). B) Satellite image (Google Earth™) of the LNPG area with local geology adapted from Groat et al. (2003). C, D) Cordierite- and andalusite-bearing metasedimentary rocks with hornfels texture from the northern part of the LNPG (see star in picture B).

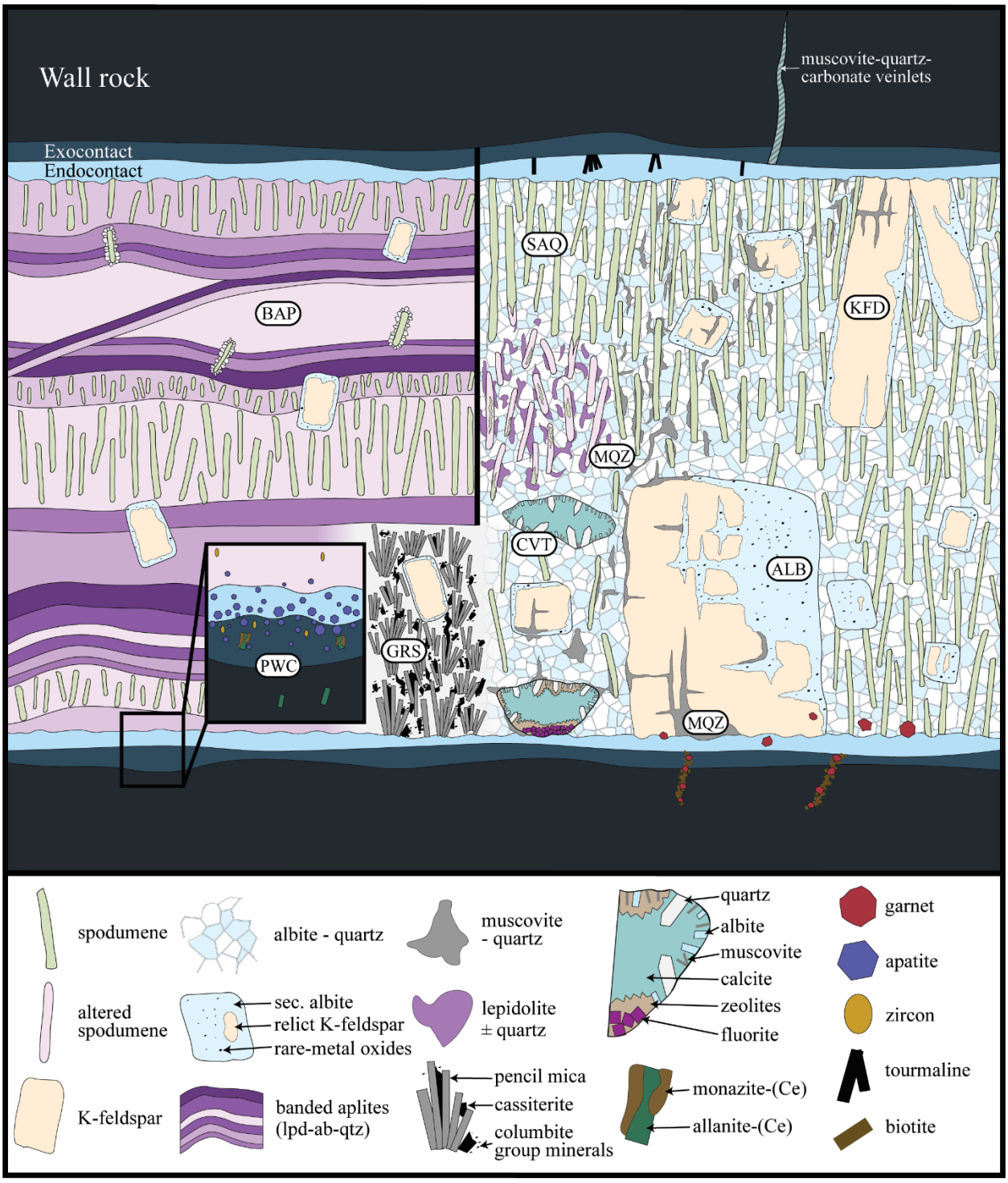
Wall rock
muscovite-quartz-carbonate veinlets
Exocontact
Endocontact
BAP
SAQ
KFD
MQZ
CVT
ALB
PWC
GRS
MQZ
spodumene
albite - quartz
muscovite - quartz
quartz
albite
muscovite
calcite
zeolites
fluorite
garnet
apatite
zircon
tourmaline
biotite
altered spodumene
sec. albite
relict K-feldspar
rare-metal oxides
lepidolite ± quartz
K-feldspar
banded aplites (lpd-ab-qtz)
pencil mica
cassiterite
columbite group minerals
monazite-(Ce)
allanite-(Ce)

FIG. 2. Schematic illustration of the different domains present in the pegmatites of LNPG. Abbreviations refer to the sections discussing each domain (see text). ALB = albitized domain; BAP = banded aplite-pegmatites; CVT = cavities; GRS = greisen-like domain; KFD = K-feldspar domain; MQZ = mica-quartz domain; PWC = pegmatite – wall-rock contact; SAQ = spodumene-albite-quartz domain. Note that not all the domains co-exist in the same dikes.

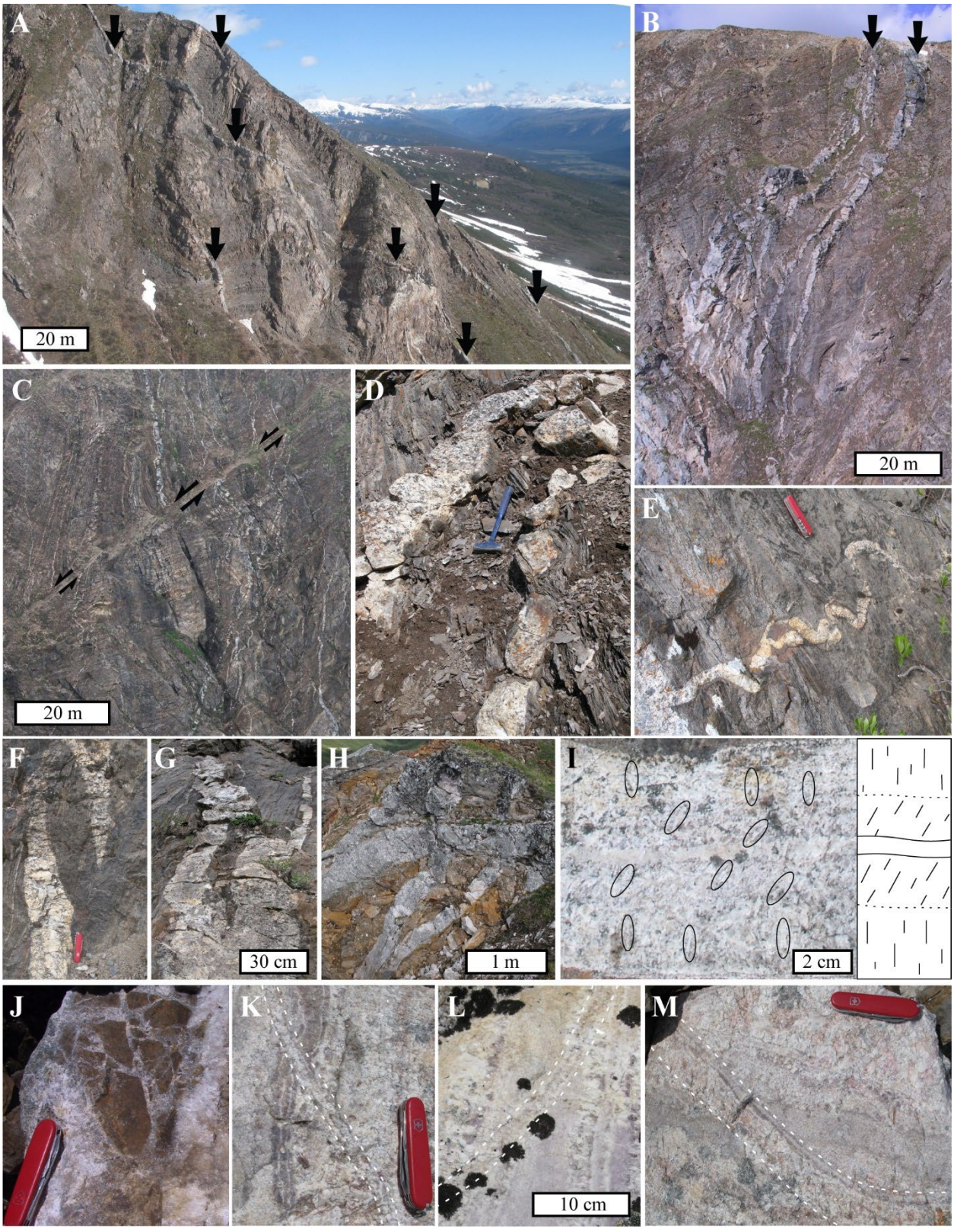
A
20 m
B
20 m
C
20 m
D
E
F
G
30 cm
H
1 m
I
2 cm
J
K
L
10 cm
M

FIG. 3. Different features of pegmatite dike rocks at LNPG. A) North wall of cirque 1N (see Fig. 1B) showing numerous sub-vertical thin pegmatite dikes intruding metasedimentary rocks. B) Vertical pegmatites exhibiting bifurcation. C) Late fault crosscutting pegmatite dikes. D) Pegmatite dikes showing boudinaging. E) Dike showing folding. F) En echelon dikes with sharp terminations. G) Dike showing bifurcation to form two dikes. H) Dikes showing rare crosscutting relationship. I) Dike with prismatic spodumene crystals (circled) and quenched core. Note the change in crystal orientation from the dike margins to its center (see schematic drawing). J) Local brecciation of wall rock material at pegmatite margin. The matrix is fine-grained quartz-albite. K, L, M) Dikes having line-rock texture or banding with alternating coarse- and fine-grained layers. Note the comb-like texture in the coarse layers and the crosscutting relationship between some of the layers (white dashed lines).

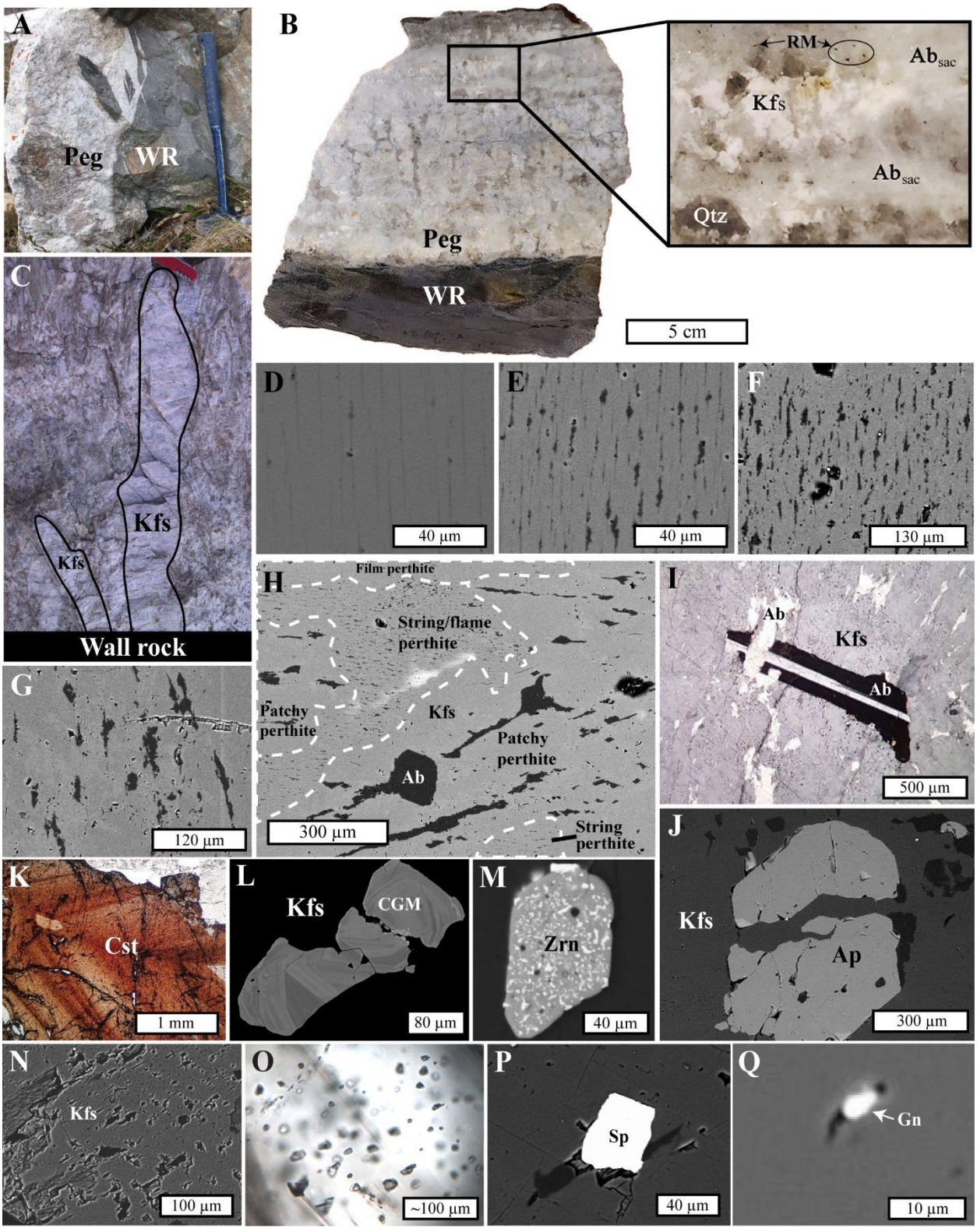
A
Peg
WR
B
RM
Ab$_{sac}$
Kfs
Ab$_{sac}$
Qtz
Peg
WR
5 cm
C
Kfs
Kfs
Wall rock
D
40 µm
E
40 µm
F
130 µm
G
120 µm
H
Film perthite
String/flame perthite
Patchy perthite
Kfs
Patchy perthite
Ab
300 µm
String perthite
I
Ab
Kfs
Ab
500 µm
J
Kfs
Ap
300 µm
K
Cst
1 mm
L
Kfs
CGM
80 µm
M
Zrn
40 µm
N
Kfs
100 µm
O
~100 µm
P
Sp
40 µm
Q
Gn
10 µm

FIG. 4. Mineralogical features of the K-feldspar - rich domain at the LNPG seen in outcrop and hand sample (A, C), in a cut slab (B), back scattered electron (BSE) images (D to H, L to N, P, Q), and in crossed nicols (I) and plane-polarized light (K, O to Z) microscopy. A) K-feldspar (Kfs) - rich pegmatite (Peg) dike exhibiting sharp contact with the wall rock (WR). B) Typical example of Kfs-rich pegmatite (Peg) dike with inset image showing alteration of Kfs to saccharoidal albite (Ab) associated with rare metal (RM; Nb, Ta, Sn) oxides. C) Early glassy grey Kfs megacrysts in a matrix of quartz-albite-spodumene. Note the Kfs exhibits high aspect-ratios and oriented perpendicular to the WR contact. D) Kfs with film perthite. The bulk composition of the field of view is $Or_{86}Ab_{14}$. E) Kfs with film and coarsening to bleb perthite. Note the sporadic micropores present. F) Kfs with film- to flame perthite and abundant micropores. G) Ksp with bleb perthite and abundant micropores. Note pores occur bright areas where Kfs is more Or-rich. H) Co-existing domains of Kfs with varying perthitic textures. Note the micropores are associated with patchy perthite domains. I) Albite micro-inclusion in megacrystic Kfs which is crosscut by perthite. J) Apatite inclusion in megacrystic Kfs with crosscutting relationship. K) Fluctuatingly-zoned cassiterite (Cst) in Kfs. L) Fluctuatingly-zoned columbite-tantalite inclusion in Kfs. M) Zircon (Zrn) in Kfs with abundant uraninite (Urn) inclusions. N) Intensely pitted Kfs. O) Abundant fluid inclusions in Kfs. P, Q) Late sphalerite (Sp) and galena (Gn) filling pits in Kfs.

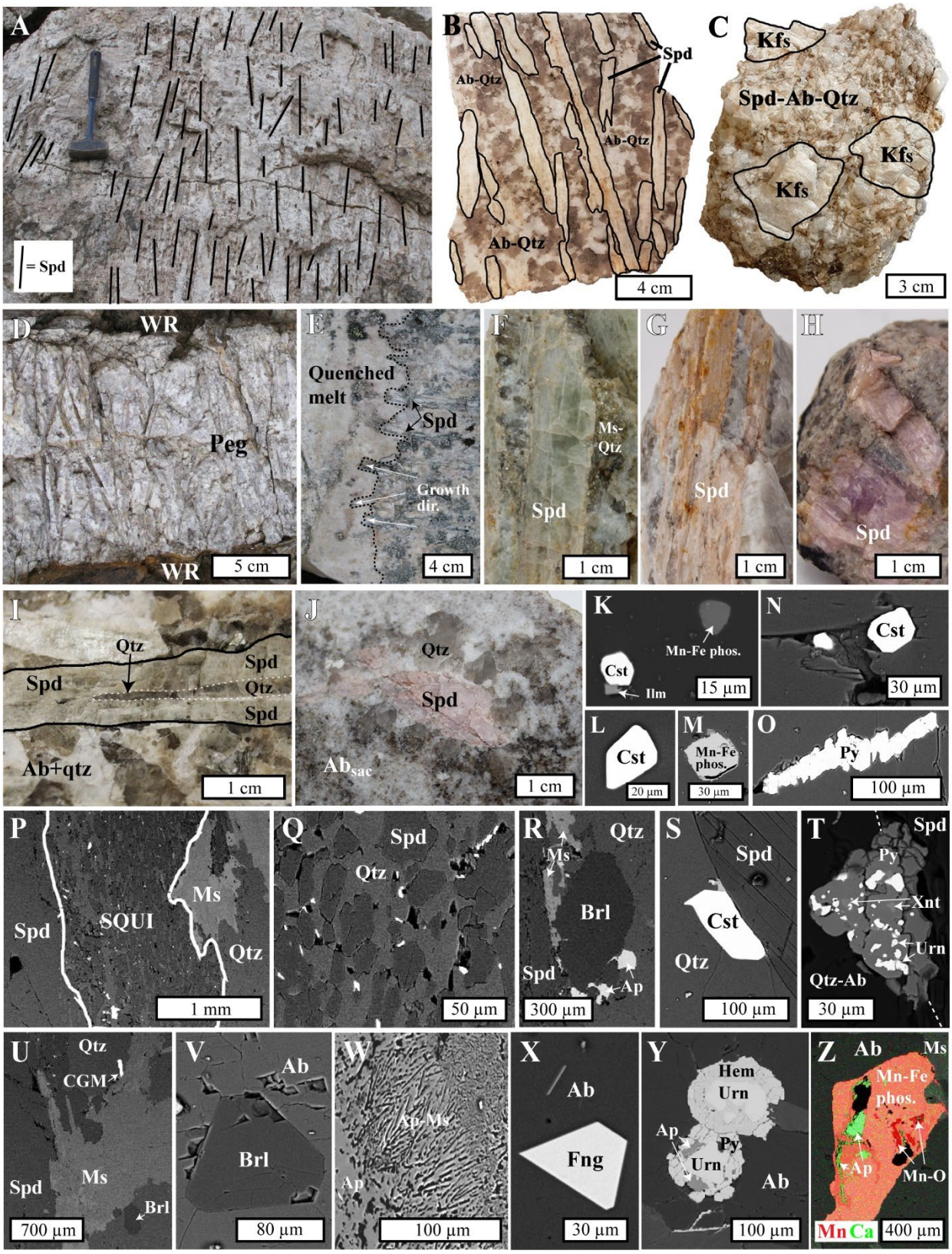
A
= Spd
B
Spd
Ab-Qtz
Ab-Qtz
Ab-Qtz
4 cm
C
Kfs
Spd-Ab-Qtz
Kfs
Kfs
3 cm
D
WR
Peg
WR
5 cm
E
Quenched melt
Spd
Growth dir.
4 cm
F
Ms-Qtz
Spd
1 cm
G
Spd
1 cm
H
Spd
1 cm
I
Qtz
Spd
Spd
Qtz
Spd
Ab+qtz
1 cm
J
Qtz
Spd
Ab$_{sac}$
1 cm
K
Mn-Fe phos.
Cst
Ilm
15 µm
N
Cst
30 µm
L
Cst
20 µm
M
Mn-Fe phos.
30 µm
O
Py
100 µm
P
Spd
SQUI
Ms
Qtz
1 mm
Q
Spd
Qtz
50 µm
R
Qtz
Ms
Brl
Spd
Ap
300 µm
S
Spd
Cst
Qtz
100 µm
T
Spd
Py
Xnt
Urn
Qtz-Ab
30 µm
U
Qtz
CGM
Spd
Ms
Brl
700 µm
V
Ab
Brl
80 µm
W
Ab-Ms
Ap
100 µm
X
Ab
Fng
30 µm
Y
Hem
Urn
Ap
Py
Urn
Ab
100 µm
Z
Ab
Ms
Mn-Fe phos.
Ap
Mn-O
Mn Ca
400 µm

FIG. 5. Summary of mineralogical feature for the spodumene-albite-quartz domain at the LNPG seen in outcrop (A, D, E), cut slabs (B, J), broken pieces (C, F to I), and back scattered electron (BSE) images (K to Z). A) High-aspect ratio spodumene crystals showing preferred orientation. B) Preferentially oriented spodumene (Spd) in albite-quartz (Ab-Qtz) matrix. C) Early K-feldspar (Kfs) included in matrix of spodumene-albite-quartz domain (SAQD). D) Comb-like texture of spodumene pegmatite (PEG) against wall rock (WR) contact. E) Fine-grained quartz-feldspar matrix (i.e., quenched melt pocket) penetrated by acicular spodumene. F) Greenish, partially glassy spodumene. Note presence of muscovite-quartz intergrowth (see discussion on mica-quartz domain). G) Pinkish cream-colored spodumene. H) Pink glassy spodumene. I) Quartz coring spodumene parallel to its c axis. J) Quartz crown around pink spodumene surrounded by saccharoidal Ab. K to O) BSE images documenting early- and late-stage inclusions in spodumene: K) Cassiterite (Cst), ilmenite (Ilm) and unidentified Mn-Fe phosphate inclusions. L) Cassiterite inclusion. M) Unidentified Mn-Fe phosphate inclusions. N) Late cassiterite in dissolution feature. O) Late pyrite (Py) filling a fracture. P to U) BSE images showing accessory phases and textures in and around spodumene: P) Spodumene-QUartz Intergrowth (SQUI) rimming earlier spodumene. Q) Close up of SQUI showing apatite (bright phases) filling pores and dissolution features. R) Na-bearing beryl (Brl) at quartz-spodumene contact. S) Cassiterite at quartz-spodumene contact. T) Uraninite (Urn) and xenotime (Xnt) along with pyrite (Py). U) Columbite group minerals (CGM) and beryl. V to Z) Accessory phases in the albite-quartz matrix of SAQD: V) Euhedral beryl in albite matrix. W) Disequilibrium-related apatite-muscovite (Ap, Ms) intergrowth. X) Ferronigerite (Fng) in albite matrix. Y) Uraninite in albite-quartz matrix with late hematite (Hem)-pyrite-apatite rims. Z) X-ray map for Mn, Ca showing unidentified Mn-Fe phosphate inclusion in albite-quartz.

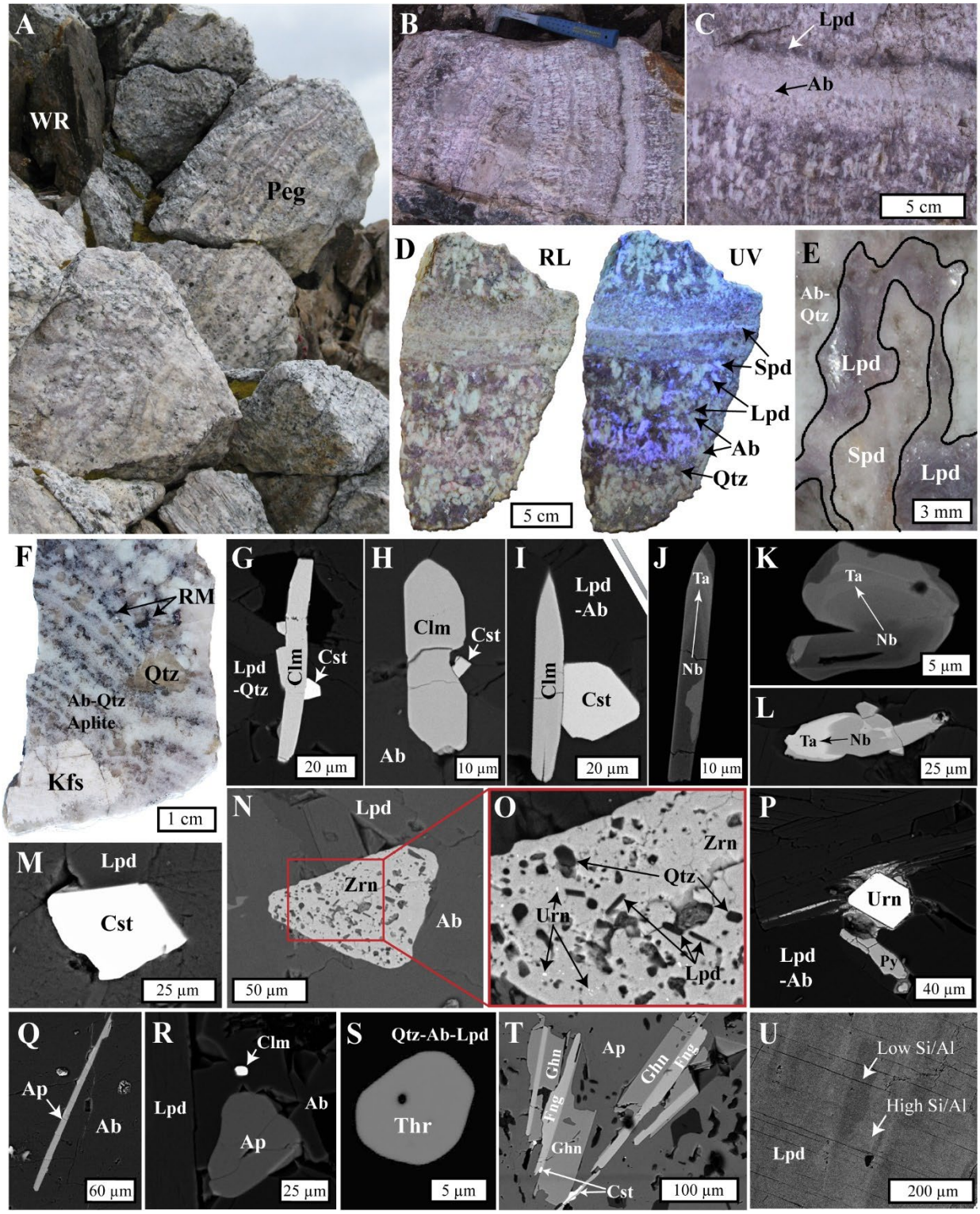
A
WR
Peg
B
C
Lpd
Ab
5 cm
D
RL
UV
Spd
Lpd
Ab
Qtz
5 cm
E
Ab-
Qtz
Lpd
Spd
Lpd
3 mm
F
RM
Qtz
Ab-Qtz
Aplite
Kfs
1 cm
G
Lpd
-Qtz
Clm
Cst
20 µm
H
Clm
Cst
Ab
10 µm
I
Lpd
-Ab
Clm
Cst
20 µm
J
Ta
Nb
10 µm
K
Ta
Nb
5 µm
L
Ta
Nb
25 µm
M
Lpd
Cst
25 µm
N
Lpd
Zrn
Ab
50 µm
O
Zrn
Qtz
Urn
Lpd
P
Urn
Lpd
-Ab
Py
40 µm
Q
Ap
Ab
60 µm
R
Clm
Lpd
Ab
Ap
25 µm
S
Qtz-Ab-Lpd
Thr
5 µm
T
Ap
Ghn
Fng
Ghn
Fng
Ghn
Cst
100 µm
U
Low Si/Al
High Si/Al
Lpd
200 µm

FIG. 6. Summary of mineralogical features for banded aplite-pegmatite dikes at the LNPG seen in outcrop (A, B, C), cut slabs (D, E, F), and back scattered electron images (G to U). A) Aplite-pegmatite (Peg) dike with banding parallel to contact with wall rock (WR). B, C) Albite-lepidolite (Ab, Lpd) banded dike with close showing monomineralic layers as indicated with arrows. Note the lack of spodumene and scarcity of quartz. D) Banded aplite-pegmatite material under regular (left, RL) and ultraviolet (right, UV) light. The UV reveals the presence of significant spodumene (Spd), including a monomineralic spodumene layer. Note abundance of quartz (Qtz, dark grey) and the sharp pegmatite-aplite transition. E) Partially resorbed spodumene crystal with surrounding mass of lepidolite. F) Earlier K-feldspar and quartz included in banded albite-quartz matrix. Note the abundance of rare metal (RM) phases along some layers and the lack of lepidolite. G, H, I) Examples of manganocolumbite (Clm) and cassiterite (Cst) association. J, K, L) Zoned columbite from Nb core to Ta rim. M) Cassiterite in lepidolite. N, O) Inclusion-rich (i.e., quartz, lepidolite, uraninite (Urn)) zircon (Zrn) in albite-lepidolite matrix. P) Uraninite in albite-lepidolite matrix with late pyrite. Q) Elongate apatite (Ap) in albite. R) Manganocolumbite and apatite in lepidolite-albite matrix. S) Thorite (Thr) in quartz-albite-lepidolite matrix. T) Gahnite (Ghn) and ferronigerite (Fng) association in apatite. U) Patchy zoning in lepidolite with various Si/Al ratios.

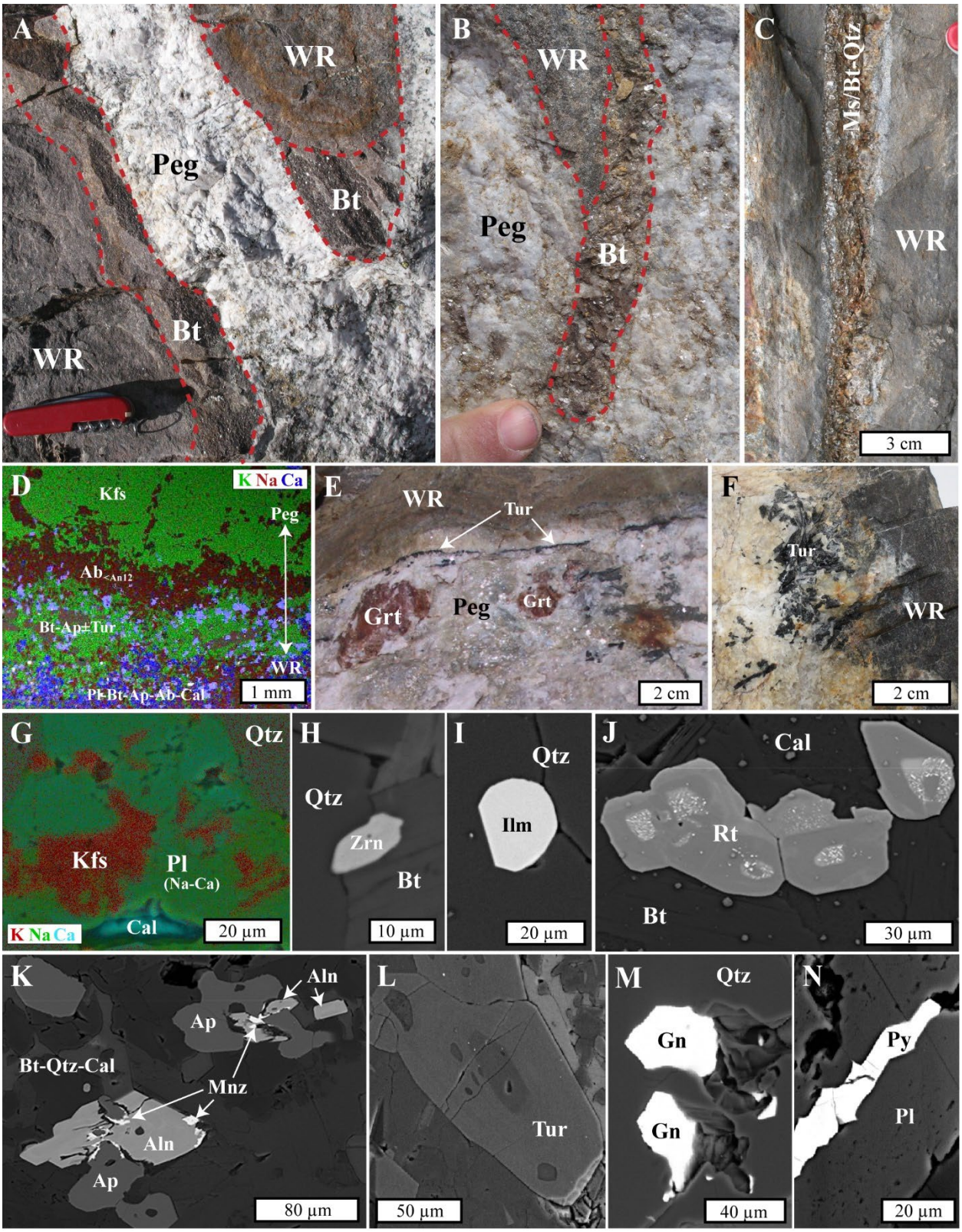
A
WR
Peg
Bt
Bt
WR
B
WR
Peg
Bt
C
Ms/Bt-Qtz
WR
3 cm
D
Kfs
K Na Ca
Peg
Ab<An12
Bt-Ap±Tur
WR
Pl-Bt-Ap-Ab-Cal
1 mm
E
WR
Tur
Grt
Peg
Grt
2 cm
F
Tur
WR
2 cm
G
Qtz
Kfs
Pl
(Na-Ca)
K Na Ca
Cal
20 µm
H
Qtz
Zrn
Bt
10 µm
I
Qtz
Ilm
20 µm
J
Cal
Rt
Bt
30 µm
K
Aln
Ap
Bt-Qtz-Cal
Mnz
Aln
Ap
80 µm
L
Tur
50 µm
M
Qtz
Gn
Gn
40 µm
N
Py
Pl
20 µm

FIG. 7. Summary of mineralogical features related to pegmatite – wall-rock interaction at the LNPG seen in outcrop (A, B, C, E, F), X-ray maps (D, G) and back scattered electron images (H to N). A) Pegmatite (Peg) cutting metasedimentary wall rock with a biotite-rich (Bt) aureole. B) Biotite-rich alteration of wall rock adjacent a branching pegmatite. C) A muscovite (Ms) – biotite-quartz veinlet originating I pegmatite seen in the wall rock. D) A false-colored X-ray map of pegmatite (top) - wall rock (bottom) contact: K-feldspar (Kfs) is bordered by albite (Ab) followed by a biotite-apatite-tourmaline (Bt-Apt-Tur) zone and then wall rock (plagioclase-biotite-apatit-albite-calcite (Pl_Bt-Apt-Ab-Cal). E) Garnet (Grt) and tourmaline near pegmatite-wall rock contact. Note that tourmaline is directly at the contact. F) Abundant tourmaline near pegmatite-wall-rock contact. G) False-colored X-ray map showing K-feldspathization of plagioclase in the exomorphic aureole. H) Zircon (Zrn) in the exomorphic aureole. Note that zircon is only found near the pegmatite contact and is absent in the distal wall rock. I) Ilmenite (Ilm) inclusion in quartz of the exomorphic aureole. J) Zoned rutile (Rt) with variable Fe, W, Nb, Sn, and Ta, as discussed in text. K) Allanite-(Ce) (Aln) partially altered to monazite-(Ce) (Mnz) when in contact with apatite originating from pegmatite-sourced P, as observed in the exomorphic aureole. Notably allanite-(Ce) in the distal wall rock is unaltered. L) Zoned tourmaline in the exomorphic aureole. M, N) Late galena (Gn) and pyrite (Py) filling dissolution generated porosity in the exomorphic aureole.

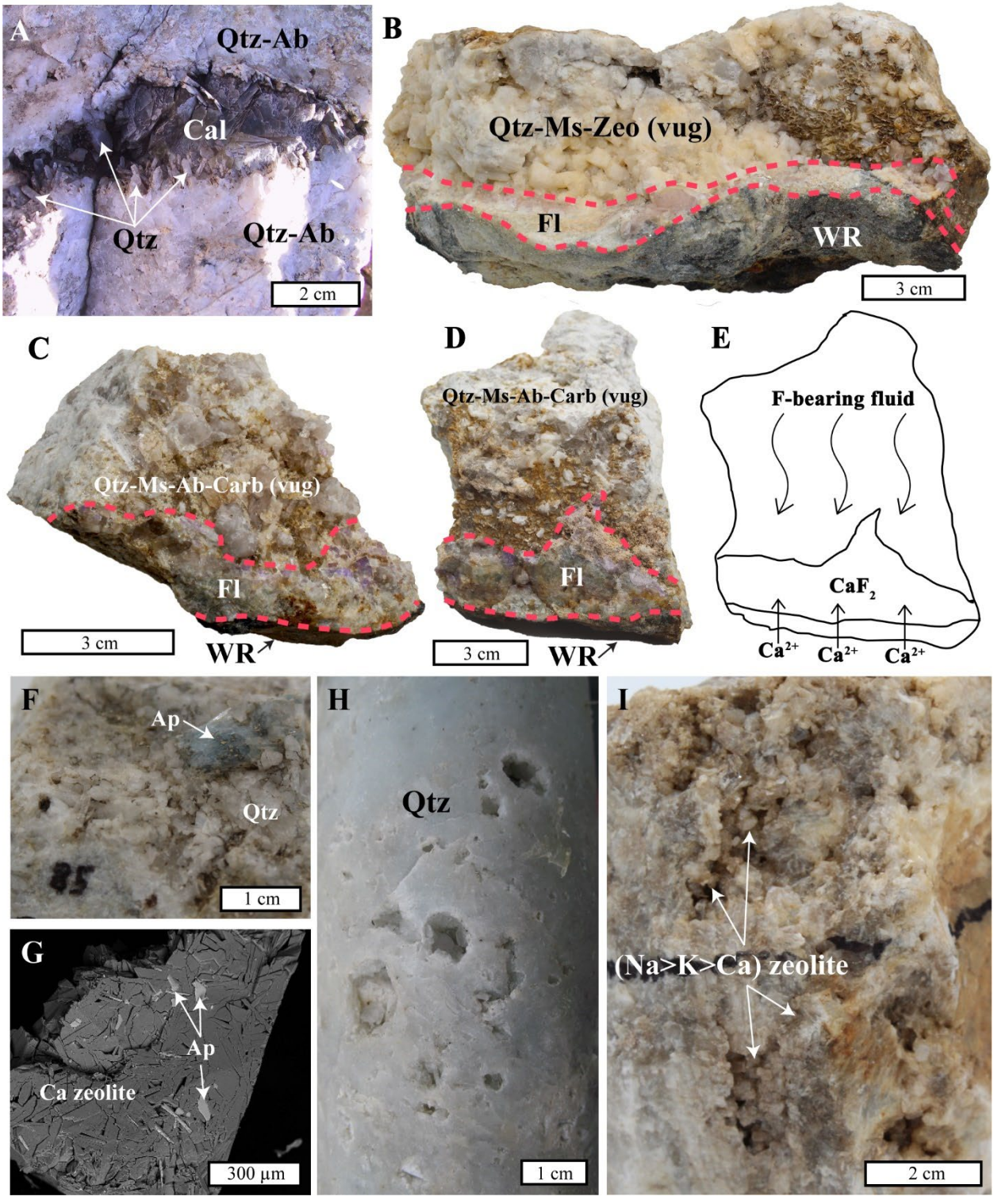
A
Qtz-Ab
Cal
Qtz
Qtz-Ab
2 cm
B
Qtz-Ms-Zeo (vug)
Fl
WR
3 cm
C
Qtz-Ms-Ab-Carb (vug)
Fl
3 cm
WR
D
Qtz-Ms-Ab-Carb (vug)
Fl
3 cm
WR
E
F-bearing fluid
CaF2
Ca2+
Ca2+
Ca2+
F
Ap
Qtz
1 cm
G
Ap
Ca zeolite
300 µm
H
Qtz
1 cm
I
(Na>K>Ca) zeolite
2 cm

FIG. 8. Summary of mineralogical features related to cavities at the LNPG seen in outcrop (A), rock pieces (B to F, H, I), and back-scattered electron (BSE) image (G). A) Possible primary miarolitic cavity lined with quartz (Qtz) and albite (Ab) with later calcite (Cal). B, C, D) Irregular-shaped cavities, due to dissolution, in pegmatites at the border with wall rock (WR). These features are lined with quartz, muscovite (Ms), zeolites (Zeol), and fluorite (Fl) with later coatings of carbonates, fine-grained zeolite, and apatite (Ap). Note that fluorite is restricted to the immediate vicinity of the wall rock contact, as shown by dashed red lines. E) Schematic representation (after sample D) of interaction between F-rich pegmatite fluid and wall-rock derived Ca which resulted in localized distribution of fluorite. F) Apatite lining dissolution cavity of albitized pegmatite. G) BSE image of late-stage coating of fluorite consisting of fine-grained Ca-dominant zeolites and apatite. This sample is from the face of a fluorite crystal in a dissolution cavity. H) Dissolution cavities in quartz in drill core. I) Dissolution cavities in spodumene-albite-quartz pegmatite sample lined with Na-dominant zeolite.

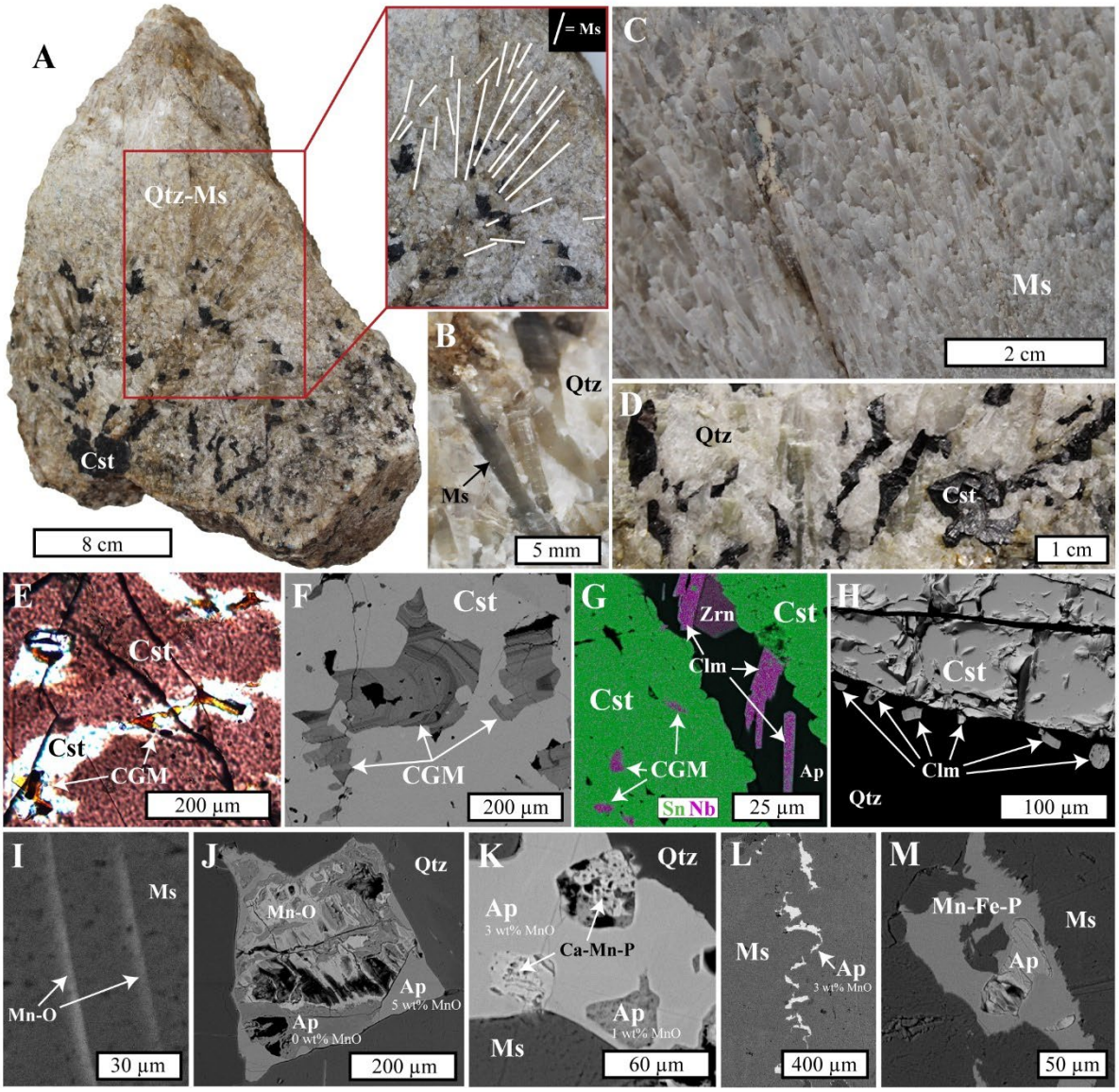

FIG. 9. Summary of mineralogical features related to the greisen-like domain at the LNPG seen in rock pieces (A, B, C, D), plane-polarized light (E), and back-scattered electron (BSE) images (F to M). A) Large sample of the greisen-like domain containing intergrowth of prismatic muscovite (Ms) and quartz (Qtz) with abundant cassiterite (Cst). Insert image shows the radiating and elongate nature of prismatic muscovite. B) Close up of prismatic muscovite (i.e., "pencil" muscovite) consisting of stacks of muscovite books. C) Mass of preferentially oriented "pencil" muscovite from a slab of greisen-like material. D) Angular cassiterite-quartz intergrowth from

same locality as image A. E) Reddish cassiterite with zoned columbite group mineral (CGM) inclusions (see image F) in veins of crosscutting clear cassiterite. Reddish cassiterite is impure (*i.e.*, contains Ta and Nb), whereas completely transparent strings and patches are stoichiometric SnO_2. F) Fragments of fluctuatingly-zoned CGM in cassiterite from the same sample shown in image E. G) False-colored X-ray map of cassiterite crosscut by apatite-manganocolumbite (Clm)-zircon (Zrn) veinlet. Note that black is apatite (vein) or empty micropores (in cassiterite). H) Manganocolumbite grains at edge of cassiterite. I) Late manganese hydroxide (Mn-O) along muscovite cleavage which is responsible for the occasionally dark color seen in pencil muscovite (see image B). J) Partially dissolved Mn-poor apatite in quartz replaced by Mn hydroxides and overgrown by Mn-bearing apatite. K) Anhedral Mn-apatite surrounded by quartz-muscovite with inclusions of an unidentified anhedral Ca-Mn phosphate (close to 1:1 ratio) and Mn-poor apatite. L) Mn-bearing apatite veinlet cutting muscovite. M) Unidentified anhedral Mn-Fe phosphate with partially dissolved earlier Mn-poor apatite in muscovite.

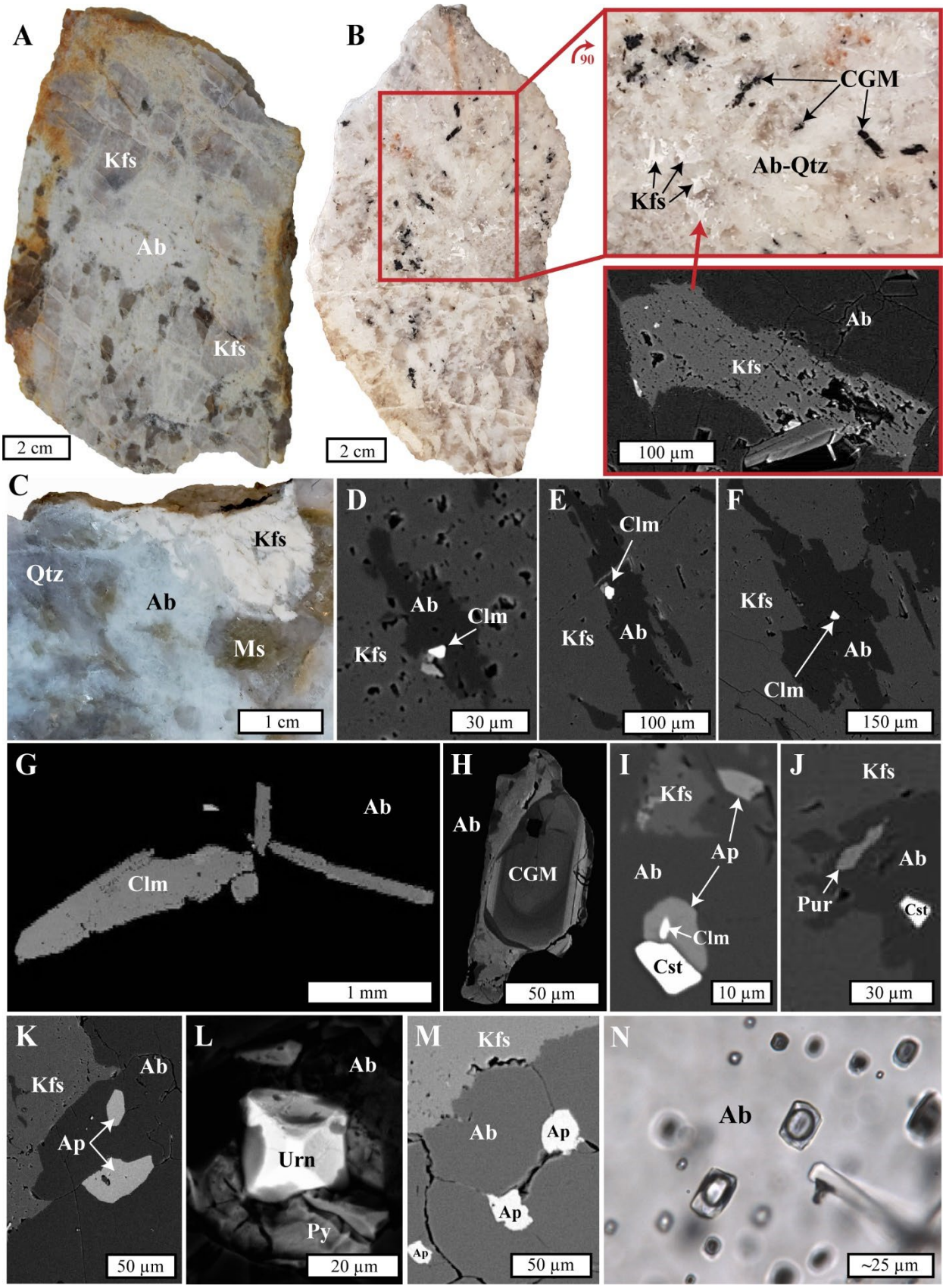
A
Kfs
Ab
Kfs
2 cm
B
90
2 cm
CGM
Ab-Qtz
Kfs
Ab
Kfs
100 µm
C
Kfs
Qtz
Ab
Ms
1 cm
D
Ab
Clm
Kfs
30 µm
E
Clm
Kfs
Ab
100 µm
F
Kfs
Ab
Clm
150 µm
G
Ab
Clm
1 mm
H
Ab
CGM
50 µm
I
Kfs
Ap
Ab
Clm
Cst
10 µm
J
Kfs
Ab
Pur
Cst
30 µm
K
Ab
Kfs
Ap
50 µm
L
Ab
Urn
Py
20 µm
M
Kfs
Ab
Ap
Ap
Ap
50 µm
N
Ab
~25 µm

FIG. 10. Summary of mineralogical features related to albitization and associated rare-metal mineralization at LNPG as seen in cut rock slabs (A, B, C) and back-scattered electron (BSE) images (D to N). A) Albitization (Ab) of glassy grey K-feldspar (Kfs) megacryst. Note irregular outlines of relict K-feldspar. B) Slab and matching close up showing saccharoidal albite-quartz with disseminated columbite group minerals (CGM) in area of former K-feldspar. Inset BSE image shows pitted nature of the relict K-feldspar. C) Close up image showing albitized K-feldspar with adjacent quartz and muscovite (Ms). D, E, F) BSE images showing common spatial association between secondary albite (after K-feldspar) and manganocolumbite (Clm). Note the lack of CGM in K-feldspar and its pitted texture. G) Elongate and homogeneous manganocolumbite crystals in saccharoidal albite matrix. H) fluctuating zoning in CGM in albite exhibiting partial dissolution and secondary CGM rim with patchy zoning. I, J, K) Development of different minerals (i.e., apatite (Ap), manganocolumbite, cassiterite (Cst), purpurite (Pur)) associated with albitization of K-feldspar. L) Late euhedral uraninite (Urn) and pyrite (Py) filling dissolution feature in saccharoidal albite. M) Late-stage apatite filling pits and intergranular fractures in secondary saccharoidal albite. N) Abundant aqueous-carbonic fluid inclusions in saccharoidal albite.

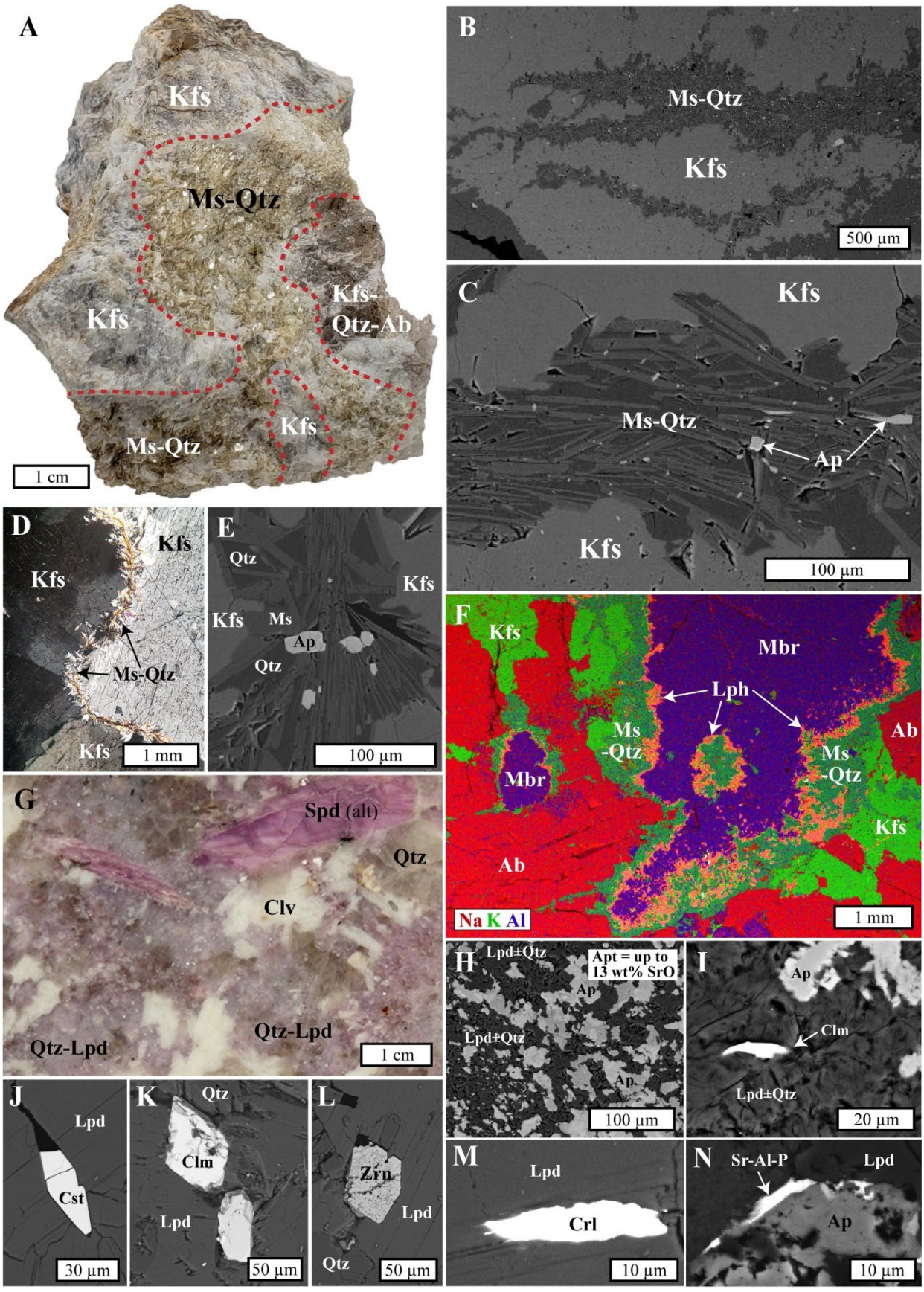
A
Kfs
Ms-Qtz
Kfs
Kfs-
Qtz-Ab
Ms-Qtz
Kfs
1 cm
B
Ms-Qtz
Kfs
500 µm
C
Kfs
Ms-Qtz
Ap
Kfs
100 µm
D
Kfs
Kfs
Ms-Qtz
Kfs
1 mm
E
Qtz
Kfs
Kfs
Ms
Ap
Qtz
100 µm
F
Kfs
Mbr
Lph
Ms
-Qtz
Ab
Ms
-Qtz
Mbr
Kfs
Ab
Na K Al
1 mm
G
Spd (alt)
Qtz
Clv
Qtz-Lpd
Qtz-Lpd
1 cm
H
Lpd±Qtz
Apt = up to
13 wt% SrO
Ap
Lpd±Qtz
Ap
100 µm
I
Ap
Clm
Lpd±Qtz
20 µm
J
Lpd
Cst
30 µm
K
Qtz
Clm
Lpd
50 µm
L
Zrn
Lpd
Qtz
50 µm
M
Lpd
Crl
10 µm
N
Sr-Al-P
Lpd
Ap
10 µm

FIG. 11. Summary of mineralogical features related to secondary muscovite and lepidolite with associated rare-metal (RM) mineralization at the LNPG as seen in rock samples (A), cut slab (G), crossed nicols (D), and back-scattered electron (BSE) images (B, C, E, F, H to N). A, B, C) Muscovite (Ms)-quartz (Qtz) assemblage replacing K-feldspar (Kfs) along fractures as best seen in BSE images (B, C). Note apatite (Ap) in quartz-muscovite intergrowth in C. D) Muscovite-quartz replacing K-feldspar along intergranular boundary. E) Accessory apatite in muscovite-quartz assemblage replacing K-feldspar. F) False-color X-ray map showing lithiophilite (Lph) rim around montebrasite (Mbr) at interface with muscovite-quartz assemblage after K-feldspar. G) Lepidolite (Lpd)-quartz-cleavelandite (Clv) assemblage. The former spodumene (Spd) is entirely altered to a mixture of clays and lepidolite. H) Fine-grained lepidolite±quartz with abundant apatite. Apatite has up to 13 wt. % SrO. I) Manganocolumbite (Clm) and anhedral apatite in fine-grained lepidolite±quartz assemblage. J, K, L, M, N) Inclusions of cassiterite (Cst), manganocolumbite, zircon (Zrn), cheralite (Crl), and unidentified Sr-Al phosphate (likely goyazite) in lepidolite-quartz matrix.

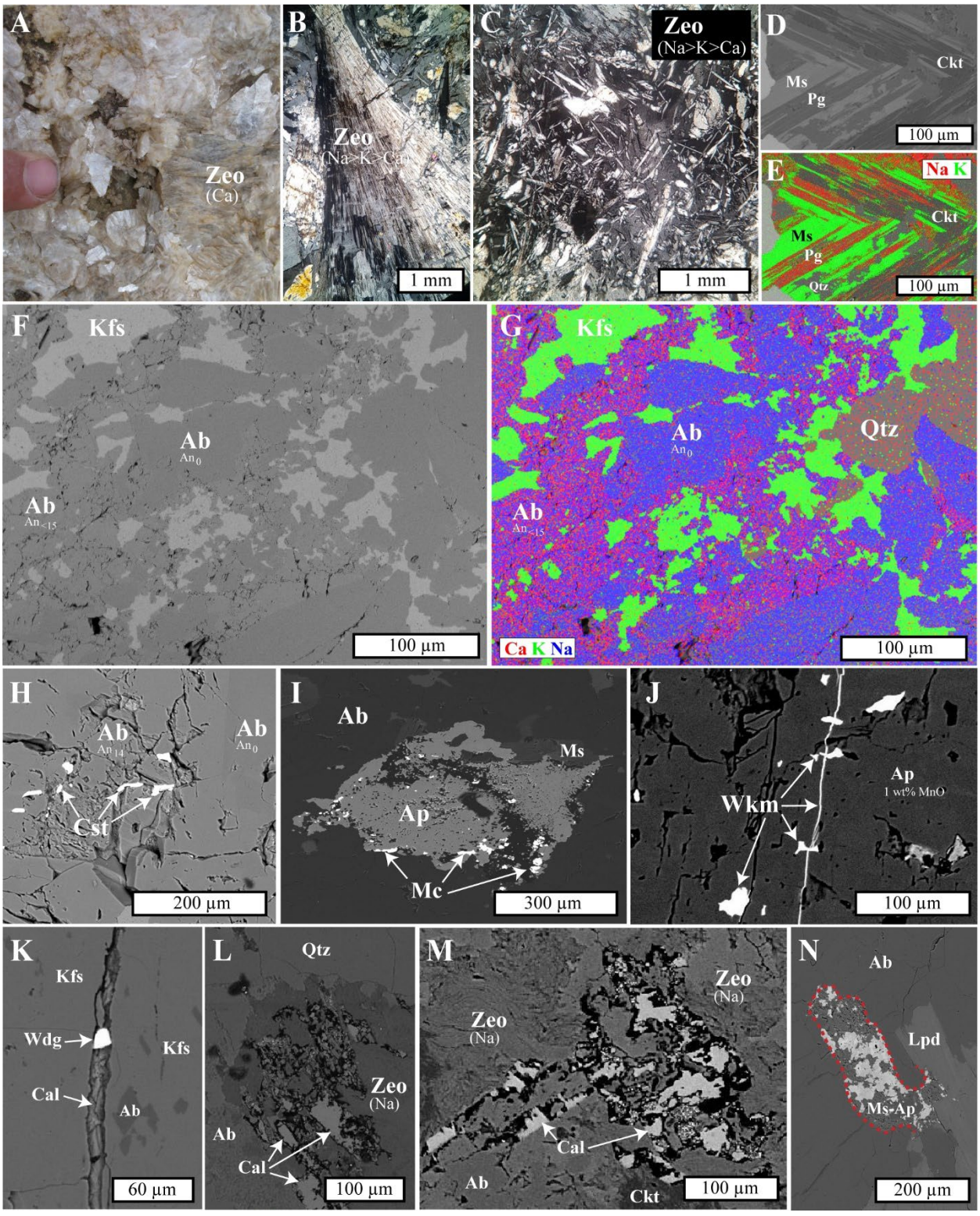
A
Zeo
(Ca)
B
Zeo
(Na>K>Ca)
1 mm
C
Zeo
(Na>K>Ca)
1 mm
D
Ckt
Ms
Pg
100 µm
E
Na K
Ckt
Ms
Pg
Qtz
100 µm
F
Kfs
Ab
An0
Ab
An<15
100 µm
G
Kfs
Ab
An0
Qtz
Ab
An<15
Ca K Na
100 µm
H
Ab
An14
Ab
An0
Cst
200 µm
I
Ab
Ms
Ap
Mc
300 µm
J
Ap
1 wt% MnO
Wkm
100 µm
K
Kfs
Wdg
Kfs
Cal
Ab
60 µm
L
Qtz
Zeo
(Na)
Ab
Cal
100 µm
M
Zeo
(Na)
Zeo
(Na)
Cal
Ab
Ckt
100 µm
N
Ab
Lpd
Ms-Ap
200 µm

FIG. 12. Summary of mineralogical features related to late stage alteration at the LNPG as seen in rock sample (A), crossed nicols (B, C), and back-scattered electron (BSE) images (D to N). A) Mass of Ca-dominant zeolite (Zeo) in a dissolution cavity. B, C) Na-dominant zeolite. D) Muscovite (Ms) partially altered to paragonite (Pg) and cookeite (Ckt) in sample rich in Na-dominant zeolites. E) False-colored X-ray map of image D showing complex intergrowth of mica types: green = muscovite, red = paragonite, and dark grey = cookeite. F, G) Grey scale and false-colored X-ray map showing Ca-plagioclase ($<An_{15}$) replacing end-member albite (An_0). Note numerous dissolution features where Ca-plagioclase (An_{15}) replaces albite (An_0) which previously replaced K-feldspar (Kfs) .Note residual quartz (Qtz). H) Cassiterite (Cst) lining dissolution pits where albite was replaced by Ca-plagioclase (An_{14}). I) Late calciomicrolite (Mc) lining pores in apatite. J) (Tetra-?)wickmanite (Wkm) filling pits and fractures in Mn-bearing apatite. K) Grain of wodginite (Wdg) in a calcite-filled fracture cutting K-feldspar. L, M) Calcite (Cal) replacing unidentified phase and filling cavities in partially dissolved mass of Na-dominant zeolite. N) Fine-grained muscovite-apatite assemblage (outlined in red) replacing extension of lepidolite (Lpd) grain.

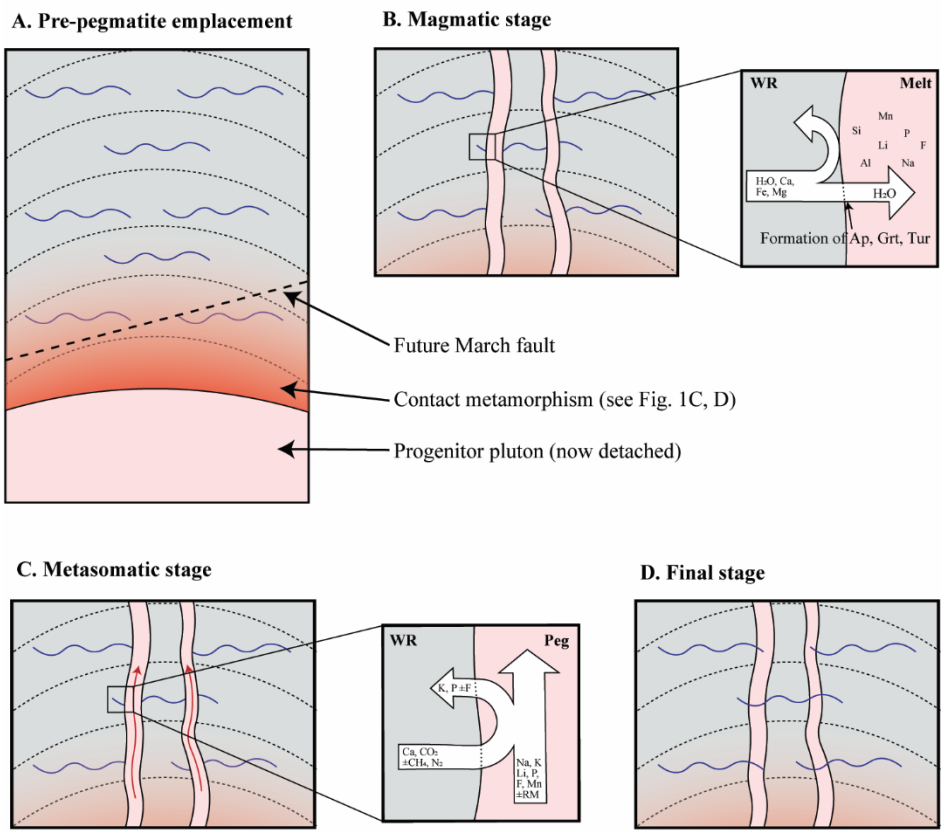

FIG. 13. Schematic illustration of the fluid-mediated exchange between pegmatite and wall rock through the evolution of the LNPG system. A) Prior to emplacement: ambient fluid trapped in strata of the Fork Anticline. Parental pluton at depth causes contact metamorphism, as observed in the northern part of the LNPG (See Fig. 1). B) Magmatic stage: volatile-undersaturated melt absorbs some of the external fluid at the time of pegmatite emplacement. Some of the solutes (e.g., Ca, Fe, Mg) react with melt-derived components at the melt-wall rock contact to form apatite, garnet, fluorite and tourmaline. C) Metasomatic stage: orthomagmatic fluid and external fluids mix, causing the observed progressive evolution of metasomatic assemblages from Na-, Li-, F-rich to Ca-rich and formation of an intermittent K-, P-, F- rich exomorphic aureole. D) Final stage: orthomagmatic fluid is completely diluted and the external fluid is now present in both the wall rock and the pegmatite causing formation of calcite and accessory sulfides in micropores and pre-

existing dissolution cavities. Eventually the regional March Fault (see A) detaches the pegmatite swarm from the progenitor granite and transports it eastwards.

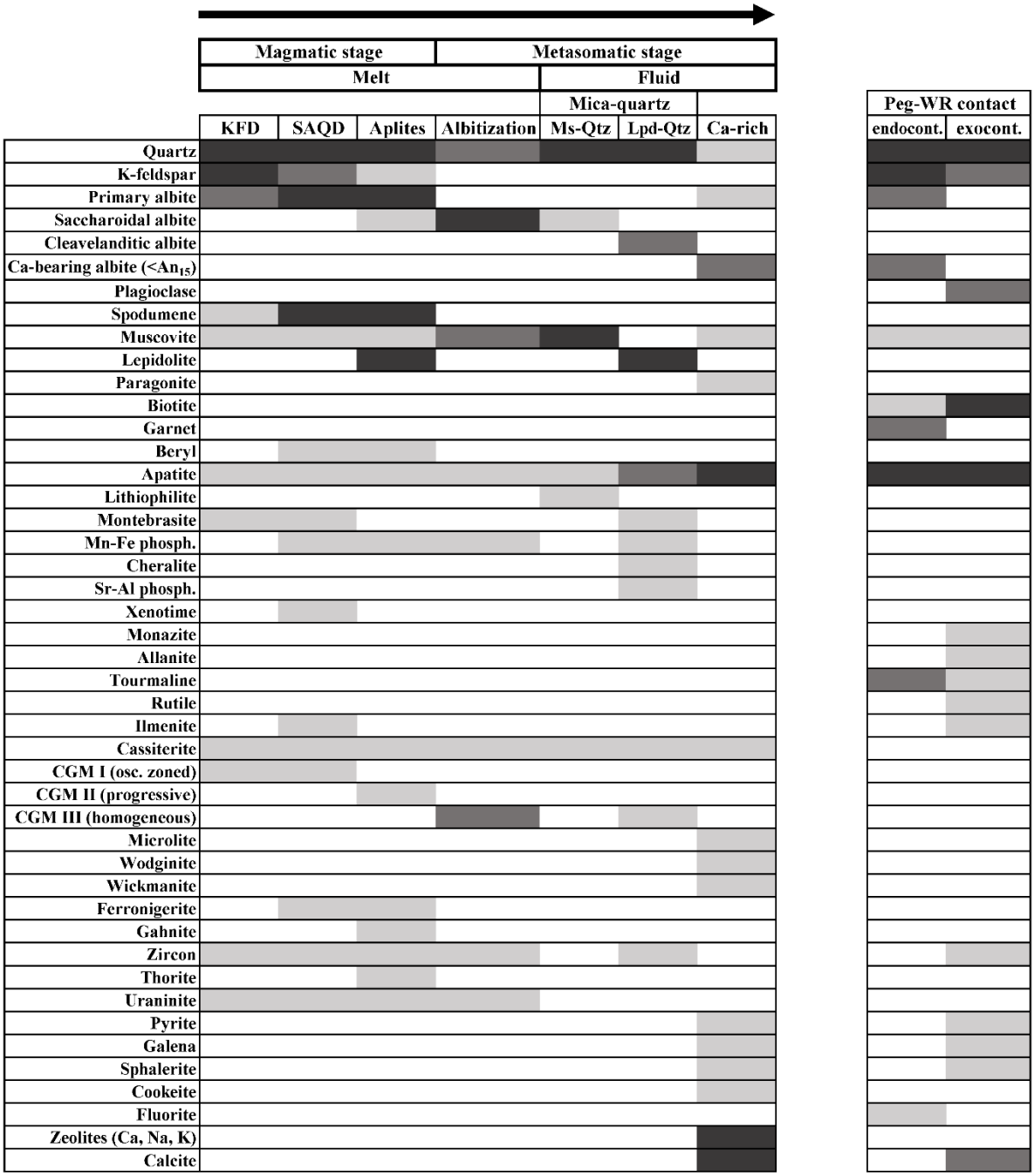

FIG. 14. Summary of mineral paragenesis at the LNPG. Major phases in dark grey, minor phases in grey, and accessory phases in light grey. The domains on the left represent the general mineralogical evolution of the LNPG as indicated by the arrow, while the domains on the right reflect pegmatite-wall rock interaction (exo- and endo-contact). See text for discussion.

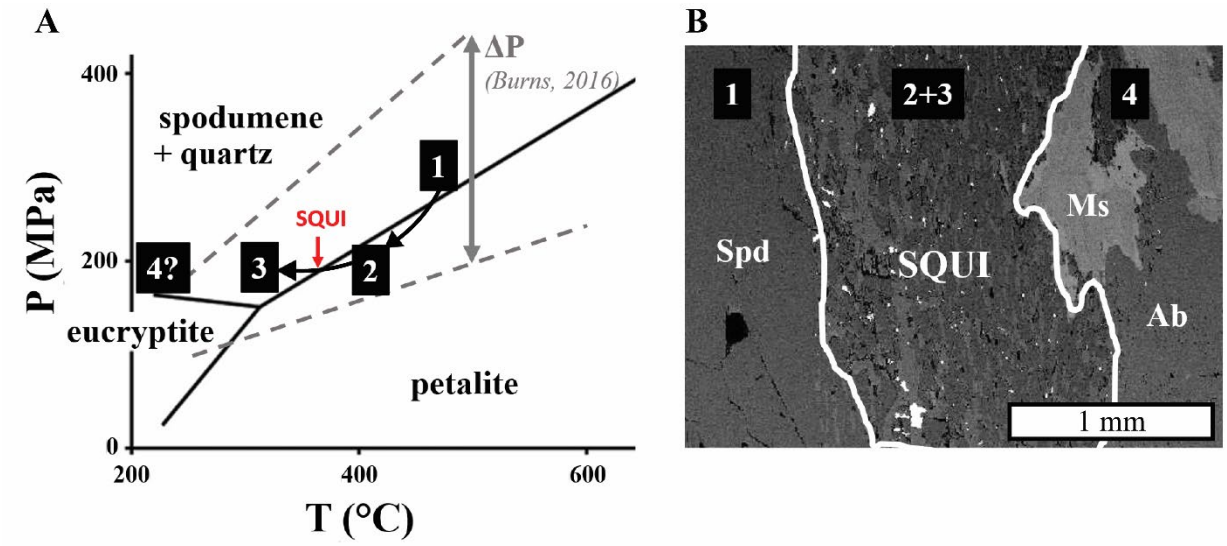

FIG. 15. A) The Li_2O-Al_2O_3-SiO_2 phase diagram after London (1984) used for LCT-type pegmatite systems along with bounding isochores for H_2O-CO_2 fluid inclusions hosted in quartz and spodumene from LNPG (Burns 2019). The stages of pegmatite evolution (1→2→3→4) are discussed in the text. Note that the cooling path in PT space is approximate. B) Back-scattered electron image of LNPG sample showing initial spodumene (Spd) surrounded by SQUI (spodumene-quartz intergrowth) which is followed by quartz (Qtz)–muscovite (Ms).

Domain	Mineralogy	Textures	Other observations
K-feldspar-rich domain (KFD)	- >30% modal K-feldspar and variable quartz, albite and rare spodumene (Fig. 4A-B). - Bulk K-feldspar composition (rastering 9 mm^2 areas) are $Or_{83}Ab_{17}$ to $Or_{92}Ab_{8}$. Where film perthite preserved, it has a composition of $Or_{86}Ab_{14}$ (Fig. 4D). Compositions of individual domains in the perthite are $Or_{95\text{-}100}$ and Ab_{100}. - Accessory phases include cassiterite, CGM, zircon and apatite (Fig. 4K-J) - Llate-stage sulfides of sphalerite and galena in pits and on fractures (Fig. 4P-Q).	- K-feldspar as large (<60 cm) megacrysts with high aspect-ratio (<8:1) are oriented perpendicular to pegmatite – WR contact (Fig. 4C). - K-feldspar exhibits various perthitic textures (i.e., film, string, flame, patch; Fig. 4D-G). These domains on mm to cm scale (Fig. 4H).	- Presence of early (i.e. pre-dating perthite texture) albite inclusions in K-feldspar (Fig. 4I). - Near-endmember K-feldspar exhibits intense porosity (Fig. 4N), abundant fluid inclusions (Fig. 4O) and is replaced by fine-grained albite (± quartz) containing abundant RM (Fig. 4B).
Spodumene - albite - quartz - domain (SAQD)	- >20% modal spodumene surrounded by an albite-quartz matrix (Fig. 5A-B) with minor muscovite and occasional K-feldspar megacrysts (Fig. 5C). - Accessory phases vary depending on their host: - Cassiterite and Mn-Fe phosphates abundant as inclusions in spodumene (along with rarer ilmenite, apatite and late-stage pyrite) (Fig. 5K-O). - More accessory phases, such as beryl, cassiterite, CGM, apatite, uraninite (± xenotime), found at the edges of spodumene crystals (Fig. 5R-U). - Beryl, apatite and Mn-Fe phosphates are abundant in albite-quartz matrix (along with rarer ferronigerite and uraninite) (Fig. 5V-Z). RM oxides are notably scarce in the albite-quartz matrix.	- Large acicular spodumene crystals oriented perpendicular to the pegmatite – WR contact (e.g. Fig. 5D) with aspect-ratio from 1:4 to 1:45 (avg. = 1:15, n = 85). - Occasionally, spodumene partially skeletal with a hollow center on the [001] face resulting in an apparent quartz core (Fig. 5I), but more common is surrounded by a "crown" of quartz (Fig. 5J). - Isochemichal **S**podumene-**QU**artz **I**ntergrowth after petalite (*i.e.* SQUI) as clots and rims (<3 mm) on spodumene (Fig. 5P-Q). SQUI areas have an average Al:Si ratio of 1:3.8 ± 0.4 (1σ, n=14) and compares to 1:4 for ideal petalite. Note porosity and apatite associated with SQUI (Fig. 5Q). - Apatite in albite-quartz matrix sometimes exhibits apatite-muscovite intergrowth reflecting disequilibrium growth conditions (Fig. 5W).	- Spodumene rarely penetrates fine-grained aplitic material (i.e. quenched residual melt), which records an inward crystallization front (Fig. 5E) - Spodumene faint green, cream-coloured or rarely pink (Fig. 5F-H).
Banded aplite-pegmatite (BAP)	- Dominated by albite and lepidolite with variable spodumene and quartz and differs from SAQD by presence of significant lepidolite. - Aplitic layers have a variable composition, thus monomineralic layers of lepidolite, spodumene, albite or more rarely quartz present (Fig. 6C-D, F).	- Alternating layers of aplitic and pegmatitic material with anisotropic fabric parallel to pegmatite – WR contact (Fig. 6A-B). - Sometimes later layers cut earlier ones (Fig. 3K-M). - Coarse K-feldspar and quartz sometimes present (Fig. 6F).	- In spodumene-bearing dikes, lepidolite is commonly found adjacent to resorbed spodumene (Fig. 6E). - The transition between fine-grained and coarser layers is either gradual or sharp, and it is not uncommon to have a layer bound by

	- Accessory phases abundant. CGM, cassiterite, apatite, zircon and uraninite common (Fig. 6G-R). Rarer accessories include various Fe-Mn(±Ca) phosphates, thorite and gahnite-ferronigerite intergrowth (Fig. 6Q-T).	- CGM exhibit normal zoning (Nb-rich core, Ta-rich rims) (Fig. 6J-L). - Zircon is porous with abundant micro-inclusions of lepidolite, quartz and uraninite (Fig. 6N-O). - Coarse lepidolite has patchy zoning due to variable Al:Si ratios (Fig. 6U).	a gradual change on one side and a sharp one on the other (*e.g.* Fig. 6D). - CGM and cassiterite usually occur together (Fig. 6G-I).
Pegmatite – WR contact (PWC)	- An intermittent biotite-rich alteration in the immediate WR is common (Fig. 7A-B), as are mica-carbonate-quartz veinlets originating from the pegmatites (Fig. 7C) - In endocontact (*i.e*. pegmatite side), fine-grained albite-oligoclase (<An_{12}), quartz, Mn-free apatite with variable amounts of K-feldspar, biotite, garnet and tourmaline (Fig. 7D-F) form a narrow aplitic margin. - Garnet and tourmaline, which are scarce and usually absent in the other domains, quite common at pegmatite – WR contacts. Garnet is Fe- and Mn-rich with minor Ca and Mg. Tourmaline of schorl-dravite series and often as radial sprays and/or aggregates of prismatic crystals (Fig. 12F). - The exocontact (*i.e.* WR side), consists mainly of plagioclase, biotite, quartz and apatite with minor albite and calcite (Fig. 7D). Accessory phases are zircon, ilmenite, Sn(±W,Nb,Ta)-bearing rutile, allanite-(Ce), monazite-(Ce), tourmaline and late sulphides (e.g., pyrite and galena (Fig. 7H-N). Calcite has <1 wt% MnO and 0.6 wt% FeO.	- Plagioclase in the exocontact is commonly partially replaced by K-feldspar (Fig. 7G). - Rutile often zoned (Fig. 7J): 1) core contains equal Fe and W (≤ 1.3 atomic % of both, or 9.1 wt% WO_3 and 3.2 wt% FeO), and likely due to ferberite micro-inclusions as suggested by texture of the cores under BSE imaging (Fig. 7J), as well as <2.4 wt% SnO_2 and 2.0 wt% Nb_2O_5; 2) intermediate zones relatively pure TiO_2; and 3) rims have <3.8 wt% Ta_2O_5, 2.9 wt% Nb_2O_5, 1.5 wt% SnO_2 and 1.5 wt% FeO. - Allanite-(Ce) only in WR and partially replaced by monazite where in contact with metasomatic apatite (Fig. 7K). - Tourmaline zoned (Fig. 7L) with rims higher in Ca and Ti.	- See Groat *et al*. (2003) for the chemistry of tourmaline and garnet.
Cavities (CVT)	- Cavities are lined with quartz, albite (var. cleavelandite), muscovite, Na-rich zeolites and fluorite (Fig. 8A-D) with later coatings of apatite, calcite and Ca-rich zeolites (Fig. 8F-G).	- Usually small (<100 cm^3), asymmetrical, and commonly localized to dike margins. - Fluorite is restricted to vugs closest to the WR, and lines the side directly adjacent WR (Fig. 8B-E).	- Majority relate to dissolution (often spodumene and K-feldspar), although a few of possible primary origin are noted (Fig. 8A). -Smaller scale (*i.e.* mm to cm) dissolution cavities are common (Fig. 8H-I), while dissolution features on the microscopic scale (*i.e.* µm) are abundant in all domains.

Greisen-like domain (GRS)	- Abundant prismatic pencil-shaped muscovite surrounded by coarse cassiterite and quartz (Fig. 9A) - Muscovite as radial sprays (Fig. 9A) and pencil-shaped crystals (Fig. 9B) <5 cm and similar to those in Karibib pegmatites, Namibia (Roda *et al.* 2007). These grains oriented at high angles to the pegmatite – WR contact and the most abundant phase in this domain (Fig. 9C). - Cassiterite (Fig. 9D) is a reddish with variable Ta (≤2.6 wt% Ta_2O_5) and Nb (≤1.9 wt% Nb_2O_5); also a clear pure form occurring as small veinlets and patches in reddish type that often include CGM inclusions (Fig. 9E). - Accessory phases are CGM, Mn-bearing apatite, zircon, various Mn-Fe(±Ca) phosphates and Mn-hydroxides (Fig. 9F-M).	- Two generations of CGM: 1) highly angular fragments of oscillatory-zoned CGM in cassiterite (Fig. 9E-F); and 2) euhedral elongated unzoned columbite-(Mn) with sporadic zircon in veinlets of Mn-bearing apatite (Fig. 9G). - Early phosphate minerals exhibit dissolution features and high porosity (Fig. 9J-K, M).	- Rarely restricted to a few dikes in both the southern (cirque 9) and northern part (cirques 1S & N; Fig. 1B).
Albitized domain (ALB)	- Albite (Ab_{98-100}) associated with minor quartz, muscovite and columbite-(Mn) (Fig. 10B-F). - Absence of CGM in early K-feldspar contrasts with its presence in secondary albite (Fig. 10D-F), thus the CGM relates to albitization and was not present prior to it. - Other accessory phases include cassiterite, apatite, and Mn-Fe phosphates (Fig. 10I-J). Late-stage uraninite, pyrite, apatite and calcite can be found in pits and fractures (Fig. 10K-M). - Rare cleavelandite associated with a similar assemblage, except for presence of lepidolite and less RM oxides.	- Two types of albite: 1) fine-grained saccharoidal; and 2) coarse cleavelandite (e.g., Fisher 1986). - Saccharoidal type replaces K-feldspar megacrysts (Fig. 10A, C). Relict K-feldspar exhibits porosity (Fig. 10B, D) and inundated with fluid inclusions (Fig. 10N). - Most CGM occurs as elongate homogeneous columbite-(Mn) (Fig. 10G). Rare fragments of oscillatory-zoned CGM exhibit CDP features with secondary patchy rims (Fig. 10H).	- All dike samples studied show some degree of albitization (*e.g.* Fig. 4B, 10A-B).
Quartz - mica domain (QMD)	- Fine- to medium-grained quartz-muscovite and quartz-lepidolite intergrowths are quite common through the LNPG. - Features with quartz-muscovite intergrowth: 1) spodumene, when present, lightly altered; 2) secondary albite, when present, is saccharoidal; and 3) accessory phases are sparse and mostly	- Such quartz-mica intergrowth often replaces earlier aluminosilicates (Fig. 11A-D) and are common along fractures (Fig. 11B-C) and intergranular boundaries (Fig. 11D). - Spatial distribution of quartz-muscovite and quartz-lepidolite assemblages controlled by earlier fractures and dissolution features with quartz-muscovite ted to proximal to such features (*i.e.* cms; Fig. 11A) and	- Apatite in this domain contains up to 8 wt% MnO and up to 13 wt% SrO, although most of it is barren of Sr.

	phosphates such as apatite, montebrasite and lithiophilite (Fig. 11C, E-F). - Features with quartz-lepidolite intergrowth: 1) spodumene is usually present and exhibit moderate to intense alteration (sometimes completely replaced by mix of illite-montmorillonite, kaolinite, lepidolite and albite; Fig 11G); 2) secondary albite, when present, is cleavelanditic (Fig. 11G); and 3) accessory phases varied, such as apatite, cassiterite, columbite-(Mn), zircon, as well as exotic phosphates (e.g. cheralite, Sr-bearing phosphates) (Fig. 11H-N).	quartz-lepidolite more extensive (Fig. 11G) and reflecting a more pervasive alteration (also suggested by higher degree of alteration of spodumene near quartz-lepidolite compared to quartz-muscovite).	
Late stage assemblage (LSA)	- Exhibits largest variation in mineralogy and is dominated by zeolites (Ca>Na>K), calcite and apatite. - Where Na-dominant zeolites present, muscovite is partially altered to paragonite and cookeite (muscovite → paragonite → cookeite; Fig. 12D-E). - Where Ca-dominant zeolites present, albite is replaced via CDP (with porosity) by calcic plagioclase (≤ An_{15}; Fig. 12F-G) and rarely occasionally with cassiterite (Fig. 12H). - RM mineralization includes calcio-microlite in CDP features in apatite (Fig. 12I), (tetra?)-wickmanite on fractures and pits in Mn-bearing apatite (Fig. 12J) and wodginite in calcite veinlets (Fig. 12K).	-Fills pre-existing voids and fractures (Fig. 8B, I, 12A) or superimposed on earlier domains (Fig. 12B-C). -Calcite latest phase to form and coats, crosscuts or replaces (Fig. 12K-M) other minerals, including zeolites. Calcite contains <0.3 wt% MnO and FeO. -Pseudomorphism is common (Fig. 12N).	- See Groat *et al.* (2003) for the identification of zeolites at the LNPG.

TABLE 1. Summary of observations for each of the domains at the LNPG. See Figures 5 to 12 for accompanying images.

	Feldspars			Micas					Other silicates					Phosphates			
	Perthitic K-feldspar	**Early albite**	**Late-stage albite**	**Biotite**	**Muscovite**		**Lepidolite**		**Spodumene**	**Beryl**	**Garnet**	**Zircon**	**Allanite-(Ce)**	**Monazite**	**Early apatite**	**Apatite**	**Cheralite**
	KFD	KFD	LSA	PWC	SAQD		MQD		SAQD	SAQD	PWC	BAP	PWC	PWC	KFD	MQD	MQD
Na_2O	1.5	11.9	10.1		0.6					1.3							
K_2O	14.0			9.8	11	11.4	10.9	9.7									
CaO		1.1	3								6.1		11.8	0.5	51.5	37.6	11.8
MgO				11.1							1						
SrO																6.3	
FeO				18.4	1.7	6.1	3.3		0.5		12.7		11.2				
MnO							1	0.5			23.4					8.2	
ZnO																	
Al_2O_3	18.7	19.6	22.8	16.6	35	24.6	22.9	34	25.5	18.5	20.2		19.9				
SiO_2	65.8	67.4	64.1	38.4	47.7	53.9	51.9	45.8	66	66.2	36.6	32.8	34.3				
TiO_2				1.7													
ZrO_2												52.1					
HfO_2												15.1					
ThO_2																	55.2
SnO_2																	
La_2O_3													7.1	18.7			
Ce_2O_3													11.4	34.9			
Pr_2O_3														4.4			
Nd_2O_3													2.3	8.7			
P_2O_5														32.8	43.5	42.9	33
U_2O_5																	
Nb_2O_5																	
Ta_2O_5																	
WO_3																	
F (>1 wt%)					Y	Y	Y	Y							Y	Y	
Not determined				OH	OH	OH	Li, OH	Li, OH	Li	Be					OH	OH	

TABLE 2. Representative semi-quantitative EDS analyses (normalized) of various minerals at the LNPG. Note that analyses of common end-member minerals (e.g. Ab_{100}, Kf_{100}, late-stage cassiterite, etc.) are not reported here due to space constraint. ALB = albitized domain; BAP = banded aplite-pegmatites; CVT = cavities; GRS = greisen-like domain; KFD = K-feldspar domain; MQD = mica-quartz domain; LSA = late-stage assemblage; PWC = pegmatite – wall-rock contact; SAQD = spodumene-albite-quartz domain.

Chapter 3

Using stable isotopes (O, H) and trace-element chemistry to assess melt source and subsolidus fluid:rock interaction for the LCT-type Little Nahanni Pegmatite Group (NWT, Canada)

Jérémie D. Pfister [a], Daniel J. Kontak [a], Lee A. Groat [b], Mostafa Fayek [c]

[a] *Harquail School of Earth Sciences, Laurentian University, Sudbury, Ontario P3E 2C6, Canada*

[b] *Department of Earth, Ocean and Atmospheric Sciences, University of British Columbia, Vancouver, British Columbia V6T 1Z4, Canada*

[c] *Department of Geological Sciences, University of Manitoba, Winnipeg, Manitoba R3B 2E9, Canada*

To be submitted to Geochimica and Cosmochimica Acta

3.1 Abstract

Previous studies of the mid-Cretaceous (*ca*. 85 Ma) LCT-type Little Nahanni Pegmatite Group (LNPG; Northwest Territories, Canada) document disequilibrium textures and pervasive metasomatism associated with rare-metal (e.g., Ta, Nb, Sn) mineralization. As in other pegmatites, the source of such pegmatite melts and the nature and origin of pervasive metasomatism remain enigmatic. To resolve these issues, an integrated study involving duel-inlet isotope ratio mass spectrometry (DI-IRMS) (O, H) analysis of mineral separates (quartz, K-feldspar, albite, muscovite, garnet), *in-situ* Secondary Ion Mass Spectrometry (SIMS) isotopic (O) analysis of quartz and albite, and *in-situ* Laser Ablation Inductively Coupled Plasma Mass Spectrometry (LA-ICP-MS) trace element analysis of quartz was complemented with cathodoluminescence (CL) imaging and petrographic observations. The high $\delta^{18}O$ values for quartz ($\delta^{18}O_{quartz}$ = 10‰ to 16.3‰) are complemented with uniform CL imaging and high Ti-in-quartz temperatures (551 ± 17°C to 603 ± 16°C). Together these data are considered to reflect their pristine character and suggests localized melt-wall rock (WR) exchange at the time of pegmatite melt emplacement and is supported by DI-IRMS $\delta^{18}O$ data from other minerals. Furthermore, the elevated $\delta^{18}O$ values indicate a crustal source (i.e. S-type granite) for the LNPG, which also overlaps with $\delta^{18}O_{quartz}$ data for granites of the regional mid- to Late-Cretaceous Selwyn Plutonic Suite of this area. The large range for $\delta^{18}O$ in metasomatic minerals such as albite (-3.0 to +18.3‰) indicates a complex evolution involving multiple oxygen isotopic reservoirs, in particular incursion of meteoric water previously equilibrated with metasedimentary wall rocks. Finally, the acute isotopic disequilibrium between mineral pairs (e.g. $\Delta_{quartz\text{-}albite}$ = -5.1‰ to +14.3‰) and abundance of dissolution features in late-stage assemblages unequivocally indicates that sub-solidus fluid:rock interaction was responsible for such large spreads in $\delta^{18}O$ and values δD values, although other processes (e.g. disequilibrium crystallization, thermal gradients, rapid cooling) might have also contributed. Application of a similar protocol to a further 60 samples from global LCT-type pegmatites reveal similarly larger ranges in $\delta^{18}O_{quartz}$. The latter we relate to post-emplacement modification of samples due to CDP processes which suggest the integrated approach used here be adopted in other studies.

3.2 introduction

Despite having been studied for over a century (e.g. Lindgren, 1913), the origin and evolution of rare-element pegmatites remain ambiguous and contentious (Černý, 1991; London, 2008, 2018; Simmons and Webber, 2008; Dill, 2015). It is now well-accepted that pegmatites, including those of the rare-elements class, can be generated either *via* fractional crystallization of a parental granitic melt (e.g. Černý, 1991; Černý and Ercit, 2005; London, 2008) or partial melting of fertile metasedimentary rocks (e.g. Simmons et al., 1995; Müller et al., 2017; Knoll et al., 2018; Webber et al., 2019). However, the origin of individual pegmatite fields, particularly those without an exposed parental pluton, remains problematic.

Additionally, the nature, extent and significance of metasomatism in pegmatites remains a contentious topic with some suggesting it is generally negligible (e.g. London, 2008, 2018) while others argue it plays an important role in formation of late-stage albitic and micaceous assemblages (e.g. Jahns, 1955, 1982; Stewart, 1978; Černý, 1982a, 1982b; Foord and Cook, 1989; Kontak et al., 2002; Kontak, 2006; Alfonso and Melgarejo, 2008; Martin and De Vito 2014; Maneta and Anderson, 2018; Pieczka et al., 2019). As such zones host important rare-metal (RM) mineralization makes their origin a significant and relevant issue. Further disagreement exists in regards to the nature and source of the metasomatising agent and whether it is derived internally *versus* externally. An internal source is suggested based on evidence for fluid exsolution during pegmatite-formation, as documented from fluid inclusions and trace elements studies (e.g. Thomas et al., 2012; Thomas and Davidson, 2013; Fredriksson, 2017; Harlaux et al., 2017; Kaeter et al., 2018), from the presence of miarolitic cavities and abundant magmatic-derived elements in the secondary assemblages (e.g. Ta, Nb, Be). In contrast, the enrichment of wall-rock- derived elements (e.g. Ca, Mg, Fe, S, biogenic C) in secondary assemblages and fluid inclusions (e.g. Kontak, 2006; Martin and De Vito 2014; Burns, 2019; Pieczka et al., 2019), as well as the frequent lack of exomorphic aureoles around pegmatites, favors an externally-derived fluid.

The application of stable isotopes can be used to address these important problems in the same manner as they have long been used to address problems related to granite petrogenesis (Taylor 1974, 1978; Taylor and Sheppard 1986), and fluids in ore systems (Taylor, 1979; Sheppard, 1986). However, only a few detailed stable isotopic studies of LCT-type pegmatites exist (e.g. Taylor et al., 1979; Taylor and Friedrichsen, 1983; Kontak and Kyser, 2009; Ashworth, 2014).

In this paper, we address the controversial issues of the source of pegmatite melts and the nature and origin of their metasomatism and related RM mineralization in a previously well-studied LCT-type pegmatite setting, the Late Cretaceous Little Nahanni Pegmatite Group (LNPG) in NWT (Canada) (Mauthner, 1996; Groat et al., 2003; Kontak et al., 2004; Barnes, 2010; Barnes et al., 2012; Kontak et al., 2016; Burns, 2019; Pfister et al., 2019; Pfister et al., 2022). This study integrates petrographic observations, cathodolominescence imaging (CL), trace elements, Ti-in-quartz geothermometer, bulk analysis for O and H stable isotopic analysis on a variety of primary and secondary phases, and *in situ* SIMS O isotopic analysis of quartz and albite in order to track the processes associated with the formation of these pegmatites. Additionally, given the lack of a large global database for $\delta^{18}O_{quartz}$ analysis for LCT-type pegmatites, we supplement the LNPG data with an additional 60 quartz samples from 16 other LCT-type pegmatite suites. The results of this study show how careful integration of petrography and mineral paragenesis with stable isotopic analysis can resolve important outstanding questions pertinent to pegmatite genesis.

3.3 Geological setting, previous work and features of the LNPG

The LNPG is located in the Selwyn Mountains, about 10 km from the Yukon- Northwestern Territories border of northern Canada (Fig. 1A). Here a suite of several hundred LCT-type pegmatite dikes traverse a mixed package of siliclastic and pelitic sedimentary rocks (with variable amount of carbonate matrix) of the Neoproterozoic Yusezyu and Narchilla formations which form part of the regionally extensive Selwyn

97 Basin of the northern Canadian part of the Cordillera (Gordey and Anderson, 1993). Compressional
98 tectonism during the Jurassic produced numerous NW-SE – trending folds and thrust faults, as well as low-
99 grade regional metamorphism (i.e. sub-greenschist facies; Gordey and Anderson, 1993; Gordey, 2013). At
100 LNPG the latter is manifest by the presence of the NW-trending, open-to-tight, upright Fork Anticline and
101 the crosscutting NNW-trending March Fault. Mid- to Late Cretaceous magmatism formed the Selwyn
102 Plutonic Suite, which consists of crust-derived granitic plutons (Rasmussen and Arehart, 2010) ranging
103 from metaluminous I-type to peraluminous S-type that cover about 8% of the Selwyn Basin (Gordey and
104 Anderson, 1993; Gordey, 2013).

105 Exposure of granitic rocks is lacking in the immediate vicinity of the study area, but several aspects are
106 relevant in the context of the source of the pegmatites. Firstly, the Lened (*ca.* 93 Ma), Cac (age unknown)
107 and Rudi (*ca.* 84-87 Ma) plutons are all within 30 km of the LNPG and many more within 50 km (Fig. 1A).
108 In this context we note the age of the LNPG is constrained to *ca.* 85 Ma based on U-Pb TIMS dating of
109 columbite (81.6 ± 0.5 Ma; Mauthner et al., 1995) in addition to *in situ* LA ICP-MS U-Pb dating of zircon
110 (87.3 ± 1.2 Ma; Kontak et al., 2016) and cassiterite (87.3 ± 1.7 Ma; Kontak, manuscript in preparation).
111 Lastly, the localized presence of a coarse-grained assemblage of andalusite-staurolite-cordiertite-garnet in
112 the norther part of the study area (i.e., cirques 0-1N; Fig. 1C, D) suggest an area of hornfels which we relate
113 to an unexposed granitic intrusion and for which estimated PT conditions of ~2 kbar and 400 - 500°C are
114 inferred based on thermobarometry (Barnes, 2010). Alternatively, the LNPG dike swarm may be hosted in
115 the structural hanging wall to the March Fault and thus detached from its progenitor intrusion.

116 The LNPG consists of a few hundred dikes covering an area of about 15 km by 5 km on the northeastern
117 limb of the Fork Anticline and SW of the regional March Fault (Fig. 1B); these pegmatites are particularly
118 well-exposed in the walls of a suite of thirteen cirques that cover most the area (Fig. 1B, 2A). Most dikes
119 are ≤2 m wide, underlie most of the area as en echelon features, and can extend over several km in length
120 (Groat et al., 2003; Fig 2A, B) which gives an anomalously high aspect-ratio for these pegmatites (up to
121 1:1000+).

The dike rocks are significantly enriched in Li, Ta, Nb, Sn and P (Groat et al., 2003; Barnes, 2010; Liverton, 2017), which are respectively hosted in spodumene (Fig. 2C), lepidolite (Fig. 2D, E, F), columbite group minerals, cassiterite and various phosphates (Groat et al., 2003; Pfister et al., 2022). Important textures include: (1) early K-feldspar megacrysts (Fig. 2G); (2) layered- and crenulate-textured aplites (Fig. 2D), which sometimes display evidence of dike-reopening (Fig. 2E, F); (3) coarse (10-30 cm), acicular spodumene oriented perpendicular to the wall-rock (WR) contact (Fig. 2C); (4) widespread albitization (Fig. 2H, I) associated importantly with Ta-Nb-Sn mineralization; (5) various secondary assemblages after earlier phases (Fig. 2 J, K); (6) abundant dissolution features (Fig. 2K); (6) limited WR alteration (Fig. 2L); and (7) various crystal morphologies (skeletal, plumose; Barnes, 2010; Pfister et al., 2022) suggestive of disequilibrium crystallization (e.g. London, 2008; Maneta and Baker, 2014; Sirbescu et al., 2017; Maneta and Anderson, 2018). These textures are comprehensively discussed by Pfister et al. (2022) and collectively indicate disequilibrium conditions and rapid cooling during the magmatic stage, as well as ubiquitous fluid-rock interaction during the metasomatic stage.

Additionally, detailed mineralogy (Groat et al., 2003), Li isotopes (Barnes, 2010; Barnes et al., 2012), whole-rock geochemistry (Barnes, 2010) and fluid inclusions (Burns, 2019) studies of the LNPG are available and are variably incorporated in the model presented below.

3.4 Methods

The LNPG samples used herein were collected during three field seasons (2004, 2007 and 2008) and consist of various pegmatitic assemblages, four samples of muscovite – quartz – carbonate – albite veins associated with the pegmatites, and a loose surface granite sample. Additional material is from archived material from previous field visits which formed the basis of Groat et al.'s (2003) earlier study. Most of the non-LNPG samples were collected in the field by Pfister and samples of reliable provenance of additional pegmatite suites that the authors did not personally visit were obtained from Dr. Ian Nicastro (samples

collected in 2017-2018), Abdur Rehman Safi (samples collected in 2016-2017) and Dan Weinrich (historical samples).

Petrographic observations were performed using an Olympus MX51 microscope and supplemented with imaging using a Jeol JSM-6400 Scanning Electron Microscope (SEM) housed at the at Micro-analytical Centre (MAC), Laurentian University (Sudbury, Ontario, Canada). The SEM is coupled to a solid-state Oxford-Sight energy dispersive spectrometer (EDS) detector and analyses were performed using a 20 kV accelerating voltage, 1 nA beam current, working distance of 15 mm and acquisition times ranging from 5 to 15 seconds. Data were processed using a combination of Oxford Instrumentation softwares AZtec and INCA. Cathodoluminescence (CL) imaging was done using a Chroma CL detector coupled to the MAC Jeol JSM-6400 SEM.

Using pure mineral fragments handpicked under a binocular microscope, high-quality mineral separates were prepared and sent to Queen's Facility for Isotope Research (QFIR) in Kingston (Ontario, Canada) for analysis of $\delta^{18}O$ and δD using duel-inlet isotope ration mass spectrometry (DI-IRMS). The BrF_5 technique of Clayton and Mayeda (1963) was used to extract oxygen from mineral separates (i.e. quartz, K-feldspar, albite, muscovite, biotite and garnet), whereas the method of Kyser and O'Neil (1984) was used for the extraction of hydrogen from micas separates. Bulk analyses were done using a Finnigan MAT 252 mass spectrometer. The results are presented in the conventional per mil (‰) notation and referenced to V-SMOW (Vienna Standard Mean Ocean Water). Analytical reproducibility of $\delta^{18}O$ on standards is ± 0.3‰, whereas for δD reproducibility is ± 3‰.

Additionally, a second selection of high-quality hand-picked mineral fragments (quartz and albite) were mounted in epoxy pucks and following grinding and polishing prepared for *in-situ* analysis with Secondary Ion Mass Spectrometry (SIMS) at the University of Manitoba using a Cameca 7F secondary ion mass spectrometer. The following parameters were used: (1) 4 nA primary ion beam of Cs+ accelerated at 10 kV; (2) spot size = 15 µm for albite and 20 µm for quartz; (3) entrance slit = 225 µm for albite and 250 µm for quartz; (4) deadtime = 27 ns; (5) 70 cycles over 10 minutes; (6) one cycle = 1 s of detection on ^{16}O and

5 s on ^{18}O; and (7) counts = $1*10^6$ for ^{16}O and $2*10^3$ for ^{18}O. Reference materials consist of Am Feldspar from Riciputi et al. (1998) for albite and UWQ1 Quartz from Kelly et al. (2007). Analytical reproducibility for $\delta^{18}O$ on quartz and albite standards is ± 0.8‰. Again, isotopic values ($\delta^{18}O$, δD) are reported using the δ notation relative to V–SMOW.

The trace element contents of the mounted quartz fragments used for SIMS analyses were also were analyzed using Laser Ablation Inductively Coupled Mass Spectrometer (LA-ICP-MS) at the Laurentian University. The laser ablation system consists of a 193 nm ArF excimer laser (Resonetic Resolution M-50 193 nm probe) coupled to a quadrupole ICP-MS Thermo Electron X Series II. The following parameters were used: (1) laser spot size = 75 µm; (2) pulse duration = 20 ns; (3) repetition rate = 8 Hz; (4) fluence = 5 J/cm^2; (5) carrier gas = He; and (6) nebulizer gas = Ar. Each spot consisted of 30 s of background followed by 30 s of ablation. ^{29}Si was used as the internal standard and reference material used consist of NIST 610 & 612 (Jochum et al., 2011) and BHVO2G (Jochum et al., 2005). QAQC data for the secondary standards (NIST 612 & BHVO2G) is provided in appendix 1. Data were processed using IOLITE v.4 software (Paton et al., 2011).

3.5 Results

3.5.1 Petrography and cathodoluminescence

Petrographic observations and CL imaging of quartz were used to address the nature (i.e. magmatic *versus* metasomatic) and degree of alteration of each sample (Table 1). Imaging magmatic quartz revealed no primary zoning, which is not uncommon for primary pegmatitic quartz (e.g. Götze et al., 2005; Ihlen et al., 2007; London et al., 2012; London, 2014) and thus most samples exhibit a homogeneous bright blue response with minor fracturing (Fig. 3A, B, C). Dissolution features were rarely observed in samples of magmatic quartz and when present in minor amounts (e.g. Fig. 3C) were avoided during *in-situ* SIMS and LA-ICP-MS analyses. In contrast, samples with an abundance of such features are generally black (Fig. 3D, E) or sometimes have a yellowish hue. These areas are interpreted to be metasomatic as they are

195 indicative of sub-solidus interaction with fluids and in detail record coupled dissolution-reprecipitation
196 (CDP; see Putnis (2002) and Plümper and Putnis (2009) for discussion). Notably, these features are widely
197 observed in magmatic-hydrothermal ore systems such as porphyry deposits (e.g. Rusk and Reed, 2002;
198 Landtwing et al., 2010).

199 3.5.2 Trace elements in quartz

200 Three spots in the immediate vicinity of target areas for SIMS $\delta^{18}O$ were analyzed for trace
201 elements and were integrated with CL imaging to assess intragranular homogeneity. Values from analyses
202 showing a sudden spike or trough in elemental contents in time-resolved spectra (using IOLITE v.4
203 software), which likely reflects ablation of an inclusion, were discarded. The ^{47}Ti, ^{72}Ge, and ^{27}Al contents
204 of the reaming quartz analyses, which are considered the most reliable in this study, are reported in Table
205 2.

206 The contents for ^{47}Ti, ^{72}Ge, and ^{27}Al in quartz (n=155) were measured with the following results.
207 For Ti values range from 4.7 ± 1.1 to 15.5 ± 1.2 ppm (n = 155; an outlier at 23.6 ± 2.8 ppm) and shows
208 intragranular homogeneity as Ti ± analytical uncertainty (reported as Int2SE in tables) for multiple analyses
209 conducted on individual samples overlap in all but three samples. The data for Ge, which ranges from 0.5
210 ± 0.1 to 9.8 ± 0.4 ppm (one outlier at 25.1 ± 7.2 ppm), is also homogeneous within individual samples, but
211 differs among them. Lastly, Al exhibits the greatest variation and ranges from 11.6 ± 0.9 to 9000 ± 1600
212 ppm.

213 Although it is not possible to discriminate magmatic from metasomatic quartz using quartz
214 chemistry alone, samples with the lowest Al and Ge values are unambiguously hydrothermal, such as for
215 late stage muscovite - quartz - calcite - albite veins that branch off pegmatite dikes (e.g. sample 07-46; see
216 Table 1) and prismatic quartz from late stage vugs (e.g. sample 226; see Table 1).

217 3.5.3 Ti-in-quartz geothermometer (TitaniQ)

The Ti-in-quartz geothermometer "TitaniQ" (Wark and Watson, 2006; Thomas et al., 2010; Huang and Audétat, 2012), which has been previously applied to granitic pegmatites (e.g. Müller et al., 2015; Ashworth et al., 2020), is used to estimate the temperature of quartz formation. Correct application of this method requires the following factors and parameters be addressed: 1) Ti diffusion in quartz; 2) presence of inclusions; and 3) accurate estimate of pressure and αTiO_2. These latter aspects are addressed individually below.

3.5.3.1 Ti diffusion

While Ti can diffuse in quartz at high temperatures, the diffusion distance at $T \leq 400°C$ is <10 μm per 100 million years (Cherniak et al., 2007). Recent thermal modeling of pegmatitic melt (650-750°C) intruding cooler host rocks (e.g. 250-350°C) suggest that a 2 m wide pegmatite cools to below 400°C in a matter of weeks (London, 2008, 2018; Simmons and Webber, 2008; Sirbescu et al., 2008). Considering the LNPG is only *ca*. 85 Ma, consists mostly of dikes of <2 m width, and intruded relatively cool rocks (i.e. sub-greenschist facies), potential diffusion of Ti in quartz likely did not exceed 10 μm at the LNPG. Thus, Ti diffusion is considerably smaller than the 75 μm ablation spot size and does not significantly affect the calculated temperatures.

3.5.3.2 Presence of inclusions

No solid inclusions were observed in the quartz samples using transmitted light microscopy, SEM-BSE imaging or CL imaging. Additionally, where fluid inclusions were present in samples they were carefully avoided, but analyses which did contain sudden spikes or troughs of trace elements in their time-resolved spectra likely indicate inclusions and thus were discarded. Overall, the consistency of the results for multiple analyses conducted on individual samples indicates that no Ti-bearing inclusions were encountered.

3.5.3.3 Pressure and Ti activity (αTiO_2)

241 Pressure at the time of emplacement of the LNPG is estimated at about 2 - 2.5 kbar based on fluid
242 inclusions studies (Barnes, 2010; Burns, 2019), the GAPQ mineral equilibria on the hornfels assemblage
243 noted above (Barnes, 2010), a maximum burial depth of the host rocks (Gordey and Anderson, 1993), and
244 lack of high-pressure aluminosilicates in the hornfels surrounding local contemporaneous plutons (Gordey
245 and Anderson, 1993; Gordey, 2013).

246 Sparse rutile and ilmenite are present in the dikes (Groat et al., 2003; Pfister et al., 2022), but were
247 only observed in this study as: 1) inclusions in columbite group minerals (CGM) and cassiterite; 2) at the
248 edge of large acicular spodumene crystals; and/or 3) at pegmatite-WR contact. This suggests that rutile is
249 not part of the equilibrium assemblage and formed as the result of: 1) exsolution from Nb-Ta-Sn oxides;
250 and 2) local TiO_2 saturation triggered by boundary-layer effects and WR contamination. Additionally, the
251 very low Ti contents (<7.5 ppm (± 0.4) for whole-rock dike analyses (Barnes, 2010) falls well below the Ti
252 solubility for evolved felsic melt at 500-600 °C (Hayden and Watson, 2007). These observations suggest
253 the melts did not reach TiO_2 saturation and thus αTiO_2 was <1.0 at the time of emplacement. Calculations
254 of αTiO_2 using the method of Hayden and Watson (2007) between 500-600 °C and the whole-rock analyses
255 in Barnes (2010) yielded αTiO_2 values ranging from 0.2 to 1.0. This large spread in values likely reflects:
256 1) nugget effect of the whole-rock analyses in pegmatites; 2) local saturation of TiO_2 in the melt (e.g.
257 boundary-layer effects, contamination); 3) the metasomatic overprint; and 4) uncertainty of extrapolating
258 the Hayden and Watson (2007) method (calibrated for 650<T<1000 °C) to temperatures of pegmatite
259 formation (e.g. 500-600 °C).

260 A TiO_2 activity of 0.5 was used for TitaniQ calculations, as using a lower αTiO_2 value results in
261 unrealistic temperatures (i.e. >650 °C) for undercooled pegmatites, and a higher αTiO_2 is unlikely
262 considering the very low Ti content of the LNPG and the lack of rutile as part of the equilibrium assemblage.
263 Note that the effect of the αTiO_2 value used in TitaniQ calculations becomes less important at low
264 temperatures (Huang and Audétat, 2012). For instance, using a αTiO_2 of 1.0 yields values that are about 50

°C lower and for 0.3 values that are about 50 °C higher, thus the temperature ranges reported here are accurate within ± 50 °C regardless of the αTiO_2 used.

3.5.3.4 Analytical uncertainty and results

Because at such low concentrations of Ti the analytical uncertainty (reported as Int2SE in Tables 2 and 3) becomes significant, the calculated temperatures are reported here as $T_{mean} \pm (1\sigma + Int2SE_{mean})$ instead of the more common $T_{mean} \pm (1\sigma)$. All values (i.e. T_{mean}, 1σ, $Int2SE_{mean}$) are reported in Table 3 and the final calculated temperature ranges are graphically summarized in Figure 4. TitaniQ values were calculated using Huang and Audétat (2012) calibration, a pressure of 3 kbar, and αTiO_2 of 0.5.

Quartz from the granite sample (07-03) yielded the highest temperature at 638 ± 38 °C. Fresh primary magmatic quartz from the pegmatites (n = 38) yielded temperatures from 551 ± 17 °C to 603 ± 16 °C, with a mean of 571 ± 17 °C. Quartz from metasomatic assemblages yielded temperatures from 552 ± 20 °C to 591 ± 21 °C. It should be noted, however, that the application of TitaniQ to low T hydrothermal systems, such as the metasomatic stage here, remains questionable and is considered instead to often just reflect a maximum possible T (Huang and Audétat, 2012). Two large quartz (±schorl) veins associated with the pegmatites returned temperatures >600 °C, while a late stage muscovite - quartz - calcite - albite vein originating from a pegmatite dike returned a temperature of 587 ± 11 °C.

3.5.2 Stable isotopes

3.5.2.1 LNPG

The results of $\delta^{18}O$ analyses on pegmatite-related material include data from 72 samples of quartz, 29 of albite, six of K-feldspar, 10 of muscovite, one each of biotite, garnet, and calcite (Table 4). As far as we know, this represents the largest and most comprehensive dataset for the study of a single pegmatite group yet assembled. The results are summarized in Figure 5 and discussed below:

1. The 72 quartz samples analyzed, which are a combination of bulk (n = 9) and SIMS (n = 63), yielded $\delta^{18}O$ values ranging from +8.6 to +16.3‰. For primary magmatic quartz (n = 50), the values range from +10.2 to +16.3‰ with mean of 12.8‰ (± 1.4‰), but for quartz collected <2 cm from the pegmatite-WR contact (n = 5) values range from +13.6 to +16.3‰ with a mean of 15.0‰ (± 0.9‰), while samples >2 cm away from the such contacts (n = 45) range from +10.2‰ to +16.2‰ and a mean of 12.6‰ (± 1.3‰). Metasomatic quartz (n = 18) ranges from +8.6 to +14.8‰ and hydrothermal quartz from large quartz veins spatially associated with the pegmatites (n = 3) range from +11.6 to +13.2‰. Finally, a quartz grain from a loose sample of granite found near the pegmatites returned a $\delta^{18}O$ value of +11.4‰.

2. For albite, 29 samples analyzed using bulk (n = 12) and SIMS (n = 17) yielded $\delta^{18}O$ values from -3.0 to +18.3‰ and thus represent the greatest range of all minerals analyzed from LNPG (Fig. 5). Virtually all albite samples display secondary textural features and host fluid inclusions, thus suggesting that these values reflect various degrees of sub-solidus fluid:mineral interaction.

3. For muscovite, 10 samples analyzed using bulk yielded $\delta^{18}O$ values ranging from +8.8 to +13.2‰. Muscovite from late stage muscovite – quartz – calcite ± albite veins branching off pegmatite dikes have values ranging from +12.6 to +13.2‰. A sample of free-standing muscovite found in a dissolution cavity yielded a $\delta^{18}O$ value of +13.0‰, and a pencil-type mica from a greisen-like domain has a $\delta^{18}O$ value of +12.9‰.

4. For K-feldspar, the five samples analyzed by bulk yielded $\delta^{18}O$ values from +6.8‰ to +13.8‰. All of these samples consist of white to grey, glassy K-feldspar megacrysts from early K-feldspar - quartz - spodumene - albite assemblages and are considered to be of magmatic origin, although the presence of secondary features (e.g. pores, fluid inclusions, and perthitic textures) seen using petrography and SEM imaging suggest these values partially reflect sub-solidus fluid:mineral interaction.

5. A single garnet analyzed has a $\delta^{18}O$ value of +10.7‰. It is of spessartine variety ($(Mn_{0.6}Fe_{0.4})_3Al_2Si_3O_{12}$) and was found 2 cm from the pegmatite-WR contact.

6. A single biotite, found at the pegmatite-WR contact, returned a $\delta^{18}O$ value of +12.7‰.

7. A single calcite analyzed has a $\delta^{18}O$ value of +14.8‰ and is part of a late stage muscovite - quartz - calcite - albite vein originating from a pegmatite.

The results of δD analyses on ten samples of muscovite and one of biotite (Table 4) are summarized below:

1. The ten samples of muscovite analyzed for $\delta^{18}O$ were also analyzed for δD. The δD values range from -67‰ to -182‰. Amongst these, muscovite from late stage muscovite – quartz – calcite ± albite veins related to the pegmatites have δD values from -83‰ to -67‰. One sample of free-standing muscovite found in a dissolution cavity in a pegmatite coexisting with albite, quartz, fluorite and zeolites returned a value of -177‰.

2. The single biotite from a pegmatite-WR contact, which was analyzed in duplicate, yielded δD values of -168 and -173‰.

3.5.2.2 Other LCT pegmatites

A compilation of pegmatite-related isotopic data available in the English literature was used to compare the LNPG with other LCT-type pegmatites. Quartz, being the most commonly analyzed phase in pegmatites, provides the most effective way of comparison. Additionally, as $\delta^{18}O$ data for LCT-type pegmatites remains relatively scarce in the literature, a suite of 60 quartz samples from 16 such pegmatites were assembled and analyzed for $\delta^{18}O$ by SIMS to complement our studies at the LNPG and literature compiled data; these results are summarized in Table 5 and Figure 6. Importantly, the additional data also provide a higher resolution than currently available in the literature due to the *in-situ* nature of SIMS analysis (i.e. most data in the literature are bulk analyses) and can be integrated with petrographic observations that are only visible under CL, which is currently lacking from other isotopic studies. In this regard, we note that the CL imaging of these sample revealed abundant CDP features in all but a few

samples (Fig. 7). Examples of such features are seen in the Anita, Authier, and Leduc pegmatite samples and yet, as far as we are aware, this feature is not described for these settings.

The results of the compilation and the new $\delta^{18}O$ analysis of quartz from this additional samples indicate the following:

1) An overall range from +5.3‰ to +16.0‰.
2) For single localities there are both limited (e.g. Maple Lode Pegmatite) and large (e.g. Alvarroes Pegmatite) ranges, although nothing which approaches that for the LNPG. There does not seem to be a correlation between the data range and number of analyses available.
3) The data generated by this study (SIMS) yield larger ranges for individual pegmatites than what the existing literature (bulk analysis) suggest.

3.6 Discussion

The results presented above are integrated with petrographic observations, as well as previously published textural, mineralogical, geochemical, and fluid inclusion data (e.g. Mauthner, 1996; Groat et al., 2003; Barnes, 2010; Burns, 2019; Kontak et al., 2016; Pfister et al., 2022) to address the following aspects: (1) the original isotopic signature of the melt and by inference its potential source; (2) evidence for pegmatite-wall rock interaction; (3) sub-solidus fluid-rock interaction; (4) nature and origin of the metasomatizing fluid(s); and (5) implications of this study for other LCT-type pegmatites.

While all the isotopic data are discussed below, the following observations form the basis of the discussion: (1) high $\delta^{18}O$ values of magmatic minerals (Table 4 and Fig. 5); (2) very low $\delta^{18}O$ values for some secondary minerals (Tables 1 and 4); (3) a large range of $\delta^{18}O$ values for both magmatic and metasomatic minerals, albeit more pronounced in the latter (Tables 1 and 4); (4) large $\Delta_{mineral\text{-}mineral}$ values which imply disequilibrium; and (5) large range of $\Delta_{mineral\text{-}mineral}$ values.

3.6.1 Initial isotopic signature of the melt and its source

The age of the LNPG (*ca*. 85 Ma) corresponds to the final stage of regional, mid-Cretaceous felsic magmatism in the Selwyn Basin which is referred to as the Selwyn Plutonic Suite (ca. 106 – 80 Ma; Gordey and Anderson 1993; Gordey 2013; and references therein). This suite consists of crust-derived granitic plutons (Ramussen and Arehart, 2010) of metaluminous I-type to peraluminous S-type (Gordey and Anderson, 1993). Importantly, S-type granites in general are considered to be a particularly fertile source of LCT-type pegmatites (Martin and De Vito, 2005; London, 2008; Simmons and Webber, 2008), thus local members of the extensive Selwyn Plutonic Suite represent potential fertile source magmas for LCT-type pegmatites such as at LNPG. Other contemporaneous deposits in the area, including some rare-element pegmatites (Marshall et al., 2004), are unequivocally associated with specific plutons of the Selwyn Plutonic Suite (e.g. O'Grady pegmatites, Ercit et al., 2003; Lened W-Be skarn, Marshall et al., 2004; Lake et al., 2017). However, LNPG's progenitor granite remains to be identified. As previously noted, not only did regional metamorphism not exceed sub-greenschist facies in the area, it also pre-dated emplacement of the LNPG dike swarm (Gordey and Anderson, 1993; Gordey, 2013). Thus, an anatectic model, as suggested for other LCT-type pegmatite fields (e.g. Simmons et al., 2016; Müller et al., 2017; Knoll et al., 2018), is precluded for the LNPG. However, despite the LNPG being ca. 30 km from the closest exposed magmatic centre (Fig. 1), the presence of low-P high-T rocks (i.e. hornfels) in the northern part of the study area strongly suggests contact metamorphism and supports the presence of a fertile felsic intrusion. The apparent lack, however, of an obvious progenitor granite in the immediate vicinity is interpreted to relate to E-directed movement on as the March Fault (Fig. 1), an interpreted regional thrust feature (Gordey and Anderson, 1993), which might have detached the pegmatites from their source and transported the pegmatites in the structural hanging wall of this feature.

The melt source to the LNPG can be partly addressed using oxygen isotopes, as the signature of potential source material is variable (Taylor, 1978; Taylor and Sheppard, 1986). Although measuring a representative bulk magmatic $\delta^{18}O$ value is precluded due to the heterogeneity of the pegmatites and variable amount of metasomatic overprint, such values can be inferred using the $\delta^{18}O$ of fresh primary

minerals. Because the diffusion rate of oxygen is slower in quartz than in feldspars and other granitic phases by several orders of magnitude (Giletti et al., 1978; Giletti and Yund, 1984; Yund and Anderson, 1978, Elphick and Graham, 1986), quartz is more resistant to isotopic re-equilibration and thus retains its original isotopic signature. Additionally, as CL imaging of the fresh magmatic quartz (Fig. 3) revealed few dissolution features, it appears the studied quartz material remained mostly unaffected by the late stage Na-metasomatism. For these reasons, quartz is considered a reliable proxy to infer the original $\delta^{18}O$ value of the progenitor melt for the LNPG.

Thus, the $\delta^{18}O$ values of +10.2 to +16.3‰ (see Fig. 8A) potentially reflect the original signature of pristine magmatic quartz. We note, however, that such a large range for $\delta^{18}O$ quartz from a single setting (i.e. magmatic reservoir) is unusual for granitoid rocks (e.g. Taylor 1974, 1979; Taylor and Sheppard, 1986) and instead suggests the $\delta^{18}O$ signature of the primary pegmatitic melt has been modified. This we attribute to the high aspect ratio of the dike bodies and their interaction with the metasedimentary wall rocks during emplacement, as discussed in more detail below. Hence we consider the primary signal to be at the low end of the range of $\delta^{18}O$ values, thus 10-12‰. Using these values and the $\Delta_{quartz\text{-}whole\text{-}rock}$ $\delta^{18}O$ value of +1.2‰ for evolved granites and pegmatites (see Kontak and Kyser, 2009; Ashworth et al., 2020), calculated $\delta^{18}O_{whole\text{-}rock}$ values fall between about +9‰ and +11‰. Such $\delta^{18}O$ values correspond best to crust-derived granites (O'Neil and Chappell, 1977; Chappell and White, 1992) and is also consistent with the inferred crustal nature of the Selwyn Plutonic Suite (Gordey and Anderson, 1993). We also note that the range of $\delta^{18}O_{quartz}$ for the LNPG of +10.2‰ to +16.3‰ is the same as the $\delta^{18}O_{quartz}$ values of +8.4‰ to +16.9‰, but with >90% between 12.5 to 16‰ (n = 91; Rasmussen and Arehart, 2010) derived from granites of the Selwyn Plutonic Suite. In summary, the genetic relationship between LNPG and the Selwyn Plutonic Suite is supported by geochemical affinity (i.e. crust-type granites and LCT-type pegmatites), overlapping $\delta^{18}O_{quartz}$ values, similar ages of emplacement, and the absence of appropriate age high-grade regional metamorphism which precludes an anatectic model.

3.6.2 Implications of $\delta^{18}O$ variation for the magmatic stage

The spread of inferred magmatic $\delta^{18}O_{whole\text{-}rock}$ values of 6‰ is too large to be attributed to a single magmatic reservoir (i.e. pegmatite-forming melt) which crystallized under equilibrium conditions (e.g. Taylor, 1978; Taylor and Sheppard, 1986; Bindeman and Valley, 2002). It should be noted, however, that although sub-solidus processes are credited for an even larger spread in $\delta^{18}O_{mineral}$ values (e.g. up to 23‰, see section 5.3), only the $\delta^{18}O$ values of the least altered magmatic quartz samples were used to infer the $\delta^{18}O_{whole\text{-}rock}$ values; i.e. quartz showing significant CDP textures under CL were excluded. Therefore, a few possible scenarios are graphically summarized in Figure 9 to account for the range of $\delta^{18}O_{whole\text{-}rock}$ values and individually explored below: 1) temperature variations, both spatial (e.g. thermal gradient) and temporal (e.g. system cooling); 2) disequilibrium crystallization; 3) open-system behaviour involving a moderate $\delta^{18}O$ melt (i.e. $\delta^{18}O_{quartz}$ = 10‰ – 12‰) interacting with an ^{18}O-enriched reservoir, or a high $\delta^{18}O$ melt (i.e. $\delta^{18}O_{quartz}$ >14‰) interacting with an ^{18}O-depleted reservoir.

3.6.2.1 Temperature-related fractionation

The temperature dependence of isotopic fractionation (e.g. Bottinga and Javoy, 1973, 1975; Zheng, 1993a, b) suggests that a rapidly cooled system, such as LNPG, combined with a significant thermal gradient can produce a large range of $\delta^{18}O_{quartz}$ values. However, there is no correlation between temperature of quartz formation (TitaniQ) and their respective $\delta^{18}O$ values (Fig. 10). Furthermore, the quartz-H_2O fractionation factor, which is greater than quartz-melt and thus represents an upper constraint, only varies by 2.4 ‰ (Zheng 1993a) between 400 and 600 °C. Thus, even if the TitaniQ temperature values are off, the large spread of magmatic $\delta^{18}O_{quartz}$ values (6‰) cannot be explained by cooling of the system and other temperature-related fluctuations. Additionally, while thermal gradients are known to produce isotopic fractionation due to Soret diffusion (Soret, 1879; Kyser et al., 1998; Bindeman et al., 2013), the rapid decay of the thermal gradients for pegmatites is within days to weeks (e.g. London, 2008; Sirbescu et al., 2008), which precludes the influence of oxygen diffusion in a granitic melt to produce a $\delta^{18}O$ gradient (Kyser et al., 1998). Based on this, we conclude the range of magmatic $\delta^{18}O_{quartz}$ values is not related to a thermal gradient.

3.6.2.2 Disequilibrium crystallization

An increasing amount of evidence suggests that undercooling-induced disequilibrium crystallization is a fundamental process for pegmatite formation (e.g. London, 2005, 2008, 2014, 2018, Simmons et al., 2008; Sirbescu et al., 2008; Maneta and Baker, 2014; Sirbescu et al., 2017). In this model, undercooling and boundary-layer effects disturb the diffusion of elements and isotopes, potentially resulting in local isotopic disequilibrium (London, 2008). Of relevance to this model is the recent experimental work on internal O isotope fractionation and melt polymerization by Dubinia and Borisov (2018) which suggests significant oxygen isotope fractionation can occur between its structural types (i.e. bridging "BO" and nonbridging "NBO" oxygen) in a melt. It is conceivable, therefore, that the formation of a flux- and volatile-rich boundary layer at the crystal-melt interface (London, 2005, 2008, 2014, 2018) triggered fractionation between the depolymerized (i.e. NBO-rich) boundary layer and the highly polymerized residual melt (i.e. BO-rich), which, in addition to the accumulation of excluded elements and isotopes in the boundary layer, can yield isotopic disequilibrium. Textural evidence of disequilibrium crystallization has been documented at the LNPG (Barnes, 2010; Pfister et al., 2022), thus it is likely that disequilibrium crystallization played a role in the large spread of $\delta^{18}O$ values. However, that $\delta^{18}O_{quartz}$ values for LCT pegmatites with disequilibrium conditions exhibit a significantly narrower range (Fig. 6A) suggest that such processes only partially account for the large spread in magmatic $\delta^{18}O_{quartz}$ values, perhaps of a few per mil, and infers that another process must have occurred.

3.6.2.3 Open system with multiple oxygen reservoirs

Previously documented mineralogical, textural and fluid inclusion evidence of pegmatite-WR interaction (e.g. Kontak et al., 2016; Burns, 2019; Pfister et al., 2022) indicate the LNPG evolved as a partially open system. Thus interaction between contrasting oxygen isotopic reservoirs during pegmatite crystallization is explored to address the noted range in magmatic $\delta^{18}O_{quartz}$ values, these being the pegmatite-forming melt and the ^{18}O-enriched metasedimentary host rocks. Fresh magmatic quartz at or near

(<2 cm) the pegmatite-WR contact has, on average, higher $\delta^{18}O$ values (15.0‰ ± 0.9‰) than fresh magmatic quartz away from the contact (12.6‰ ± 1.3‰). Since Soret diffusion can be ignored due to the rapid decay of the thermal gradient and, as noted above, there is no apparent correlation between $\delta^{18}O_{quartz}$ and TitaniQ values (Fig. 10), this suggests these higher $\delta^{18}O_{quartz}$ values likely reflect a WR influence rather than the presence of a thermal gradient. In turn, this implies the large spread in magmatic $\delta^{18}O_{quartz}$ and derived $\delta^{18}O_{whole\text{-}rock}$ values is due to local interaction between the pegmatite-forming melt and the ^{18}O-enriched metasedimentary host rocks at the time of dike emplacement.

Interaction between a high $\delta^{18}O$ melt (i.e. $\delta^{18}O_{quartz}$ >14‰) and an ^{18}O-depleted reservoir is also conceivable, although the only potential ^{18}O-depleted reservoir present at the time of dike emplacement consists of meteoric water (see discussion in 5.3) and there is a lack of evidence for water-melt interaction (i.e. lack of miarolitic cavities, scarcity of primary hydrated phases).

Based on the above discussion, we infer the best estimate of the $\delta^{18}O_{quartz}$ to in the initial or primitive pegmatitic melt to be around +10‰ to +12‰ (see Figs. 5, 8), with higher values reflecting melt-WR interaction. Of relevance to our model is the very high aspect-ratio of the pegmatites, rarely exceeding 2 m in width but collectively reaching many kilometers in length (Groat et al., 2003), thus facilitating extensive pegmatite–WR interaction. Similar pre- and syn-crystallization isotopic exchange between WR and the pegmatite-forming melt was also documented in Californian pegmatites by Taylor et al. (1979).

Finally, Rayleigh fractionation might have caused depletion in ^{18}O and contributed to some of the spread of $\delta^{18}O_{quartz}$ values, but there is ample evidence of open system behavior at the LNPG. Furthermore, since Rayleigh fractionation is likely a common process in pegmatites in general, it would be surprising that it caused such a large spread of $\delta^{18}O_{quartz}$ values only at the LNPG and not in other pegmatite systems (see Fig. 6).

3.6.2.4 Isotopic Zoning in the LNPG

480 The potential for $\delta^{18}O$ variation in pegmatites on the scale such as for LNPG has never been
481 explored. The current dataset is thus used to examine this feature. To address the potential for such isotopic
482 zonation, the $\delta^{18}O$ values of fresh magmatic quartz (a proxy of the original magmatic isotopic signature,
483 see section 5.2) and the $\delta^{18}O$ values of albite (a proxy of the metasomatic isotopic signature, see section
484 5.3.1) are plotted per cirque (i.e. following the NNW-SSE trend of the pegmatite field; Fig. 1) in Figure 11.
485 As the plots show, there is no apparent regional isotopic zoning associated with either the magmatic or
486 metasomatic stages.

487 3.6.3 Metasomatic stage and isotopic evolution of the pegmatites

488 Using a $\delta^{18}O$ value of ~10-12‰ for magmatic quartz and its crystallization temperature of 570°C
489 (Fig. 4), the initial $\delta^{18}O$ values for the accompanying magmatic phases were calculated using the
490 fractionation-factors of Bottinga and Javoy (1975) for hydrous phases and Zheng (1993a) for anhydrous
491 phases, as shown by circles in Figure 5. Relative to these calculated values, two trends in ^{18}O are noted –
492 either relative enrichment (quartz, albite, K-feldspar, muscovite, biotite, garnet) or depletion (albite, K-
493 feldspar).

494 In addition to the remarkably large spread in $\delta^{18}O$ values for minerals (Fig. 5), mineral pairs
495 analyzed for $\delta^{18}O$ (e.g. Qtz-Kf, Qtz-Ab, Qtz-Ms, Ab-Ms; see Table 6 and Fig. 13) reveal strong isotopic
496 disequilibria. Using the appropriate fractionation-factors (Bottinga and Javoy, 1975; Zheng, 1993a, b;
497 Chacko et al., 1996), most mineral pairs values translate into unrealistic temperatures (i.e. outside 300 to
498 700°C; Table 6). While no petrological significance is inferred for these calculated temperatures, they
499 illustrate both the degree (i.e. max $|\Delta_{A\text{-}B}|$ measured – equilibrium $|\Delta_{A\text{-}B}|$) and complexity (i.e. total spread in
500 Δ values) of isotopic disequilibrium (see Fig. 12 for a visual explanation of intensity *versus* complexity of
501 isotopic disequilibrium). For instance, $\Delta_{quartz\text{-}albite}$ records both the strongest and most complex isotopic
502 discordance between mineral pairs with Δ values ranging from -5.1 to 14.3‰ (Table 6 and Fig. 13). This
503 large spread in Δ values suggests a complex isotopic evolution caused by multiple processes and/or oxygen

reservoirs. Interestingly, we note that $\Delta_{quartz\text{-}albite}$ values for other rare-element pegmatites also shown in Figure 13 do not exhibit the same intensity or complexity of isotopic disequilibrium.

While a large range of $\delta^{18}O$ values can be caused by a variety of processes (e.g. Rayleigh fractionation, temperature fluctuations, contamination, multiple magma pulses, source heterogeneity, magma mixing, thermal gradients, variation in melt polymerization; see section 5.2), such acute isotopic disequilibrium as noted here for the LNPG data suggests two possible explanations: 1) extreme disequilibrium crystallization; and/or 2) post-crystallization fluid-rock interaction (i.e. metasomatism).

As previously discussed, at least some degree of disequilibrium crystallization occurred at the LNPG based on the observed textures (Barnes, 2010; Pfister et al., 2022) in the current context of pegmatite petrology (e.g. Manetta and Baker, 2014; Sirbescu et al., 2017) and thus probably played a role in the large spread in both $\delta^{18}O$ and Δ values. However and as already noted, the intensity and complexity of isotopic disequilibrium at the LNPG is significantly greater than is observed for other rare-element pegmatites (Figs. 6, 13). Additionally, abundant evidence of late-stage fluid-rock interaction and pervasive metasomatism has been documented across the entire exposure of the LNPG (Groat et al., 2003; Kontak et al., 2004; Burns, 2019; Pfister et al., 2019; Pfister et al., 2022). Both of these observations suggest that LNPG's acute isotopic disequilibrium and large spread in $\delta^{18}O$ and Δ values are best explained by sub-solidus fluid-rock interaction.

3.6.3.1 Nature and origin of the metasomatizing fluids

While feldspars and micas are a poor proxy for the original isotopic signature of the pegmatite-forming melt because of their sensitivity to isotopic re-equilibration, this means they are ideally suited to assess sub-solidus processes and the nature of fluids which accompany such modification during the later stages of pegmatite evolution (e.g. Kontak et al., 2002; Carruzzo et al., 2004; Kontak and Kyser, 2006). At the LNPG, this sensitivity to sub-solidus processes is both texturally and isotopically evident. For example, as shown elsewhere (Burns, 2019; Pfister et al., 2022), both transmitted light microscopy and SEM imaging

528 reveal significantly more secondary features, (e.g. porosity and dissolution features, abundance of
529 secondary fluid inclusions) in feldspars than quartz. Additionally, as seen in Figure 5 the $\delta^{18}O$ values of
530 feldspars cover a substantially larger range (21.3‰ for albite) than quartz (7.5‰). For these reasons,
531 feldspars and micas are best suited to infer the isotopic signature and thus address the origin and nature of
532 the fluid(s) involved in the sub-solidus evolution of the LNPG.

533 The $\delta^{18}O$ values of the metasomatizing fluid(s) in equilibrium with feldspars and muscovite were
534 calculated using the appropriate mineral-H_2O fractionation factors from Zheng (1993a, b) at 500, 400 and
535 300°C (Table 7). Thus the $\delta^{18}O_{H2O}$ values at 500°C are -4.3‰ to +17.0‰ (feldspars) and +9.5‰ to +13.9‰
536 (muscovite), at 400°C -5.4‰ to +15.9‰ (feldspars) and +8.8‰ to +13.2‰ (muscovite), and at 300°C -
537 7.4‰ to +13.9‰ (feldspars) and +7.3‰ to +11.7‰. As the previous studies of Burns (2019) indicate
538 secondary fluid inclusions were trapped below 350°C, the $\delta^{18}O_{H2O}$ values for 300°C are considered to best
539 approximate sub-solidus conditions. Note that while the TitaniQ values for metasomatic and altered quartz
540 samples do not reflect these low temperatures, we note above that application of TitaniQ to low-T
541 hydrothermal quartz remains questionable and often considered to reflect a maximum values (Huang and
542 Audétat, 2012). Using the $\delta^{18}O_{H2O}$ values for 300°C, the data are divided in three groups: 1) values similar
543 to the isotopic signature of the pegmatite-forming melt (i.e. +8‰ to +12‰, which includes analytical
544 uncertainty); 2) values reflecting an ^{18}O-depleted fluid (<8‰); and 3) values reflecting an ^{18}O-enriched
545 fluid (>12‰). Notably, 64% (n = 39) of the data reflect an ^{18}O-depleted fluid, 33% (n = 20) the inferred
546 isotopic signature of the original melt, and only 3% (n = 2) potentially reflect an ^{18}O-enriched fluid.

547 About two thirds of the calculated $\delta^{18}O_{H2O}$ values indicate the presence of an ^{18}O-depleted fluid,
548 which could either be due to an orthomagmatic fluid that has evolved in a closed system (i.e. Rayleigh
549 fractionation) or involvement of an external ^{18}O-depleted fluid. Rayleigh fractionation is assessed using an
550 initial $\delta^{18}O_{H2O}$ value of +10‰ and, as seen in Figure 14A, the lowest inferred $\delta^{18}O_{H2O}$ value of -7.4‰ (at
551 300°C) is achieved after 98% of the fluid is consumed. However, this scenario is not without issues. First,
552 a cumulative distribution plot (Fig. 14B) comparing $\delta^{18}O_{albite}$ data with the Rayleigh fractionation model for

553 300°C shows significant differences. About 40% of the actual $\delta^{18}O_{albite}$ data fall below 5‰, whereas only
554 about 10% of it should according to the model for 300°C. Furthermore, since much of the albite (i.e.
555 saccharoidal and cleavandite types; Pfister et al., 2022) with low $\delta^{18}O$ values originated by replacing K-
556 feldspar *via* CDP (Pfister et al., 2022) which would have released additional ^{18}O into the residual fluid, this
557 precludes the intrinsic requirement of a closed system needed to attained these strongly depleted values *via*
558 Rayleigh fractionation. Finally, the presence of considerable WR-derived components in the metasomatic
559 assemblages (Groat et al., 2003; Pfister et al., 2022) and also in secondary fluid inclusions (Burns, 2019)
560 suggest the pegmatites evolved in an open system during metasomatism, which could counteract the effect
561 of Rayleigh distillation. Thus we considered it unlikely that the ^{18}O-depleted signature of the fluid is solely
562 due to Rayleigh distillation of an orthomagmatic fluid fractionation.

563 In contrast to a closed-system model, metasomatism may have been mediated by an externally-
564 sourced fluid. Its highly depleted $\delta^{18}O_{H2O}$ signature suggests meteoric water, the value which is approaching
565 inferred values for this paleo-latitude (i.e. about -20‰; Dansgaard, 1964). Further support for such a fluid
566 is evidenced from; 1) the abundance of low-salinity secondary fluid inclusions (i.e. near 0 wt. % equiv.
567 NaCl) in quartz and the feldspars (Burns, 2019); and 2) the very low δD values for secondary micas (i.e. -
568 188‰, Table 4), although we note such low signatures can also be produced by interaction of fluids with
569 organic matter (Sheppard, 1986). Incursion of meteoric water to similar depths has been suggested in
570 various magmatic-hydrothermal systems (e.g. Carruzzo et al., 2004; Seedorff et al., 2005; Menzies et al.,
571 2014; Fekete et al., 2016; Ryan-Davis et al., 2019), including LCT pegmatites in southern California
572 (Taylor et al., 1979). While Taylor et al. (1979) concluded incursion of the fluid preceded pegmatite
573 emplacement on the basis of D-depletion in the noritic wall rocks, the lack of low $\delta^{18}O$ values for fresh
574 magmatic phases at the LNPG suggests the incursion of meteoric water was later and overlapped the
575 metasomatic stage. Finally, documentation of transient pressure cycling between lithostatic-hydrostatic
576 conditions (Burns, 2019), as well as textural evidence of dike re-opening (Pfister et al., 2022; Fig. 2E, F),

suggest influx of meteoric fluid *via* the same set of fractures occupied by the pegmatites rather than via percolation, as also suggested by Taylor et al. (1979) for the Californian pegmatites.

About a third of the inferred $\delta^{18}O_{H2O}$ values overlap with and are thus similar isotopically to the pegmatite-forming melt. Thus, such a fluid could either be internally-derived (i.e. orthomagmatic fluid) or a modified external fluid (e.g. meteoric water that exchanged with the metasedimentary WR) which coincidently has the same value. Evidence for both scenarios is present at the LNPG. The abundance of RM oxides associated with secondary albite, a feature globally observed in LCT pegmatites (Černý, 1982a, 1989; Suwimonprecha et al., 1995; Fuertes-Fuente and Martin-Izard, 1998; Lumpkin, 1998; Sweetapple and Collins, 2002; Kontak, 2006; Wise and Brown 2011; Kaeter et al., 2018; Fuchsloch et al., 2019) along with up to 1.7 ppm Nb, 2.8 ppm Ta and 37.5 ppm Sn (as well as Li, Be, W) in secondary aqueous-carbonic fluid inclusions (Burns, 2019) suggest a fluid of magmatic origin, as these elements are predominantly derived from evolved felsic melts. Additionally, the relative paucity of these elements in unaltered magmatic assemblages of the LNPG (Pfister et al., 2022) suggests that they were not locally re-mobilized from the original magmatic assemblage, but instead enriched by the metasomatizing fluid.

In contrast to the evidence for an orthomagmatic fluid, there is also evidence of WR-derived components during metasomatism, including an increasing amount of Ca, Fe, Mg and S in the late-stage mineral assemblages (Groat et al., 2003; Barnes, 2010; Burns, 2019; Pfister et al., 2022), as well as the presence of exotic volatiles (e.g. N_2, CH_4) and biogenic carbon ($\delta^{13}C$ = -10‰ to -28‰) in secondary fluid inclusions (Burns, 2019). These observations indicate some part of the metasomatizing fluid originated in the WR. Because the pegmatites' hydrothermal aureoles are small and sporadic, it is unlikely that the orthomagmatic fluid had significantly interacted with the wall rocks, as suggested for other pegmatites (e.g. Martin and De Vito, 2014). Furthermore, the inferred $\delta^{18}O_{H2O}$ values are too close to the original magmatic $\delta^{18}O$ signature to reflect significant exchange between orthomagmatic fluid and ^{18}O-enriched metasedimentary WR. In contrast, meteoric fluid would have traversed through kilometers of ^{18}O-enriched metasedimentary rock before reaching the pegmatites. Because the initial isotopic signature of the

pegmatite-forming melt is somewhere between those of meteoric water and the metasedimentary host rocks, various degree of isotopic exchange between these two reservoirs would result in a range of $\delta^{18}O$ values covering the signature of the former. Note that variation in the degree of meteoric water – metasedimentary rocks interaction is supported by pressure fluctuation between lithostatic and hydrostatic conditions (i.e. less interaction with overlying rocks during hydrostatic condition, and *vice-versa*) documented by Burns (2019).

In summary, the presence of considerable amounts of both WR-derived components (e.g. Ca, Fe, Mg, S, N_2, biogenic carbon) and magma-derived components (e.g. Ta, Nb, Sn, W, Be) in the metasomatic assemblages and secondary fluid inclusions suggest a combination of orthomagmatic fluid and meteoric water, with the later having chemically and isotopically exchanged with the host metasedimentary rocks before interacting with the pegmatites. Our isotopic data unequivocally confirm the presence of meteoric water, and support interaction of surface-derived fluids (i.e. meteoric water) with metasedimentary rocks, as well as the presence of an orthomagmatic fluid.

As for the two $\delta^{18}O_{H2O}$ values suggesting a ^{18}O-enriched fluid, these could either reflect a lower temperature of formation (i.e. larger $\Delta_{albite\text{-}H2O\ factor}$) or a greater degree of fluid-WR exchange prior to fluid-pegmatite interaction, but do not imply the presence of an additional non-magmatic, non-meteoric fluid.

3.6.4 LNPG *versus* other pegmatites

LNPG shows a larger range of $\delta^{18}O$ values (Figs. 5, 6) and a much greater spread of Δ values (Fig. 13 and Table 6) than other LCT-type pegmatites. A few non-geological factors might have contributed to this difference in the range of $\delta^{18}O$ values (Fig. 6). First, the number of analyses (n = 72) is greater than for other pegmatites [ranging from n = 2 to n = 14; one outlier at n = 43 for the Himalaya Pegmatite (Taylor et al., 1979)], which translates into a greater probability of including outlier values. Secondly, the method of analysis (i.e. *in-situ* SIMS *versus* bulk analysis) is quite relevant. While bulk analyses have a greater analytical precision (<0.3‰) than the SIMS employed in this study (± 0.8‰), the sample preparation (i.e.

626 crushing and digestion) averages the $\delta^{18}O$ for the mineral separate, which is an issue given the presence of
627 abundant secondary features (Fig. 7), most of which are only visible under CL. In contrast, *in-situ* SIMS
628 with a high spatial resolution (herein 15-20 µm spot size) allows one to target both primary and secondary
629 features (Figs. 3, 7) and thus provide a more accurate assessment of the respective isotopic signatures. This
630 is conspicuous in Figure 6, where $\delta^{18}O_{quartz}$ values for this study determined with SIMS exhibit a greater
631 range than the literature values determined by bulk analysis. Particularly relevant in this regard are data for
632 the late Cretaceous southern Californian pegmatites determined using bulk analysis by Taylor et al. (1979)
633 (i.e. Himalaya, Little Three, Stewart, Angel Field, Oceanview, Spessartine, Tourmaline Queen, and Victor
634 Mine pegmatites) versus by SIMS in this study (i.e. Cryo-Genie, Blue Chihuahua, Blue Lady, Esmeralda
635 Gem, Anita and Maple Lode pegmatites), as summarized in Figure 6B. The difference in $\delta^{18}O$ values
636 between these different pegmatites reflect local settings as discussed by Taylor et al. (1979), but the
637 difference in the individual ranges of $\delta^{18}O$ values between the data of Taylor et al. (1979) and ours illustrates
638 the higher resolution of SIMS. Thus it is suggested that the isotopic data currently reported in the literature
639 for pegmatites likely shows an artificially narrower range of $\delta^{18}O$ values and potentially conceals isotopic
640 evidence of sub-solidus fluid:rock interactions.

641 With this being said, our bulk $\delta^{18}O_{quartz}$ data still display a remarkably large range (Fig. 5) and by
642 far the largest ranges in $\delta^{18}O_{albite}$ and $\Delta_{albite\text{-}quartz}$ values reported in the literature for any rare-element
643 pegmatite (e.g. Taylor, 1978; Taylor et al., 1979; Taylor and Friedrichsen, 1983; Damm et al., 1992; Linnen
644 and Williams-Jones, 1994; Kontak and Kyser 2009; Ashworth et al., 2020). It is therefore evident that the
645 LNPG had a particularly complex evolution and was influenced by multiple external reservoirs.

646 Furthermore, SEM-CL imaging of the non-LNPG quartz grains (Fig. 7), despite having been carefully
647 selected while viewed under the binocular microscope to be the freshest fragments, reveals abundant
648 secondary features indicating important sub-solidus fluid-rock interaction in all pegmatites sampled. This
649 suggests that the spread of isotopic data reported for pegmatites likely reflects sub-solidus fluid-rock
650 interaction and that metasomatism is an important process in the evolution of pegmatites to their present-

651 day composition. This is especially true when spreads in $\delta^{18}O$ are accompanied by Δ values indicating
652 isotopic disequilibrium, which is almost always the case (e.g. Taylor et al., 1979; Taylor and Friedrichsen,
653 1983; Nabelek et al., 1992; Kontak and Kyser, 2009; Ashworth et al., 2020).

654 ### 3.6.5 Implications of $\delta^{18}O_{quartz}$ data for source of LCT-type pegmatite melts

655 The compilation of previously published $\delta^{18}O_{quartz}$ data for LCT-type pegmatites combined with the
656 newly generated data from this study (Fig. 6) provide a sufficiently large amount of robust data to address
657 the long standing issue of the source and generation of these evolved melts. Although we cannot address
658 the issue of how such magmas were generated (i.e. partial melts *via* anatexis or fractionation of felsic
659 magmas), the $\delta^{18}O$ data provide the basis for assessing the source of such melts. Despite some overlap,
660 there are distinct populations at each end of the spectrum (Fig. 6): (1) low $\delta^{18}O$ (e.g. Maple Lode, Authier,
661 North Plumbago, Oceanview, Brazil Lake pegmatites); and (2) high $\delta^{18}O$ (e.g. Ampasogona, Usakos, Uis,
662 Mount Mica pegmatites). This suggests LCT-type pegmatite melts and parental granitic melts related to
663 such pegmatites can be generated *via* partial melting of basic to intermediate rocks (or metasedimentary
664 rocks derived from them; the low $\delta^{18}O$ group) or a more aluminous source such as clay-rich
665 metasedimentary rocks to account for the ^{18}O enrichment (the high $\delta^{18}O$ group).

666 ## 3.7 Conclusions

667 This study, the most exhaustive ever for $\delta^{18}O$ in any pegmatite setting, provides strong evidence for
668 involvement of multiple oxygen reservoirs in the evolution of the LCT-type LNPG, including melt,
669 metasedimentary wall rocks, and meteoric water, and thus suggests that pegmatites can evolve as partially
670 open systems. The presence of meteoric water documented here also suggests that metasomatizing fluids
671 does need not be internally-derived and thus reconciles the prevalence of secondary assemblages (i.e. late-
672 stage fine-grained albitic and/or mica-rich units) observed in evolved rare-element pegmatites with
673 experimental and empirical evidence suggesting that pegmatite-forming melts can be volatile-
674 undersaturated. Additionally, incursion of heated and WR equilibrated or modified meteoric water provides

675 an alternative explanation for the commonly observed late-stage enrichment in WR-derived elements, such
676 as the Ca-miniflood (see discussion above), and need not involve assimilation of WR material nor leaching
677 of the immediate WR, for which evidence is generally lacking (see discussion above). Furthermore, we
678 suggest that the highly depleted $\delta^{18}O$ values documented at the LNPG (compared to other pegmatites)
679 reflect periods of when hydrostatic condition prevailed, for which independent evidence exists (Burns,
680 2019), which allowed incursion of meteoric water through the overlying rocks and resulting isotopic
681 exchange. While strongly depleted $\delta^{18}O$ values of pegmatites are uncommon in the literature, depleted δD
682 values are common (*e.g*. Taylor et al., 1979; Holcombe and Velasquez, 1997; Dyar et al., 1999; Kelly,
683 2012; Whattam, 2016) and might reflect the different rates of isotopic re-equilibration of H and O between
684 meteoric water and rocks, as crustal rocks contain abundant O (e.g. >45%), but little H (e.g. <2%). This
685 suggests that meteoric water incursion is not unique to the LNPG, but that such fluid usually loses its
686 isotopic oxygen signature prior to its interaction with the pegmatites.

687 That pegmatites exhibit large ranges of $\delta^{18}O$ values (e.g. Fig. 6A) can be explained by a combination
688 of analytical artefacts (e.g. *in-situ versus* bulk analysis of mineral separate, analytical precision, etc.) and
689 geological features, such as melt source (i.e. partial melting of source material dominated by basic to
690 intermediate rocks *versus* a more aluminous and clay-rich source to account for the ^{18}O enrichment) and
691 sub-solidus processes (i.e. fluid-rock interaction, metasomatism) with lesser contributions from other
692 geological processes (e.g. disequilibrium crystallization, pegmatite-WR interaction, Rayleigh fractionation,
693 rapid cooling of the system, Soret diffusion, etc.).

694 Finally, this study indicates that future isotopic studies of pegmatites should include *in-situ* analysis
695 (e.g. SIMS) where possible due to its higher spatial resolution and integration of such analysis with
696 petrographic observations and CL imaging.

697 3.8 ACKNOWLEDGMENTS

The authors are particularly grateful to Ryan Sharpe for performing the SIMS analyses at the University of Manitoba. We would also like to thank Dr. Joe Petrus for his help with LA-ICP-MS analyses and William Zhe for his assistance regarding the calibration and usage of the SEM-EDS and SEM-CL at the Laurentian University. Additionally, while most samples from LCT pegmatites were collected by the authors, we are grateful to Dr. Ian Nicastro, Abdur Rehman Safi and Dan Weinrich for providing samples of reliable provenance from pegmatites that the authors could not personally visit. Finally, we would like to extend our gratitude to Dr. William "Skip" Simmons, Dr. Karen Webber, Al Falster, as well as the rest of the organizers and participants of the Maine Pegmatite Workshop for providing access to numerous pegmatites included in this study and for multiple discussions which improved this publication.

3.9 Funding and declaration of competing interest

This study was supported financially by an NSERC discovery grant to Dr. Daniel Kontak. The authors declare that they have no known competing financial interests or personal relationships that could have appeared to influence the work reported in this paper.

3.10 References

Ackerman L., Zachariáš J. and Pudilová M. (2007) P-T and fluid evolution of barren and lithium pegmatites from Vlastějovice, Bohemian Massif, Czech Republic. *Int. J. Earth Sci.* **96**, 623–638.

Alfonso P. and Melgarejo J. C. (2008) Fluid evolution in the zoned rare-element pegmatite field at Cap de Creus, Catalonia, Spain. *Can. Mineral.* **46**, 597–617.

Ashworth L. (2014) Mineralised Pegmatites of the Damara Belt , Namibia : Fluid inclusion and geochemical characteristics with implications for post- collisional mineralisation. University of the Witwatersrand.

Ashworth L., Kinnaird J. A., Nex P. A. M., Harris C. and Müller A. B. (2020) Origin of rare-element-mineralized Damara Belt pegmatites: A geochemical and light stable isotope study. *Lithos* **372**–**373**, 105655.

Barnes E. M. (2010) Emplacement and geological setting of the Little Nahanni Pegmatite Group, Northwest Territories and its geochemical and lithium isotopic evolution. University of British Columbia,.

Barnes E. M., Weis D. and Groat L. A. (2012) Significant Li isotope fractionation in geochemically

727 evolved rare element-bearing pegmatites from the Little Nahanni Pegmatite Group, NWT, Canada.
728 *Lithos* **132**–**133**, 21–36.

729 Bindeman I. N., Lundstrom C. C., Bopp C. and Huang F. (2013) Stable isotope fractionation by thermal
730 diffusion through partially molten wet and dry silicate rocks. *Earth Planet. Sci. Lett.* **365**, 51–62.

731 Bindeman I. N. and Valley J. W. (2002) Oxygen isotope study of the Long Valley magma system,
732 California. *Contrib Mineral Petrology*

733 Bottinga Y. and Javoy M. (1973) Comments on stable isotope geothermometry: the system quartz-water.
734 *Earth Planet. Sci. Lett.* **84**, 406–414.

735 Bottinga Y. and Javoy M. (1975) Oxygen isotope partitioning among the minerals in igneous and
736 metamorphic rocks. *Rev. Geophys.* **13**, 401–418.

737 Burns M. G. (2019) A fluid inclusion study of the Little Nahanni LCT-type pegmatite group, NWT
738 Canada: Implications for the nature and origin of fluids in LCT-type pegmatites and pegmatite
739 evolution. Laurentian University.

740 Carruzzo, S., Kontak, D.J. and Clarke, D.B. (2004) Stable isotope study of mineralization in the New
741 Ross area, South Mountain Batholith, Nova Scotia: evidence for multiple source reservoirs.
742 *Canadian Mineralogist* **42**, 1425-1442.

743 Černý P. (1982a) Anatomy and classification of granitic pegmatites. *Mineral. Assoc. Canada, Short*
744 *Course Handb.* **8**, 1–39.

745 Černý P. (1982b) The Tanco pegmatite at Bernic Lake, southeastern Manitoba. *Mineral. Assoc. Canada,*
746 *Short Course Handb.* **8**, 527–543.

747 Černý P. (1989) Characteristics of pegmatite deposits of tantalum. In *Lanthanides, Tantalum and*
748 *Niobium* Berlin. pp. 195–239.

749 Černý P. (1991) Rare-element granitic pegmatite: Anatomy and internal evolution of pegmatite deposits.
750 *Geosci. Canada* **18(2)**, 49–67.

751 Černý P. and Ercit T. S. (2005) The classification of granitic pegmatites revisited. **43**, 2005–2026.

752 Chacko T., Hu X., Mayeda T. K., Clayton R. N. and Goldsmith J. R. (1996) Oxygen isotope
753 fractionations in muscovite, phlogopite, and rutile. *Geochim. Cosmochim. Acta* **60**, 2595–2608.

754 Chappell B. W. and White A. J. R. (1992) I- and S-type granites in the Lachlan Fold Belt. *Trans. R. Soc.*
755 *Edinb. Earth Sci.* **83**, 1–26.

756 Cherniak D. J., Watson E. B. and Wark D. A. (2007) Ti diffusion in quartz. *Chem. Geol.* **236**, 65–74.

757 Clayton R. N. and Mayeda T. K. (1963) The use of bromine pentafluoride in the extraction of oxygen
758 from oxides and silicates for isotopic analysis. *Geochim. Cosmochim. Acta* **27**, 43–52.

759 Damm K. -W, Harmon R. S., Heppner P.-M. and Dornsiepen U. (1992) Stable isotope constraints on the
760 origin of the Cabo de Creus garnet-tourmaline pegmatites, Massif des Alberes, Eastern Pyrenees,
761 Spain. *Geol. J.* **27**, 75–86.

762 Dansgaard W. (1964) Stable isotopes in precipitation. *Tellus* **16**, 436–468.

763 Dill H. G. (2015) Pegmatites and aplites: Their genetic and applied ore geology. *Ore Geol. Rev.* **69**, 417–
764 561.

765 Dubinina E. O. and Borisov A. A. (2018) Structure and composition effects on the oxygen isotope

fractionation in silicate melts. *Petrology* **26**, 414–427.

Dyar M. D., Guidotti C. V., Core D. P., Wearn K. M., Wise M. A., Francis C. A., Johnson K., Brady J. B., Robertson J. D. and Cross L. R. (1999) Stable isotope and crystal chemistry of tourmaline across pegmatite – country rock boundaries at Black Mountain and Mount Mica, southwestern Maine, USA. *Eur. J. Mineral.* **11**, 281–294.

Elphick S. C., Dennis P. F. and Graham C. M. (1986) An experimental study of the diffusion of oxygen in quartz and albite using an overgrowth technique. *Contrib. to Mineral. Petrol.* **92**, 322–330.

Ercit T. S., Groat L. A. and Gault R. A. (2003) Granitic pegmatites of the O'Grady batholith, N.W.T., Canada: A case study of the evolution of the elbaite subtype of rare-element granitic pegmatite. *Can. Mineral.* **41**, 117–137.

Fekete S., Weis P., Driesner T., Bouvier A. S., Baumgartner L. and Heinrich C. A. (2016) Contrasting hydrological processes of meteoric water incursion during magmatic–hydrothermal ore deposition: An oxygen isotope study by ion microprobe. *Earth Planet. Sci. Lett.* **451**, 263–271.

Foord E. E. and Cook R. B. (1989) Mineralogy and paragenesis of the McAllister Sn-Ta-bearing pegmatite, Coosa County, Alabama. *Can. Mineral.* **27** pt **1**, 93–105.

Fredriksson J. R. (2017) Fluid inclusion and trace-element analysis of the rare- element pegmatite bodies Altim and Tamanduá from the Borborema Province, Brazil. University of Helsinki.

Fuchsloch W. C., Nex P. A. M. and Kinnaird J. A. (2019) The geochemical evolution of Nb–Ta–Sn oxides from pegmatites of the Cape Cross–Uis pegmatite belt, Namibia. *Mineral. Mag.* **83**, 161–179.

Fuertes-Fuente M. and Martin-Izard A. (1998) The Forcarei Sur rare-element granitic pegmatite field and associated mineralization, Galicia, Spain. *Can. Mineral.* **36**, 303–325.

Giletti B. J., Semet M. P. and Yund R. A. (1978) Studies in diffusion-III. Oxygen in feldspars: an ion microprobe determination. *Geochim. Cosmochim. Acta* **42**, 45–57.

Giletti B. J. and Yund R. A. (1984) Oxygen diffusion in quartz. *J. Geophys. Res.* **89**, 4039–4046.

Gordey S. P. (2013) *Evolution of the Selwyn Basin region, Sheldon Lake and Tay River map areas, central Yukon*.

Gordey S. P. and Anderson R. G. (1993) *Evolution of the northern Cordilleran miogeocline, Nahanni map area (105I), Yukon and Northwestern Territories.*

Götze J., Plötze M. and Trautmann T. (2005) Structure and luminescence characteristics of quartz from pegmatites. *Am. Mineral.* **90**, 13–21.

Groat L. A., Mulja T., Mauthner M. H. F., Ercit T. S., Raudsepp M., Gault R. A. and Rollo H. A. (2003) Geology and mineralogy of the Little Nahanni rare-element granitic pegmatites, Northwest Territories. *Can. Mineral.* **41**, 139–160.

Harlaux M., Mercadier J., Bonzi W. M. E., Kremer V., Marignac C. and Cuney M. (2017) Geochemical signature of magmatic-hydrothermal fluids exsolved from the beauvoir rare-metal granite (Massif Central, France): Insights from LA-ICPMS analysis of primary fluid inclusions. *Geofluids*.

Hayden L. A. and Watson E. B. (2007) Rutile saturation in hydrous siliceous melts and its bearing on Ti-thermometry of quartz and zircon. *Earth Planet. Sci. Lett.* **258**, 561–568.

Holcombe B. and Velasquez M. (1997) Stable isotope variations in the pegmatite systems associate with the Sebago Batholith, southwestern Maine. , 191–194.

Huang R. and Audétat A. (2012) The titanium-in-quartz (TitaniQ) thermobarometer: A critical examination and re-calibration. *Geochim. Cosmochim. Acta* **84**, 75–89.

Ihlen P. M., Müller A., Larsen R. B. and Henderson I. (2007) Transformation of igneous quartz to high-purity quartz in granitic pegmatites of South Norway. In *Granitic Pegmatites: International Symposium* pp. 6–12.

Jahns R. H. (1955) The study of pegmatites. *Econ. Geol.* **50th Anniv**, 1025–1130.

Jahns R. H. (1982) Internal Evolution of Pegmatite Bodies. *Mineral. Assoc. Canada, Short Course Handb.* **8**, 293–327.

Jochum K. P., Weis U., Stoll B., Kuzmin D., Yang Q., Raczek I., Jacob D. E., Stracke A., Birbaum K., Frick D. A., Günther D. and Enzweiler J. (2011) Determination of reference values for NIST SRM 610-617 glasses following ISO guidelines. *Geostand. Geoanalytical Res.* **35**, 397–429.

Jochum K. P., Willbold M., Raczek I., Stoll B. and Herwig K. (2005) Chemical characterisation of the USGS reference glasses GSA-1G, GSC-1G, GSD-1G, GSE-1G, BCR-2G, BHVO-2G and BIR-1G using EPMA, ID-TIMS, ID-ICP-MS and LA-ICP-MS. *Geostand. Geoanalytical Res.* **29**, 285–302.

Kaeter D., Barros R., Menuge J. F. and Chew D. M. (2018) The magmatic–hydrothermal transition in rare-element pegmatites from southeast Ireland: LA-ICP-MS chemical mapping of muscovite and columbite–tantalite. *Geochim. Cosmochim. Acta* **240**, 98–130.

Kelly J. C. (2012) The fluid evolution of the Mount Mica and Irish Pit pegmatites. California State University, Long Beach.

Kelly J. L., Fu B., Kita N. T. and Valley J. W. (2007) Optically continuous silcrete quartz cements of the St. Peter Sandstone: High precision oxygen isotope analysis by ion microprobe. *Geochim. Cosmochim. Acta* **71**, 3812–3832.

Knoll T., Schuster R., Huet B., Mali H., Onuk P., Horschinegg M., Ertl A. and Giester G. (2018) Spodumene pegmatites and related leucogranites from the austroalpine unit (eastern Alps, central Europe): field relations, petrography, geochemistry, and geochronology. *Can. Mineral.* **56**, 489–528.

Kontak D. J. (2006) Nature and origin of an LCT-suite pegmatite with late-stage sodium enrichment, Brazil Lake, Yarmouth County, Nova Scotia. I. Geological setting and petrology. *Can. Mineral.* **44**, 563–598.

Kontak D. J., Dostal J., Kyser K. and Archibald D. A. (2002) A petrological, geochemical, isotopic and fluid-inclusion study of 370Ma pegmatite-aplite sheets, Peggys Cive, Nova Scotia, Canada. *Can. Mineral.* **40**, 1249–1286.

Kontak, D.J., Groat, L., and Barnes, E. (2004) A visit to the Little Nahanni rare-element pegmatites, N.W.T., and other curiosities along the way. *In* Newsletter of the *Mineralogical Association of Canada* **42**, Part 5, p. 1, 4, 5, 20, 21.

Kontak D. J., Groat L., Burns M.G., Archibald D.A. and Creaser R. (2016) Documenting the complex evolution of a rare-metal pegmatite swarm: The Little Nahanni Pegmatite Group, NWT, Canada. *Geological Association of Canada, Mineralogical Association of Canada, Whitehorse, YK, Canada, Program with Abstracts*. **39**.

Kontak D. J. and Kyser T. K. (2009) Nature and origin of an LCT-suite pegmatite with late-stage sodium enrichment, Brazil Lake, yarmouth county, Nova Scotia. II. Implications of stable isotopes (δ18O, δD) for magma source, internal crystallization and nature of sodium metasomatism. *Can. Mineral.* **47**, 745–764.

Kyser K. and O'Neil J. R. (1984) Hydrogen isotope systematics of submarine basalts. *Geochim. Cosmochim. Acta* **48**, 2123–2133.

Kyser T. K., Lesher C. E. and Walker D. (1998) The effects of liquid immiscibility and thermal diffusion on oxygen isotopes in silicate liquids. *Contrib. to Mineral. Petrol.* **133**, 373–381.

Lake D. J., Groat L. A., Falck H., Mulja T., Cempírek J., Kontak D., Marshall D., Giuliani G. and Fayek M. (2017) Genesis of emerald-bearing quartz veins associated with the lened W skarn mineralization, Northwest Territories, Canada. *Can. Mineral.* **55**, 561–593.

Landtwing M. R., Furrer C., Redmond P. B., Pettke T., Guillong M. and Heinrich C. A. (2010) The Bingham Canyon porphyry Cu-Mo-Au deposit. III. Zoned copper-gold ore deposition by magmatic vapor expansion. *Econ. Geol.* **105**, 91–118.

Lindgren W. (1913) *Mineral deposits*., McGraw-Hill, New York.

Linnen R. L. and Williams-Jones A. E. (1994) The evolution of pegmatite-hosted Sn-W mineralization at Nong Sua, Thailand: Evidence from fluid inclusions and stable isotopes. *Geochim. Cosmochim. Acta* **58**, 735–747.

Liverton T. (2017) *Geology and summary report of the Little Nahanni Pegmatite prospect*.

London D. (2005) Granitic pegmatites: An assessment of current concepts and directions for the future. *Lithos* **80**, 281–303.

London D. (2008) *Pegmatites*, The Canadian Mineralogist, Special Publication 10, Quebec.

London D. (2014) A petrologic assessment of internal zonation in granitic pegmatites. *Lithos* **184**–**187**, 74–104.

London D. (2018) Ore-forming processes within granitic pegmatites. *Ore Geol. Rev.* **101**, 349–383.

London D., Morgan G. B., Paul K. A. and Guttery B. M. (2012) Internal evolution of miarolitic granitic pegmatites at the little three Mine, Ramona, California, USA. *Can. Mineral.* **50**, 1025–1054.

Lumpkin G. R. (1998) Rare-element mineralogy and internal evolution of the Rutherford #2 pegmatite, Amelia County, Virginia: a classic locality revisited. *Can. Mineral.* **36**, 339–353.

Maneta V. and Anderson A. J. (2018) Monitoring the crystallization of water-saturated granitic melts in real time using the hydrothermal diamond anvil cell. *Contrib. to Mineral. Petrol.* **173**, 1–18.

Maneta V. and Baker D. R. (2014) Exploring the effect of lithium on pegmatitic textures: An experimental study. *Am. Mineral.* **99**, 1383–1403.

Marshall D. D., Groat L. A., Falck H., Giuliani G. and Neufeld H. (2004) The lened emerald prospect, Northwest Territories, Canada: Insights from fluid inclusions and stable isotopes, with implications for northern Cordilleran emerald. *Can. Mineral.* **42**, 1523–1539.

Martin R. F. and De Vito C. (2005) The patterns of enrichment in felsic pegmatites ultimately depend on tectonic setting. *Can. Mineral.* **43**, 2027–2048.

Martin R. F. and De Vito C. (2014) The late-stage miniflood of Ca in granitic pegmatites: An open-system acid-reflux model involving plagioclase in the exocontact. *Can. Mineral.* **52**, 165–181.

Mauthner M. H. F. (1996) Mineralogy, geochemistry, and geochronology of the Little Nahanni Pegmatite Group, Logan Mountains, Southwestern Northwest Territories. University of British Columbia.

Mauthner M. H. F., Mortensen J. K., Groat L. A. and Ercit T. S. (1995) Geochronology of the Little

Nahanni pegmatite group, Selwyn Mountains, southwestern Northwest Territories. *Can. J. Earth Sci.* **32**, 2090–2097.

Menzies C. D., Teagle D. A. H., Craw D., Cox S. C., Boyce A. J., Barrie C. D. and Roberts S. (2014) Incursion of meteoric waters into the ductile regime in an active orogen. *Earth Planet. Sci. Lett.* **399**, 1–13.

Müller A., Ihlen P. M., Snook B., Larsen R. B., Flem B., Bingen B. and Williamson B. J. (2015) The chemistry of quartz in granitic pegmatites of southern Norway: Petrogenetic and economic implications. *Econ. Geol.* **110**, 1737–1757.

Müller A., Romer R. L. and Pedersen R. B. (2017) The sveconorwegian pegmatite province -thousands of pegmatites without parental granites. *Can. Mineral.* **55**, 283–315.

Nabelek P. I., Russ-Nabelek C. and Haeussler G. T. (1992) Stable isotope evidence for the petrogenesis and fluid evolution in the Proterozoic Harney Peak leucogranite, Black Hills, South Dakota. *Geochim. Cosmochim. Acta* **56**, 403–417.

O'Neil J. R. and Chappell B. W. (1977) Oxygen and hydrogen isotope relations in the Berridale batholith. *J. Geol. Soc. London.* **133**, 559–571.

Paton C., Hellstrom J., Paul B., Woodhead J. and Hergt J. (2011) Iolite: Freeware for the visualisation and processing of mass spectrometric data. *J. Anal. At. Spectrom.* **26**, 2508–2518.

Pfister J. D., Kontak D. J., Groat L. and Fayek M. (2019) Textural and isotopic studies of the Cretaceous Little Nahanni pegmatite Group (NWT, Canada) suggests mixed fluid reservoirs during its evolution. *Can. Mineral.* **57**, 771–773.

Pfister J. D., Kontak D. J. and Groat L. (2022) Textural and mineralogical evolution of the Little Nahanni Pegmatite Group (NWT, Canada) with implications for metasomatism, rare-metal mineralization and pegmatite-wall rock interaction. *Can. Mineral.* Accepted with revisions.

Pieczka A., Szuszkiewicz A., Szełęg E. and Nejbert K. (2019) Calcium Minerals and Late-stage Ca-metasomatism in the Julianna Pegmatitic System, the GÓry Sowie Block, SW Poland. *Can. Mineral.* **57**, 775–777.

Plümper O. and Putnis A. (2009) The complex hydrothermal history of granitic rocks: Multiple feldspar replacement reactions under subsolidus conditions. *J. Petrol.* **50**, 967–987.

Putnis A. (2002) Mineral replacement reactions: from macroscopic observations to microscopic mechanisms. *Mineral. Mag.* **66**, 689–708.

Rasmussen K. L. and Arehart G. B. (2010) Radiogenic and Stable Isotopic Compositions of mid-Cretaceous Intrusions in the Selwyn Basin , Yukon and Northwest Territories. *Yukon Explor. Geol.*, 279–292.

Riciputi L. R., Paterson B. A. and Ripperdan R. L. (1998) Measurement of light stable isotope ratios by SIMS: Matrix effects for oxygen, carbon, and sulfur isotopes in minerals. *Int. J. Mass Spectrom.* **178**, 81–112.

Rusk B. and Reed M. (2002) Scanning electron microscope-cathodoluminescence analysis of quartz reveals complex growth histories in veins from the Butte porphyry copper deposit, Montana. *Geology* **30**, 727–730.

Ryan-Davis J., Lackey J. S., Gevedon M., Barnes J. D., Lee C. T. A., Kitajima K. and Valley J. W. (2019) Andradite skarn garnet records of exceptionally low δ18O values within an Early Cretaceous

hydrothermal system, Sierra Nevada, CA. *Contrib. to Mineral. Petrol.* **174**, 1–19.

Seedorff E., Dilles J., Proffett J., Einaudi M., Zurcher L., Stavast W., Johnson D. and Barton M. (2005) Porphyry deposits: characteristics and origin of hypogene features. *Econ. Geol.* **100th anni**, 251–298.

Sheppard S. M. F. (1986) Characterization and isotopic variations in natural waters. *In* Stable Isotopes in High Temperature Geological Processes. *Reviews in Mineralogy and Geochemistry*; **16** (1): 165–183.

Siegel K., Wagner T., Trumbull R. B., Jonsson E., Matalin G., Wälle M. and Heinrich C. A. (2016) Stable isotope (B, H, O) and mineral-chemistry constraints on the magmatic to hydrothermal evolution of the Varuträsk rare-element pegmatite (Northern Sweden). *Chem. Geol.* **421**, 1–16.

Simmons, W., Foord, E.E., Falster, A.U., and King, V.T. (1995) Evidence for an anatectic origin of granitic pegmatites, Western Maine, USA. Geological Society of America Annual Meeting, New Orleans, Louisiana, Abstracts with Programs 27, p A411.

Simmons W. and Webber K. L. (2008) Pegmatite genesis: state of the art. *Eur. J. Mineral.* **20**, 421–438.

Simmons W., Falster A., Webber K., Roda-Robles E., Boudreaux A. P., Grassi L. R. and Freeman G. (2016) Bulk composition of Mt. Mica Pegmatite, Maine, USA: Implications for the origin of an LCT type pegmatite by anatexis. *Can. Mineral.* **54**, 1053–1070.

Sirbescu M. L. C., Schmidt C., Veksler I. V., Whittington A. G. and Wilke M. (2017) Experimental crystallization of undercooled felsic liquids: Generation of pegmatitic texture. *J. Petrol.* **58**, 539–568.

Sirbescu M. L. C., Hartwick E. E. and Student J. J. (2008) Rapid crystallization of the Animikie Red Ace Pegmatite, Florence county, northeastern Wisconsin: Inclusion microthermometry and conductive-cooling modeling. *Contrib. to Mineral. Petrol.* **156**, 289–305.

Soares D. R., Sial A. N. and Ferreira, V. P. (2007) Preliminary Study of Oxygen Isotopes in Tourmaline, Quartz and Muscovite from Three Granitic Pegmatites of the Borborema Pegmatite Province, Northeastern Brazil. Instituto Federal de Educação, Ciência e Tecnologia da Paraíba. Available at: www.americangeosciences.org/sites/default/files/igc/1427.pdf

Soret, C. (1879). Etat d'équilibre des dissolutions dont deux parties sont portées à des températures différentes. *Arch. Sci. Phys. Nat. Genève*. **2**, 48-64.

Stewart D. B. (1978) Petrogenesis of lithium-rich pegmatites. *Am. Mineral.* **63**, 970–980.

Suwimonprecha P., Černý P. and Friedrich G. (1995) Rare metal mineralization related to granites and pegmatites, Phuket, Thailand. *Econ. Geol.* **90**, 603–615.

Sweetapple M. T. and Collins P. L. F. (2002) Genetic framework for the classification and distribution of Archean rare metal pegmatites in the North Pilbara Craton, Western Australia. *Econ. Geol.* **97**, 873–895.

Taylor B. E., Foord E. E. and Friedrichsen H. (1979) Stable isotope and fluid inclusion studies of gem-bearing granitic pegmatite-aplite dikes, San Diego Co., California. *Contrib. to Mineral. Petrol.* **68**, 187–205.

Taylor B. E. and Friedrichsen H. (1983) Light stable isotope systematics of granitic pegmatites from North America and Norway. *Chem. Geol.* **41**, 127–167.

Taylor H. P. (1974) The application of oxygen and hydrogen isotope studies to problems of hydrothermal

alteration and ore deposition. *Econ. Geol.* **69**, 843–883.

Taylor H. P. (1978) Oxygen and hydrogen isotope studies of plutonic granitic rocks. *Dev. Petrol.* **5**, 177–210.

Taylor H. P. (1979) Oxygen and Hydrogen isotope relationship in Hydrothermal mineral deposit. In *Geochemistry of hydrothermal ore deposits.* New York. pp. 237-277.

Taylor H. P. and Sheppard S.M.F. (1986) Igneous rocks. I. Processes of isotopic fractionation and isotope system¬atics. In Stable Isotopes in High Temperature Geological Processes. *Rev. Mineral*. **16**, 227-272.

Thomas J. B., Watson E. B., Spear F. S., Shemella P. T., Nayak S. K. and Lanzirotti A. (2010) TitaniQ under pressure: The effect of pressure and temperature on the solubility of Ti in quartz. *Contrib. to Mineral. Petrol.* **160**, 743–759.

Thomas R. and Davidson P. (2012) Water in granite and pegmatite-forming melts. *Ore Geol. Rev.* **46**, 32–46.

Thomas R. and Davidson P. (2013) The missing link between granites and granitic pegmatites. *J. Geosci. (Czech Republic)* **58**, 183–200.

Thomas R., Davidson P. and Beurlen H. (2012) The competing models for the origin and internal evolution of granitic pegmatites in the light of melt and fluid inclusion research. *Mineral. Petrol.* **106**, 55–73.

Wark D. A. and Watson E. B. (2006) TitaniQ: A titanium-in-quartz geothermometer. *Contrib. to Mineral. Petrol.* **152**, 743–754.

Webber K. L., Simmons W. B., Falster A. U. and Hanson S. L. (2019) Anatectic pegmatites of the Oxford County pegmatite field, Maine, USA. *Can. Mineral.* **57**, 811–815.

Whattam J. L. (2016) Oxygen and hydrogen isotopic analysis of tourmaline by secondary ion mass spectrometry. University of Manitoba.

Wise M. A. and Brown C. D. (2011) Chemical composition of coexisting columbite-group minerals and cassiterite from the Black Mountain pegmatite, Maine. *Eur. J. Mineral.* **23**, 817–828.

Yund R. A. and Thomas Anderson F. (1978) The effect of fluid pressure on oxygen isotope exchange between feldspar and water. *Geochim. Cosmochim. Acta* **42**, 235–239.

Zheng Y. (1993a) Calculation of oxygen isotope fractionation in anhydrous silicate minerals. *Geochim. Cosmochim. Acta* **57**, 1079–1091.

Zheng Y. (1993b) Calculation of oxygen isotope fractionation in hydroxyl-bearing silicates. *Earth Planet. Sci. Lett.* **121**, 247–263.

3.11 Figures and tables

`

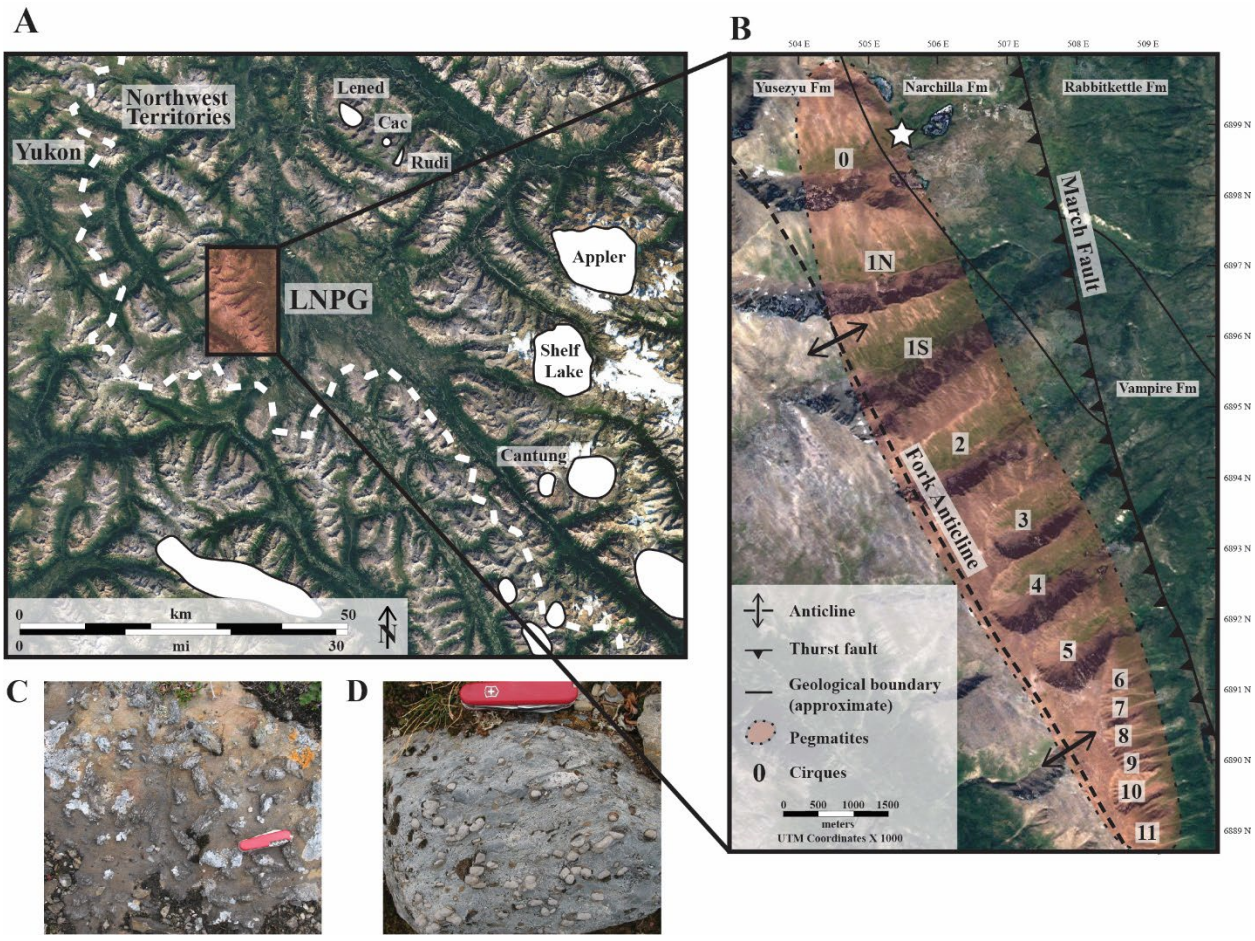

Fig.1. A) Satellite image (Google Earth ©) showing the location of: LNPG, Yukon-Northwest Territories border, local plutons of the Selwyn Plutonic Suite (Lened, Cac, Rudi, Appler, Shelf Lake, Cantung and five unnamed plutons). B): Satellite image (Google Earth ©) of the LNPG area with the local geology adapted from Groat et al. (2003). C, D) Cordierite-, staurolite- and andalusite-bearing metasedimentary wall rock (i.e. hornfels) in the northern part of the LNPG (see star in picture B).

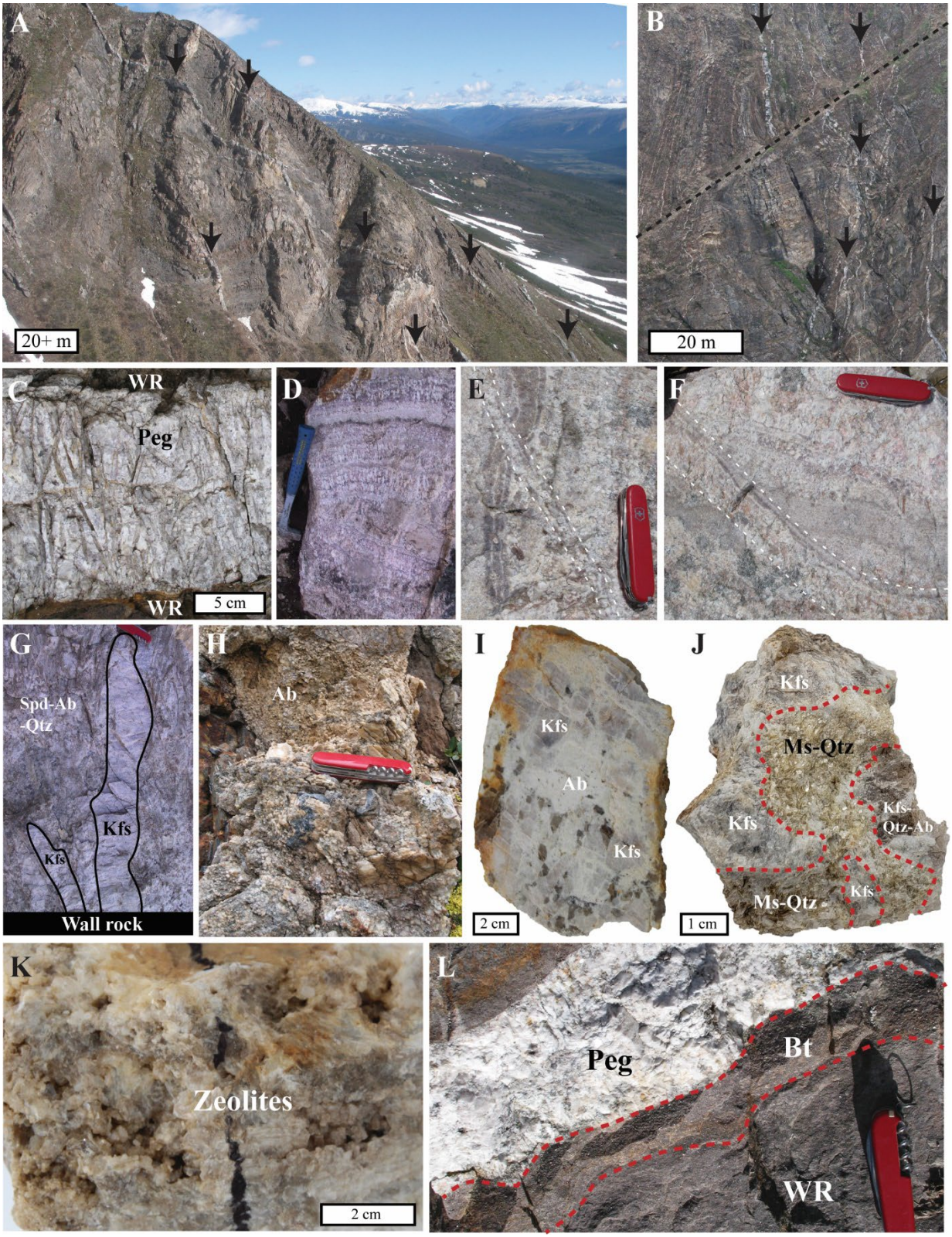

1017

1018 Fig. 2. Photographs of outcrops and samples from the LNPG. A, B) Cirque walls showing

numerous sub-vertical thin pegmatite dikes intruding the metasedimentary wall rocks. C) Acicular spodumene crystals in an spodumene—quartz-K-feldspar-albite pegmatite showing preferred orientation perpendicular to WR contact. D) Albite – lepidolite-quartz banded dike. E, F) Banded aplites displaying evidence of dike re-opening (crosscutting layers). G) Early coarse oriented K-feldspar (Kfs) megacrysts in a spodumene (Spd) – albite (Ab) – quartz (qtz) matrix. H) Pervasively altered pegmatite dike consisting mostly of secondary saccharoidal albite. I) Partial albitization (Ab) of early glassy K-feldspar (Kfs) megacryst. J) Medium-grained muscovite (Ms) – quartz (qtz) assemblage replacing early K-feldspar (Kfs) megacryst. K) Late-stage zeolites replacing spodumene and feldspars. Note the dissolution cavities. L) Narrow biotite-rich (Bt) aureole around a fresh pegmatite dike.

Sample	Rock type	Domain	Petrographic observations	Mineral analyzed	CL (quartz only)	Nature of mineral analyzed
07-01	Quartz vein	Other: -Large quartz vein associated with pegmatites.	Massive quartz.	Quartz	No primary zoning. Homogeneous bright blue. Secondary quartz along fractures avoided.	Hydrothermal
07-03	Granite	Other: -Granite with pegmatitic segregations.	Fine-grained granite. Quartz, feldspars, biotite, some accessory apatite.	Quartz	No primary zoning. Homogeneous bright blue.	Magmatic
07-06	Pegmatite	Pegmatite-WR contact	Large quartz mass with some altered feldspars at contact with WR.	Quartz	No primary zoning. Homogeneous bright blue. Secondary quartz along fractures avoided.	Magmatic
07-07	Pegmatite	SQAD	Coarse spodumene, quartz and albite assemblage.	Quartz	No primary zoning. Homogeneous bright blue. Secondary quartz along fractures avoided.	Magmatic
07-12	Pegmatite	BKF	Coarse quartz and K-feldspar assemblage.	Quartz	No primary zoning. Homogeneous bright blue. Secondary quartz along fractures avoided.	Magmatic
07-13	Quartz vein	Other: -Large quartz ± schorl vein associated with pegmatites.	Massive quartz with radiating sprays of schorl.	Quartz	No primary zoning. Homogeneous bright blue.	Hydrothermal
07-15	Pegmatite	BKF	Coarse quartz and K-feldspar assemblage.	Quartz	No primary zoning. Homogeneous bright blue.	Magmatic

					Secondary quartz along fractures avoided.	
07-22	Pegmatite	Banded aplites	Fine-grained albite, quartz, lepidolite and spodumene assemblage in banded aplite.	Quartz	No primary zoning. Homogeneous bright blue.	Magmatic
07-27	Pegmatite	?	Coarse fragments of quartz in calcite cement	Quartz	No primary zoning. Homogeneous bright blue. Secondary quartz along fractures avoided.	Metasomatic
07-28	Pegmatite	Albitized	Fine-grained albite, quartz and muscovite replacing K-feldspar.	Quartz	No primary zoning. Homogeneous bright blue. Secondary quartz along fractures avoided.	Metasomatic
07-29	Pegmatite	Banded aplites	Fine-grained albite, quartz, lepidolite and spodumene assemblage in banded aplite.	Quartz	No primary zoning. Homogeneous bright blue.	Magmatic
07-32	Pegmatite	Banded aplites	Fine-grained albite, quartz, lepidolite and spodumene assemblage in banded aplite.	Quartz	No primary zoning. Homogeneous bright blue. Secondary quartz along fractures avoided.	Magmatic
07-35	Pegmatite	Banded aplites	Fine-grained albite, quartz and minor spodumene assemblage in banded aplite. Lots of disseminated RM oxides.	Quartz	No primary zoning. Homogeneous bright blue.	Magmatic
07-36C	Pegmatite	Banded aplites	Fine-grained albite, quartz, lepidolite and spodumene assemblage in banded aplite.	Quartz	No primary zoning. Homogeneous bright blue.	Magmatic
07-38B	Pegmatite	SQAD	Coarse spodumene, quartz and albite assemblage. Minor K-feldspar present.	Quartz	No primary zoning. Homogeneous bright blue. Secondary quartz along fractures avoided.	Magmatic
07-40	Pegmatite	SQAD	Coarse spodumene, quartz and albite assemblage. Minor K-feldspar present.	Quartz	No primary zoning. Homogeneous bright blue. Secondary quartz along fractures avoided.	Magmatic
07-41	Pegmatite	Late stage Ca	Coarse quartz and zeolite.	Quartz	No primary zoning. Homogeneous bright blue. Highly fractured. Secondary quartz along fractures avoided.	Metasomatic
07-42	Pegmatite	BKF	Small quartz inclusions in K-feldspar megacryst.	Quartz	No primary zoning. Homogeneous bright blue.	Magmatic
07-43	Pegmatite	Banded aplites	Fine-grained albite, quartz, lepidolite and spodumene assemblage in banded aplite.	Quartz	No primary zoning. Homogeneous bright blue.	Magmatic
07-44	Pegmatite	?	Large mass of quartz with some feldspars and a beryl near WR contact.	Quartz	No primary zoning. Homogeneous bright blue.	N/A
07-45	Pegmatite	SQAD	Coarse spodumene, quartz and albite assemblage. Minor K-feldspar present.	Quartz	No primary zoning. Homogeneous bright blue.	Magmatic

07-46	Quartz vein	Late stage muscovite-quartz-calcite veins originating from pegmatite dikes.	1 cm-wide vein consisting of coarse muscovite, quartz, carbonates and rare albite.	Quartz	Asymmetrical zoning. Zoning mimics the morphology of mica, although the quartz grain analyzed did not reveal any mica inclusion under transmitted light.	Hydrothermal
L-3	Pegmatite	SQAD	Coarse spodumene, quartz and albite assemblage. Minor K-feldspar present.	Quartz	No primary zoning. Homogeneous bright blue.	Magmatic
L-8	Pegmatite	BKF	Coarse quartz and K-feldspar assemblage.	Quartz	No primary zoning. Homogeneous bright blue.	Magmatic
L-10	Pegmatite	SQAD?	Quenched melt pocket in SAQD. Fine-grained quartz, albite, spodumene, muscovite and minor K-feldspar.	Quartz	No primary zoning. Homogeneous bright blue.	Magmatic
C10-A	Pegmatite	SQAD	Coarse spodumene, quartz and albite assemblage. Minor K-feldspar present.	Quartz	No primary zoning. Homogeneous bright blue.	Magmatic
C10-D	Pegmatite	SQAD – now albitized	Originally a coarse spodumene, quartz and feldspars assemblage. Primary quartz still look fresh and glassy, but the rest of the sample is intensely altered.	Quartz	No primary zoning. Homogeneous bright blue. Secondary quartz along fractures avoided.	Metasomatic
226	Pegmatite	Vug/cavities	Quartz in dissolution cavity, along with albite, muscovite, zeolites and minor fluorite.	Quartz	No primary zoning visible. Extremely fractured with multiple generations of quartz. Analyses were done on the first generation of quartz.	Metasomatic
359	Pegmatite	?	Quartz, albite, muscovite and minor K-feldspar assemblage near a dissolution cavity lined with zeolites.	Quartz	No primary zoning. Homogeneous bright blue.	Metasomatic
04-01	Pegmatite	BKF	Coarse quartz and K-feldspar assemblage.	Quartz	No primary zoning. Homogeneous bright blue.	Magmatic
04-02	Pegmatite	SQAD	Coarse spodumene, quartz and albite assemblage.	Quartz	No primary zoning. Homogeneous bright blue.	Magmatic
11-01	Pegmatite	SQAD	Coarse spodumene, quartz and albite assemblage. Dissolution cavity with secondary phases present on one side of the sample.	Quartz	No primary zoning. Homogeneous bright blue. Secondary quartz along fractures avoided.	Magmatic
08-01	Pegmatite	SQAD	Coarse spodumene, quartz and albite assemblage.	Quartz	No primary zoning. Homogeneous bright blue.	Magmatic
08-02	Pegmatite	BKF	Small quartz inclusions in K-feldspar megacryst.	Quartz	No primary zoning. Homogeneous bright blue. Secondary quartz along fractures avoided.	Magmatic

08-05	Pegmatite	SQAD	Coarse spodumene, quartz and albite assemblage.	Quartz	No primary zoning. Homogeneous bright blue.	Magmatic
08-06	Pegmatite	SQAD	Coarse spodumene, quartz and albite assemblage.	Quartz	No primary zoning. Homogeneous bright blue. Secondary quartz along fractures avoided.	Magmatic
08-12	Pegmatite	SQAD	Coarse spodumene, quartz and albite assemblage.	Quartz	No primary zoning. Homogeneous bright blue.	Magmatic
08-15	Pegmatite	SQAD	Coarse spodumene, quartz and albite assemblage.	Quartz	No primary zoning. Homogeneous bright blue.	Magmatic
08-19	Pegmatite	Albitized	Fine-grained albite, quartz and muscovite replacing K-feldspar.	Quartz	No primary zoning. Homogeneous bright blue.	Metasomatic
08-20	Pegmatite	Albitized	Fine-grained albite, quartz, muscovite and RM oxides replacing K-feldspar.	Quartz	No primary zoning. Homogeneous bright blue.	Metasomatic
08-23	Pegmatite	Banded aplites	Fine-grained albite, quartz, lepidolite and spodumene assemblage in banded aplite.	Quartz	No primary zoning. Homogeneous bright blue.	Magmatic
08-26	Pegmatite	SQAD	Coarse spodumene, quartz and albite assemblage.	Quartz	No primary zoning. Homogeneous bright blue.	Magmatic
08-33	Pegmatite	Albitized	Fine-grained albite, quartz and muscovite replacing K-feldspar.	Quartz	No primary zoning. Homogeneous bright blue. Secondary quartz along fractures avoided.	Metasomatic
08-35	Pegmatite	Pegmatite-WR contact	Large quartz mass at the contact with WR.	Quartz	No primary zoning, but clearly two generations of quartz. Primary quartz is homogeneous bright blue. Secondary quartz is black. Analyses were done on the first generation of quartz.	Magmatic
08-40	Pegmatite	BKF	Coarse quartz, K-feldspar and albite assemblage.	Quartz	No primary zoning. Homogeneous bright blue.	Magmatic
08-43	Pegmatite	Greisen-like	Coarse quartz, cassiterite and “pencil” mica assemblage.	Quartz	No primary zoning. Homogeneous bright blue.	Metasomatic
08-47	Pegmatite	?	Coarse quartz and albite assemblage.	Quartz	No primary zoning. Homogeneous bright blue.	Magmatic
08-54	Pegmatite	?	Large mass of saccharoidal quartz. No other minerals observed.	Quartz	No primary zoning. Homogeneous bright blue.	Metasomatic
08-56	Pegmatite	Pegmatite-WR contact	Coarse quartz, albite and minor muscovite assemblage at the contact with WR.	Quartz	No primary zoning. Homogeneous bright blue. Secondary quartz along fractures avoided.	Magmatic
08-62B	Pegmatite	SQAD	Coarse spodumene, quartz and albite assemblage.	Quartz	No primary zoning. Homogeneous bright blue.	Magmatic
08-64	Pegmatite	SQAD	Coarse spodumene, quartz and albite assemblage.	Quartz	No primary zoning. Homogeneous bright blue.	Magmatic
08-73	Pegmatite	SQAD	Coarse spodumene, quartz and albite assemblage.	Quartz	No primary zoning. Homogeneous bright blue.	Magmatic

08-79	Pegmatite	Pegmatite-WR contact	Coarse quartz and muscovite assemblage at the contact with WR.	Quartz	No primary zoning. Homogeneous bright blue. Secondary quartz along fractures avoided.	Magmatic
07-28	Pegmatite	Pegmatite-WR contact	Biotite at the contact with WR	Biotite	N/A	Metasomatic
07-42	Pegmatite	BKF	K-feldspar megacryst	K-feldspar	N/A	Magmatic
07-45	Pegmatite	SQAD	Coarse spodumene, quartz and albite assemblage. Minor K-feldspar present.	Quartz K-feldspar	N/A	Magmatic
07-46	Quartz vein	Late stage muscovite-quartz-calcite veins originating from pegmatite dikes.	1 cm-wide vein consisting of coarse muscovite, quartz, carbonates and rare albite.	Muscovite Albite	N/A	Hydrothermal
C10-C	Pegmatite	Albitized	Coarse quartz in a matrix of cleavelanditic albite and fine-grained muscovite.	Quartz Albite	N/A	Metasomatic
C10-D	Pegmatite	SQAD/albitized	Originally a coarse spodumene, quartz and feldspars assemblage. Intensely altered with abundant cleavelandite and fine-grained muscovite/lepidolite-quartz replacing early K-feldspar and fine-grained albite, lepidolite and clays replacing spodumene.	Quartz Albite Muscovite	N/A	Metasomatic
L-1	Pegmatite	SQAD	Coarse spodumene, quartz and albite assemblage. Minor K-feldspar present.	Quartz K-feldspar	N/A	Magmatic
L-2	Pegmatite	SQAD	Coarse spodumene, quartz and albite assemblage. Minor K-feldspar present.	Quartz K-feldspar	N/A	Magmatic
L-9	Pegmatite	Pegmatite-WR contact	Coarse garnet with quartz, K-feldspar and muscovite at the contact with WR.	Quartz Garnet	N/A	Magmatic
L-11	Pegmatite	BKF	K-feldspar megacryst	K-feldspar	N/A	Magmatic
L-13	Quartz vein	Late stage muscovite-quartz-calcite veins originating from pegmatite dikes.	1 cm-wide vein consisting of coarse muscovite, quartz and carbonates.	Muscovite	N/A	Hydrothermal
L-14	Quartz vein	Late stage muscovite-quartz-calcite veins originating from pegmatite dikes.	1 cm-wide vein consisting of coarse muscovite, quartz, carbonates and rare albite.	Muscovite Albite	N/A	Hydrothermal
254	Pegmatite	BKF	Coarse quartz and K-feldspar.	Quartz	N/A	Magmatic
362	Pegmatite	?	Muscovite book	Muscovite	N/A	Magmatic
440	Pegmatite	Vug	Dissolution cavity lined with quartz, albite, muscovite, and zeolites.	Albite	N/A	Metasomatic

11-01	Pegmatite	Vug	Dissolution cavity in SAQD lined with quartz, albite, muscovite, zeolites and fluorite.	Quartz Albite	N/A	Metasomatic
08-22	Pegmatite	Pegmatite-WR contact	Muscovite at contact with WR	Muscovite	N/A	Magmatic
08-30	Pegmatite	Vug	Dissolution cavity lined with quartz, muscovite and calcite.	Muscovite	N/A	Metasomatic
08-42	Pegmatite	Greisen-like	Coarse quartz, cassiterite and "pencil" mica assemblage.	Muscovite Quartz	N/A	Metasomatic
08-43	Pegmatite	Greisen-like	Coarse quartz, cassiterite and "pencil" mica assemblage.	Albite Muscovite	N/A	Metasomatic
08-72	Pegmatite	SQAD	Coarse spodumene, quartz and albite assemblage.	Quartz	N/A	Magmatic
08-79	Pegmatite	Pegmatite-WR contact	Coarse quartz and muscovite assemblage at the contact with WR.	Muscovite	N/A	Magmatic

Table 1. LNPG samples with summary of petrographic observations (naked eye, SEM, CL) and their inferred nature (i.e., magmatic versus metasomatic). Samples are split in two groups: (1) mineral fragments used for *in-situ* SIMS analysis; and (2) mineral separates used for bulk analysis.

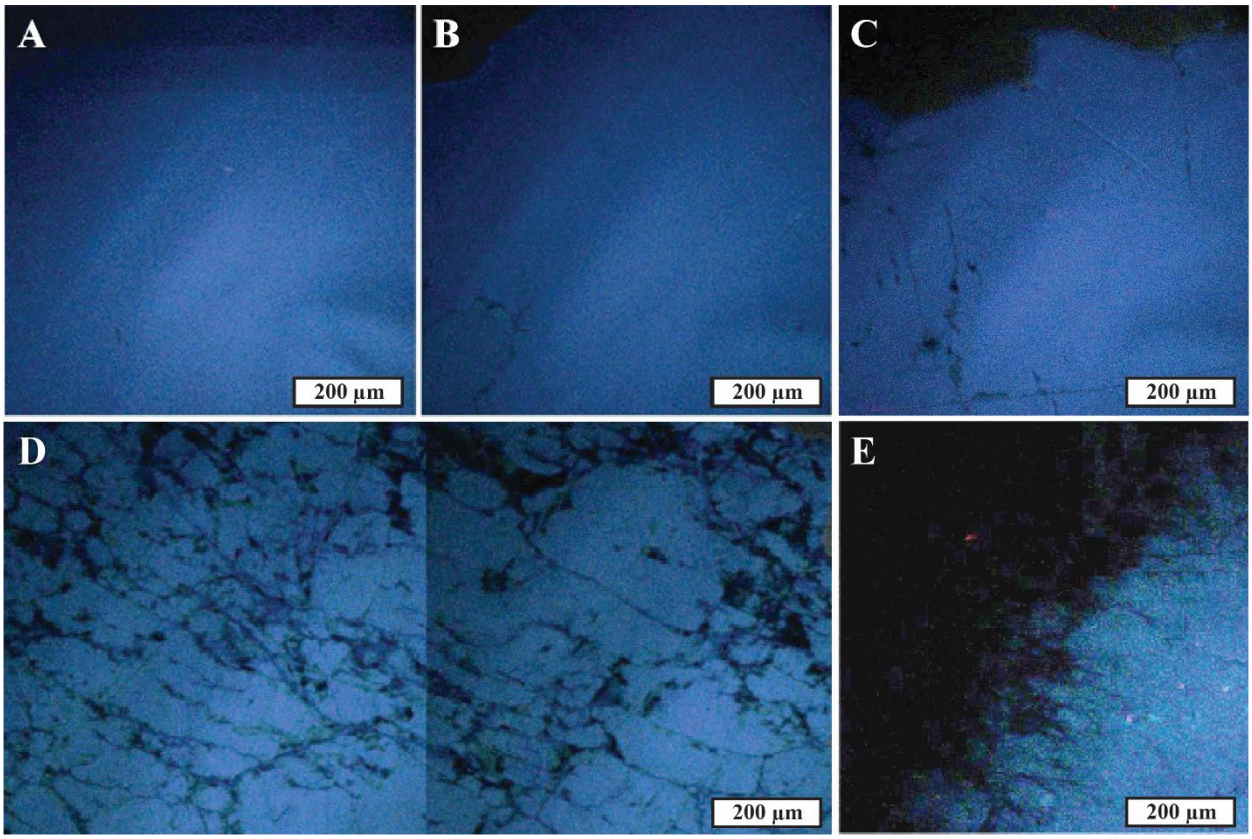

Fig. 3. Cathodoluminescence (SEM-CL) pictures of selected quartz grains from LNPG analyzed for *in-situ* ^{18}O. A, B, C) Typical uniform bright blue response of fresh magmatic quartz samples. Note the presence of shadow effects, but lack of zoning. Secondary features range from non-existent (A) to minor fracturing (C). D, E) Metasomatic quartz samples displaying abundant secondary features and multiple generations of quartz. Picture D exhibits three generations of quartz: (1) primary bright blue quartz; (2) secondary black quartz filling fractures and pits; and (3) tertiary yellowish quartz filling late fractures. Note that image E exhibits strong dissolution-precipitation features with two generations of quartz: (1) primary bright blue; and (2) secondary black quartz.

Analysis	Ti (ppm)	Ti Int2SE (ppm)	Al (ppm)	Al Int2SE (ppm)	Ge (ppm)	Ge Int2SE (ppm)
07_01	15.1	1.2	1000	380	3.41	0.24
07_01_1	15.5	1.2	490	110	2.08	0.18
07_03	12.6	1	18.6	1.5	0.87	0.17
07_03_1	23.6	2.8	53.8	6.8	0.51	0.15
07_03_2	14.5	2.5	32.3	8.6	0.65	0.16
07_06	10.2	1	540	350	2.03	0.2
07_06_1	10.4	1.1	119	89	2.37	0.23
07_06_2	9.86	0.9	169	84	2.44	0.23
07_07	8.88	0.86	285	61	8.87	0.32
07_07_1	9.41	0.87	231	18	9.1	0.36
07_07_2	9.61	0.85	200	18	8.68	0.31
07_12	8.9	1.1	471	56	4.87	0.27
07_12_1	10.41	0.84	412	40	4.83	0.28
07_12_2	8.97	0.89	880	240	5.05	0.27
07_13	14	1.1	137	16	2.34	0.24
07_13_1	12.2	1.2	179	55	2.29	0.25
07_13_2	12.4	1.2	170	49	2.53	0.23
07_15	8.7	0.89	583	36	4.87	0.32
07_15_1	8.5	1	665	85	5.46	0.4
07_15_2	8.3	1.1	601	27	5.48	0.33
07_22	8.5	1.1	673	39	5.27	0.34
07_22_1	9.06	0.85	236	13	5.12	0.3
07_22_2	9.9	1.1	272	23	5.05	0.33
07_27	9.7	0.8	2420	660	1.21	0.17
07_27_1	9.97	0.95	680	320	1.1	0.16
07_27_2	8.86	0.85	460	240	1.03	0.16
07_28	8.57	0.81	270	120	6.25	0.27
07_28_1	7.65	0.88	471	53	5.81	0.26
07_28_2	8.32	0.86	465	95	6.83	0.32
07_29	9	0.9	730	310	8.67	0.34
07_29_1	9.1	0.95	188.8	5.4	9.33	0.44
07_29_2	7.67	0.94	192.8	6.2	9.78	0.41
07_32	7.63	0.9	255	21	9.64	0.43
07_32_1	9.12	0.91	700	180	8.71	0.42
07_32_2	8.53	0.93	235.1	6.4	8.81	0.39
07_35	8.99	0.82	636	69	6.16	0.26
07_35_1	8.38	0.79	9000	1600	6.73	0.29
07_36C	7.6	1	892	48	3.86	0.3
07_36C_1	8.7	1	1870	260	25.1	7.2
07_36C_2	8.39	0.95	542	81	3.18	0.29
07_38B	8.51	0.93	193.9	8.8	4.26	0.29
07_38B_1	8.26	0.82	720	250	4.3	0.26
07_38B_2	9	1	790	220	5.52	0.31
07_40	7.79	0.87	1560	140	4.33	0.26
07_40_1	7.77	0.81	212	15	5.39	0.29
07_40_2	8	0.91	431	16	5.53	0.32
07_41	10.9	2.6	155	11	4.28	0.31
07_41_1	9.5	1.2	268	59	4.24	0.28
07_41_2	8.93	0.94	170	25	4.58	0.26
07_42	9.72	0.97	119	36	2.54	0.21
07_42_1	8.97	0.82	280	190	2.9	0.2
07_42_2	9.8	1.1	330	190	2.97	0.27
07_43	8.7	1	310	83	5.61	0.34
07_43_1	7.58	0.95	800	310	5.71	0.31
07_43_2	6.44	0.79	730	250	6.04	0.38
07_44	9.7	1	417	58	4.32	0.29
07_44_1	9.7	1.1	424	43	4.41	0.3
07_44_2	9.8	1	427	29	4.65	0.28
07_45	8.2	1.3	795	52	3.16	0.29
07_45_1	7	1	1140	140	2.88	0.29

07_45_2	7.87	0.97	705	85	2.36	0.28
07_46	8.97	0.89	11.59	0.86	0.89	0.16
07_46_1	9.86	0.87	29.6	1.1	1.06	0.15
07_46_2	9.13	0.78	38.1	3.6	1.17	0.14
L_3	8.59	0.83	396	11	3.17	0.22
L_3_1	6.81	0.74	580	180	3.29	0.21
L_3_2	6.87	0.8	1710	200	3.4	0.23
L_8	7.84	0.88	1507	63	3.35	0.2
L_8_1	8.15	0.99	1004	43	3.43	0.24
L_8_2	8.92	0.98	957	34	3.19	0.27
L_10	8.68	0.93	485	23	3.27	0.28
L_10_1	8.3	1	324.2	9.5	3.44	0.28
L_10_2	8.1	1.1	769	68	3.04	0.3
C10_A	7	1	385.9	7.5	5.36	0.37
C10_A_1	5.67	0.96	435	38	4.95	0.34
C10_A_2	7.2	1	3830	910	5.51	0.38
C10_D	7.59	0.97	324	26	5.46	0.42
C10_D_1	7.7	1.2	450	190	4.78	0.31
C10_D_2	6.9	1	424	34	4.12	0.28
226	8	1.3	43	25	1.17	0.27
226_1	7.2	1	36	18	1.16	0.22
226_2	6.94	0.95	27	14	0.87	0.16
359	7.23	0.97	418	47	4.19	0.31
359_1	7.52	0.88	4100	1300	4.17	0.29
359_2	7.04	0.94	1560	160	4.14	0.29
04_01	7.37	0.99	1270	150	4.48	0.32
04_01_1	11.5	1.2	2500	380	4.97	0.33
04_01_2	7.5	0.96	310	110	4.4	0.3
04_02	6.94	0.84	930	300	5.08	0.31
04_02_1	7.9	1.3	1080	430	4.88	0.35
04_02_2	6.77	0.77	443	81	4.86	0.23
11_01	7.97	0.87	780	220	3.94	0.27
11_01_1	6.7	1	343	93	3.2	0.23
08_01	6.6	0.97	730	280	3	0.28
08_01_1	8.5	1.2	590	32	3.1	0.26
08_01_2	7.15	0.98	365	18	3.29	0.28
08_02	6.64	0.95	461	11	2.8	0.27
08_02_1	7.14	0.97	405	11	3.1	0.26
08_02_2	6.7	0.95	422	10	2.78	0.27
08_05	8.1	1.1	628	73	2.6	0.31
08_05_1	8.7	1.2	303	12	3.11	0.35
08_05_2	8.2	1.1	275	29	3.89	0.36
08_06	7.3	1.2	293.5	6.3	5.2	0.33
08_06_1	7.7	1.2	303.2	6.2	5.33	0.34
08_06_2	5.97	0.97	1380	150	5.16	0.31
08_12	6.69	0.93	1270	190	3.09	0.28
08_12_1	6.3	1.1	6500	1000	3.17	0.26
08_12_2	6.77	0.99	2120	150	3.01	0.23
08_15	6.1	1.1	1150	650	3.34	0.29
08_15_1	6	1	489	74	3.58	0.29
08_15_2	7.1	1	474	11	3.51	0.31
08_19_1	7.43	0.93	610	180	2.85	0.29
08_19_2	6.28	0.9	404	28	2.93	0.22
08_20	7.7	1	314	27	3.23	0.29
08_20_1	7.8	1.2	520	180	3.12	0.27
08_20_2	7.13	0.99	2600	1000	3.24	0.23
08_23	6.64	0.92	1100	160	6.27	0.37
08_23_1	5.73	0.87	710	360	6.68	0.34
08_23_2	5.7	0.73	410	150	6.59	0.37
08_26	8	1	290	64	3.9	0.28
08_26_1	8.04	0.86	272	11	4.26	0.32
08_26_2	7.6	1	193.6	3.7	4.62	0.31

08_33	6.9	1.2	3280	430	5.11	0.41
08_33_1	5.72	0.97	490	31	5.78	0.33
08_33_2	5.62	0.85	940	120	6.69	0.42
08_35	5.7	1.1	210	170	1.39	0.24
08_35_1	6.73	0.93	155	93	1.14	0.22
08_35_2	8	1.1	1330	500	1.3	0.24
08_40	8.04	0.93	1500	300	4.52	0.29
08_40_1	6.57	0.89	630	250	4.39	0.3
08_40_2	6.49	0.77	570	170	4.15	0.27
08_43	6.46	0.96	906	42	5.29	0.35
08_43_1	4.7	1.1	1340	270	5.51	0.47
08_43_2	5.7	1.1	504	34	5.44	0.41
08_47	10.3	1.5	246	19	4.27	0.3
08_47_1	11.1	1.2	118.1	5.1	4.43	0.3
08_47_2	12.1	1.2	400	210	4.65	0.37
08_54	6.97	0.92	150	140	1.45	0.22
08_54_1	7	2.1	78	52	1.26	0.21
08_54_2	6.7	0.99	57	23	1.55	0.23
08_56	7.6	1	255	21	7.56	0.34
08_56_1	6.52	0.89	213	53	7.14	0.44
08_56_2	6.9	1.1	720	320	6.72	0.42
08_62B	7.1	1.1	1640	330	3.89	0.3
08_62B_1	6.7	1	4780	890	4.36	0.37
08_62B_2	7.7	1.3	400	110	4.3	0.38
08_64	6.9	0.9	217	14	4.76	0.32
08_64_1	6.86	0.99	1540	460	4.58	0.36
08_64_2	4.63	0.85	492	61	4.45	0.32
08_73	6.3	1.1	2900	3500	3.72	0.31
08_73_1	6.7	1	2210	700	3.81	0.29
08_73_2	7.95	0.95	463	81	4.15	0.29
08_79	7.7	1.1	320	150	5.99	0.39
08_79_1	6.63	0.98	280	98	6.03	0.38
08_79_2	5.66	0.81	199	11	6.26	0.37

Table 2. Summary of in-situ LA-ICP-MS analyses on quartz samples. Int2SE = analytical uncertainty. LOD ≤ Int2SE for most analyses. See table 1 for samples #.

Analysis	Ti (ppm)	Ti Int2SE (ppm)	T (°C)	(Int2SE) T (°C)	Mean T (°C)	SD (1σ) (°C)	Mean Int2SE (°C)	Final T range (°C)
07_01	15.1	1.2	631	±7	632	±1	±7	632 (±8)
07_01_1	15.5	1.2	633	±7				
07_03	12.6	1	614	±7	638	±26	±12	638 (±38)
07_03_1	23.6	2.8	675	±12				
07_03_2	14.5	2.5	627	±16				
07_06	10.2	1	595	±9	595	±2	±9	595 (±11)
07_06_1	10.4	1.1	597	±9				
07_06_2	9.86	0.9	592	±8				
07_07	8.88	0.86	583	±8	587	±3	±8	587 (±11)
07_07_1	9.41	0.87	588	±8				
07_07_2	9.61	0.85	590	±8				
07_12	8.9	1.1	583	±10	588	±6	±8	588 (±14)
07_12_1	10.41	0.84	597	±7				
07_12_2	8.97	0.89	584	±8				
07_13	14	1.1	623	±7	616	±6	±8	616 (±14)
07_13_1	12.2	1.2	611	±9				
07_13_2	12.4	1.2	612	±9				
07_15	8.7	0.89	581	±9	579	±2	±10	579 (±12)
07_15_1	8.5	1	579	±10				
07_15_2	8.3	1.1	577	±11				
07_22	8.5	1.1	579	±11	586	±5	±10	586 (±15)
07_22_1	9.06	0.85	585	±8				
07_22_2	9.9	1.1	592	±10				
07_27	9.7	0.8	591	±7	589	±4	±8	589 (±12)
07_27_1	9.97	0.95	593	±8				
07_27_2	8.86	0.85	583	±8				
07_28	8.57	0.81	580	±8	576	±4	±9	576 (±13)
07_28_1	7.65	0.88	571	±9				
07_28_2	8.32	0.86	578	±9				
07_29	9	0.9	584	±9	580	±7	±9	580 (±16)
07_29_1	9.1	0.95	585	±9				
07_29_2	7.67	0.94	571	±10				
07_32	7.63	0.9	570	±10	579	±6	±9	579 (±15)
07_32_1	9.12	0.91	585	±9				
07_32_2	8.53	0.93	580	±9				
07_35	8.99	0.82	584	±8	581	±3	±8	581 (±12)
07_35_1	8.38	0.79	578	±8				
07_36C	7.6	1	570	±11	577	±5	±10	577 (±15)
07_36C_1	8.7	1	581	±10				
07_36C_2	8.39	0.95	578	±10				
07_38B	8.51	0.93	580	±9	580	±3	±9	580 (±12)
07_38B_1	8.26	0.82	577	±8				
07_38B_2	9	1	584	±9				
07_40	7.79	0.87	572	±9	573	±1	±9	573 (±10)
07_40_1	7.77	0.81	572	±9				
07_40_2	8	0.91	574	±9				

07_41	10.9	2.6	601	±21	591	±7	±14	591 (±21)
07_41_1	9.5	1.2	589	±11				
07_41_2	8.93	0.94	584	±9				
07_42	9.72	0.97	591	±9	589	±3	±9	580 (±12)
07_42_1	8.97	0.82	584	±8				
07_42_2	9.8	1.1	592	±10				
07_43	8.7	1	581	±10	569	±10	±10	569 (±20)
07_43_1	7.58	0.95	570	±10				
07_43_2	6.44	0.79	557	±10				
07_44	9.7	1	591	±9	591	±0	±9	591 (±9)
07_44_1	9.7	1.1	591	±10				
07_44_2	9.8	1	592	±9				
07_45	8.2	1.3	576	±13	571	±5	±12	571 (±17)
07_45_1	7	1	563	±12				
07_45_2	7.87	0.97	573	±10				
07_46	8.97	0.89	584	±8	587	±4	±8	587 (±12)
07_46_1	9.86	0.87	592	±8				
07_46_2	9.13	0.78	585	±7				
L_3	8.59	0.83	580	±8	568	±9	±9	568 (±18)
L_3_1	6.81	0.74	561	±9				
L_3_2	6.87	0.8	562	±9				
L_8	7.84	0.88	573	±9	577	±5	±9	577 (±14)
L_8_1	8.15	0.99	576	±10				
L_8_2	8.92	0.98	583	±9				
L_10	8.68	0.93	581	±9	578	±2	±10	578 (±12)
L_10_1	8.3	1	577	±10				
L_10_2	8.1	1.1	575	±11				
C10_A	7	1	563	±12	559	±8	±12	559 (±20)
C10_A_1	5.67	0.96	547	±13				
C10_A_2	7.2	1	566	±11				
C10_D	7.59	0.97	570	±11	568	±4	±12	568 (±16)
C10_D_1	7.7	1.2	571	±13				
C10_D_2	6.9	1	562	±12				
226	8	1.3	574	±14	568	±5	±12	568 (±17)
226_1	7.2	1	566	±11				
226_2	6.94	0.95	563	±11				
359	7.23	0.97	566	±11	566	±2	±11	566 (±13)
359_1	7.52	0.88	569	±10				
359_2	7.04	0.94	564	±11				
04_01	7.37	0.99	568	±11	581	±18	±10	581 (±28)
04_01_1	11.5	1.2	606	±9				
04_01_2	7.5	0.96	569	±11				
04_02	6.94	0.84	563	±10	566	±6	±11	566 (±17)
04_02_1	7.9	1.3	573	±14				
04_02_2	6.77	0.77	561	±9				
11_01	7.97	0.87	574	±9	567	±7	±11	567 (±18)
11_01_1	6.7	1	560	±12				
08_01	6.6	0.97	559	±12	568	±9	±12	568 (±21)
08_01_1	8.5	1.2	579	±12				
08_01_2	7.15	0.98	565	±11				
08_02	6.64	0.95	559	±11	561	±3	±11	561 (±14)
08_02_1	7.14	0.97	565	±11				
08_02_2	6.7	0.95	560	±11				
08_05	8.1	1.1	575	±11	578	±3	±11	578 (±14)
08_05_1	8.7	1.2	581	±12				
08_05_2	8.2	1.1	576	±11				

08_06	7.3	1.2	567	±13	563	±9	±13	563 (±22)
08_06_1	7.7	1.2	571	±13				
08_06_2	5.97	0.97	551	±13				
08_12	6.69	0.93	560	±11	559	±3	±12	559 (±15)
08_12_1	6.3	1.1	555	±14				
08_12_2	6.77	0.99	561	±12				
08_15	6.1	1.1	552	±14	556	±6	±13	556 (±19)
08_15_1	6	1	551	±13				
08_15_2	7.1	1	565	±11				
08_19_1	7.43	0.93	568	±10	562	±7	±11	562 (±18)
08_19_2	6.28	0.9	555	±11				
08_20	7.7	1	571	±11	569	±3	±12	569 (±15)
08_20_1	7.8	1.2	572	±13				
08_20_2	7.13	0.99	565	±11				
08_23	6.64	0.92	559	±11	551	±6	±11	551 (±17)
08_23_1	5.73	0.87	548	±12				
08_23_2	5.7	0.73	547	±10				
08_26	8	1	574	±10	573	±2	±10	572 (±12)
08_26_1	8.04	0.86	575	±9				
08_26_2	7.6	1	570	±11				
08_33	6.9	1.2	562	±14	552	±7	±13	552 (±20)
08_33_1	5.72	0.97	547	±13				
08_33_2	5.62	0.85	546	±12				
08_35	5.7	1.1	547	±15	561	±11	±12	561 (±23)
08_35_1	6.73	0.93	560	±11				
08_35_2	8	1.1	574	±11				
08_40	8.04	0.93	575	±10	564	±8	±10	564 (±18)
08_40_1	6.57	0.89	558	±11				
08_40_2	6.49	0.77	557	±9				
08_43	6.46	0.96	557	±12	546	±10	±15	546 (±25)
08_43_1	4.7	1.1	532	±18				
08_43_2	5.7	1.1	547	±15				
08_47	10.3	1.5	596	±13	603	±6	±11	603 (±17)
08_47_1	11.1	1.2	602	±10				
08_47_2	12.1	1.2	610	±9				
08_54	6.97	0.92	563	±11	562	±2	±16	562 (±18)
08_54_1	7	2.1	563	±25				
08_54_2	6.7	0.99	560	±12				
08_56	7.6	1	570	±11	563	±5	±12	563 (±17)
08_56_1	6.52	0.89	558	±11				
08_56_2	6.9	1.1	562	±13				
08_62B	7.1	1.1	565	±13	565	±5	±13	565 (±18)
08_62B_1	6.7	1	560	±12				
08_62B_2	7.7	1.3	571	±14				
08_64	6.9	0.9	562	±11	552	±14	±12	552 (±26)
08_64_1	6.86	0.99	562	±12				
08_64_2	4.63	0.85	531	±14				
08_73	6.3	1.1	555	±14	563	±8	±12	563 (±20)
08_73_1	6.7	1	560	±12				
08_73_2	7.95	0.95	574	±10				
08_79	7.7	1.1	571	±12	559	±10	±12	559 (±22)
08_79_1	6.63	0.98	559	±12				
08_79_2	5.66	0.81	547	±11				

1058

Table 3. TitaniQ values for LNPG quartz calculated using the Huang and Audétat (2012) calibration with a P = 3 kbar and $\alpha TiO_2 = 0.5$ (see text for discussion). Values are reported in the text as $T_{mean} \pm (1\sigma + Int2SE_{mean})$; see right column.

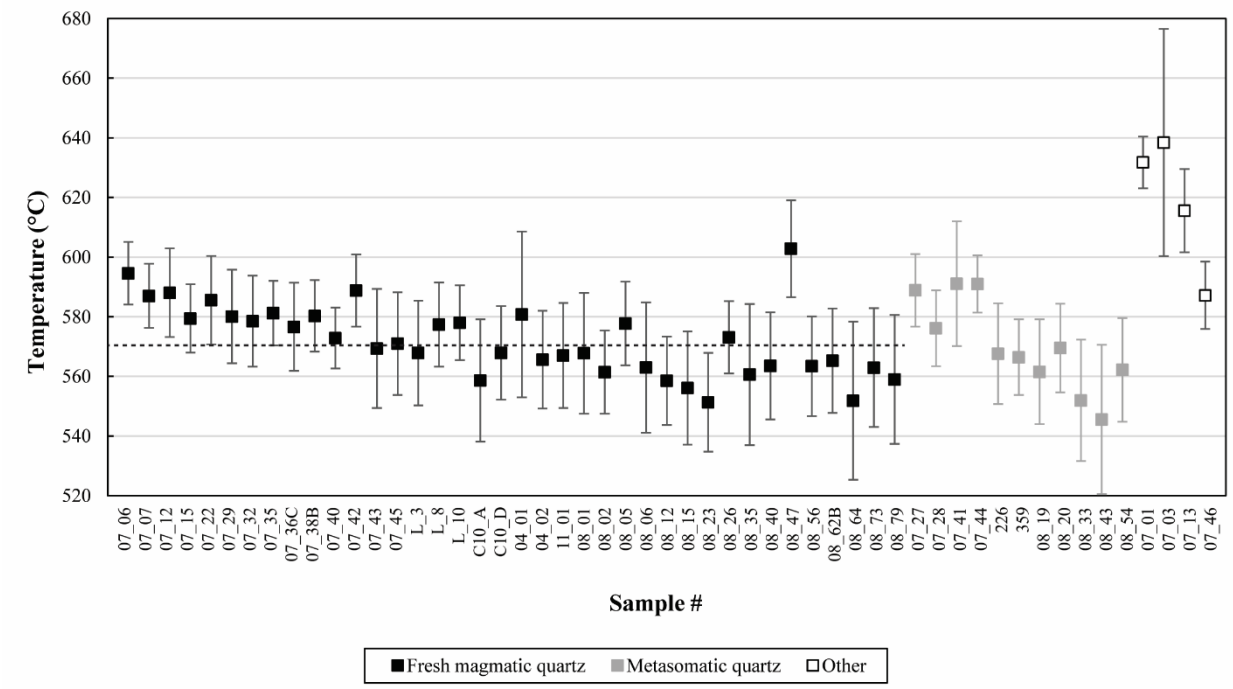

Fig. 4. Summary of the calculated TitaniQ values for LNPG quartz for each sample; see Table 1 for sample # and details. Horizontal dashed line is the overall mean temperature of magmatic quartz samples (571°C). "Other" = hydrothermal veins associated with the pegmatite and a sample of granite (07_03).

	SIMS (± 0.8‰)		DI-IRMS ($\delta^{18}O$ ± 0.3‰; δD ± 3‰)								
Sample	**$\delta^{18}O_{qtz}$**	**$\delta^{18}O_{ab}$**	**$\delta^{18}O_{qtz}$**	**$\delta^{18}O_{Kf}$**	**$\delta^{18}O_{ab}$**	**$\delta^{18}O_{grt}$**	**$\delta^{18}O_{ms}$**	**δD_{ms}**	**$\delta^{18}O_{bt}$**	**δD_{bt}**	**$\delta^{18}O_{cal}$**
07-01	12.2										
07-03	11.4										
07-06	15.2										
07-07	14.1 13.1										
07-12	14.8										
07-13	13.2										
07-15	12.4	16.0 17.5									
07-22	12.6 13.6										
07-27	11.0										
07-28	11.2								12.7 12.7	-173 -168	
07-29	12.9 11.2										
07-32	14.6	15.3 11.9									
07-35	15.3										
07-36A		-0.6 -0.6									
07-36B		-0.3 -1.7									
07-36C	12.6 11.7										
07-38B	13.9										
07-40	12.8	-1.5 -1.5									
07-41	15.0 12.4										
07-42	12.0			13.8 12.4							
07-43	13.2										
07-44	13.0 10.6										
07-45	14.7 11.4		13.8	9.5							
07-46	11.6				0.4		13.1	-69			
L-1			14.8	9.5							
L-2			12.3	7.2							
L-3	12.3										
L-5		-3.0 3.9									
L-8	11.0 12.2	12.5 7.7									
L-9		13.4 18.3	14.7			10.7					
L-10	13.2										

L-11				6.8							
L-13							12.6	-67			14.8
L-14					8.8		13.2	-83			
Leise 2008		12.0 12.2									
C10-A	12.4										
C10-C		2.0 1.0	14.9		7.9 8.8						
C10-D	8.6 10.5		14.3		0.4 1.6		8.8	-174			
85		11.1 10.2									
226	13.3										
254		10.4 15.7	10.2								
359	10.8										
362							11.6	-79			
394		4.6 4.4									
440					5.0						
04-01	12.9										
04-02	11.1 10.8										
11-01	12.0		13.0		10.6						
08-01	13.7 10.5	9.0 12.2									
08-02	10.3										
08-05	11.6										
08-06	13.8										
08-12	13.4										
08-13		10.4 12.3									
08-15	13.1 12.3										
08-19	11.3										
08-20	12.6										
08-22							10.4	-182			
08-23	11.6 11.9										
08-26	11.9										
08-30		13.1 12.9					13	-177			
08-33	12.7 12.4										
08-35	13.6										
08-40	12.1	15.5 13.0									
08-42			14.8				12.9	-85			
08-43	11.2 13.1				12.4 14.9			-84			
08-47	12.4										

08-54	12.5											
08-56	16.2											
08-62B	16.3 13.4											
08-64	10.9											
08-72					6.2 4.3							
08-73	12.6 11.8											
08-79	15.2						9.6	-110				

Table 4. Summary of the measured $\delta^{18}O$ and δD values analysed using both SIMS and DI-IRMS.

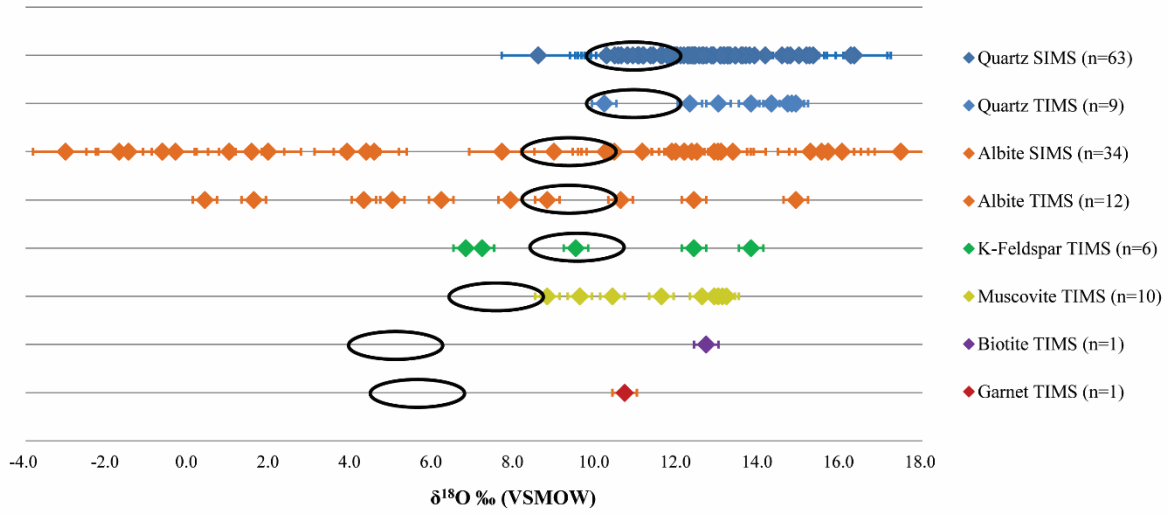

Fig. 5. Graphical summary of measured mineral $\delta^{18}O$ values determined by SIMS and DI-IRMS. Circles represent calculated $\delta^{18}O$ values of minerals in equilibrium with $\delta^{18}O_{quartz}$ = 10-12‰, as discussed in the text, using fractionation factors of Bottinga and Javoy (1975) for hydrous phases and Zheng et al. (1993a) for anhydrous phases at a temperature of 570°C based on TitaniQ values (Fig. 4).

Locality	Sample and analysis no.	$\delta^{18}O_{qtz}$
Ampasogona Pegmatite, Madagascar	AMP-3-1	15.2
	AMP-4-1	15.2
	AMP-4-1a	15.6
Anita Pegmatite, California, USA	ANI-1-1	9.9
	ANI-2-1	8.6
	ANI-3-1	7.8
	ANI-4-1	6.5
	ANI-4-1a	7.5
Unnamed pegmatite near Aracuai, Brazil	ARA-1-1	12.8
	ARA-2-1	11.1
	ARA-2-1a	12.8
	ARA-2-2	8.6
	ARA-3-1	9.0
	ARA-4-1	9.6
	ARA-4-1a	9.9
Authier (formerly Colombe) Pegmatite, Quebec, Canada	AUT-1-1	7.7
	AUT-2-1	7.3
	AUT-2-2	8.4
	AUT-3-1	8.0
	AUT-4-1	8.9
Alvarroes Pegmatite, Portugal	AVR-1-1	13.1
	AVR-1-2	14.0
	AVR-2-1	8.9
	AVR-3-1	5.3
	AVR-3-2	7.8
	AVR-4-1	5.6
Blue Chihuahua Pegmatite, California, USA	BCH-1-1	9.0
	BCH-2-1	10.2
	BCH-3-1	8.6
	BCH-4-1	11.0
Blue Lady Pegmatite, California	BLD-1-1	10.2
	BLD-2-1	10.9
	BLD-3-1	11.9
	BLD-4-1	11.5
Black Mountain Pegmatite, Maine, USA	BLM-1-1	8.6
	BLM-2-1	12.2
	BLM-3-1	13.6
	BLM-4-1	13.2
Cryo-Genie Pegmatite, California	CRY-1-1	13.8
	CRY-2-1	11.3
	CRY-3-1	11.1
	CRY-4-1	12.6
Leduc Pegmatite, Quebec, Canada	DUC-1-1	13.2
	DUC-2-1	11.6
	DUC-3-1	12.8
San Piero in Campo Pegmatites, Elba Island, Italy	ELB-1-1	11.1
	ELB-2-1	8.9
	ELB-3-1	8.6
	ELB-4-1	8.7
Esmeralda Pegmatite, California, USA	ESM-1-1	8.2
	ESM-2-1	9.8
	ESM-3-1	6.2
	ESM-4-1	9.9
Havey Pegmatite, Maine, USA	HVY-1-1	10.2
	HYV-2-1	13.1
	HVY-3-1	13.4
	HVY-4-1	11.4
Maple Lode Pegmatite, USA	MPL-1-1	7.9
	MPL-2-1	7.5
	MPL-3-1	8.4

	MPL-3-2	8.1
	MPL-4-1	8.5
North Morning Star Pegmatite, Arizona, USA	NMS-1-1	11.6
	NMS-2-1	11.8
	NMS-3-1	9.7
	NMS-4-1	9.4
North Plumbago Pegmatite, Maine, USA	NPL-1-1	5.8
	NPL-2-1	9.5
	NPL-3-1	7.4
	NPL-4-1	9.7
Paprok Pegmatite, Afghanistan	PRK-1-1	10.1
	PRK-3-1	11.3
	PRK-4-1	14.2
Uto pegmatites (LCT only), Sweden	UTO-1-1	11.9
	UTO-2-1	9.3

Table 5. List of LCT pegmatites samples and their measured $\delta^{18}O_{quartz}$ values.

A

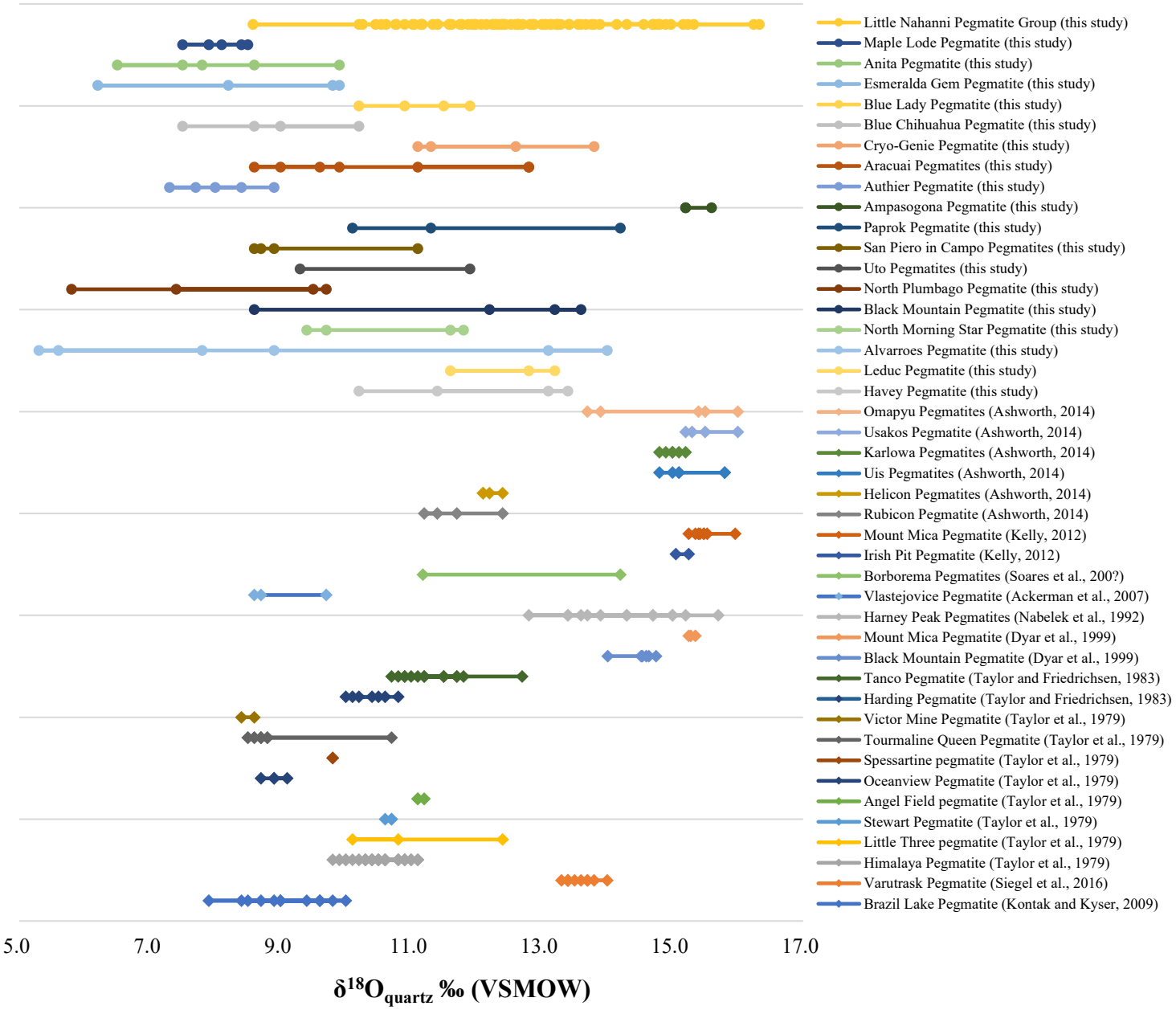
Little Nahanni Pegmatite Group (this study)
Maple Lode Pegmatite (this study)
Anita Pegmatite (this study)
Esmeralda Gem Pegmatite (this study)
Blue Lady Pegmatite (this study)
Blue Chihuahua Pegmatite (this study)
Cryo-Genie Pegmatite (this study)
Aracuai Pegmatites (this study)
Authier Pegmatite (this study)
Ampasogona Pegmatite (this study)
Paprok Pegmatite (this study)
San Piero in Campo Pegmatites (this study)
Uto Pegmatites (this study)
North Plumbago Pegmatite (this study)
Black Mountain Pegmatite (this study)
North Morning Star Pegmatite (this study)
Alvarroes Pegmatite (this study)
Leduc Pegmatite (this study)
Havey Pegmatite (this study)
Omapyu Pegmatites (Ashworth, 2014)
Usakos Pegmatite (Ashworth, 2014)
Karlowa Pegmatites (Ashworth, 2014)
Uis Pegmatites (Ashworth, 2014)
Helicon Pegmatites (Ashworth, 2014)
Rubicon Pegmatite (Ashworth, 2014)
Mount Mica Pegmatite (Kelly, 2012)
Irish Pit Pegmatite (Kelly, 2012)
Borborema Pegmatites (Soares et al., 200?)
Vlastejovice Pegmatite (Ackerman et al., 2007)
Harney Peak Pegmatites (Nabelek et al., 1992)
Mount Mica Pegmatite (Dyar et al., 1999)
Black Mountain Pegmatite (Dyar et al., 1999)
Tanco Pegmatite (Taylor and Friedrichsen, 1983)
Harding Pegmatite (Taylor and Friedrichsen, 1983)
Victor Mine Pegmatite (Taylor et al., 1979)
Tourmaline Queen Pegmatite (Taylor et al., 1979)
Spessartine pegmatite (Taylor et al., 1979)
Oceanview Pegmatite (Taylor et al., 1979)
Angel Field pegmatite (Taylor et al., 1979)
Stewart Pegmatite (Taylor et al., 1979)
Little Three pegmatite (Taylor et al., 1979)
Himalaya Pegmatite (Taylor et al., 1979)
Varutrask Pegmatite (Siegel et al., 2016)
Brazil Lake Pegmatite (Kontak and Kyser, 2009)
5.0
7.0
9.0
11.0
13.0
15.0
17.0
δ18Oquartz ‰ (VSMOW)

1091

1092

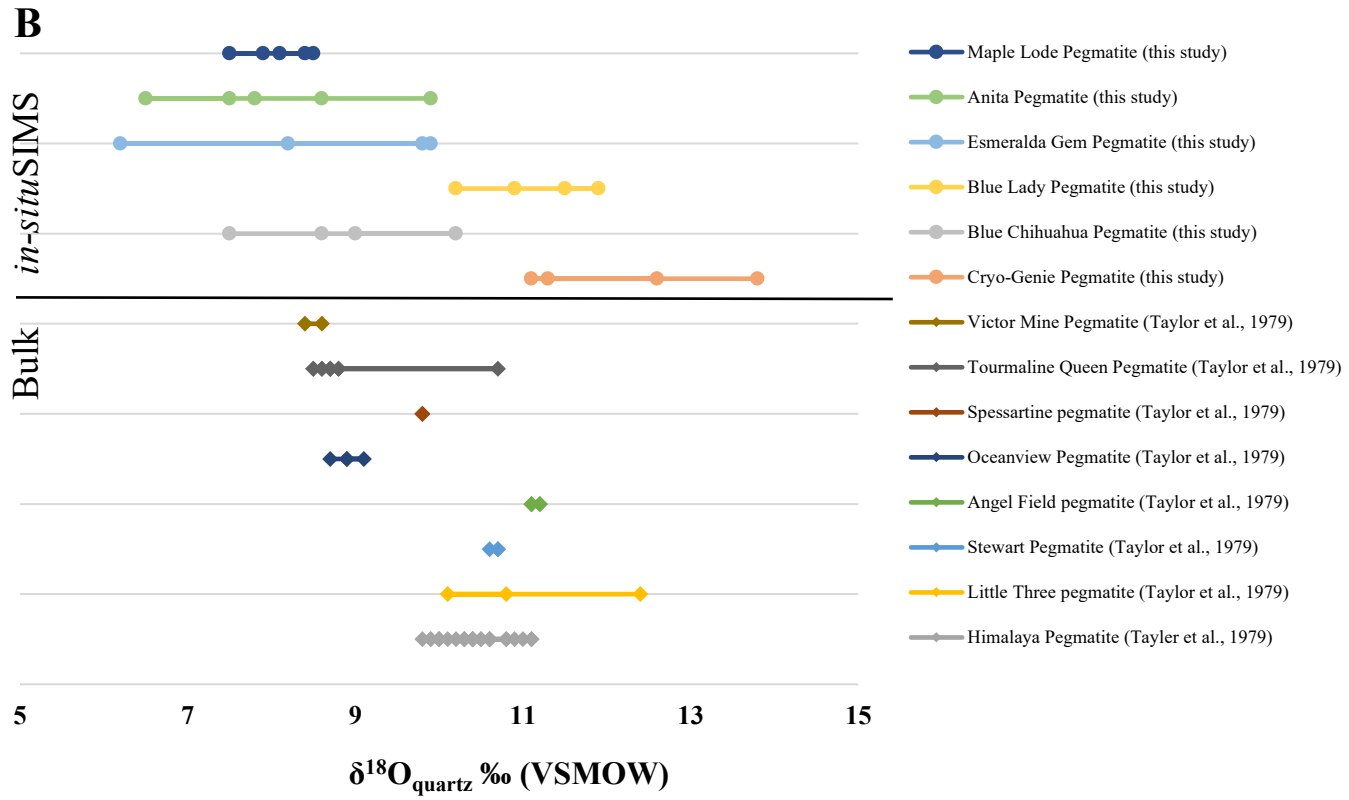

Fig. 6. A. Compilation of $\delta^{18}O_{quartz}$ values from this study and the literature. Circles = *in-situ* SIMS analysis, diamonds = bulk analysis of mineral separates. See legend for references. B. Comparison of $\delta^{18}O_{quartz}$ values from the Cretaceous Southern California pegmatites using bulk (literature) *versus in-situ* SIMS (this study). Note that analytical error is ~ ± 0.3‰ for bulk analyses and ~ ± 0.8‰ for SIMS analyses.

1107

1108

1109

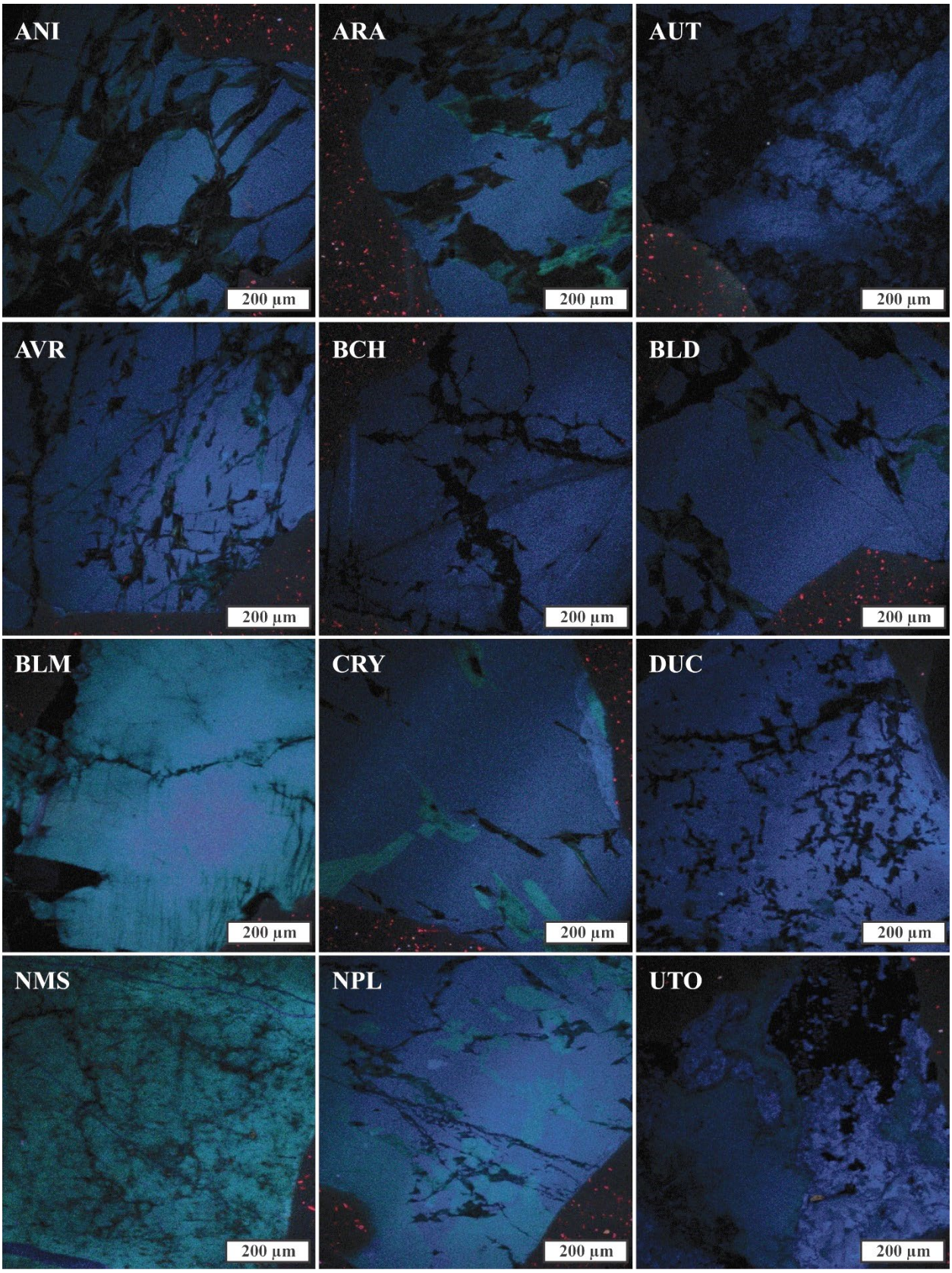
ANI
200 µm
ARA
200 µm
AUT
200 µm
AVR
200 µm
BCH
200 µm
BLD
200 µm
BLM
200 µm
CRY
200 µm
DUC
200 µm
NMS
200 µm
NPL
200 µm
UTO
200 µm

1110

1111 Figure 7. CL images of quartz samples from various LCT pegmatites showing the presence of
1112 abundant secondary features and multiples generations of quartz. Note the occurrence of shadow
1113 effects which are artifacts of the imaging. See Table 5 for abbreviations. Note that all images show
1114 variable degrees of post-crystallization overprinting indicted by the dull to dark zones along
1115 irregular fractures. Note that the brightness (+20%) and contrast (-20%) of the pictures were
1116 modified for this figure.

1117

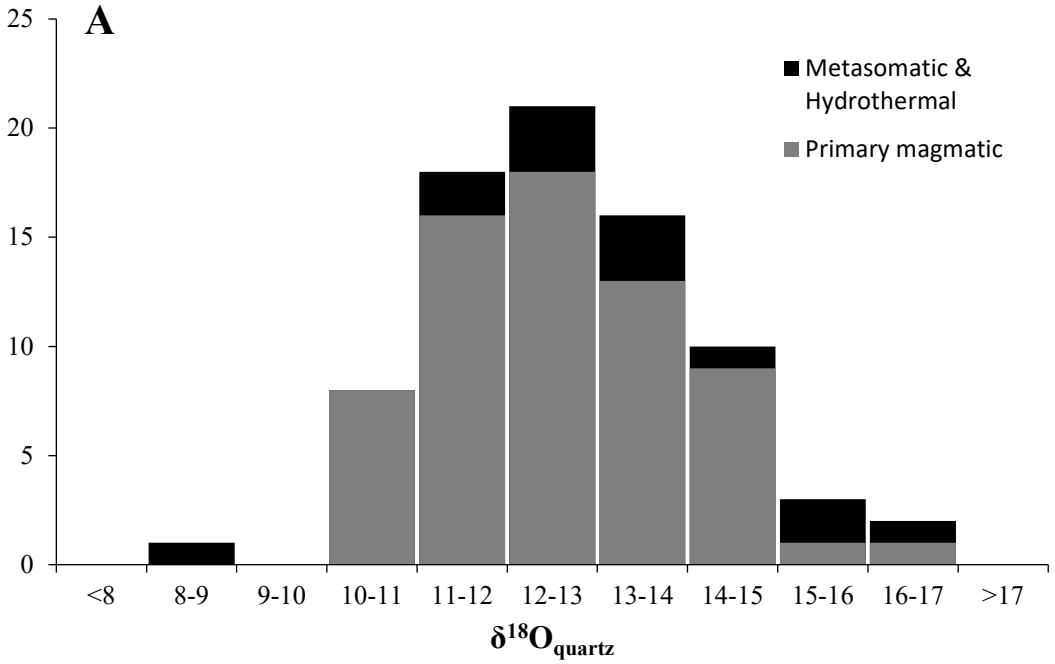

1118

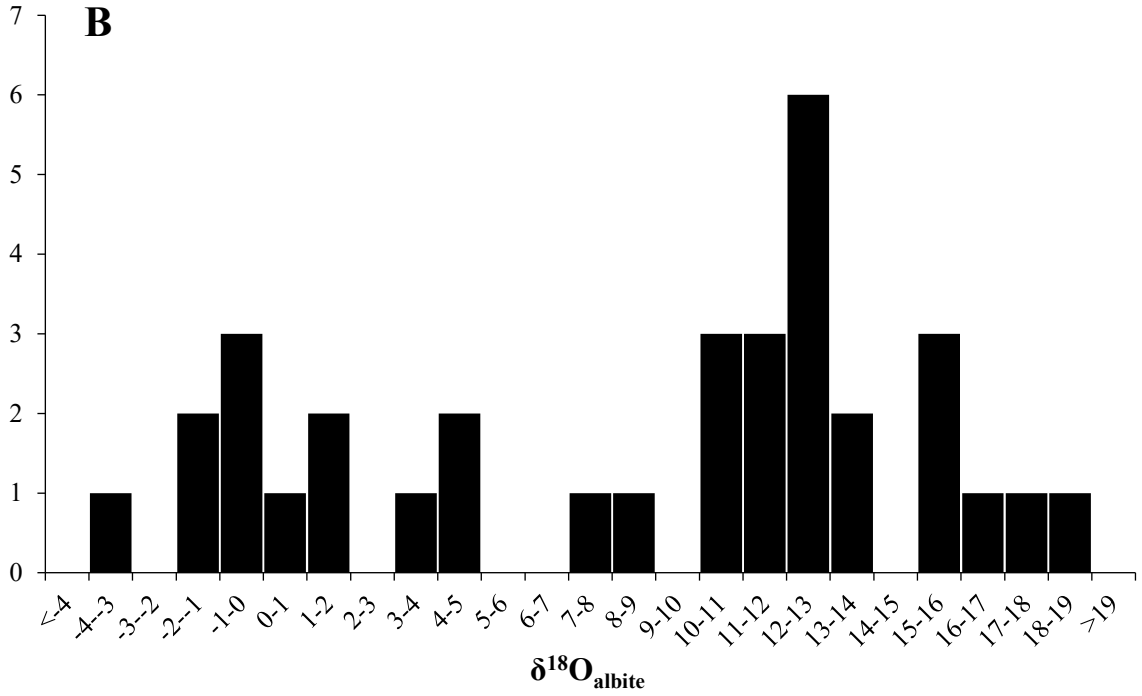

Fig. 8. Histograms showing the distribution of $\delta^{18}O$ values for quartz (A) and albite (B). A) Most $\delta^{18}O$ values for magmatic quartz fall between +10 and +15‰. Note that the amount of magmatic *versus* metasomatic quartz samples does not reflect their proportion at the LNPG, as magmatic quartz was targeted to address the source of the melt. B) $\delta^{18}O$ values for albite exhibit a particularly large range, including some exceptionally low values (e.g. -3‰). Note that it was not possible to differentiate between magmatic and metasomatic albite due to the abundance of secondary features (e.g. dissolution features, fluid inclusions) in every grain and the lack of a CL response. See text for discussion.

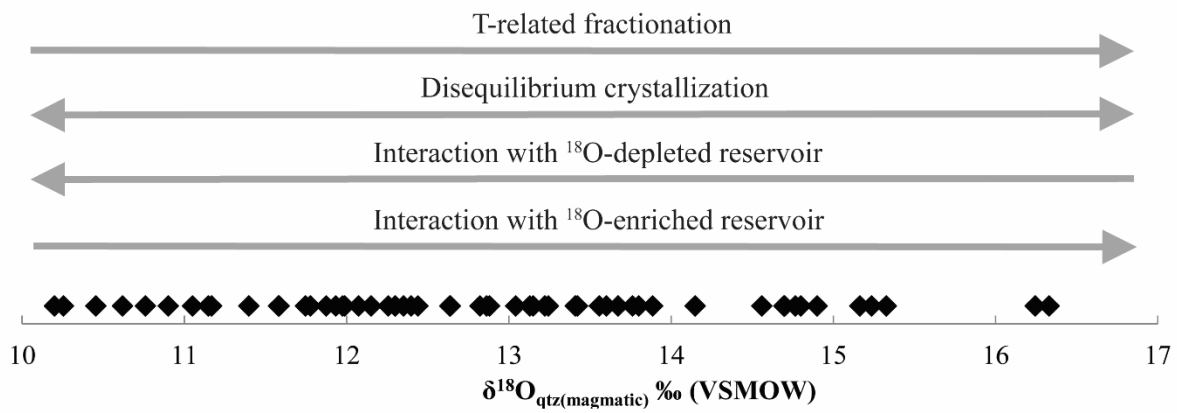

1130

1131 Fig. 9. Schematic diagram showing the various scenarios used to explain the large range of $\delta^{18}O$

1132 values in fresh magmatic quartz. See text for discussion.

1133

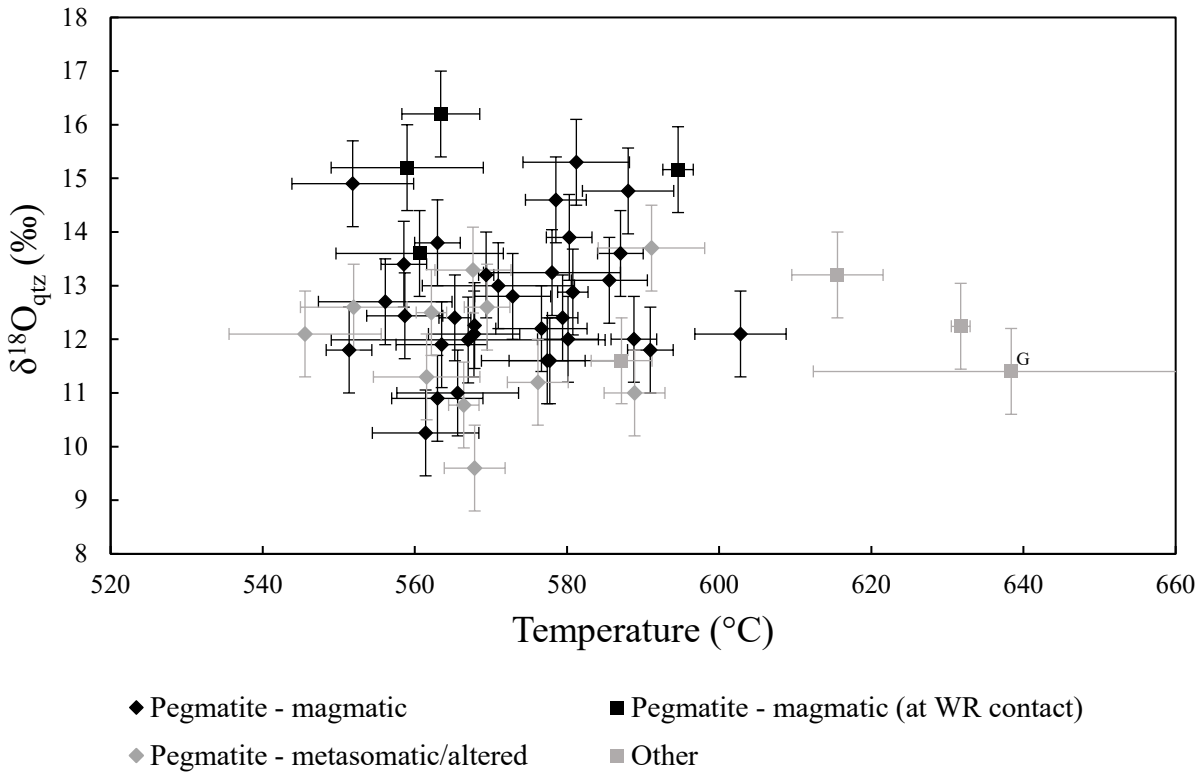

1134

Fig. 10. Plot of $\delta^{18}O_{quartz}$ values versus temperature of quartz formation based on TitaniQ (see Fig. 4 and text). "Other" = hydrothermal veins associated with the pegmatite and a sample of granite, denoted with the letter "G". See text for discussion.

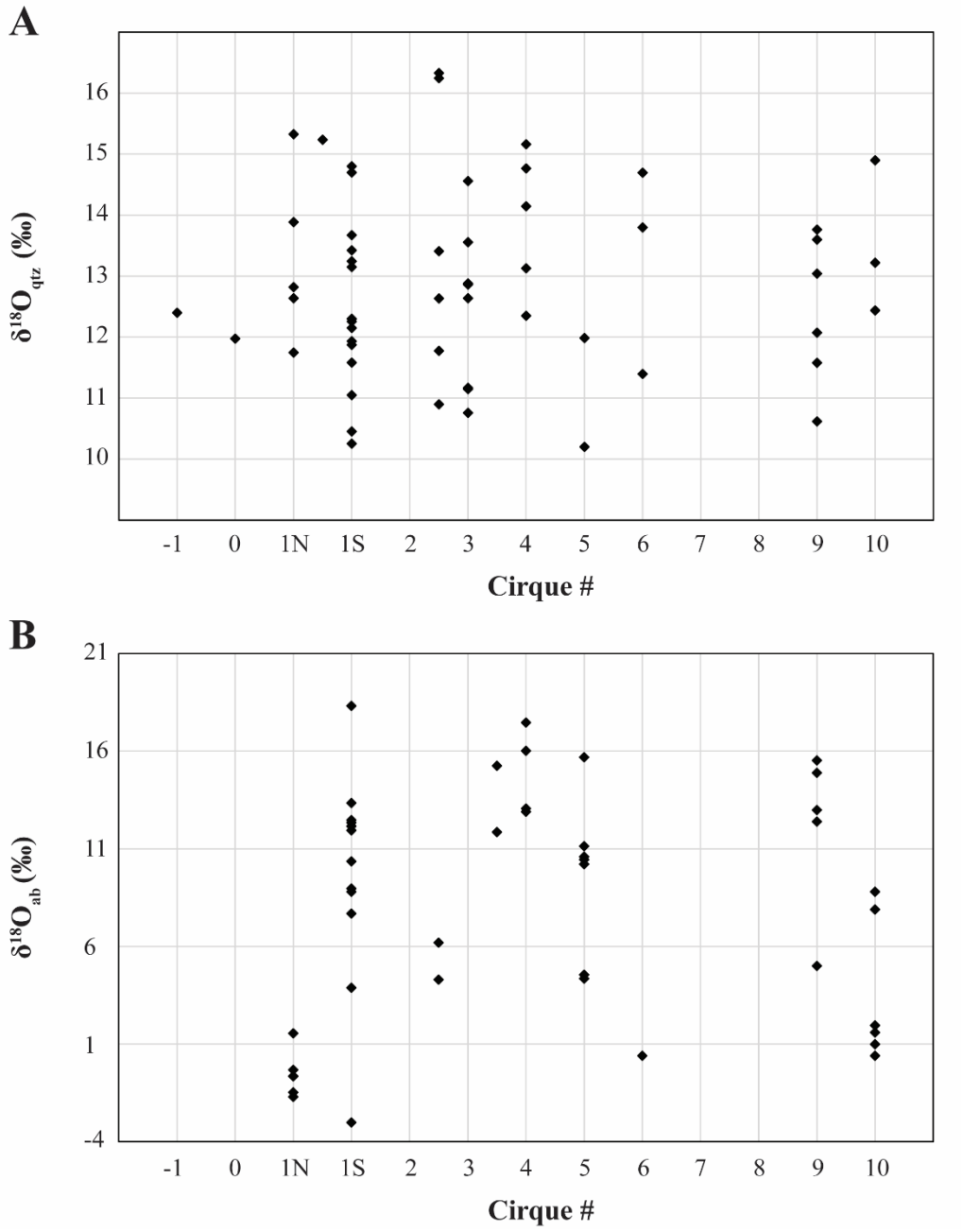

Fig. 11. A) $\delta^{18}O_{quartz}$ values plotted by location (i.e., per cirque). B) $\delta^{18}O_{albite}$ values plotted by location (i.e., per cirque). Note that data plotted between cirques represent samples collected on ridges. See Figure 1 for cirques numbers and thus locations.

Sample	ΔQtz-Kf (‰)	ΔQtz-Ab (‰)	ΔQtz-Ms (‰)	ΔQtz-Bt (‰)	ΔMs-Ab (‰)	ΔQtz-Gt (‰)	ΔMs-Cal (‰)	T (°C) (Bottinga & Javoy 1973)	T (°C) (Zheng 1993a)	T (°C) (Chacko et al. 1996)
07-15		-3.6 -5.1							-- --	
07-28				1.5				--		
07-32		-0.6 2.7							-- --	
07-40		14.3							--	
07-42	1.8 0.4								439 --	
07-45	4.1								--	
07-46		11.2	-1.5		12.7			--	--	--
L-1	5.3								--	
L-2	5.1								--	
L-8		-1.5 3.3 -0.3 4.5							-- -- -- --	
L-9		1.3 -3.6				4.0			565 -- 610	
L-13							-2.2			390
L-14					4.4			--		
C10-C		7.0 6.1 12.9 13.9							-- -- -- --	
C10-D		13.9 12.7 10.1 8.9 8.2 7.0	5.5 1.7 -0.2		8.4 7.2			-- --	-- -- -- -- -- --	-- 630 --
254		-0.2 -5.5							-- --	
11-01		2.4 1.4							-- 527	
08-01		4.7 1.5 1.5 -1.7							-- 492 492 --	
08-30					0.1 -0.1			-- --		
08-40		-3.4 -0.9							-- --	
08-42			1.9							582
08-43		-1.2 -3.7 0.7 -1.8							-- -- -- --	
08-79			5.6							--

1157

Table 6. Summary of measured mineral-mineral Δ values and corresponding temperatures using calibrations of Bottinga and Javoy (1973), Zheng (1993a) and Chacko et al. (1996). Dashes means that the calculated temperature falls outside of the 300-700°C range. See Table 1 for sample numbers. Abbreviations: Ab = albite; Bt = biotite; Cal = calcite; Gt = garnet; Kf = K-feldspar; Ms = muscovite; Qtz = quartz.

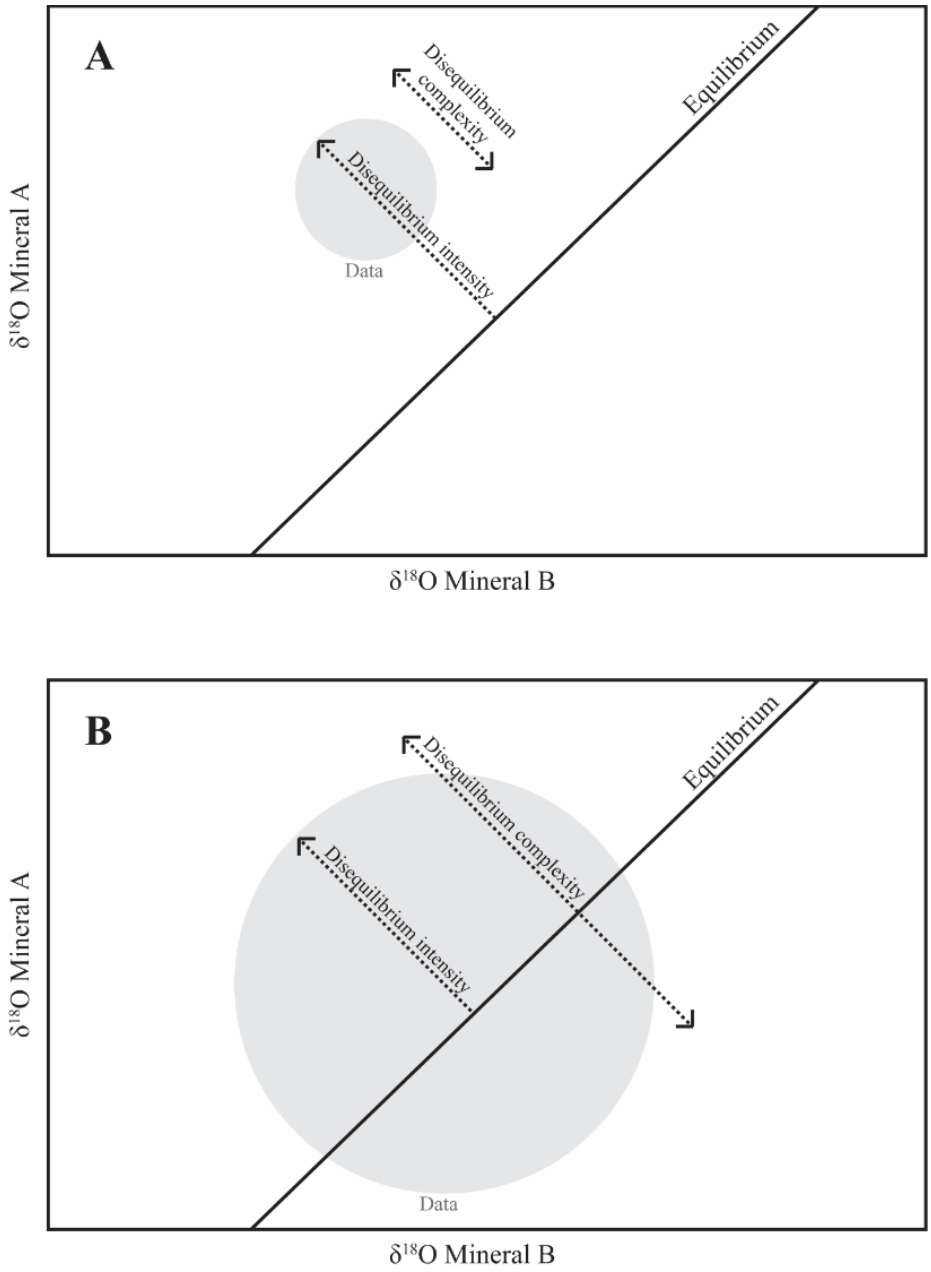

Fig. 12. Schematic representation of the concept of isotopic disequilibrium complexity (i.e. $\Delta_{A\text{-}B}$ range) and disequilibrium intensity (i.e. max $|\Delta_{A\text{-}B}|$ measured – equilibrium $|\Delta_{A\text{-}B}|$). Both scenarios A and B have the same degree of disequilibrium intensity (same arrow length), but different degree of complexity. Scenario A represents a simple case of acute disequilibrium, which can be explained by a single process or event enriching mineral A and/or B in ^{18}O. Scenario B represents

a complex case of acute disequilibrium, which has to be explained by multiple processes and/or events resulting in both enrichment and depletion of both minerals A and B.

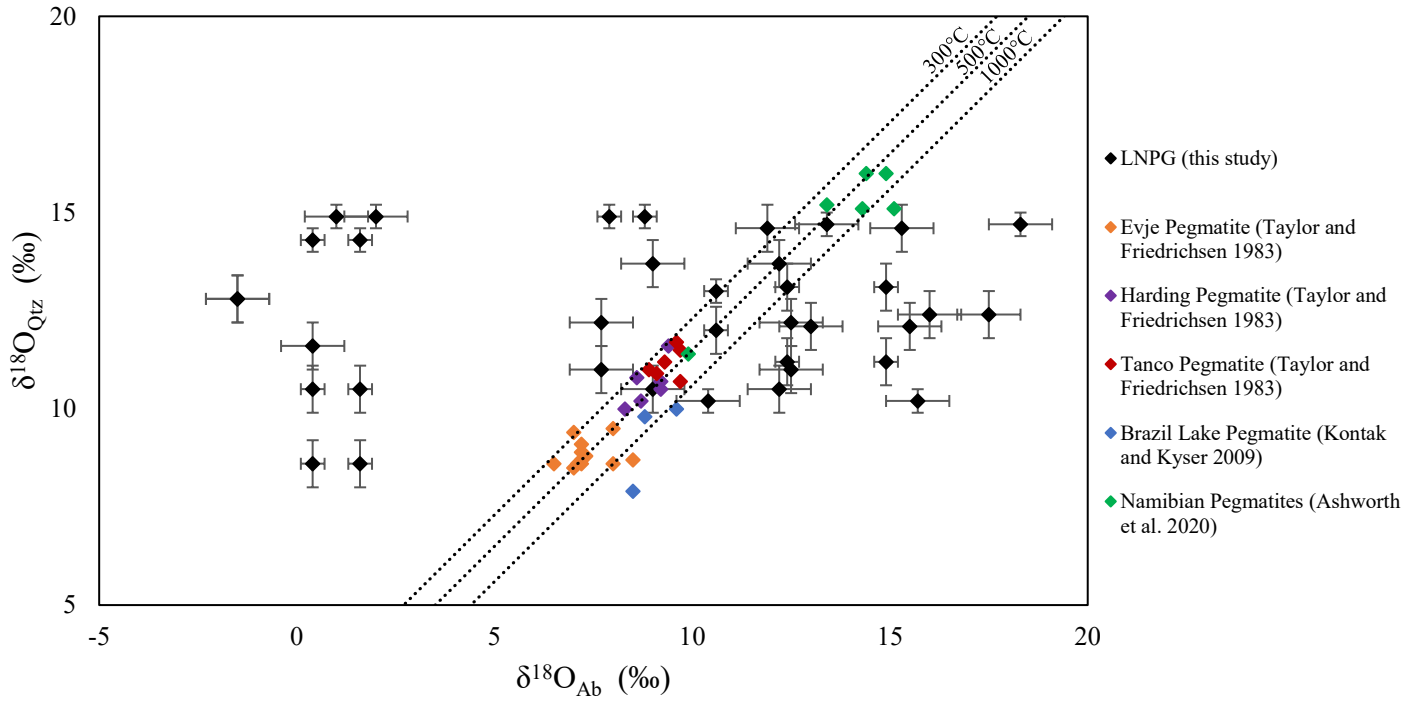

Fig. 13. Plot of $\delta^{18}O_{quartz}$ versus $\delta^{18}O_{albite}$ values for samples where both were analyzed (see Table 6). Equilibrium lines at 300, 500 and 1000°C were calculated using the fractionation factor of Zheng (1993a). The results for quartz-albite pairs from other LCT-type pegmatites are shown for comparison. See text for discussion.

Sample	$\delta^{18}O$	$\delta^{18}O_{H2O}$ *(Zheng 1993a)*						$\delta^{18}O_{H2O}$ *(Zheng 1993b)*		
		Albite			K-feldspar			Muscovite		
		500°C	**400°C**	**300°C**	**500°C**	**400°C**	**300°C**	**500°C**	**400°C**	**300°C**
07-15-01	16.0	14.7	13.6	11.6						
07-15-02	17.5	16.2	15.1	13.1						
07-32-01	15.3	14.0	12.9	10.9						
07-32-02	11.9	10.6	9.5	7.5						
07-36A-01	-0.6	-1.9	-3.0	-5.0						
07-36A-02	-0.6	-1.9	-3.0	-5.0						
07-36B-01	-0.3	-1.6	-2.7	-4.7						
07-36B-02	-1.7	-3.0	-4.1	-6.1						
07-40-01	-1.5	-2.8	-3.9	-5.9						
07-40-02	1.5	0.2	-0.9	-2.9						
07-46	0.4	-0.9	-2.0	-4.0						
C10-C-01	2.0	0.7	-0.4	-2.4						
C10-C-02	1.0	-0.3	-1.4	-3.4						
C10-C-03	8.8	7.5	6.4	4.4						
C10-C-04	7.9	6.6	5.5	3.5						
C10-D-01	0.4	-0.9	-2.0	-4.0						
C10-D-02	1.6	0.3	-0.8	-2.8						
08-01-01	9.0	7.7	6.6	4.6						
08-01-02	12.2	10.9	9.8	7.8						
08-13-01	10.4	9.1	8.0	6.0						
08-13-02	12.3	11.0	9.9	7.9						
08-30-01	13.1	11.8	10.7	8.7						
08-30-02	12.9	11.6	10.5	8.5						
08-40-01	15.5	14.2	13.1	11.1						
08-40-02	13.0	11.7	10.6	8.6						
08-43-01	14.9	13.6	12.5	10.5						
08-43-02	12.4	11.1	10.0	8.0						
08-72-01	6.2	4.9	3.8	1.8						
08-72-02	4.3	3.0	1.9	-0.1						
11-01	10.6	9.3	8.2	6.2						
#85-01	11.1	9.8	8.7	6.7						
#85-02	10.2	8.9	7.8	5.8						
#254-01	10.4	9.1	8.0	6.0						
#254-02	15.7	14.4	13.3	11.3						
#394-01	4.6	3.3	2.2	0.2						
#394-02	4.4	3.1	2.0	0.0						
#440	5	3.7	2.6	0.6						
Leise2008-01	12.0	10.7	9.6	7.6						
Leise2008-02	12.2	10.9	9.8	7.8						
L-5-01	-3.0	-4.3	-5.4	-7.4						
L-5-02	3.9	2.6	1.5	-0.5						
L-8-01	12.5	11.2	10.1	8.1						
L-8-02	7.7	6.4	5.3	3.3						
L-9-01	13.4	12.1	11.0	9.0						
L-9-02	18.3	17.0	15.9	13.9						
L-14	8.8	7.5	6.4	4.4						
07-42-01	13.8				12.7	11.6	9.3			
07-42-02	12.4				11.3	10.2	7.9			

07-45	9.5		8.4	7.3	5			
L-1	9.5		8.4	7.3	5			
L-2	7.2		6.1	5	2.7			
L-11	6.8		5.7	4.6	2.3			
07-46	13.1					13.8	13.1	11.6
08-22	10.4					11.1	10.4	8.9
08-30	13					13.7	13	11.5
08-42	12.9					13.6	12.9	11.4
C10-D	8.8					9.5	8.8	7.3
#362	11.6					12.3	11.6	10.1
L-13	12.6					13.3	12.6	11.1
L-14	13.2					13.9	13.2	11.7

Table 7. Calculated values of $\delta^{18}O_{H2O}$ assuming equilibrium with feldspars and muscovite at 300, 400 and 500°C using fractionation factors from Zheng (1993a, b).

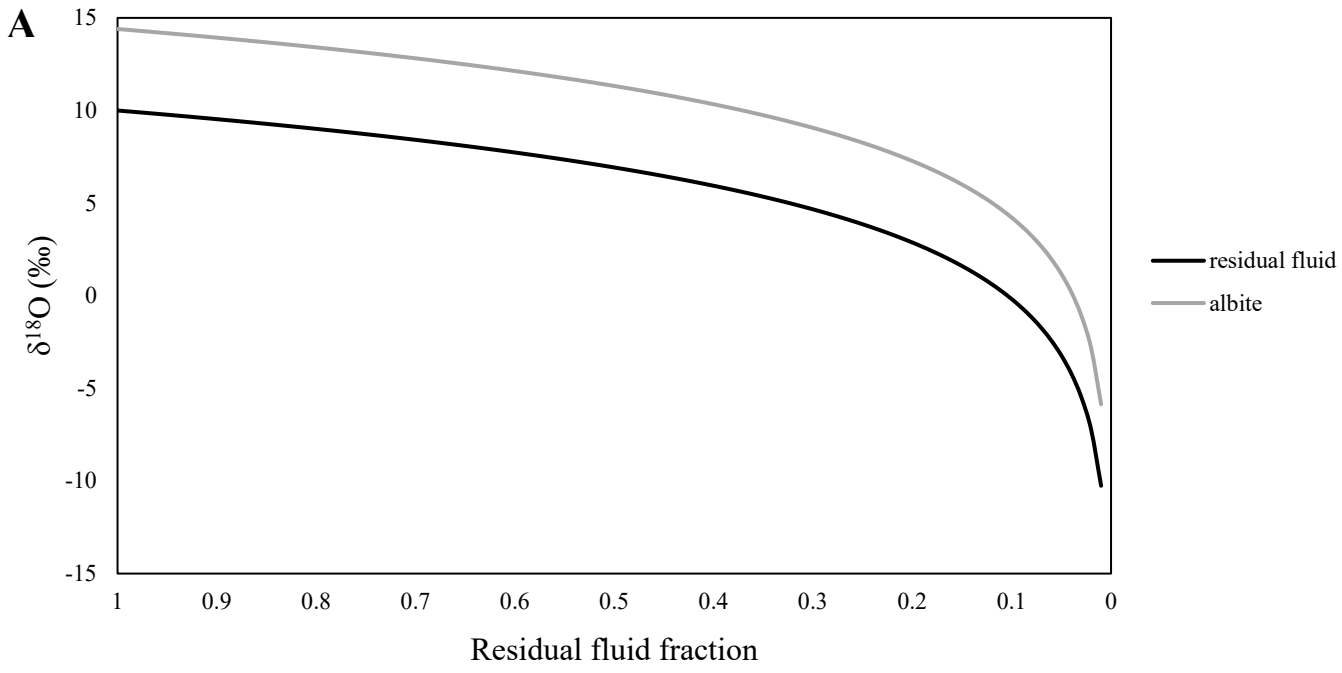

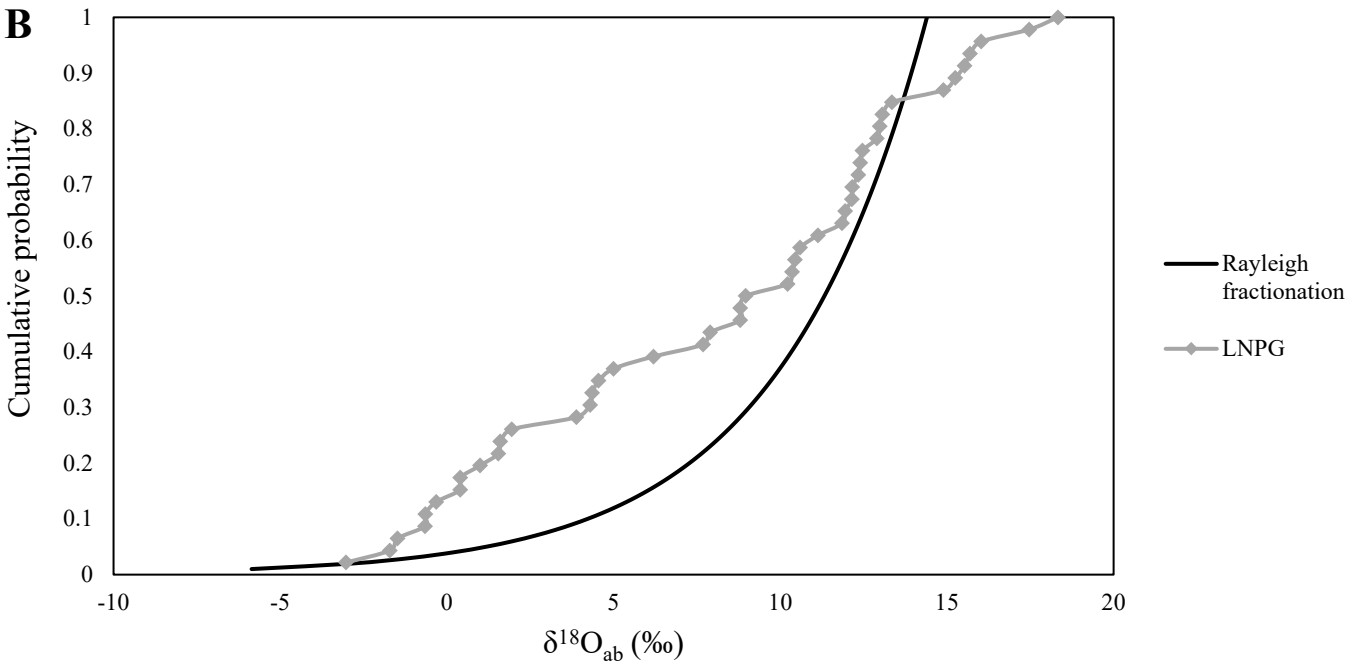

Fig. 14. A) Rayleigh fractionation model for a fluid with an initial $\delta^{18}O$ value of +10‰ and albite forming from this fluid at 300°C using albite-H_2O fractionation factor from Zheng (1993a). B) Cumulative probability plot of the Rayleigh fractionation model (see A) and LNPG $\delta^{18}O_{albite}$ data.

Chapter 4

Unraveling 800 Ma of pegmatite formation in the western Grenville Front Tectonic Zone near Sudbury, Canada

Jérémie D. Pfister [a], Daniel J. Kontak [a], Jeffrey H. Marsh [a]

[a] *Harquail School of Earth Sciences, Laurentian University, Sudbury, Ontario P3E 2C6, Canada*

Submitted and accepted with revision to Precambrian Geology

Abstract

The origin of pegmatites has been at the core of petrological research for decades, but despite much effort their origin remains controversial – protracted fractionation of a causative felsic magma versus anatexis. To address the latter, here we present the results of U-Pb analyses (zircon (n=774), monazite (n=230), xenotime (n=295)) for 32 well characterized pegmatites from an extensive swarm of felsic dike rocks, along a 12 km transect on Highway 69 ca. 12 km south of Sudbury (Ontario, Canada) in the westernmost part of the Grenville Front Tectonic Zone (GFTZ). Collectively these rocks exhibit a remarkably large morphological, textural and mineralogical variation related to the crystallization of three distinct pegmatite-forming events that span 800 Ma. Th derived concordant U-Pb ages of the dated phases coincide with the late Paleoproterozoic (*ca*. 1740 Ma) Yavapai orogeny, the Mesoproterozoic (*ca*. 1450-1430 Ma), Chieflakian event, and the early Neoproterozoic (*ca*. 1000-970 Ma) Grenville orogeny. Field observations and related geochemical data suggest the two older events are genetically related to regional magmatism (*i.e*., fractionation of a progenitor), whereas the Neoproterozoic pegmatites were generated via partial melting of appropriate source-rocks at depth. The data therefore support a duality of models for pegmatite genesis. We emphasize the important role of imaging (CL and BSE) as an integral part of our protocol, as this revealed widespread coupled dissolution-precipitation (CDP) replacement textures and metamictization in both zircon and xenotime, the latter due to high U contents (*i.e.*, >1000 pm). Interestingly, the Neoproterozoic pegmatites show similar U(±Th), Nb(±Ta) and REE enrichments like their contemporaneous Sveconorwegian counterparts. Finally, many zircon record U-Pb system resetting at *ca*. 220-200 Ma which is possibly related to the far-field effects of the early Central Atlantic Magmatic Province (CAMP) magmatism related to the opening of the Atlantic Ocean.

1.0 Introduction

Granitic pegmatites and their equivalent fine-grained dikes are considered to originate either *via* fractionation of a progenitor melt (*e.g*. Cerny 1991, London 2008) or partial melting of appropriate source-rocks during high-grade regional metamorphism (*e.g*. Fuchsloch et al. 2018; Konzett et al. 2018; Müller et al. 2022; Rosing-Schow et al. 2023). As these processes relate to large-scale tectono-magmatic events (*e.g.*, Martin and De Vito, 2005), it is paramount to differentiate between primary *versus* secondary features and mineral phases in pegmatites, particularly where the latter are used for geochronology. Furthermore, pegmatites are high aspect-ratio systems (London, 2008) and therefore susceptible to post-emplacement fluid:rock interaction that can occur on a wide range of timescales (i.e., from co-temporal with pegmatite emplacement to hundreds of millions of years after crystallization). The challenge of identifying and dating these events necessitates careful integration of petrography with imaging (*i.e.*, cathodoluminescence (CL), back-scattered electron (BSE)), which therefore needs to be a protocol in such studies. Important advances in instrumentation that aid in resolving the latter issue is in *in-situ* analyses, coinciding with the advent of petrochronology (*e.g.*, Kylander-Clark et al., 2013; Engi, 2017), that provides simultaneous determination of geochronological ages and trace element concentrations. It is now possible chemically fingerprint events associated with different stages of mineral growth and equate these to regional scale tectono-magmatic phenomenon. The latter is of particular relevance where complex geological histories are identified in metamorphic terranes (*e.g.*, Marsh et al., 2012; Culshaw et al., 2016).

The Highway 69 granitic pegmatite swarm located in the western Grenville Province ca. 12 km south of Sudbury, Ontario, Canada, provides an excellent field area to study the contrasting modes of pegmatite petrogenesis. As part of our extensive field and geochemical studies of these rocks along a 12 km transect of the swarm focused on resolving their diverse petrographic, geochemical and textural features (van Walraven, 2011; Lorenzo, 2017; Lorenzo and Kontak, 2017; Kontak 2017), we conducted an extensive program involving U-Pb dating of accessory phases (zircon, monazite and xenotime) in order to ascertain the timing of both primary versus secondary events and thus address relevant petrogenetic issues. In addition, the trace-element contents of these phases, in particular their chondritic-normalized REE patterns (REE_{CN}) (McDonough and Sun, 1995), are used to assess the geochemical fingerprint of the different suites. The data reveals a complicated protracted history derived from a mixture of xenocrystic, magmatic, and metasomatic sources.

2.0 Geological Background

2.1 Regional Geological Setting

The study area is located 12 km south of Sudbury, Ontario, Canada (Fig. 1) in the southern part of the Canadian Shield, within the Grenville Province which is southeast of its juncture with the Superior and Southern provinces (Fig. 1). Specifically, the area lies within the Grenville Front Tectonic Zone (GFTZ), where the Grenville Province has been thrusted northwards over the Southern Province and possibly even the Superior Province (Craddock et al., 2013).

The Superior Craton locally consists of the ca. 2750-2675 Ma granite-greenstone lithologies of the Wawa-Abitibi terrane (Ayer et al., 2002), including the 2711 Ma high-grade Levack tonalite gneisses (Petrus et al., 2015). These rocks are exposed ca. 10 km to the north of

1294 the GFTZ near Sudbury, and are overlain by Paleoproterozoic supracrustal rocks of the Huronian
1295 Supergroup closer to the Grenville Front.

1296 The Southern Province comprises the Paleoproterozoic (*i.e.*, 2452 Ma; *e.g.*, Ames et al.,
1297 2008; Craddock et al., 2013; see Petrus et al. (2015) for recent summary) metavolcanic rocks and
1298 metasedimentary rocks of the Huronian Supergroup, which were deposited along the southern
1299 margin of the Superior Craton during its transition from rifted to passive continental margin
1300 (Craddock et al., 2013). The local timing of the Blezardian orogeny was constrained by bracketing
1301 deformation in the Creighton pluton which yielded ages of 2415 to 2219 Ma (Raharimahefa et al.,
1302 2014). The event is recorded as large anticlines and synclines in the Southern Province west of the
1303 Sudbury impact structure (Riller et al., 1999). The southern part of the Southern Province was later
1304 reworked during the younger *ca.* 1.7 Ga Yavapai orogeny, which is associated with regional
1305 granitic magmatism, including the 1744 ± 29 Ma Eden Lake Complex about 10 km NW of the
1306 study area (Raharimahefa et al., 2014). Both the Superior Craton and the overlying Southern
1307 Province are cross-cut by olivine diabase dikes of the 1238 ± 4 Ma Sudbury Swarm (Krogh et al.,
1308 1987), thus providing an important reference marker for characterizing subsequent Grenvillian
1309 deformation.

1310 In the area hosting the Highway 69 pegmatite swarm, the Grenville province consists of
1311 various packages of locally migmatitic amphibole-rich orthogneisses and biotite-rich paragneisses,
1312 as well as gneissic granite and minor quartzite, all metamorphosed to upper-amphibolite grade
1313 (Thomson, 1959; Lumbers, 1976a; Ames et al., 2008). These rocks, as well as many of the cross-
1314 cutting dikes, are generally oriented SW-NE, parallel to the trend of the Grenville Front (Fig. 2).
1315 This NE trend reflects the dominance of the youngest penetrative deformation in the area which is
1316 constrained to between 1100 and 900 Ma based on K-Ar and Rb-Sr dating of pegmatite-hosted

muscovite (see data and references in Fig. 2). The NE-trending fold axes and related penetrative fabric both increase in intensity to the NW towards the Grenville Front (Fig. 2).

In addition to the aforementioned gneisses, several mafic and felsic intrusions occur proximal the study area and include (see Fig. 2 for relevant locations and references): 1) the *ca*. 1.74 Ga Wanapitei mafic complex; 2) the undated mafic Cleland stock; 3) the *ca*. 1.74 Ga Eden Lake granitic complex; 4) the *ca.* 1.74 Ga Estaire granitic pluton; 5) the *ca*. 1.74 Ga (?) Daisy Lake granitic pluton; 6) the *ca*. 1.45 Ga Chief Lake granitic complex; and 7) a few, small undated granitic plutons located W and NW of the hamlet of Wanup. Despite a lack of detailed study, several pegmatites have been dated since the 1950s, collectively yielding ages that range from *ca*. 1880 Ma to 910 ± 70 Ma (summary in Fig. 2). These plutons, pegmatites and the metamorphosed country rocks are associated with the three major tectono-metamorphic events in the study area: 1) the *ca*. 1.7 Ga Yavapai orogeny (Raharimahefa et al., 2014); 2) the *ca*. 1.4 Ga Chieflakian event (Krogh, 1994; Fan, 1995; Davidson, 2001); and 3) the *ca*. 1.0 Ga Grenville orogeny (Krogh, 1994; Carr et al., 2000; Rivers et al., 2002; Ames et al., 2008).

2.2 The Highway 69 Pegmatite Group

While granitic pegmatites are not uncommon in this part the GTFZ (*e.g.*, Hewitt, 1952; Lumbers, 1976a, 1976b; Easton and Murphy, 2000; Easton and TerMeer, 2004), there is a notably higher concentration of such rocks near the local communities of Wanup and Estaire (Figs. 2, 3). These pegmatites are notable for their elevated concentrations of U(±Th), Nb(±Ta), REE, which was observed early on resulting in the discovery of the now-discredited U-Nb mineral “toddite” (Ellsworth, 1926). Many of these pegmatites (Fig. 3) were quarried for industrial material from ca.

1910-1936 and produced an estimated ~18,000 tons of feldspar, ~750,000 tons of quartz, as well as minor quantities of garnet and micas (Spencer, 1932; Hewitt, 1952; Lumbers, 1976a). Exploration of the area included several campaigns for uranium in the 1950s and 1960s (Lumbers, 1976a), but commercial production was not economically viable.

In 2009, the extension of a major highway in this part of northern Ontario provided new and exceptional exposures of numerous pegmatites. From these exposures, a partial section (ca. 12 km) was selected for investigation with 53 sites subsequently visited and studied in varying detail. Representative examples of the pegmatites, which are typical of the road-cut exposures, are shown in Figure 4 and 5 in order to highlight their diversity, which includes: 1) strongly zoned dikes (Fig. 4A, B); 2) thin, high aspect-ratio, homogeneous pegmatites (Fig. 4C); and 3) thick poorly zoned pegmatitic dikes (Fig. 4D, E). As shown in Figure 5, the outcrops also provide excellent field relationships of cross-cutting features, thus providing the opportunity to unravel the complicated temporal evolution of the varied pegmatites, which are the focus of this study. Previous studies of these pegmatites (van Walraven, 2011; Lorenzo, 2017; Lorenzo and Kontak, 2017; Kontak 2017) collectively suggest the following: (1) exhibit a remarkably large spectrum of primary and secondary features (*i.e.*, textures, internal zoning, mineralogy); (2) might be composite (*i.e.* different generations of pegmatites); (3) are of the NYF-type (Nb-Y-F) with enrichment in Nb(±Ta), U(±Th) and Y+REE; (4) record widespread sub-solidus fluid:rock interaction which locally remobilized rare-metals mineralization (*i.e.*, Nb, Ta, Y, REE, U, Th); and (5) underwent some wallrock (WR) contamination during emplacement.

3.0 Methods

3.1 Sampling

Following on earlier studies of the pegmatite swarm noted above and our more recent extensive studies, numerous localities were visited for geochronological sampling to resolve the noted ambiguous field relationships. From the 53 sites identified in Figure 3, bulk samples of 1-6 kg were collected and the following criteria used to cull the sits and samples down for further study: 1) high abundance of least altered minerals, in particular feldspars which are particularly sensitive to sub-solidus processes (*e.g.*, Putnis, 2002; Plümper and Putnis, 2009); 2) as few secondary features as possible, such as dissolution cavities, muscovitization, pseudomorphism and crosscutting quartz-carbonate-actinolite-epidote veinlets; 3) suitably distant from contacts, to reduce influence of wall-rock contamination (inner domains of zoned pegmatites and >10 cm away from the contact in unzoned pegmatites) ; and 4) the presence of primary garnet or rare-metal (Nb, Ta, U, REE) minerals, as dateable minerals such as zircon, monazite and xenotime tend to be associated with these phases in the pegmatites based on our previous studies.

Following visual assessment of the above bulk samples, 30 of the most representative pegmatites were selected for U-Pb dating. Pegmatites that were presumed to be connected at depth (*e.g.*, pegmatites 38 and 40) or that were seen to be contiguous along strike across the highway (*e.g.*, pegmatites 10 and 43 or 15-17 and 30-36), as well as minor pegmatites (*e.g.*, <10 cm wide unzoned dikes such as pegmatites 2 and 50) were not selected. A description of each pegmatite site and the respective material sampled, in addition to the rational for inclusion in analysis are summarized in Sup. File 1. In addition to the above, six polished thin sections from four samples containing zircon, monazite and/or xenotime were also used for *in situ* U-Pb dating. Thus a total of 32 pegmatites and the Estaire granitic pluton were dated using the protocol provided below.

1384 *3.2 Preparation of heavy mineral concentrates*

1385 Selected bulk samples were prepared at the Harquail School of Earth Sciences (Sudbury,
1386 Ontario). Material was first crushed, milled and sieved to ≤1 mm. Subsequently a heavy mineral
1387 concentrate was produced for each sample using a combination of a Wilfley table and heavy-liquid
1388 separation using methylene iodide (3.3 g/cm^3). From this concentrate, magnetite (± spessartine and
1389 ilmenite) were magnetically separated. Of the 30 sample concentrates, 21 were mounted into epoxy
1390 pucks while the other nine contained too much garnet and required hand picking using a binocular
1391 microscope before mounting. These pucks were subsequently ground down using a series of grits
1392 with the final being a 10 μm paste.

1393

1394 *3.3 Characterization of concentrates, imaging and mineral identification*

1395 All of the prepared mineral concentrates were examined to identify and characterize zircon,
1396 monazite, and xenotime for dating using a scanning electron microscope (SEM) coupled to energy-
1397 dispersive spectroscope (EDS) with cathodoluminescence (CL) and back-scattered electron (BSE)
1398 imaging capability. The latter was done using a Tescan Vega 3 SEM with an integrated CL detector
1399 coupled with a Bruker EDS system with 60 mm^2 X-ray detector housed in the Harquail School of
1400 Earth Sciences. The EDS analyses were done using a 20 kV accelerating voltage, 1.2 nA beam
1401 current, working distance ranging from 15 to 18 mm and acquisition time of 3 s. BSE and CL
1402 imaging were done using a 15 kV accelerating voltage and a 1.0 nA beam current.

1403

1404 *3.4. LA-ICP-MS analyses and data processing*

LA-ICP-MS analyses were conducted at the Mineral Exploration Research Centre isotope Geochemistry Lab (MERC-IGL), Laurentian University. Laser ablation sampling was performed using a Photon Machine Analyte G2 ArF excimer laser, with the ablated aerosol split downstream of the sample cell, so that U-Pb and TE measurements could be conducted simultaneously. U-Pb isotope measurements were conducted using a Thermo Scientific Neptune Plus multicollector (MC) ICP-MS, while TE measurements were conducted using a Thermo Scientific iCap-TQ ICP-MS. The following parameters were used: (1) spot size of 25 μm (10μm for xenotime from pegmatite #24); (2) fluence rate of 2 J/cm^2; (3) repetition rate of 7 Hz; (4) carrier gases: He (cup) = 0.6 L/min, He (cell) = 0.10 L/min, Ar = 0.725 L/min, N2 = 0.008 L/min; (5) ablation duration of 30 s; (6) ablation depth of 15 μm; and (7) ablation rate of 0.5 μm/s.

Given the complexity of the observed intracrystalline zoning and age spectra for most samples, careful evaluation of the precision and reproducibility of the U-Pb analyses is critical. For the analytical uncertainty of individual analyses, the within-run variance in the measured ratios for the primary reference material (RM; OG1 (Stern et al., 2009) for zircon and KM03 (MacLachlan et al., 2004) for monazite and xenotime) was propagated into the measured (internal) uncertainty to obtain the total propagated 2SE uncertainty. No additional uncertainty was added to the $^{207}Pb/^{206}Pb$ ages, as the verification RMs consistently analyzed along with the unknowns in the MERC-IGL have no long-term excess variance in their measured $^{207}Pb/^{206}Pb$ ratios (MSWD < 1; See Horstwood et al., 2016). Multiple verification RMs were analyzed during each session to ensure accuracy of the U-Pb ratios and to demonstrate the propagated uncertainty is adequate to account for dispersion of the measured ratios (i.e., MSWD ≤ 1 for the RMs). All verification RMs yield mean ages within uncertainty of their published TIMS ages and MSWDs ≤ 1. Note that OG1 was chosen as a primary reference material as: (1) ages as old as 2.8 Ga were expected for

xenocrystic zircon; and (2) the Highway 69 pegmatite swarm is a U-enriched system, thus high U content in zircon was expected and OG1 contains high U.

The high U concentration common in many of the samples has ostensibly resulted in radiation-damaged crystal structures (metamictization) and potential for open-system chemical exchange. Thus, U-Pb data for each analysis were evaluated in terms of concordance and trace element alteration indicators, and filtered to remove data with disturbed U-Pb systematics (see diagrams C and D for each sample in Sup. File 3). The threshold values used for data filtering vary between samples (Sup. File 3), corresponding to differences in Concordia topology and U-Pb alteration indicator relations between samples, and to avoid over-filtering data that may illuminate later recrystallization events. Dates affected by Pb-loss were identified by negative correlation between age and Sr concentration (Sup. File 3). The effect of common Pb was mitigated by omitting analyses with high ^{204}Pb concentration (Sup. File 3). Finally, U-Pb ratios with discordance >10% were filtered in samples where the above alteration indicators failed to eliminate all significantly discordant data. The filter criteria used for each sample is shown displayed graphically on the geochronology results figure for each sample in supplementary file 3.

The trace element data was processed using the Internal Standard DRS method within Iolite v.4 (Paton et al., 2011). For calibration, National Institute of Standards in Technology (NIST) 610 and 612 glasses (Pearce et al., 1997) were used as primary and secondary standards, respectively. Additional secondary standards used to assess the precision and accuracy of the analyses included 91500 (zircon; Wiedenbeck et al., 2004) and USGS BCR-2G (glass; Jochum et al., 2005). Data were plotted in Concordia diagrams using the Isoplot v.4.15 software (Ludwig, 2012). Reported age errors are 2σ.

4.0 Results

4.1 Geological and mineralogical features of the pegmatites

Details from our petrological studies on the dike swarm are presented elsewhere, thus here we provide only the necessary information to give context for the dating results. In general, the pegmatites conform to simple types dominated by quartz and feldspars with locally abundant micas and a Nb-Y-F (NYF) signature (*e.g.*, Černý and Ercit, 2005); however they still exhibit a remarkably large range of both primary (morphology, textures, mineralogy) and secondary (deformation, alteration, mineralogy) features. The degree of deformation recorded in the pegmatites is quite variable and for simplicity is subdivided into three groups. Where most intense (sites 3, 47, 53; Fig. 6A, B, C), pegmatites are aligned parallel to the host rock fabric (NE-SW) and are almost entirely recrystallized with the exception of quartz cores (Fig. 6A); the latter thus attests to the original nature of these otherwise fine-grained felsic dike rocks. Where moderately deformed (Fig. 6D-G), the pegmatites contain remnant K-feldspar ± albite megacrysts (Fig. 6E, G), abundant quartz pods and/or cores, and primary micas are absent. They are also oriented parallel to the fabric in the host rock gneisses and commonly exhibit some degree of boudinage (Fig. 6D). Most frequently, however, the pegmatites are only mildly deformed (Fig. 6H, I) and exhibit significant variability in thickness, morphology, zoning, textures, and mineralogy (Fig. 4). They range from thick, strongly zoned and convoluted (Fig. 6H), to thin, homogeneous dike (Fig. 6I) which are discordant to the host rock fabric (*e.g.*, Fig. 6H, I, L, M); they consist mostly of K-feldspar, Ca-bearing albite (An_{10-20}), quartz, muscovite and/or biotite with accessory garnet, magnetite, apatite, allanite and various REE, U, Nb(±Ta) and Ti phases. Crosscutting relationships

between pegmatites are rare, but pegmatite 38, an albite-rich variety, crosscuts pegmatite 39, a moderately deformed K-feldspar - rich variety (Fig. 5).

Disequilibrium textures, particularly common in the undeformed, zoned pegmatites, include: 1) graphic intergrowths of K-feldspar and quartz (Fig. 7A) as well as garnet (*i.e.*, spessartine) and quartz (Fig. 7B); 2) dendritic quartz crystals (Fig. 7C); and 3) layers of spessartine around K-feldspar megacrysts (Fig. 7D). The graphic-like garnet-quartz intergrowth texture is rarely reported in pegmatites, but is similar to features Zhang et al. (2001) have documented in Italian pegmatites. A similar texture from Norwegian pegmatites is also documented in Fig. 2 of Müller *et al*. (2012). The presence of these diverse disequilibrium textures indicate the pegmatites underwent undercooling (*e.g.*, London, 2005, 2008; Maneta and Baker, 2014; Siberscu et al., 2017).

Finally, while these pegmatites are relatively simple and primitive with respect to their dominant mineralogy, they are enriched in: 1) HREE, which are mostly hosted in primary garnet (up to wt. %) and accessory xenotime; 2) LREE, which are mostly hosted in primary allanite (Fig. 7E), monazite (Fig. 7F) and secondary LREE fluorocarbonates; 3) Nb, which is hosted in various Nb, Ta, (±Ti, U) oxides (Fig. 7G); 4) U, which is mostly hosted in uraninite (Fig. 7H) and various U, Nb, Ti oxides; and 5) Th, which is mostly hosted in thorite (Fig. 7I). Pseudomorphs of allanite by LREE fluorocarbonates (Fig. 7J) are quite common through the entire field area.

Partial melting is common through the extent of the study area and beyond (*i.e.*, both south and north) with abundant cm- to dm-wide anatectic sweats observed in the host amphibolites and gneisses (Fig. 6J). The sweats sometime coalesce to form larger domains of leucosomes (Fig. 6K); locally such features are crosscut by the undeformed pegmatites (Fig. 6L, M).

Sparse evidence of partial melting within pegmatite dikes was also observed (Fig. 7 K-M). In detail, the zones of partial melting consist of intergranular (Fig. 7K) and intragranular (*e.g.*, along fractures; Fig. 7L, M) masses of fine-grained microcline, albite, quartz with abundant accessory chlorapatite and xenotime (Fig. 7M). These fine-grained masses often exhibit cuspate morphologies. Both the first generation (in the coarse pegmatite; Mc_I) and second generation (in the intergranular fine-grained assemblage; Mc_{II}) microcline exhibit perthitic texture and area analysis indicate relatively primitive compositions ($Or_{80}Ab_{20}$ and $Or_{82}Ab_{18}$, respectively; Fig. 7N, O) indicative of an origin from a melt rather than a hydrothermal fluid.

4.2 Cathodoluminescence (CL) and back-scattered electron imaging

Cathodoluminescence imaging of zircon reveal four distinct types: 1) those with xenocrystic cores (*e.g.,* Fig. 8A); 2) those exhibiting partial fluctuating/oscillatory zoning (Fig. 8B-F); 3) unzoned types with partial to complete metamictization and/or alteration (Fig. 8G-L); and 4) those with abundant micro-inclusions and partial re-crystallization (Fig. 8M-N). Zircon of the third type are by far the most common with two main domains separated by a bright alteration front: an original unzoned domain (*e.g.*, light grey in Fig. 8H, K, L) and a zone of amorphous (*i.e.*, metamict) material (*e.g.*, dark grey in Fig. 8G, H, K, L).

Back-scattered imaging of monazite revealed only a handful of moderately zoned grains (Fig. 8O) and instead hundreds of unzoned fresh grains (Fig. 8P, Q) among the material studied. Monazite appears bright yellow and gemmy under transmitted light microscopy; it is the freshest mineral of the three phases dated. Whereas xenotime and zircon often occur together, monazite usually occurs alone.

Back-scattered imaging of xenotime revealed two varieties in similar quantities: 1) those with minor inclusions and scarce secondary features (Fig. 8R); and 2) ones with abundant micro-inclusions and a moderate amount of secondary features (Fig. 8S). Note that some of the inclusion-rich xenotime have crystallographically-controlled thorite inclusions (Fig. 8S, T) that likely originate from exsolution of $ThSiO_4$ and $(HREE)PO_4$ from a higher T $(HREE,Th)(P,Si)O_4$ phase.

4.3 U-Pb Geochronology

Due to the general lack of zoning in the studied minerals, as was noted above, spot analyses were made in the least-fractured and inclusion-poor parts of crystals, preferably within cores. The complete analytical data are reported in Supplementary File 2 along with the resulting ages and 2σ errors. Wetherill and Tera-Wasserburg Concordia diagrams, weighted mean diagrams, and REE_{CN} plots are reported for each accessory phase from all of the dated dike samples in Supplementary File 3. In order to contextualize the results of the samples analyzed, representative examples of data are first presented and discussed below before referring to the summary of results in Table 1.

Figure 9 is an example of data for monazite from pegmatite site #47 (see Fig. 3 for location) which shows three distinct age populations, with Concordia or upper intercept ages of 1740.7 ± 5.4 Ma, 1458.4 ± 6.8 Ma, and 995.7 ± 5.3 Ma. These ages correspond to the Yavapai, Chieflakian, and Grenvillian events, as noted above. In addition, the REE_{CN} plots indicate that the Grenvillian-aged monazite grains (*i.e.,* the youngest population) are relatively enriched in HREE, in particular Y to Lu, which is not affected by discordance.

In contrast, zircon from pegmatite site #3 shows a much more complicated population distribution (Fig. 10), which we note is a common feature for many of the samples analysed. As

1538 other authors have done (*e.g.*, Villa and Hanchar, 2017), we interpret this distribution of data to
1539 reflect: 1) inheritance of ca. 2500 Ma xenocrystic zircon; 2) partial or complete resetting and/or
1540 new growth of zircon at 1432 Ma and 995 Ma relating to the later Yavapai and Grenvillian events,
1541 respectively; 3) variable amounts of incorporation of common Pb during the event at 1432 Ma that
1542 would have moved the zircon off the Concordia growth curve (green line in plot); and 4) the effect
1543 of partial resetting at ca. 200 Ma with related Pb loss (blue dashed lines on the plot).

1544 Lastly, the data for pegmatite sites #3, 6, 29 and 48 collectively illustrate a variety of
1545 concordant zircon ages at *ca*. 2500 Ma, *ca*. 1715 Ma, *ca*. 1430-1450 Ma, and *ca*. 970 to 995 Ma
1546 which, as noted already, have geological significance. In addition, however, these zircon also
1547 record variable degrees of Pb loss and/or partial resetting at ca. 200 to 220 Ma (Fig. 11).

1548 All of the age data for zircon (n = 774), monazite (n = 230) and xenotime (n = 295) from
1549 32 pegmatites and the Estaire Granite are summarized in Table 1. Based on concordant ages, the
1550 results collectively reveal five generations of zircon growth and/or resetting: 1) Neoarchean (ca.
1551 2.5 to 2.8 Ga); 2) late Paleoproterozoic (ca. 1700-1750 Ma); 3) early Mesoproterozoic (ca. 1400-
1552 1450 Ma); 4) early Neoproterozoic (ca. 950-1000 Ma); and 5) late Triassic/early Jurassic (ca. 220-
1553 200 Ma). Monazite is almost invariably early Neoproterozoic (ca. 960-1000 Ma), but a few
1554 exceptions occur with similar Meso-Paleoproterozoic timeframe as that recorded in coexisting
1555 zircon in pegmatites #12 (1719.8 ± 9.1 Ma) and #47 (1740.7 ± 5.4 Ma and 1458.4 ± 6.8 Ma). All
1556 of the xenotime analysed yielded early Neoproterozoic ages (ca. 950-1000 Ma).

1557

1558 *4.4 Trace element data*

Whereas the results of the trace-element chemistry of accessory phases are to be discussed in a separate publication focused on the geochemistry of the pegmatites, they are used here to identify disturbed U-Pb systematics, thus the data are summarized in Supplementary File 3 and Figure 12. Additionally, trace element systematics of our samples can help differentiate between stages of mineral growth and degree of concordance for each mineral population (Fig. 12). It is worth noting that all accessory phases are U-rich, thus 93% of the zircon contain >1000 ppm U, 75% of the monazite contain >1000 ppm U, and 100% of the xenotime contain >1000 ppm U (with 38% having >10,000 ppm U). These high U contents account for the metamict nature of so many zircon and, as expected, related discordant ages. It is also worth noting that metamict parts of zircon (*e.g.*, Fig. 8K, L) contain up to several wt. % Fe and Ca, which can only be accommodated *via* metamictization (Geisler et al., 2003).

5.0 Interpretation

The results of an extensive program of U-Pb dating of accessory phases in 32 pegmatites selected out of a total of 53 sites along a 12 km traverse though high-grade Paleoproterozoic para- and orthogneisses revealed the presence of many concordant ages. It is evident that the wide range of ages observed in our samples must reflect events other than simply the generation and emplacement of pegmatites, including inheritance and subsequent resetting events. In order to address the actual ages of pegmatite formation and related magmatism, each of the pegmatites containing multiple concordant ages are discussed separately below.

5.1 Pegmatites with multiple generations of accessory minerals

Several pegmatites (n = 9) yielded multiple generations of accessory minerals (see Table 1) and are discussed individually below in order to assess and interpret the data in the context of xenocrysts (*i.e.*, inheritance), autocrysts (*i.e.*, pegmatite formation), and subsequent post-pegmatite crystallization events (*i.e.*, tectono-metamorphic reworking or metasomatism) (Miller et al., 2007).

Pegmatite #1 contains a population of concordant zircon with an age of 1425.7 ± 7.8 Ma (Table 1 and Sup. File 3), as well as single grains of monazite and xenotime which yielded ages of 965.7 ± 8.0 and 968 ± 8.0 Ma, respectively. The following suggest the pegmatite is likely of early Mesoproterozoic age: 1) it is intensely deformed and aligned parallel to the host gneiss, as with many other early Mesoproterozoic pegmatites; 2) it generally lacks primary micas, a feature often observed in early Mesoproterozoic pegmatites; and 3) the dike is located closest to the ca. 1.45 Ga Chief Lake granitic complex (Figs. 2 and 3). As for the monazite and xenotime, they were either reset by or formed during regional metamorphism associated with the Grenville orogeny, the former related to the fact that REE-bearing phosphates have lower closure temperatures than zircon (Dahl, 1997; Smith and Giletti, 1997; Hodges, 2013). We also note the partial resetting of the zircon by the ca. 200 Ma event which is also seen as the incorporation of common Pb and modification of the REE_{CN} profiles with LREE enrichment in the discordant population (Sup. File 3).

Pegmatite #3 is one of the most intensely deformed pegmatites and is almost entirely recrystallized with the exception of its quartz core (Fig. 6). It lacks REE-bearing phosphates, but has three populations of concordant zircon at ca. 2.5 Ga, 1432 ± 20 Ma and 995.3 ± 5.7 Ma. The ca. 2.5 Ga zircon have weak fluctuating zoning (Fig. 8B, C) and are considered xenocrystic which suggests either the presence of Archean basement in the area or they were detrital grains inherited from paragneiss. The 1432 ± 20 Ma population consists of mostly unzoned, euhedral, grains that

1604 are variably metasomatized and/or altered. Finally, the 995.3 ± 5.7 Ma population is similar to the
1605 Mesoproterozoic population (*i.e.*, euhedral and unzoned). In addition, these two zircon populations
1606 exhibit similar REE profiles (see Sup. File 3). Lastly, that most Neoproterozoic pegmatites formed
1607 at 980-960 Ma suggests that the 995 Ma age is more likely due to peak metamorphism versus
1608 pegmatite emplacement. Considering the above, including the intensity of deformation, it is likely
1609 that this pegmatite is of Mesoproterozoic age.

1610 Pegmatite #12 has two concordant zircon at 1701 ± 12 Ma and 1381 ± 12 Ma, but most
1611 grains are discordant and fall on a discordia from ca. 950 Ma (*i.e.*, Neoproterozoic) to ca. 200 Ma.
1612 In addition is a single concordant monazite at 1719.8 ± 9.1 Ma, and a dominant population of
1613 concordant xenotime of 961.9 ± 2.6 Ma. The undeformed nature of the pegmatite and its
1614 crosscutting relationship to the host rock fabric (Fig. 6I) is thus consistent with the Neoproterozoic
1615 ages for both zircon and xenotime whereas an inheritance origin for the older zircon and monazite
1616 grains, possibly from the nearby undated Wanup granitic pluton (Fig. 2), is preferred. Again we
1617 note the LREE enrichment for the discordant zircon that record the much later ca. 200 Ma event.

1618 Pegmatite #24 exhibits clear evidence of deformation, such as sheared K-feldspar and
1619 quartz megacrysts, an internal foliation parallel to the host gneiss fabric, and evidence of partial
1620 melting (Fig. 7K-M). The zircon grains are mostly concordant and yielded an age of 1442.9 ± 6.1
1621 Ma, whereas xenotime grains in local areas of partial melting (Fig. 7M) yielded an age of 947 ±
1622 27 Ma. Thus this pegmatite was most likely emplaced in the Mesoproterozoic and subsequently
1623 underwent partial melting during the early Neoproterozoic.

1624 Pegmatite #25 is deformed, aligned parallel to the host rock fabrics, exhibits boudinage
1625 and lacks primary micas (Fig. 6D, E). It contains several concordant zircon populations: 1) ca. 2.8
1626 Ga xenocryst; 2) a small number of euhedral zircon exhibiting fluctuating zoning (Fig. 8D) and

ages of 1727 ± 52 Ma; 3) unzoned euhedral zircon of 1422.2 ± 9.9 Ma; and 4) unzoned euhedral zircon of 983.0 ± 7.0 Ma. Whereas the Archean age is attributed to inheritance and the Neoproterozoic age to resetting, both the Mesoproterozoic and Paleoproterozoic zircon have textures and CL zoning that is consistent a primary magmatic origin. A Mesoproterozoic age for pegmatite emplacement is also supported by the presence of a swarm of Mesoproterozoic pegmatites in this part of the study area. Alternatively, a Paleoproterozoic age is supported by the proximity of the ca. 1.74 Ga Estaire granite <1 km away (Fig. 2). Either of these two ages is considered plausible for emplacement of this pegmatite.

The most deformed dike in the study area, pegmatite #47, is almost entirely recrystallized, with the exception of its quartz core (Fig. 6A, B). It contains a population of inherited Neoarchean zircon (2678 ± 39 Ma) (Fig. 8A), as well as a couple of zircon yielding an age of 1662 ± 100 Ma with a discordia to ca. 200 Ma. The sample also contains three concordant populations of monazite at 1740.7 ± 5.4, 1458.4 ± 6.8 and 995.7 ± 5.3 Ma (see Fig. 9), as well as a couple of xenotime crystals yielding an age of 996.2 ± 6.5 Ma. Just like the 995.3 Ma zircon population in pegmatite #3 (see above), the 996 Ma monazite and xenotime populations in pegmatite #47 likely represent a later overprinting event rather than pegmatite emplacement, as does also the ca. 1458 Ma monazite. Considering both the Paleoproterozoic zircon and monazite populations and that the pegmatite is significantly more deformed (and re-crystallized) than any other Mesoproterozoic pegmatites, pegmatite #47 was likely emplaced in the Paleoproterozoic.

Pegmatite #48 is undeformed and intrudes the ca. 1740 Ma deformed Estaire granite. It contains a Paleoproterozoic (1714 ± 11 Ma) xenocrystic zircon, which was likely inherited from the host granite, as well as two populations of zircon at 1447.3 ± 12 and 990.9 ± 8.2 Ma. The two populations are virtually undistinguishable in terms of morphology, zoning (unzoned and partially

metasomatized/altered; see Fig. 8K) and trace elements (see Sup. File 3). Therefore, either of these two ages is considered plausible for pegmatite emplacement.

Pegmatite #49 contains two populations of concordant zircon at 1425.1 ± 5.6 and 986.4 ± 9.8 Ma with the former reflecting partial Pb loss at ca. 200 Ma. Similarly to pegmatite #48, these zircon populations are undistinguishable based on their morphology, lack of primary zoning, and their overlapping REE_{CN} patters (see Sup. File 3). Thus, both ages are plausible for emplacement of this pegmatite.

Pegmatite #53 contains a large population (n = 21) of concordant zircon at 1435.5 ± 7.2 Ma with a single anomalous zircon at 1716 ± 15 Ma. The later was likely inherited from the proximal Paleoproterozoic Estaire granite. Thus the age for emplacement of this pegmatite is Mesoproterozoic. It should be noted that this is the only pegmatite containing zoned zircon of Mesoproterozoic age (Fig. 8F).

6.0 Discussion

The four generations of accessory minerals dated at *ca*. 2.8-2.5 Ga, 1750-1700 Ma, 1450-1400 Ma and 1000-950 Ma as well as the resetting event at *ca*. 200 Ma are discussed separately to address the following issues: 1) nature of the accessory zircon, monazite and xenotime populations (*e.g.*, xenocrystic, autocrystic, altered); 2) nature of the pegmatite generating events (*i.e.*, anatectic *versus* pluton-related); and 3) nature of the tectonic events at the time of pegmatite formation (*e.g.*, Grenville orogeny, Yavapai orogeny, etc.).

6.1 The significance of different age events

The results of U-Pb age dating indicate many different ages for the accessory phases. Given that these ages are based on their concordance, they are considered to be of geological significance. We explore the implications of these results below in the context of the complex magmatic and tectonothermal history of the study area (Fig. 13).

6.1.1 The 2.8-2.5 Ga event

The population of Neoarchean-aged zircon are inferred to be xenocrysts; while there are undoubtedly no Archean pegmatites in the study area, the pegmatites containing these zircon are significantly more deformed and recrystallized than most of the pegmatite swarm. There are three possible reasons for an Archean component in their source. First, given the area is underlain by paragneisses, it is possible that detrital zircon could be sourced from assimilation of these rocks. In fact, Neo- and Mesoarchean-age zircon (*i.e.*, 2.5-3.0 Ga) are reported in equivalent metasedimentary rocks in different parts of the Grenville Province (*e.g.*, Culshaw et al., 2013, 2016; Peck et al., 2019). Second, the zircon may have been sourced from the nearby metasedimentary rocks of the Southern Province at depth, which outcrops west of the GFTZ and is bounded on its west by the Archean Superior Craton (Fig. 2). Relevant is that recent studies documented Archean zircon in these rocks (*e.g.*, Petrus et al., 2015). Third, Archean-age zircon may have been sourced at depth from the underlying Superior Craton basement, which is supported by the presence of appropriate basement rocks in this part of the GFTZ (Ames et al., 2008 and references therein) and near North Bay (Krogh, 1994).

6.1.2 The ca. 1750-1700 Ma event

Paleoproterozoic granitic intrusions are common in the study area (Fig. 2 a) which includes the ca. 1.74 Ga Eden Lake Complex (Sullivan and Davidson, 1993; Ames et al., 2008; Raharimahefa et al., 2014), the ca. 1.74 Ga Estaire pluton (this study), possibly the Daisy Lake pluton (see discussions in Davidson, 1992 and Davidson and Van Breemen, 1994), multiple granitic dikes (Krogh and Davis, 1969; La Tour and Fullager, 1986) and pegmatites (Davis et al., 1970; Krogh; 1994), as well as the Killarney Complex about 20 km southwest of the study area (Fan, 1995). While some of the Paleoproterozoic zircon (and a few monazite) dated in this study are xenocrystic (Fig. 8E), such as in pegmatites #12, #48 and #53, several are magmatic based on morphology, textures and CL zoning (Fig. 8D) and are thus considered to represent the age of dike emplacement for pegmatite #47 and possibly also pegmatite #25. Based on the abundance of granitic plutons of similar age in the area, it is likely these Paleoproterozoic pegmatites are intrusion-related, although further work is being done to confirm their petrogenetic relationship. This interval of granitic magmatism is associated with the Yavapai orogeny (Raharimahefa et al., 2014), which resulted in NW-directed regional thrusting and folding associated with crustal thickening that ultimately culminated in magmatism. We also note the relevant work of Dickin (1998) and Dickin et al. (2007) which dated multiple granitic plutons and gneisses at ca. 1.74 Ga west and south of the study area which were attributed to a plutonic overprinting and reworking of older terranes by the Killarnean ensialic arc. Note that a similar 1780-1750 Ma pegmatite-forming event related to widespread granite magmatism is also documented in Norway (Müller et al. 2022).

6.1.3 The ca. 1450-1400 Ma event

Several Mesoproterozoic intrusions are known in the area (Fig. 2), including the ca. 1.45 Ga Chief Lake Complex and the 1.45 Ga Bell Lake granite 20 km west of the study area. Both of these intrusions are associated with simple-type pegmatites (Krogh and Davis, 1969; Van Breemen and Davidson, 1988; Krogh, 1994; Raharimahefa, 2014). Most of our Mesoproterozoic zircon (± monazite) populations are magmatic (Fig. 8 F-I) and thus represent the age of pegmatite emplacement for sites #1, #3, #23, #24, #51, #53, and possibly #25, #48, and #49. These sites represent two clusters of pegmatites: 1) #1 and #3 in the northernmost part of the study area proximal to the potentially petrogenetically-related Chief Lake Complex ~5 km to the west; and 2) #23, #24, #51, and #53 (possibly #25, #48, and #49) in the southernmost part of the study area, which are not spatially associated with any exposed granitic pluton of this age. This Mesoproterozoic period of felsic plutonism, known as the Chieflakian event (*ca*. 1.5-1.45 Ga) (Krogh, 1994; Davidson, 2001; Ames et al., 2008; Rahamifahera et al., 2014), is responsible for development of some of the regional gneissic foliation, in particularly to the east of the study area (Krogh, 1994). We also note the relevant studies of Ketchum et al. (1994) and Culshaw et al. (2016), which dated an episode of high-grade tectono-metamorphism (granulite facies migmatization) at ca. 1450 Ma in the Britt and Kiosk domains of the Grenville Province southeast of the study area.

6.1.4 The ca. 1000-950 Ma event

Despite the lack of Neoproterozoic granitic plutons in the area, similar aged pegmatites are abundant based on earlier studies (Cumming et al., 1955; Shilliberg and Cumming, 1956; Davis et al., 1970; Krogh, 1994; Easton and Hrominchuk, 1999; Ames et al., 2008). As noted above, zircon, monazite and xenotime of this age are abundant in the sampled pegmatites, with zircon subdivided

into two groups: 1) a ca. 995 Ma population of zoned grains that occurs in association with monazite and/or xenotime (Fig. 8J). These are only found in the most deformed pegmatites having older zircon populations (*e.g.,* pegmatites #3 and #47); and 2) a ca. 990-960 Ma population lacking primary zoning that exhibits variable degrees of metamictization (Fig. 8K, L), alteration or containing abundant micro-inclusions (Fig. 8M, N). The ca. 995 Ma population most likely represents resetting of an older zircon domain during subsequent metamorphism, whereas the <990 Ma, high-U zircon represents a primary igneous age recording pegmatite emplacement. Most pegmatites in the study area conform to this latter group (sites 4, 5, 6, 7, 8, 9, 12, 15, 18, 19, 22, 27, 29, 32, 38, 43, 44, 45, and 42, and possibly 25, 48, and 49).

The abundant leucosomes and anatectic sweats in the host rocks in the study area were dated by Corfu and Easton (2000) at 987 ± 3 and 995 ± 3 Ma, in addition to the pegmatitic leucosome adjacent to pegmatite #6 ("P6 leuco ") which yielded an age of 981.7 ± 1.6 Ma (Table 1). Additionally, partial melting within pegmatite #24 was dated herein at 947 ± 27 Ma. The lack of any potential granitic progenitor in the area, in addition to the abundant evidence of partial melting on the regional scale, suggests the Grenvillian-aged pegmatites are not related to a progenitor pluton and instead are anatectic, thus similar to the Sveconorwegian/Grenvillian pegmatites in Norway (Müller et al., 2015; Müller et al., 2017) and other pegmatites fields (Simmons et al., 2016; Knoll et al., 2018; Webber et al., 2019). It is worth noting, however, that while the leucosomes represent *in-situ* melting, the Grenvillian pegmatites clearly crosscut and intrude the host rocks (Fig. 6L-M) and thus were generated *via* partial melting at depth (*i.e.*, the adjacent host rocks are not the source material of the pegmatitic melt).

6.1.5 The post-Grenville event

No zircon of primary igneous affiliation are identified as having a post-Grenvillian age in the present study, however several populations of zircon indicate extensive overprinting at ca. 200-220 Ma (Fig. 11). No event of this age is known in the study area, but more distal events are well documented. A potential explanation is the early rifting related to opening of the North Atlantic Ocean and widespread CAMP magmatism along eastern North America (*e.g.*, Seidler et al., 2004; Müller et al., 2008; Jourdan et al., 2009). Such resetting is not without precedent: a similar resetting of ca. 620 Ma zircon hosted in granites of the Arabian-Nubian Shield at 18 Ma has been related to fluid circulation associated with opening of the Red Sea (Geisler et al., 2003a), while resetting of ca. 900 Ma zircon in the Gavilgarh-Tan Shear Zone in central India has been related to circulation of heated basinal fluids at ca. 100 Ma related to the Narmada-Tapti rift in response to break-up of Indian plate from East Gondwana (Kontak et al., 2014). In the case of the Highway 69 pegmatite group, we emphasize the proximity of the study are to the GFTZ, a major crustal-scale structural feature (Krogh, 1994), that may have facilitated the focusing of fluids in much the same way that other major structural features do. Lastly and relevant to our conclusion, Budzyń et al. (2023) report a similar resetting event at ca. 200 Ma in Neoproterozoic (*i.e.*, 988 ± 5.9 Ma) pegmatites from Norway related to fluid-mediated CDP processes.

6.2 Zircon alteration and its chemical signature

Although the details and implication of the REE_{CN} and other trace element data are to be presented elsewhere, we address some of these aspects as they pertain to the results and implications of the U-Pb dating such as the chemical signature of reset domains.

Although zircon generally remains unmodified post crystallization and thus a preferred chronometer, it has been well documented in recent years that it is, as are most minerals, subject to modification due to fluid-mediated CDP processes (*e.g.*, Geisler et al., 2007; Kontak et al., 2014; Gysi and Williams-Jones, 2013; also see below). The textures in zircon which record CDP processes in the present study are evident in both CL and BSE imaging (Fig. 8M, N), as has been noted by others (*e.g.*, Geisler et al., 2003a, b; Geisler et al., 2007). Accompanying this alteration is also enrichment in Ca, Fe, Sr, and the LREE, as was noted above. The observations herein that areas of resetting with a non-stoichiometric chemistry equates to metamictization due to high U contents has been reported elsewhere and also noted that in such cases substitution is not limited by the crystal-chemical controls that generally govern exchange in zircon (Geisler et al., 2003a, b; Geisler et al., 2007). The widespread departure of the chemistry of discordant domains from concordant domains in zircon attests to how common this process was in the sampled material.

The enrichment of the metamict and secondary domains in the LREE is very notable. There is a general increase from 20 to 600 times chondritic values, or an absolute enrichment of 30 times, for the LREE. That the LREE can be mobilized by fluids is well documented in both natural settings such as alteration zones related to hydrothermal ore deposits (*e.g.*, Westhues et al., 2017; Abdelnasser et al., 2018; Katz et al., 2021) or actual LREE deposits related to fluid:rock interaction (Gysi et al., 2016) and also from experimental work (*e.g.*, Williams-Jones et al., 2012). Hydrothermal LREE enrichment, such as observed in this study, is likely caused by the widespread circulation of fluids through felsic rocks and sedimentary rocks with elevated LREE signatures. However, the LREE source does not need to be distal in the case of the Highway 69 pegmatites, as pervasive alteration of pegmatite-hosted allanite-(Ce) (Fig. 7J) is observed through the entire

study area, which released considerable amount of LREE as indicated by the abundance of secondary LREE fluorocarbonates in the pegmatites.

6.3 Implications for pegmatite models

Granitic pegmatites are formed by two processes: 1) fractionation of granites (*e.g.* London, 2008); and 2) partial melting of metamorphic rocks (*e.g.* Knoll et al., 2018; Webber et al., 2019). This, as well as their geochemical signature (*i.e.*, LCT (Li-Cs-Ta) *versus* NYF (Nb-Y-F)), reflect different tectonic settings and related lithological units (Martin and De Vito, 2005). Our study demonstrates that there are several pegmatite-forming events in the study area and suggest these might be related to granitic magmatism in the case of the *ca.* 1700 and *ca.* 1450 Ma events, but not for the *ca*. 950 Ma event. Whereas the former can be related to well-documented magmatism in the region (with over a dozen plutons within 30 km of the study area and six within 10 km; see Fig. 2), the latter event relates to the Grenville orogeny due to the collision of Laurentia and Amazonia and the associated crustal thickening of a mixed package of metasedimentary and metavolcanic rocks (Tollo et al., 2004). The presence of widespread partial melting of these latter rocks within the high-grade domains of this orogeny is well documented (*e.g.*, Corfu et al., 2000; Marsh et al., 2012; Culshaw et al., 2016). We therefore relate the generation of the Grenvillian-age pegmatites in the study area to such a process, like their Norwegian counterpart (*e.g.*, Müller et al., 2017; Rosing-Schow et al., 2023).

7. Conclusions

1826 The results of our extensive field work and related geochronological studies of the
1827 Highway 69 pegmatite swarm south of Sudbury (Ontario, Canada) hosted in a Proterozoic
1828 sequence of ortho- and paragneissic rocks indicate the following:

1829 1. Although most pegmatite swarms are formed by a single intrusive event or multiple
1830 intrusions over a short amount of time (*e.g.*, Mauthner et al., 1995; Kontak et al., 2005; Van
1831 Lichtervelde et al., 2017; Mulja and Williams-Jones, 2018; Yan et al. 2022), the Highway 69
1832 pegmatite swarm is a rare example of a true composite pegmatite swarm with multiple generations
1833 of pegmatites associated with different geotectonic events spanning over hundreds of million of
1834 years.

1835 2. The presence of Paleoproterozoic (*ca*. 1740 Ma), Mesoproterozoic (*ca*. 1450-1430 Ma)
1836 and Neoproterozoic (*ca*. 1000-970 Ma) pegmatites record the complex tectonic history with the
1837 western GTFZ, including the Yavapai, Chieflakian and Grenville orogenies.

1838 3. Zircon and xenotime record an overprinting hydrothermal event at ca. 220-200 Ma,
1839 which is possibly related to far-field effects of CAMP magmatism and initial rifting during the
1840 opening of the Atlantic Ocean. This fluid-mediated event caused enrichment of the younger,
1841 metamict, zircon domains in LREE, Ca, Fe, LREE and Sr.

1842 4. The Highway 69 pegmatite swarm reflects the presence of two processes of pegmatite
1843 formation: fractionation of a granitic melt and partial melting. The Neoproterozoic pegmatites,
1844 which are associated with the Grenville orogeny and formed *via* partial melting, are notably more
1845 enriched in U(±Th), Nb(±Ta), REE than the older intrusion-related pegmatites. Similar
1846 geochemical enrichment is observed in contemporaneous pegmatites along the ~5000 km long
1847 Grenville Front (*e.g.*, Ercit, 2005; Müller, 2017; Turlin et al., 2017; Rosing-Schow et al., 2023),

most of which are also being interpreted as unrelated to pluton-scale magmatism (*e.g*. Müller, 2017). Together, these Grenvillian and Sveconorwegian pegmatites, separated by the Atlantic Ocean, form one of the largest REE-enriched pegmatite provinces in the world (Ercit, 2005).

8. Acknowledgements and Funding

The authors would like to thank Longbo Yang and Willard Desjardins for their help with sample preparation. This study was supported financially by an NSERC Discovery Grant to Dr. Daniel Kontak.

9. References

Abdelnasser A., Kumral M., Zoheir B., Karaman M. and Weihed P. (2018) REE geochemical characteristics and satellite-based mapping of hydrothermal alteration in Atud gold deposit, Egypt. *J. African Earth Sci.* **145**, 317–330.

Ames D. E., Davidson A. and Wodicka N. (2008) Geology of the Giant Sudbury Polymetallic Mining Camp, Ontario, Canada. *Econ. Geol.* **103**, 1057–1077.

Ayer J., Amelin Y., Corfu F., Kamo S., Ketchum J., Kwok K. and Trowell N. (2002) Evolution of the southern Abitibi greenstone belt based on U-Pb geochronology: Autochthonous volcanic construction followed by plutonism, regional deformation and sedimentation. *Precambrian Res.* **115**, 63–95.

Budzyń, B., Wirth,R. Slámac, J., Kozub-Budzyń, G.A., Konečnýe, P., Rzepad, G., and Schreiberb, A. (2023) Micro- to nanoscale constraints on metasomatic alterations of xenotime, inclusions of Th-, U- and Pb-phases and their geochronological implications (Ås pegmatite, Evje and Hornnes, S Norway). *Chem. Geol*. https://doi.org/10.1016/j.chemgeo.2023.121538.

Carr S. D., Easton R. M., Jamieson R. A. and Culshaw N. G. (2000) Geologic transect across the Grenville orogen of Ontario and New York. *Can. J. Earth Sci.* **37**, 193–216.

Černý P. (1991) Rare-element Granitic pegmatite:Anatomy and internal evolution of pegmatite deposits. *Geosci. Canada* **18(2)**, 49–67.

Černý P., & Ercit T.S. (2005) The classification of granitic pegmatites revisited. The Canadian Mineralogist 43, 2005–2026.

Corfu F. and Easton R. M. (2000) U–Pb evidence for polymetamorphic history of Huronian rocks within the Grenville front tectonic zone east of Sudbury, Ontario , Canada. *Chem. Geol.* **172**, 149–171.

Craddock J. P., Rainbird R. H., Davis W. J., Davidson C., Vervoort J. D., Konstantinou A., Boerboom T., Vorhies S., Kerber L. and Lundquist B. (2013) Detrital zircon geochronology and provenance of the Paleoproterozoic Huron (~2.4-2.2 Ga) and Animikie (~2.2-1.8 Ga) basins, southern Superior province. *J. Geol.* **121**, 623–644.

Culshaw N., Foster J., Marsh J., Slagstad T. and Gerbi C. (2016) Kiosk domain, Central Gneiss Belt, Grenville Province, Ontario: A Labradorian palimpsest preserved in the ductile deep crust. *Precambrian Res.* **280**, 249–278.

Culshaw N. G., Slagstad T., Raistrick M. and Dostal J. (2013) Geochemical, geochronological and isotopic constraints on the origin of members of the allochthonous Shawanaga and basal Parry Sound domains, Central Gneiss Belt, Grenville Province, Ontario. *Precambrian Res.* **228**, 131–150.

Cumming, G. L., Farquhar, R. M., Russell, R. D., and Wilson, J. T. (1955) Some dates and subdivisions of the Canadian Shield. *Proceedings of the Geological Society of Canada*, **7,** 270-279.

Dahl P. S. (1997) A crystal-chemical basis for Pb retention and fission-track annealing systematics in U-bearing minerals, with implications for geochronology. *Earth Planet. Sci. Lett.* **150**, 277–290.

Davidson A. (1992) *Relationship between faults in the Southern Province and the Grenville Front southeast of Sudbury, Ontario*. Geological Survey of Canada, paper 92-1C.

Davidson A. (2001) The Chief Lake complex revisited, and the problem of correlation across the Grenville Front south of Sudbury, Ontario. *Precambrian Res.* **107**, 5–29.

Davidson A. and Van Breemen O. (1994) *U-Pb ages of granites near the Grenville Front, Ontario*. Geological Survey of Canada. Radiogenic age and isotopic studies: Report 8.

Davidson A., Van Breemen O. and Sullivan R. W. (1992) *Circa 1.75 Ga ages for plutonic rocks from the Southern Province and adjacent Grenville Province: what is the expression of the Penokean orogeny?*

Davis G.L., Krogh T.E., and Hart S.R. (1970) The Age of Metamorphism in the Grenville Province and the Age of the Grenville Front; Carnegie Inst. Year Book. **68**, 307-314.

Dickin A. P. (1998) Nd isotope mapping of a cryptic continental suture, Grenville Province of Ontario. *Precambrian Res.* **91**, 433–444.

Dickin A. P., Moretton K. and North R. (2008) Isotopic mapping of the Allochthon Boundary Thrust in the Grenville Province of Ontario, Canada. *Precambrian Res.* **167**, 260–266.

Dubé, B., and Mercier-Langevin, P. (2020) Gold deposits of the Archean Abitibi greenstone belt, Canada. Chapter in *Geology of the World's Major Gold Deposits and Provinces.* Society of Economic Geologists.

Easton, R.M., and Hrominchuk, J.L., 1999, Geology and copper-platinum group element mineral potential of Dana and Crerar Townships, River Valley area, Grenville province: Ontario Geological Survey Open File Report 6000 , p. 30–1 to 30–36.

Easton, R.M., and Murphy, E., (2000) Geology of Street Township: Ontario Geological Survey, Preliminary Map P.3427 , scale 1:20,000.

Easton R. M. and TerMeer M. (2004) Map 3535 - Geology of the Henry and Loughrin Townships. *Ontario Geol. Surv.*, 22222.

Ellsworth H. V. (1926) Toddite - A new Uranium mineral from Sudbury District, Ontario. *Am. Mineral.* **11**, 332–334.

Engi M. (2017) Petrochronology Based on REE-Minerals: Monazite, Allanite, Xenotime, Apatite. *Rev. Mineral. Geochemistry* **83**, 365–418.

Ercit T. S. (2005) REE-Enriched Granitic Pegmatites. Rare-element geochemistry and mineral deposits, *GAC short course notes* **17**, 175–199.

Fan X. (1995) Structural studies of the Killarney igneous complex, Ontario and their tectonic implications.

Fuchsloch W. C., Nex P. A. M. and Kinnaird J. A. (2018) Classification, mineralogical and geochemical variations in pegmatites of the Cape Cross-Uis pegmatite belt, Namibia. *Lithos* **296**–**299**, 79–95.

Geisler T., Pidgeon R. T., Kurtz R., van Bronswijk W. and Schleicher H. (2003) Experimental hydrothermal alteration of partially metamict zircon. *Am. Mineral.* **88**, 1496–1513.

Geisler T., Rashwan A. A., Rahn M. K. W., Poller U., Zwingmann H., Pidgeon R. T., Schleicher H. and Tomaschek F. (2003) Low-temperature hydrothermal alteration of natural metamict zircon from the Eastern Desert, Egypt. *Mineral. Mag.* **67**, 485–508.

Geisler T., Schaltegger U. and Tomaschek F. (2007) Re-equilibration of zircon in aqueous fluids and melts. *Elements* **3**, 43–50.

Gysi A. P., Williams-Jones A. E. and Collins P. (2016) Lithogeochemical vectors for hydrothermal processes in the Strange Lake peralkaline granitic REE-Zr-Nb deposit. *Econ. Geol.* **111**, 1241–1276.

Gysi A. P. and Williams-Jones A. E. (2013) Hydrothermal mobilization of pegmatite-hosted REE and Zr at Strange Lake, Canada: A reaction path model. *Geochim. Cosmochim. Acta* **122**, 324–352.

Harley S. L. and Kelly N. M. (2007) Zircon: Tiny but timely. *Elements* **3**, 13–18.

Hewitt D. F. (1952) *Feldspar in Ontario*. Ontario Geological Survey

Hodges, K. (2013). Thermochronology in Orogenic Systems. *In The Crust* (Vol. 4, pp. 281-308). Elsevier Inc.

Horstwood M. S., Košler J., Gehrels G., Jackson S. E., McLean N. M., Paton C., Pearson N.J., Sircombe K., Sylvester P., Vermeesch P., Bowring J.F., Condon D.J. and Schoene B. (2016) Community-derived standards for LA-ICP-MS U-(Th-) Pb geochronology–Uncertainty propagation, age interpretation and data reporting. *Geostandards and Geoanalytical Research*, **40**, 311-332.

Jochum K. P., Willbold M., Raczek I., Stoll B. and Herwig K. (2005) Chemical characterisation of the USGS reference glasses GSA-1G, GSC-1G, GSD-1G, GSE-1G, BCR-2G, BHVO-2G and BIR-1G using EPMA, ID-TIMS, ID-ICP-MS and LA-ICP-MS. *Geostand. Geoanalytical Res.* **29**, 285–302.

Jourdan F., Marzoli A., Bertrand H., Cirilli S., Tanner L. H., Kontak D. J., McHone G., Renne P. R. and Bellieni G. (2009) 40Ar/39Ar ages of CAMP in North America: Implications for the Triassic-Jurassic boundary and the 40K decay constant bias. *Lithos* **110**, 167–180.

Katz L. R., Kontak D. J., Dubé B., McNicoll V., Creaser R. and Petrus J. A. (2021) An archean porphyry-type gold deposit: The Côté Gold Au(-Cu) deposit, Swayze Greenstone Belt, Superior Province, Ontario, Canada. *Econ. Geol.* **116**, 47–89.

Knoll T., Schuster R., Huet B., Mali H., Onuk P., Horschinegg M., Ertl A. and Giester G. (2018) Spodumene pegmatites and related leucogranites from the austroalpine unit (eastern alps, central europe): Field relations, petrography, geochemistry, and geochronology. *Can. Mineral.* **56**, 489–528.

Kontak, D.J. (2017) Coupled Dissolution Precipitation (CDP) Processes Applied to Rare-Metal Ore Systems. SGA Meeting, Quebec, Canada, August 2017, Volume Proceedings of Extended Abstracts.

Kontak D. J., Archibald D. A., Creaser R. A. and Heaman L. M. (2009) Dating Hydrothermal Alteration Attending IOCG Mineralization Along a Terrane Bounding Fault Zone: The Copper Lake Deposit, Nova Scotia. *Atl. Geol.* **44**, 146–166.

Kontak D. J., Creaser R. A., Heaman L. M. and Archibald D. A. (2005) U-Pb tantalite, Re-Os molybdenite, and 40Ar/39Ar muscovite dating of the Brazil Lake pegmatite, Nova Scotia: A possible shear-zone related origin for an LCT-type pegmatite. *Atl. Geol.* **41**, 17–29.

Kontak, D.J., Chattpadhyay, A., Petrus, J.A., and Fayek, M. (2014) *Zircon is not always robust: A case example of dissolution-reprecipitation and variable discordance in zircon from syn-tectonic Neoproterozoic granitoids in the Gavilgarh-Tan shear zone, central India.* Geological Association of Canada-Mineralogical Association of Canada Annual Meeting, Program with Abstracts, **vol. 37**.

Konzett J., Schneider T., Nedyalkova L., Hauzenberger C., Melcher F., Gerdes A. and Whitehouse M. (2018) Anatectic granitic pegmatites from the eastern alps: A case of variable rare-metal enrichment during high-grade regional metamorphism - i: Mineral assemblages, geochemical characteristics, and emplacement ages. *Can. Mineral.* **56**, 555–602.

Krogh T. E. (1994) Precise U-Pb ages for Grenvilan and pre-Grenan thrusting of Proterozoic and Archean metamorphic assemblages in the Grenville Front tectonic zone, Canada. *Tectonics* **13**, 963–982.

Krogh T. E. and Davis G. L. (1968) Geochronology of the Grenville Province: Carnegie Institution of Washington Yearbook **67**, 224-230.

Krogh T. E. and Davis G. L. (1969) Isotopic ages along the Grenville Front in Ontario: Carnegie Institution of Washington Yearbook **68**, 309-313.

Krogh T.E., Corfu F., Davis D.W., Dunning G.R., Kamo S.L., Greenough J., Nakamura E. (1987) Precise U-Pb isotopic ages of diabase dykes and gabbros using trace baddeleyite. In Mafic Dyke Swarms. Halls HC, Fahrig WH (eds) *Geological Association of Canada Special Paper* **33**, 147-152.

Kylander-Clark A. R. C., Hacker B. R. and Cottle J. M. (2013) Laser-ablation split-stream ICP petrochronology. *Chem. Geol.* **345**, 99–112.

La Tour T. E. and Fullagar P. D. (1986) Rb-Sr study of mylonitic rocks at the Grenville Front near Coniston, Ontario: Some preliminary results, in Moore, J. M., Davidson, A., and Baer, A. J., (eds.), *The Grenville Province: Geological Association of Canada Special Paper* **31,** 221-231.

Lichtervelde M. Van, Homme A. G., Saint-blanquat M. De, Olivier P., Gerdes A., Paquette J., Melgarejo J. C., Druguet E. and Alfonso P. (2017) U-Pb geochronology on zircon and columbite-group minerals of the Cap de Creus pegmatites , NE Spain. *Mineral. Petrol.*, 1–21.

London D. (2005) Granitic pegmatites: An assessment of current concepts and directions for the future. *Lithos* **80**, 281–303.

London D. (2008) *Pegmatites*. The Canadian Mineralogist, Special Publication 10, Quebec.

Lorenzo R. I. (2017) Relevance of fluid:rock interaction in Proterozoic pegmatites near Sudbury, Ontario to mineralization in rare-metal pegmatite settings. Laurentian University.

Lorenzo, R. and Kontak, D.J. (2017) *Relevance of fluid:rock interaction in Proterozoic pegmatites near Sudbury, Ontario to mineralization in rare-metal pegmatite settings*. Geological Association of Canada-Mineralogical Association of Canada Annual Meeting, Program with Abstracts, **vol. 40**.

Ludwig K. R. (2012) User's Manual for Isoplot Version 3.75–4.15: a Geochronological Toolkit for Microsoft Excel. *Berkeley Geochronological Center Special Publication*, **5.**

Lumbers S. B. (1976a) Geology of the Burwash Area Districts of Nipissing, Parry Sound, and Sudbury. *Ontario Geol. Surv.*

Lumbers S. B. (1976b) Map 1196 - Mattawa-Deep River area (western half), District of Nipissing. *Ontario Geol. Surv.*

MacLachlan K., Rayner N., Dunning G., and Leugner C. (2004), New results and ideas from the Rottenstone Domain project, in *Summary of Investigations 2004 [CD-ROM]*, Misc. Rep. 2004-4.2, vol. 2, p. 21, Ind. Resour., Saskatchewan Geol. Surv., Saskatchewan, Canada.

Maneta V. and Baker D. R. (2014) Exploring the effect of lithium on pegmatitic textures: An experimental study. *Am. Mineral.* **99**, 1383–1403.

Marsh J. H., Gerbi C. C., Culshaw N. G., Johnson S. E., Wooden J. L. and Clark C. (2012) Using zircon U-Pb ages and trace element chemistry to constrain the timing of metamorphic events, pegmatite dike emplacement, and shearing in the southern Parry Sound domain, Grenville Province, Canada. *Precambrian Res.* **192**–**195**, 142–165.

Martin R. F. and De Vito C. (2005) The patterns of enrichment in felsic pegmatites ultimately depend on tectonic setting. *Can. Mineral.* **43**, 2027–2048.

Mathieu L., Wasuita T. D., Sherlock R., Speidel F., Marsh J. H., Dubé B. and Côté-Mantha O. (2022) Zircon from Altered Monzonite Rocks Provides Insights into Magmatic and Mineralizing Processes at the Douay Au Project, Abitibi Greenstone Belt. *Geosci.* **12**.

Mauthner M. H. F., Mortensen J. K., Groat L. A. and Ercit T. S. (1995) Geochronology of the Little Nahanni pegmatite group, Selwyn Mountains, southwestern Northwest Territories. *Can. J. Earth Sci.* **32**, 2090–2097.

Mcdonough W. F. and Sun S. S. (1995) The composition of the Earth. *Chemical* **120**, 223–253.

Miller, J. S., Matzel, J. E., Miller, C. F., Burgess, S. D., & Miller, R. B. (2007). Zircon growth and recycling during the assembly of large, composite arc plutons. *Journal of Volcanology and Geothermal Research*, **167**, 282-299.

Monecke T, Mercier-Langevin P., Dubé B. and Frieman, B. M. (2017). Geology of the Abitibi Greenstone Belt. Chapter in *Archean base and precious metal deposits, southern Abitibi greenstone belt, Canada*. Society of Economic Geologists.

Mulja T. and Williams-Jones A. E. (2018) The physical and chemical evolution of fluids in rare-element granitic pegmatites associated with the Lacorne pluton, Québec, Canada. *Chem. Geol.* **493**, 281–297.

Müller A., Kearsley A., Spratt J. and Seltmann R. (2012) Petrogenetic implications of magmatic garnet in granitic pegmatites from Southern Norway. *Can. Mineral.* **50**, 1095–1115.

Müller A., Ihlen P. M., Snook B., Larsen R. B., Flem B., Bingen B. and Williamson B. J. (2015) The chemistry of quartz in granitic pegmatites of southern Norway: Petrogenetic and economic implications. *Econ. Geol.* **110**, 1737–1757.

Müller A., Romer R. L. and Pedersen R. B. (2017) The Sveconorwegian pegmatite province -thousands of pegmatites without parental granites. *Can. Mineral.* **55**, 283–315.

Müller A., Romer R. L., Augland L. E., Zhou H., Rosing-Schow N., Spratt J. and Husdal T. (2022) Two-

stage regional rare-element pegmatite formation at Tysfjord, Norway: implications for the timing of late Svecofennian and late Caledonian high-temperature events. *Int. J. Earth Sci.* **111**, 987–1007.

Müller D. R., Sdrolias M., Gaina C. and Roest W. R. (2008) Age, spreading rates, and spreading asymmetry of the world's ocean crust. *Geochemistry Geophys. Geosystems* **9**, Q04006.

Murphy J. B., Waldron J. W. F., Kontak D. J., Pe-Piper G. and Piper D. J. W. (2011) Minas Fault Zone: Late Paleozoic history of an intra-continental orogenic transform fault in the Canadian Appalachians. *J. Struct. Geol.* **33**, 312–328.

Paton C., Hellstrom J., Paul B., Woodhead J. and Hergt J. (2011) Iolite: Freeware for the visualisation and processing of mass spectrometric data. *J. Anal. At. Spectrom.* **26**, 2508–2518.

Pearce N. J. G., Perkins W. T., Westgate J. A., Gorton M. P., Jackson S. E., Neal C. R. and Chenery S. P. (1997) A compilation of new and published major and trace element data for NIST SRM 610 and NIST SRM 612 glass reference materials. *Geostand. Newsl.* **21**, 115–144.

Peck W. H., Quinan M. P. and Selleck B. W. (2019) Detrital zircon constraints on Grenville sedimentation at the margin of Laurentia. *Precambrian Res.* **331**, 105342.

Petrus J. A., Kenny G. G., Ayer J. A., Lightfoot P. C. and Kamber B. S. (2016) Uranium-lead zircon systematics in the Sudbury impact crater-fill: Implications for target lithologies and crater evolution. *J. Geol. Soc. London.* **173**, 59–75.

Plümper O. and Putnis A. (2009) The complex hydrothermal history of granitic rocks: Multiple feldspar replacement reactions under subsolidus conditions. *J. Petrol.* **50**, 967–987.

Poulsen H.K. (2017) The Larder Lake-Cadillac Break and Its Gold Districts. Chapter in *Archean base and precious metal deposits, southern Abitibi greenstone belt, Canada*. Society of Economic Geologists.

Prevec S. A. (1995) Sm-Nd isotopic evidence for crustal contamination in the ca. 1750 Ma Wanapitei Complex, western Grenville Province, Ontario. *Can. J. Earth Sci.* **32**, 486–495.

Putnis A. (2002) Mineral replacement reactions: from macroscopic observations to microscopic mechanisms. *Mineral. Mag.* **66**, 689–708.

Raharimahefa T., Lafrance B. and Tinkham, D.K. (2014) New structural, metamorphic, and U–Pb geochronological constraints on the Blezardian Orogeny and Yavapai Orogeny in the Southern Province, Sudbury, Canada. *Can. J. Earth Sci.* **51**, 750–774.

Riller U., Schwerdtner W. M., Halls H. C. and Card K. D. (1999) Transpressive tectonism in the eastern Penokean orogen, Canada consequences for Proterozoic crustal kinematics and continental fragmentation. *Precambrian Res.* **93**, 51–70.

Rivers T., Ketchum J., Indares A. and Hynes A. (2002) The High Pressure belt in the Grenville Province: architecture, timing, and exhumation. *Can. J. Earth Sci.* **39**, 867–893.

Rollinson, H. (1993). *Using geochemical data. Evaluation, presentation, interpretation*, **1**. Cambridge: Cambridge University Press.

Rosing-Schow N., Romer R. L., Müller A., Corfu F., Škoda R. and Friis H. (2023) Geochronological constraints for a two-stage history of the Sveconorwegian rare-element pegmatite province formation. *Precambrian Res.* **384.**

Seidler L., Steel R. J., Stemmerik L. and Surlyk F. (2004) North Atlantic marine rifting in the Early Triassic: New evidence from East Greenland. *J. Geol. Soc. London.* **161**, 583–592.

Shillibeer H. A. and Cumming G. L. (1956) The bearing of age determination on the relation between the Keewatin and Grenville provinces, in: The Grenville Problem: *The Royal Society of Canada Special Publications*. **1**, 54-73.

Simmons W., Falster A., Webber K., Roda-Robles E., Boudreaux A. P., Grassi L. R. and Freeman G. (2016) Bulk composition of MT. Mica Pegmatite, Maine, USA: Implications for the Origin of An LCT Type Pegmatite by Anatexis. *Can. Mineral.* **54**, 1053–1070.

Simmons W. B. S. and Webber K. L. (2008) Pegmatite genesis: state of the art. *Eur. J. Mineral.* **20**, 421–438.

Sirbescu M. L. C., Schmidt C., Veksler I. V., Whittington A. G. and Wilke M. (2017) Experimental crystallization of undercooled felsic liquids: Generation of pegmatitic texture. *J. Petrol.* **58**, 539–568.

Smythe D. J. and Brenan J. M. (2015) Cerium oxidation state in silicate melts: Combined fO2, temperature and compositional effects. *Geochim. Cosmochim. Acta* **170**, 173–187.

Spence H.S. (1932) Feldspar. Canada Dept. Mines, Mines Br. **731**, 145.

Stern R.A., Bodorkos S., Kamo S.L., Hickman A.H. and Corfu F. (2009) Measurement of SIMS instrumental mass fractionation of Pb isotopes during zircon dating. *Geostandards and Geoanalytical Research*. **33**, 145–168.

Sullivan R. W. and Davidson A. (1993) *Monazite age of 1747 Ma confirms post-Penokean age for the Eden Lake complex, Southern Province, Ontario*.

Tollo R. P., Corriveau L., McLelland J. and Mervin J. B. (2004) Proterozoic tectonic evolution of the Grenville orogen in North America: An introduction". In Tollo, Richard P.; Corriveau, Louise; McLelland, James; et al. (eds.). Proterozoic tectonic evolution of the Grenville orogen in North America. *Geological Society of America Memoir.* **197,** 1–18.

Thomson J. E. (1959) Map 2017 - Broder, Dill, Neelon and Dryden Townships. *Ontario Geol. Surv.*

Turlin F., André-Mayer A. S., Moukhsil A., Vanderhaeghe O., Gervais F., Solgadi F., Groulier P. A. and Poujol M. (2017) Unusual LREE-rich, peraluminous, monazite- or allanite-bearing pegmatitic granite in the central Grenville Province, Québec. *Ore Geol. Rev*. **89**, 627–667.

Van Breemen O. and Davidson A. (1989) Northeast extension of Proterozoic terranes of mid-continental North America: Discussion. *Bull. Geol. Soc. Am.* **101**, 755–756.

Van Walraven P. (2011) A textural and mineralogical study of pegmatites on Highway 69, Sudbury, Ontario, with implications for the London model. BSc honor thesis. Laurentian University.

Villa, I. M., & Hanchar, J. M. (2017). Age discordance and mineralogy. *American Mineralogist*, **102**(12), 2422-2439.

Webber K. L., Simmons W. B., Falster A. U. and Hanson S. L. (2019) Anatectic pegmatites of the Oxford County pegmatite field, Maine, USA. *Can. Mineral.* **57**, 811–815.

Westhues, A., Hanchar, J. M., Voisey, C. R., Whitehouse, M. J., Rossman, G. R., & Wirth, R. (2017). Tracing the fluid evolution of the Kiruna iron oxide apatite deposits using zircon, monazite, and whole rock trace elements and isotopic studies. *Chemical Geology*, **466**, 303-322.

Wiedenbeck M., Hanchar J. M., Peck W. H., Sylvester P., Valley J., Whitehouse M., Kronz A., Morishita Y. and Nasdala L. (2009) Further Characterisation of the 91500 Zircon Crystal. *Geostand. Geoanalytical Res.* **28**, 9–39.

Williams-Jones A. E., Migdisov A. A. and Samson I. M. (2012) Hydrothermal mobilisation of the rare earth elements-a tale of “ceria” and “yttria.” *Elements* **8**, 355–360.

Yan Q.-H., Wang H., Chi G., Wang Q., Hu H., Zhou K. and Zhang X.-Y. (2022) Recognition of a 600-km-long late Triassic rare metal (Li-Rb-Be-Nb-Ta) pegmatite belt in the western Kunlun Orogenic belt, western China. *Econ. Geol.* **117**, 213–236.

Zhang C., Giere R., Stiinitz H., Brack P. and Ulmer P. (2001) Quartz-garnet intergrowths in granitic pegmatites from Bergell and Adamello, Italy. *Schweizer Mineral. und Petrogr. Mitteilungen* **81**, 89-113.

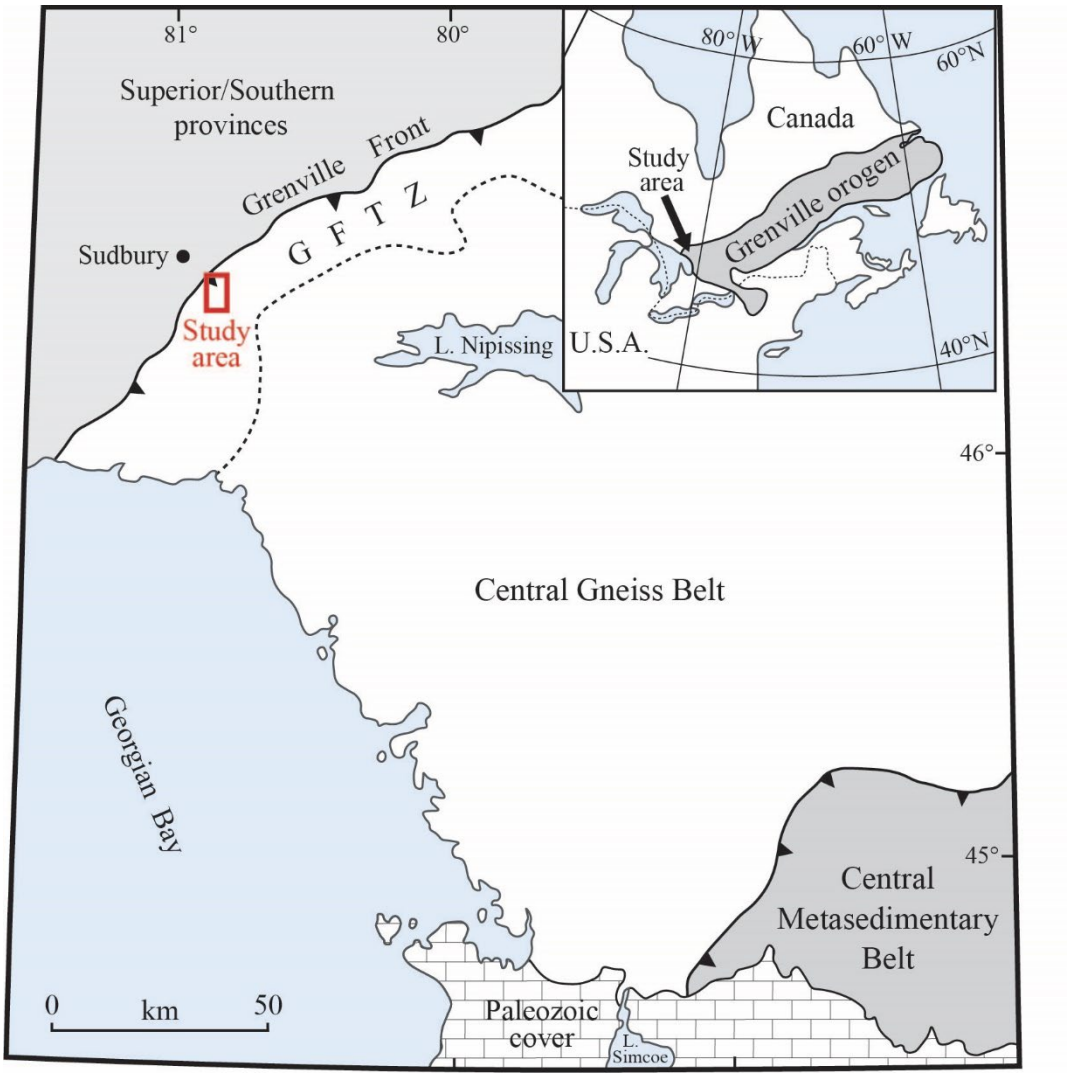

2144

2145 Fig. 1. Simplified geological map of southern Ontario, Canada, showing the extent of the Grenville
2146 Province and location of the study area (in red) south of Sudbury (modified after Marsh et al., 2012).
2147 GFTZ = Grenville Front Tectonic Zone.

2148

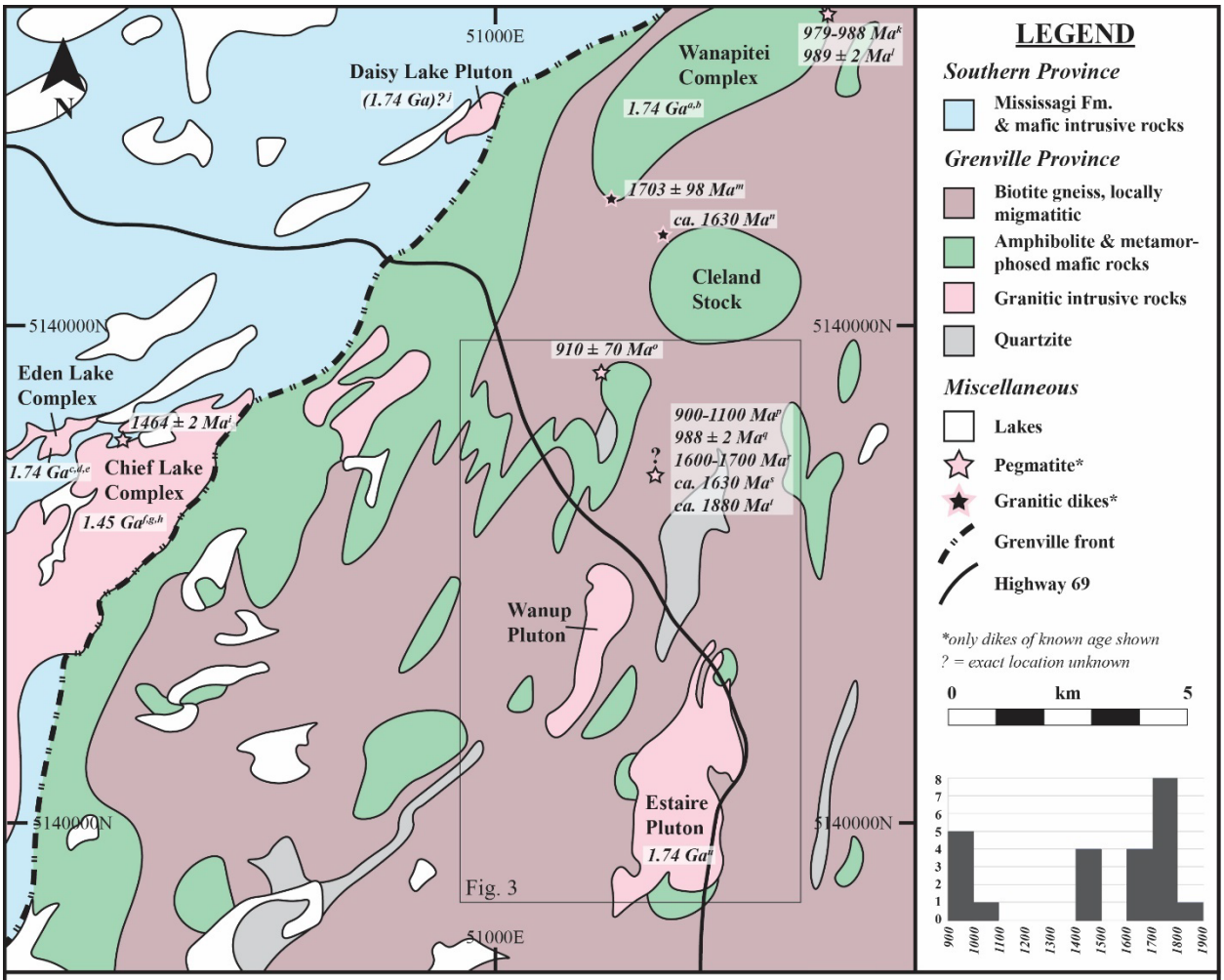

	Intrusion	Method	Reference
a	Wanapitei Complex	U-Pb zircon	Prevec (1995)
b	Wanapitei Complex	U-Pb zircon	Ames et al. (2008)
c	Eden Lake Complex	U-Pb zircon	Ames et al. (2008)
d	Eden Lake Complex	U-Pb zircon & monazite	Sullivan and Davidson (1993)
e	Eden Lake Complex	U-Pb zircon	Raharimahefa et al. (2014)
f	Chief Lake Complex	U-Pb zircon	Raharimahefa et al. (2014)
g	Chief Lake Complex	U-Pb zircon	Davidson and Van Breemen (1994)
h	Chief Lake Complex	U-Pb zircon	Ames et al. (2008)
i	Granitic pegmatite	U-Pb zircon	Davidson and Van Breemen (1994)
j	Daisy Lake Granodiorite	N/A; *See discussion in Davidson (1992) and Davidson and Van Breemen (1994)*	
k	Granitic pegmatite	U-Pb zircon & monazite	Easton et al. (1999)
l	Granitic pegmatite	U-Pb zircon	Ames et al. (2008)
m	Granitic aplite intruding paragneiss	Rb-Sr whole-rock	La Tour and Fullager (1986)
n	Granitic dike	U-Pb zircon	Krogh and Davis (1969)
o	Elizabeth pegmatite	K-Ar muscovite	Cumming et al. (1955)
p	Granitic pegmatite "near Wanup"	U-Pb zircon; K-Ar mica	Shillibeer and Cumming (1956)
q	Granitic pegmatite "near Wanup"	U-Pb monazite	Krogh (1994)
r	Granitic pegmatite "near Wanup"	U-Pb zircon	Davis et al. (1970)
s	Granitic pegmatite "near Wanup"	Rb-Sr muscovite	Krogh (1994)
t	Granitic pegmatite "near Wanup"	Rb-Sr whole-rock	Davis et al. (1970)
u	Estaire Pluton	U-Pb zircon	This study (see Results)

2149

Fig. 2. Simplified regional geological map of the study area (modified after Lumbers, 1976a) showing the locations of previously dated samples along with the respective dating methods used and relevant references. Note the inset histogram showing the distribution of ages which highlights three prominent peaks at ca. 1700-1800 Ma, ca. 1450 Ma, and ca. 950 Ma.

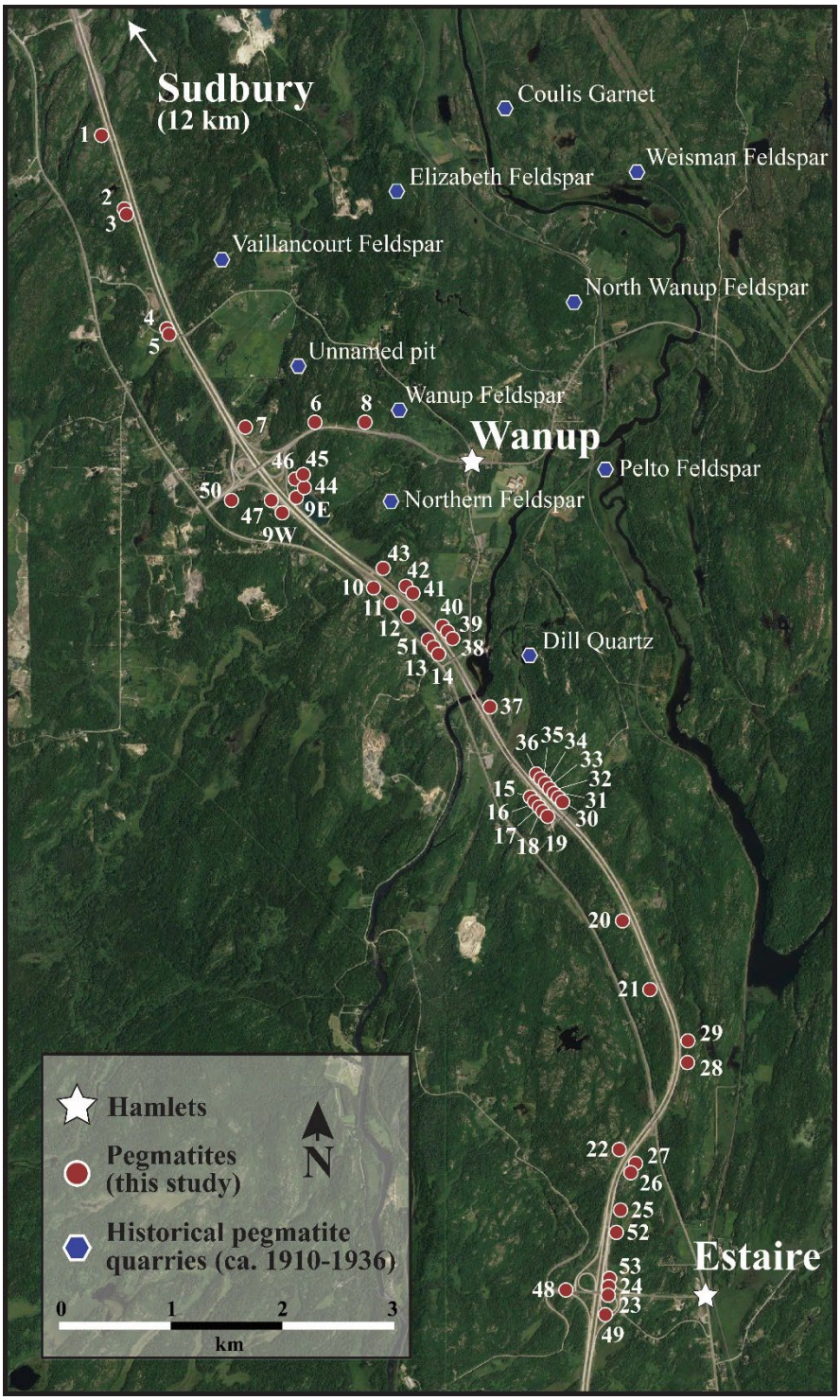

Fig. 3. Satellite image (© Google Earth 2021) of the study area along provincial Highway 69 south of Sudbury showing the location of historical K-feldspar-rich pegmatite quarries (blue hexagons) and the pegmatites discussed in this study (red circles). Note that the numbers assigned to pegmatites have no meaning other than in the context of this study (i.e., sample locations).

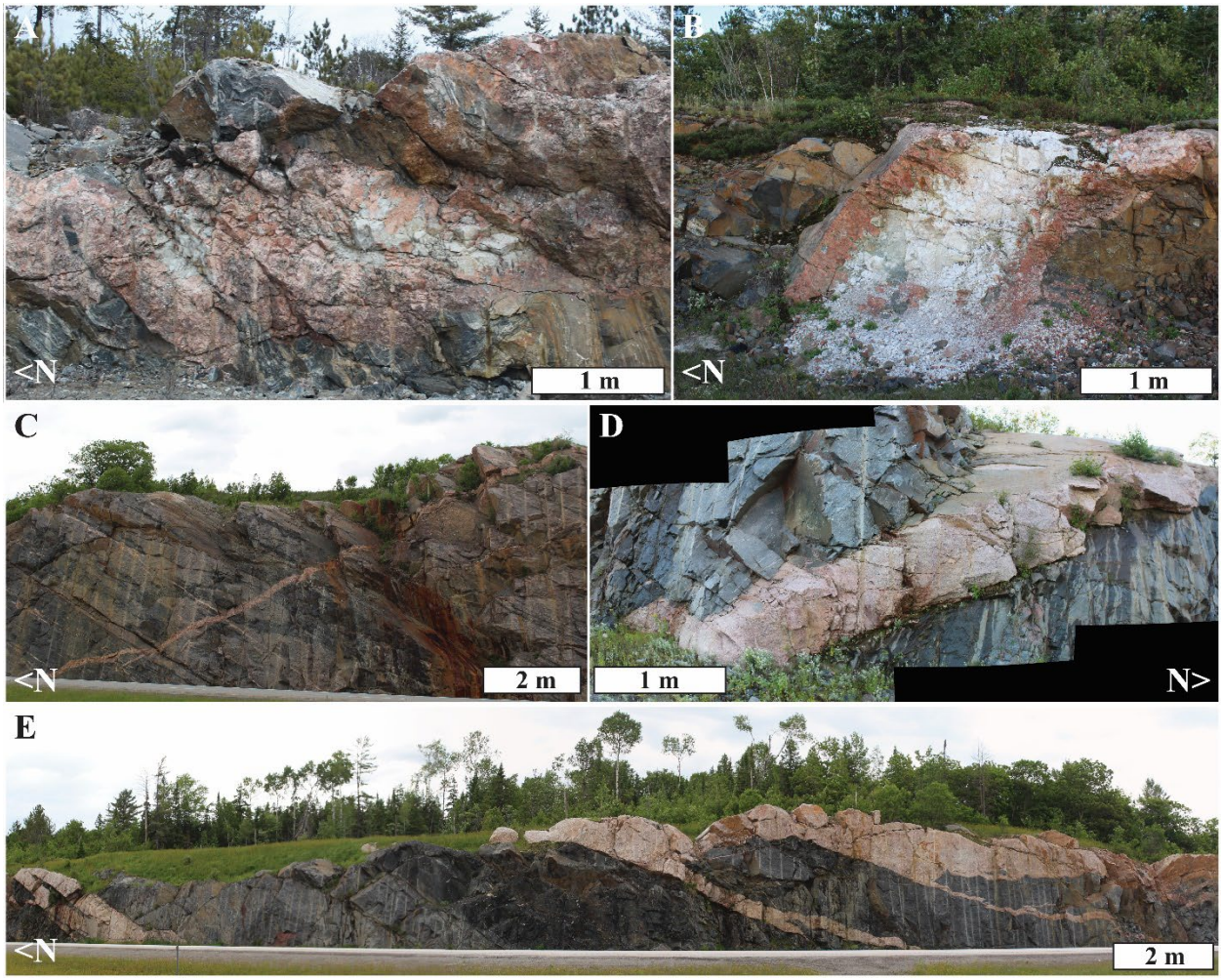

Fig. 4. Typical exposure of pegmatites in road cuts along Highway 69 south of Sudbury. A) Large zoned K-feldspar-rich pegmatite (#7) with a quartz core. B) Zoned pegmatite (#29) with red albite border and particularly well-developed quartz core. C) Thin unzoned pegmatite (#42) that crosscuts the northeast trending wall-rock fabric. D) Thick unzoned albite-rich pegmatite (#16) crosscutting northeast-trending wall-rock fabric. E) Unzoned pegmatites (#32-34) aligned subparallel to northeast-trending wall-rock fabric.

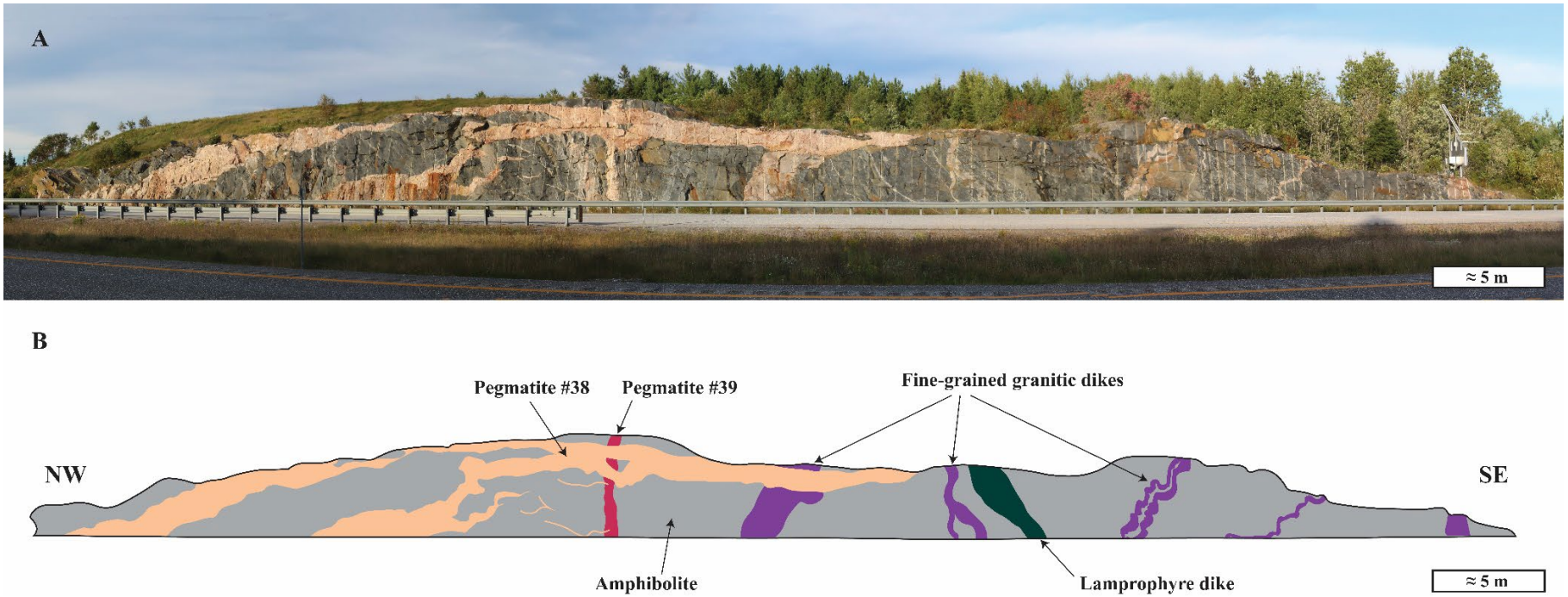

Fig. 5. Road cut showing crosscutting relationships with the subhorizontal pegmatite #38 (albite-rich) crosscutting subvertical pegmatite #39 (K-feldspar-rich) and fine-grained granitic dikes. Note that the alteration halo around the lamprophyre dike to the right overprints the fine-grained granitic dike to its left.

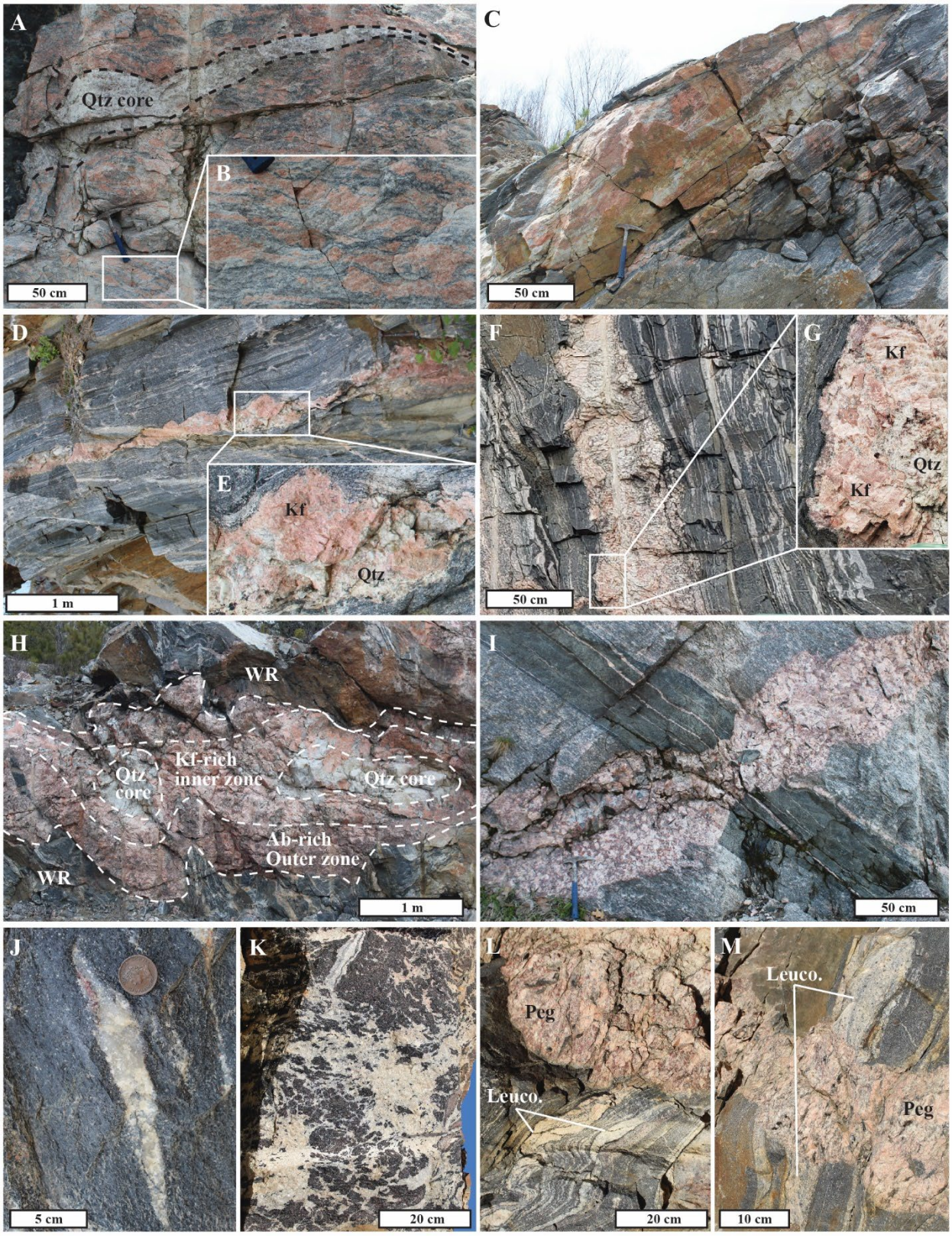
A
Qtz core
B
50 cm
C
50 cm
D
1 m
E
Kf
Qtz
F
50 cm
G
Kf
Qtz
Kf
H
WR
Qtz core
Kf-rich inner zone
Qtz core
Ab-rich Outer zone
WR
1 m
I
50 cm
J
5 cm
K
20 cm
L
Peg
Leuco.
20 cm
M
Leuco.
Peg
10 cm

Fig. 6. Outcrop photos of pegmatites along Highway 69 south of Sudbury. Ab = albite; Kf = K-feldspar; Leuco. = leucosome; Peg = pegmatite; Qtz = quartz. A, B) Highly deformed pegmatite (#47) with remnant quartz core. Note that this is one of only three pegmatites with Archean (or early Paleoproterozoic) xenocrystic zircon. Close up image shows its internal fabric (recrystallized Kf megacrysts). C) Highly deformed pegmatite (#3) with recrystallized K-feldspar masses and parallel alignment with the wall-rock fabric. D, E) Moderately deformed pegmatite (#25) with slight development of boudinage fabric. Note how the pegmatite is aligned with the host rock fabric. Close up image shows remnant K-feldspar megacrysts and the lack of mica. F, G) Moderately deformed pegmatite (#39) showing remnant K-feldspar megacrysts and lack of mica. H) Undeformed zoned pegmatite (#7) with a well-developed quartz core, K-feldspar-rich inner zone and sodic plagioclase-rich outer zone. I) Undeformed and unzoned pegmatite (#12) crosscutting the host rock fabric. J) Anatectic sweat (leucosomes) in host amphibolite. These features are widespread through the study area. K) Amphibolite-hosted leucosomes which have coalesced. L, M) Crosscutting relationships between undeformed pegmatites and amphibolite-hosted leucosomes.

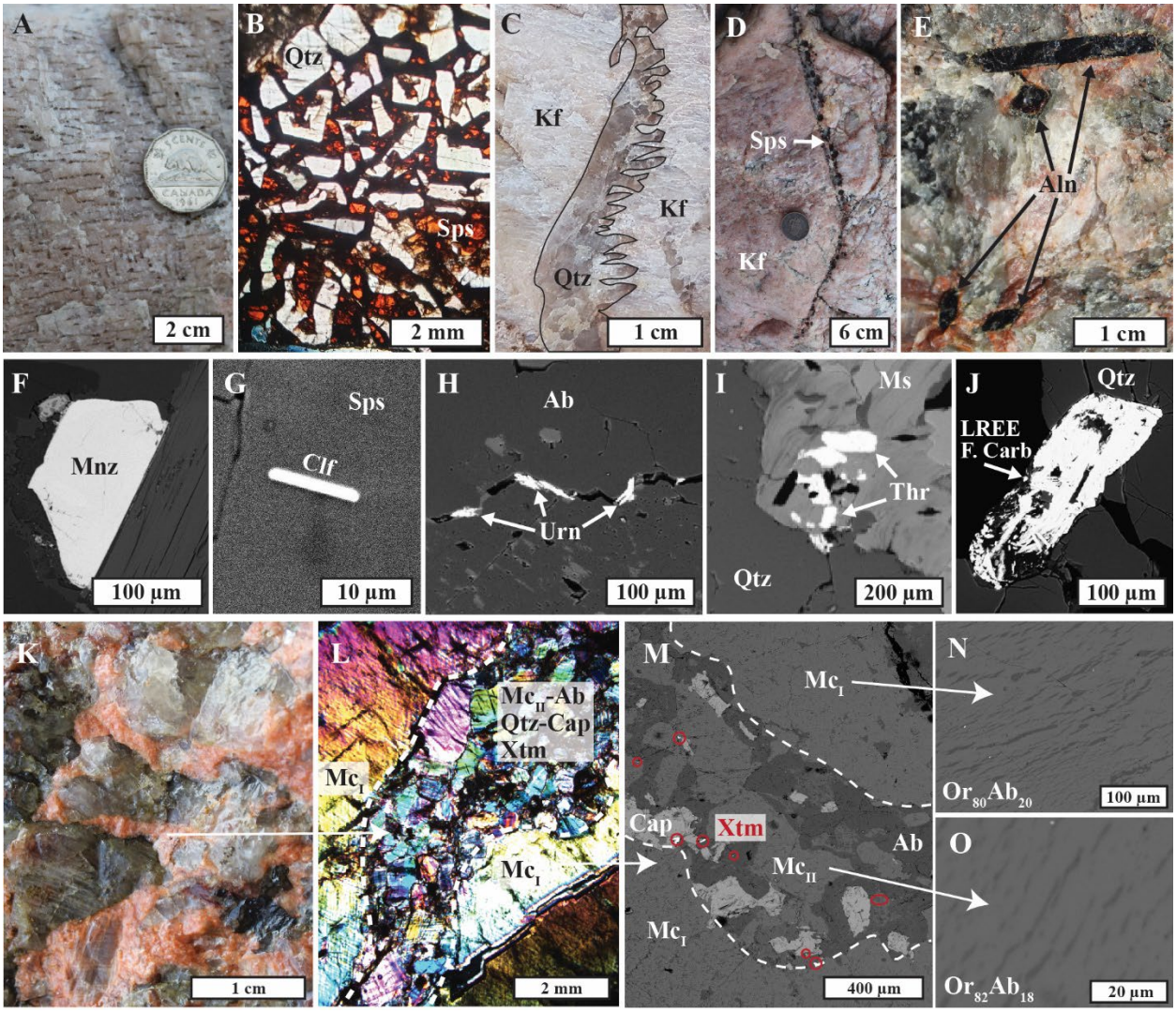

Fig. 7. Outcrop photos along with photomicrographs and BSE images of samples and pegmatites along Highway 69 south of Sudbury. Ab = albite; Aln = allanite-(Ce); Cap = chlorapatite; Clf = ferrocolumbite; Kf = K-feldspar; LREE F. Carb = LREE fluorocarbonates; Mc = microcline; Mnz = monazite; Ms = muscovite; Or = orthoclase; Qtz = quartz; Sps = spessartine; Thr = thorite; Urn = uraninite; Xtm = xenotime. A) Graphic texture in pegmatite #9W. B) Graphic-like intergrowth of quartz and spessartine in pegmatite #44. C) Dendritic quartz crystal in pegmatite #5. D) Spessartine garnet layer along the margin of a K-feldspar megacryst in pegmatite #44. E) Coarse crystals of allanite-(Ce) in pegmatite #6. F) BSE image of monazite in pegmatite #11. G) BSE image of ferrocolumbite inclusion in spessartine from pegmatite #13. H) BSE image of secondary uraninite in fracture from pegmatite #14. I) BSE image of thorite in pegmatite #14. J) BSE image of secondary, bladed LREE fluorocarbonates typical of what is observed in most pegmatites. Image J shows the LREE fluorocarbonate pseudomorphing allanite-(Ce). K) Close up of intergranular material with textures (e.g., cuspate outlines and isolated pockets) suggesting partial melting in pegmatite #24. L) Transmitted light image in crossed nicols of pegmatite #24 showing intergranular material of fine-grained perthitic microcline, albite, quartz, chlorapatite and accessory xenotime (± monazite). Note that the host microcline (Mc_I) is crystallographically continuous. M) BSE imaging of the intergranular material of pegmatite #24 (same area than picture L). Note the abundance of chlorapatite and disseminated xenotime (red circles). N) Close up of the host perthitic microcline (Mc_I) in

pegmatite #24. O) Close up of the secondary perthitic microcline (Mc_{II}) in the intergranular material in pegmatite #24. See text for discussion.

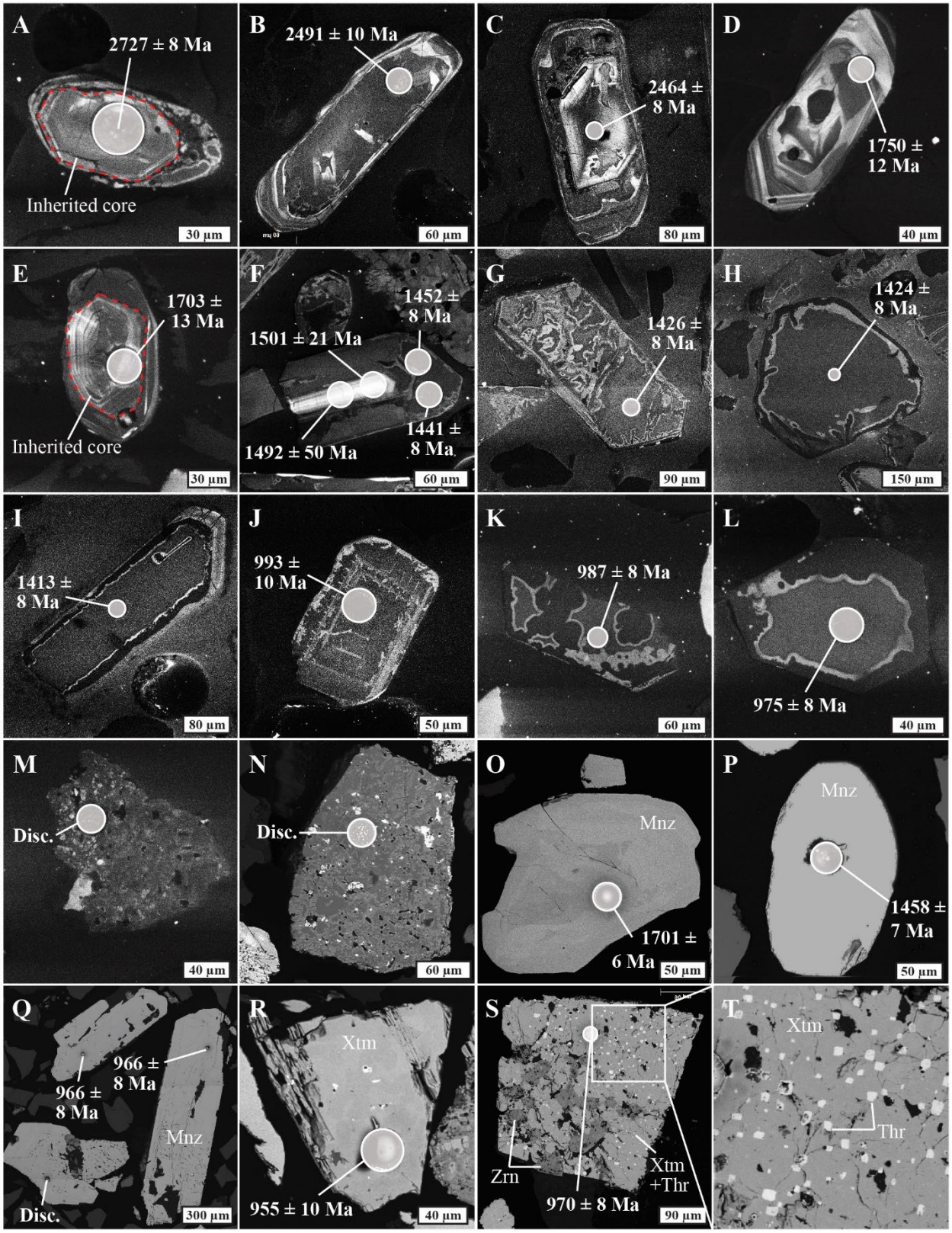

Fig. 8. CL (A-M) and BSE (N-T) images of representative zircon (A-N), monazite (O-Q) and xenotime (R-T) crystals. Disc = discordant; Mnz = monazite; Thr = thorite; Xtm = xenotime; Zrn = zircon. A)

Neoarchean inherited zircon core showing weak fluctuating zoning. B, C) Early Paleoproterozoic zircon showing a combination of patchy and weak fluctuating zoning. D) Late Paleoproterozoic zircon exhibiting complex fluctuating zoning. E) Late Paleoproterozoic inherited zircon core with well-developed fluctuating zoning. F) Mesoproterozoic zircon with internal zoning. This is the only pegmatite (#53) containing zoned zircon of Mesoproterozoic age. Note that the core yields slightly older but less precise ages. The bright core contains higher REE content but lower U, Th, Hf concentrations (see Supplementary File 2). G, H, I) Typical Mesoproterozoic zircon exhibiting an unzoned crystalline core with various degrees of alteration and metamictization along the rims and internal fractures. J) Neoproterozoic zircon showing weak internal zoning and a low degree of alteration. Note that zoned zircon of Neoproterozoic age are only found in two pegmatites (#3, #48) which also contain older populations of zircon of concordant ages. Additionally, zoned zircon of Neoproterozoic age yield slightly older ages than the more common unzoned ones. K, L) Neoproterozoic zircon exhibiting unzoned crystalline core and metamict rims. The dark metamict rims contain wt. % levels of Ca, Fe, as well as elevated Sr and LREE content. Note that this is by far the most common type of zircon encountered in this study and are visually indistinguishable from most Mesoproterozoic zircon (e.g., H, I). M, N) Mineral-inclusion rich and altered Neoproterozoic zircon. Inclusions observed includes uraninite, xenotime, xenotime, apatite and quartz. Note that these zircon are rarely euhedral and heavily pitted (suggestive of CDP). Such zircon were found in most Neoproterozoic pegmatites and invariably yielded discordant ages. O) Late Paleoproterozoic monazite showing weak internal zoning. P) Mesoproterozoic monazite lacking internal zoning. Q) Neoproterozoic monazite crystals. Note the large size, euhedral habit and lack of internal zoning. R) Neoproterozoic xenotime crystal with weak patchy zoning. S, T) Heavily included and pitted Neoproterozoic xenotime. Inclusions observed include zircon and thorite. Note that the thorite inclusions are crystallographically oriented. See text for discussion. Reported age errors are 2σ.

	Zircon		Monazite		Xenotime	
	Age	n =	Age	n =	Age	n =
P1	1425.7 ± 7.8 [2]	8/29	965.7 ± 8.0 [3]	1/1	968 ± 8 [3]	1/1
P3	(ca. 2.5 Ga) 1432 ± 20 [2] 995.3 ± 5.7 [1]	5/32 6/32 7/32				
P4	990 ± 9 [3]	1/23			968.7 ± 2.9 [2]	7/25
P5	Ø	0/20	974.7 ± 4.1 [2]	4/7	972.8 ± 6.9 [2]	6/20
P6(leuco)	981.7 ± 1.6 [2]	38/50				
P6(Kf)	977.3 ± 2.4 [2]	13/37			957 ± 20 [1]	2/13
P7	Ø	0/19	964.8 ± 4.2 [1]	10/12	970.4 ± 4.9 [1]	6/19
P8	Ø	0/15	968.6 ± 4.2 [1]	10/12	967.7 ± 12 [1]	3/22
P9	Ø	0/7	960.1 ± 9.4 [1]	4/4	969.1 ± 8.1 [2]	10/38
P12	1703 ± 13 [1]	1/27	1719.8 ± 9.1 [3]	1/1	961.9 ± 2.6 [2]	10/12
P15	Ø	0/4	962.4 ± 3.6 [1]	17/25	963.2 ± 6.0 [2]	3/7
P18	Ø	0/7	964.3 ± 4.8 [1]	6/9	965.2 ± 5.8 [1]	3/10
P19	Ø	0/28			966.9 ± 8.7 [1]	1/3
P22			969.9 ± 8.6 [1]	20/31		
P23	1438.0 ± 5.7 [2]	21/41				
P24	1442.9 ± 6.1 [1]	6/14			947 ± 27 [1]	3/10
P25	2798 ± 13 [1] 1727 ± 52 [2] 1422.2 ± 9.9 [1] 983.0 ± 7.0 [2]	1/27 3/27 1/27 2/27				
P26	Ø	0/11				
P27	969.2 ± 8.5 [2]	3/24	Ø	0/1	956.2 ± 7.7 [2]	10/23
P29	968 ± 10 [3]	1/25			Ø	0/25
P32	954 ± 10 [3]	1/17	970.1 ± 3.8 [1]	14/15	955 ± 11 [2]	8/19
P38	987.0 ± 2.8 [2]	13/20	967.3 ± 6.6 [2]	2/2		
P39	Ø	0/20				
P43	Ø	0/8	972 ± 18 [2]	4/4	952.8 ± 8.9 [1]	1/3
P44			975.4 ± 5.9 [1]	18/18		
P45	955 ± 11 [1]	1/18	968.3 ± 6.6 [1]	9/16	956.7 ± 8.4 [2]	5/15
P47	2678 ± 39 [2] 1662 ± 100 [2] Ø Ø	7/14 2/14 0/14 0/14	Ø 1740.7 ± 5.4 [1] 1458.4 ± 6.8 [2] 995.7 ± 5.3 [1]	0/30 8/30 17/30 4/30	Ø Ø Ø 996.2 ± 6.5 [1]	0/6 0/6 0/6 2/6
P48	1714 ± 11 [1] 1447.3 ± 12 [1] 990.9 ± 8.2 [1]	1/36 4/36 7/36				

P49	1425.1 ± 5.6 [1] 986.4 ± 9.8 [1]	10/32 5/32				
P51	1446.3 ± 2.1 [2]	47/50				
P52	980.7 ± 6.2 [1]	4/8	976.7 ± 9.7 [2]	2/35	937.7 ± 14 [1]	3/6
P53	1716 ± 15 [1] 1435.5 ± 7.2 [2]	1/31 21/31	Ø Ø	0/7 0/7		
GE	1745 ± 17 [2]	65/79				

Table 1. Summary of U-Pb ages for zircon, monazite and xenotime from the pegmatites along Highway 69 south of Sudbury (see Figure 3). Note that some of the pegmatites contain multiple generations of each phase. See supplementary data for more information, such as Tera-Wasserburg and Wetherill Concordia diagrams, for each sample. Where for example 10/32 is provided it means 10 grains were used in the age calculation. [1] = Concordia age (Wetherill; Isoplot v4.15); [2] = Upper intercept (Wetherill; Isoplot v4.15); [3] = $^{207}Pb/^{206}Pb$ age of single, near-concordant (>95%) zircon/xenotime/monazite; GE = Granite Estaire.

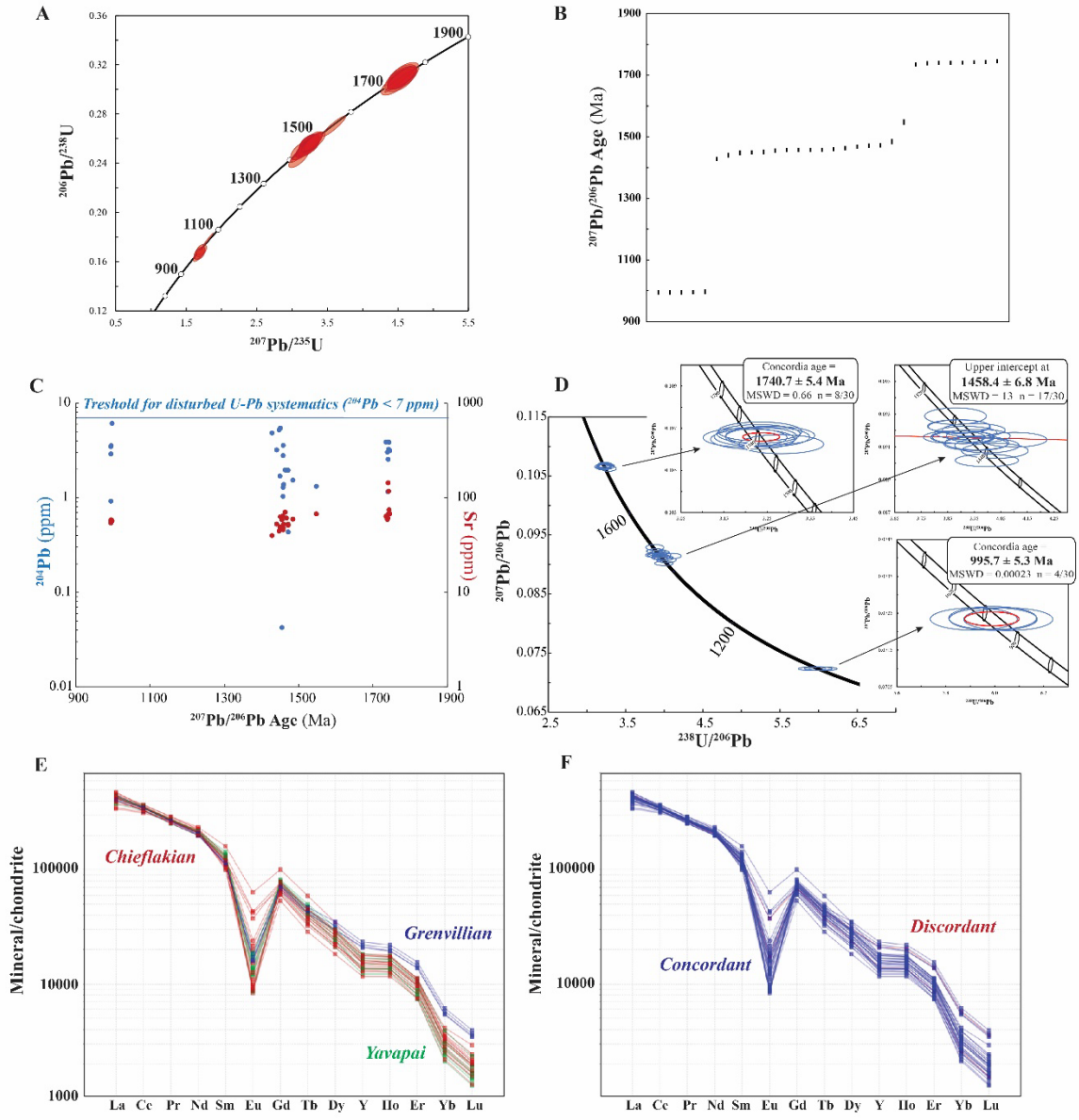

Fig. 9. A representative example showing the various U-Pb geochronology diagrams and chondrite-normalized (McDonough and Sun 1995) REE plots for dated monazite for pegmatite from site #47. See summary of all results in Supplementary File 2. A) Tera-Wasserburg Concordia diagram with all data shown. Note there are three concordant age populations defined. B) Summary of all the $^{207}Pb/^{206}Pb$ ages with 2σ error bars. All data shown. C) Trace elements (i.e., ^{204}Pb, Sr) versus $^{207}Pb/^{206}Pb$ ages with threshold levels of ^{204}Pb which is considered to be indicative of common (non-radiogenic) Pb. D) Tera-Wasserburg Concordia diagram showing calculated Concordia and upper intercept ages for each concordant population (inset plots). E) Chondrite-normalized REE diagram for concordant data colour-coded by age (i.e., Yavapai, Chieflakian, Grenvillian). F) Chondrite-normalized REE diagram colored-coded for concordant versus discordant monazite data. Note that Pm is omitted in the REE diagrams.

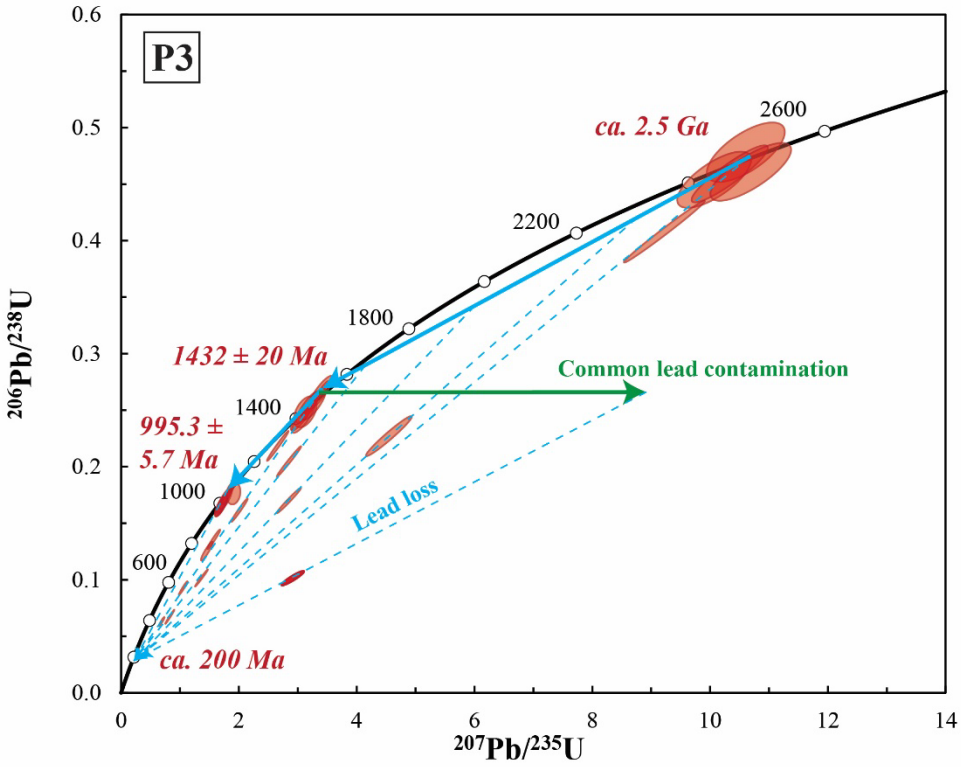

Fig. 10. Wetherhill Concordia diagram for zircon from pegmatite #7 highlighting the fact the zircon from this pegmatite exhibit concordant behaviour for three populations at ca. 2500 Ma, 1432 Ma, and 995 Ma with additional analysis showing discordant behaviour. The solid blue lines represent possible resetting events and/or new zircon growth, whereas the dashed blue lines are trajectories for Pb loss related to a possible ca. 200 Ma event experienced by each of the older zircon populations. In regards to the latter note, however, that for some of the data their position suggests they would have originally plotted on the solid blue line between 2600 Ma and 1432 Ma, hence partially reset. Lastly the solid green line represents an example of inferred common Pb related to the formation of, in this case, the ca. 1432 Ma zircon since the upper intercept with Concordia would give an unrealistic old age of ca. 3400 Ma. See text for further discussion.

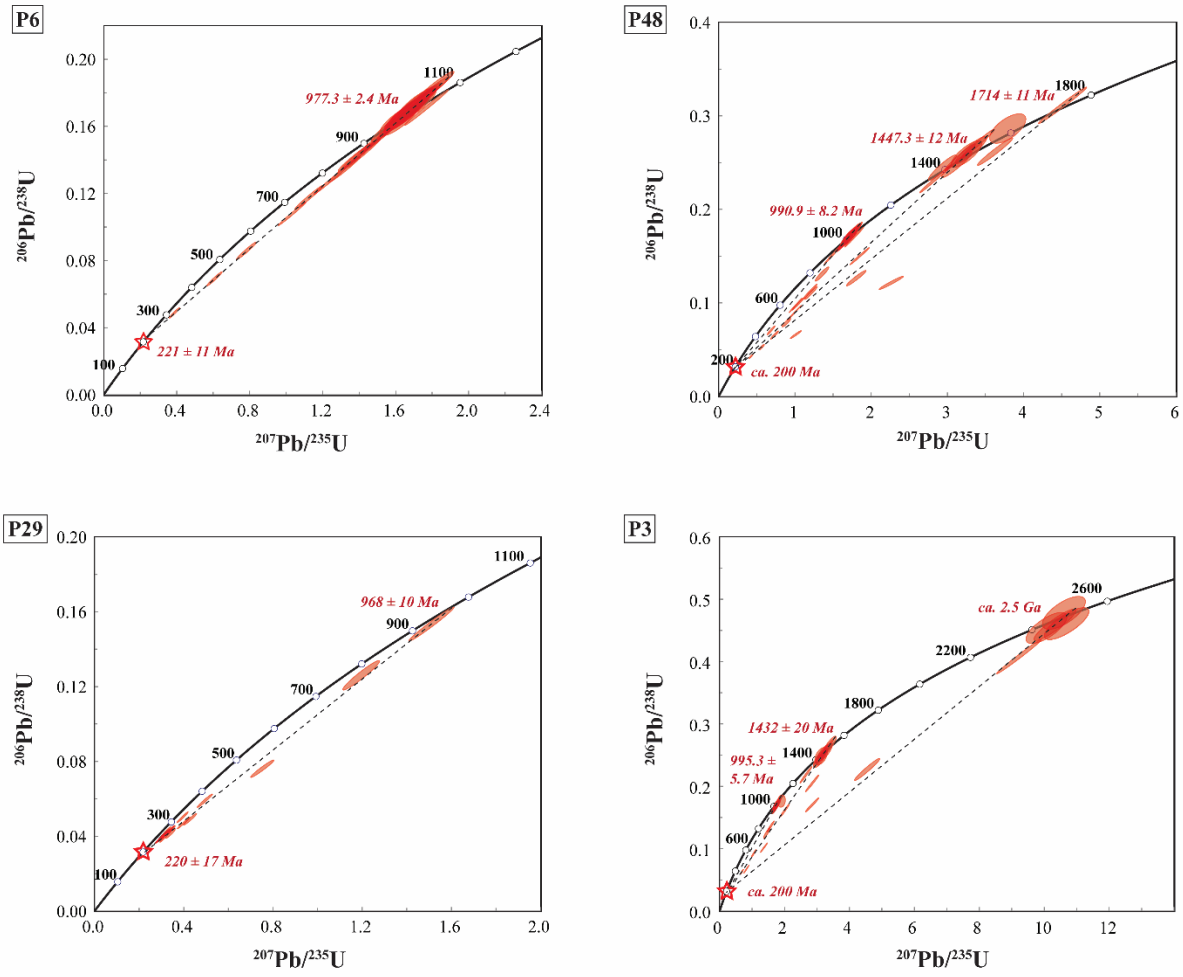

Fig. 11. Wetherill Concordia diagrams for zircon from pegmatites # 3, 6, 29, and 48. Note that in each case there is a well-defined discordia for all samples which indicates the same resetting event at ca. 200-220 Ma.

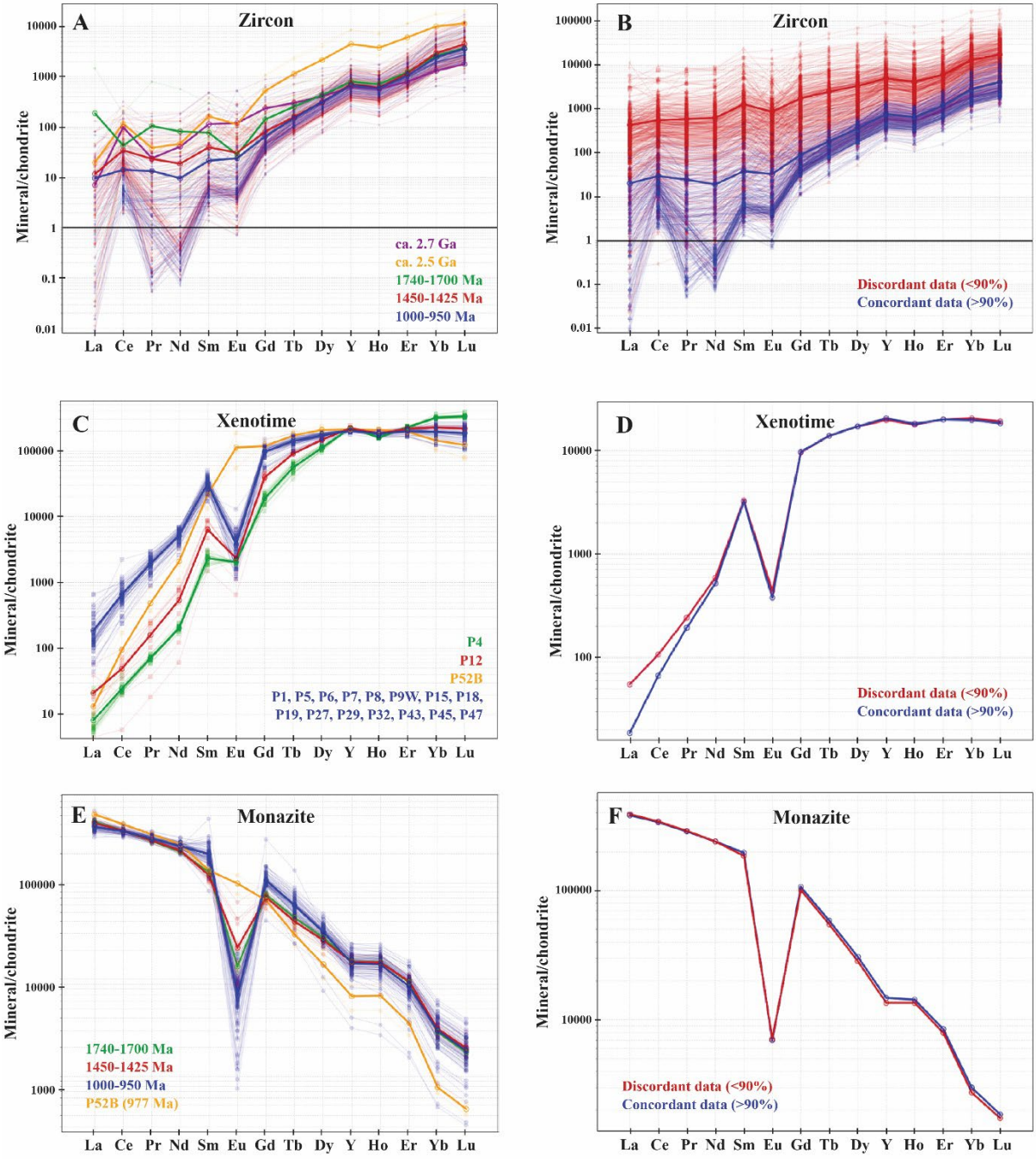

Fig. 12. Examples of chondrite-normalized (McDonough and Sun, 1995) REE profiles for zircon, monazite and xenotime in Highway 69 pegmatites south of Sudbury. Note the minerals are color-coded for their age except for xenotime which are invariably Grenvillian and that the bold lines represent averages. A, B) Plots for different zircon age generations based on concordant (A) versus discordant (B) ages. Note that the LREE enrichment observed in discordant zircon is also observed in other settings with significant sub-solidus fluid-rock interaction (e.g., Westhues et al., 2017) C, D) Plots for xenotime from various Grenvillian-age pegmatites. Note that xenotime from pegmatites 4, 12 and 52, which are color-coded, have very different profiles and are shown on their own whereas xenotime from all other pegmatites have similar profiles. Figure D shows the average for concordant versus discordant xenotime.

E, F) Plots for different age monazite generations based on concordant (E) versus discordant (F) ages. Note that pegmatite 52B is shown on its own as it has a very different REE signature for monazite.

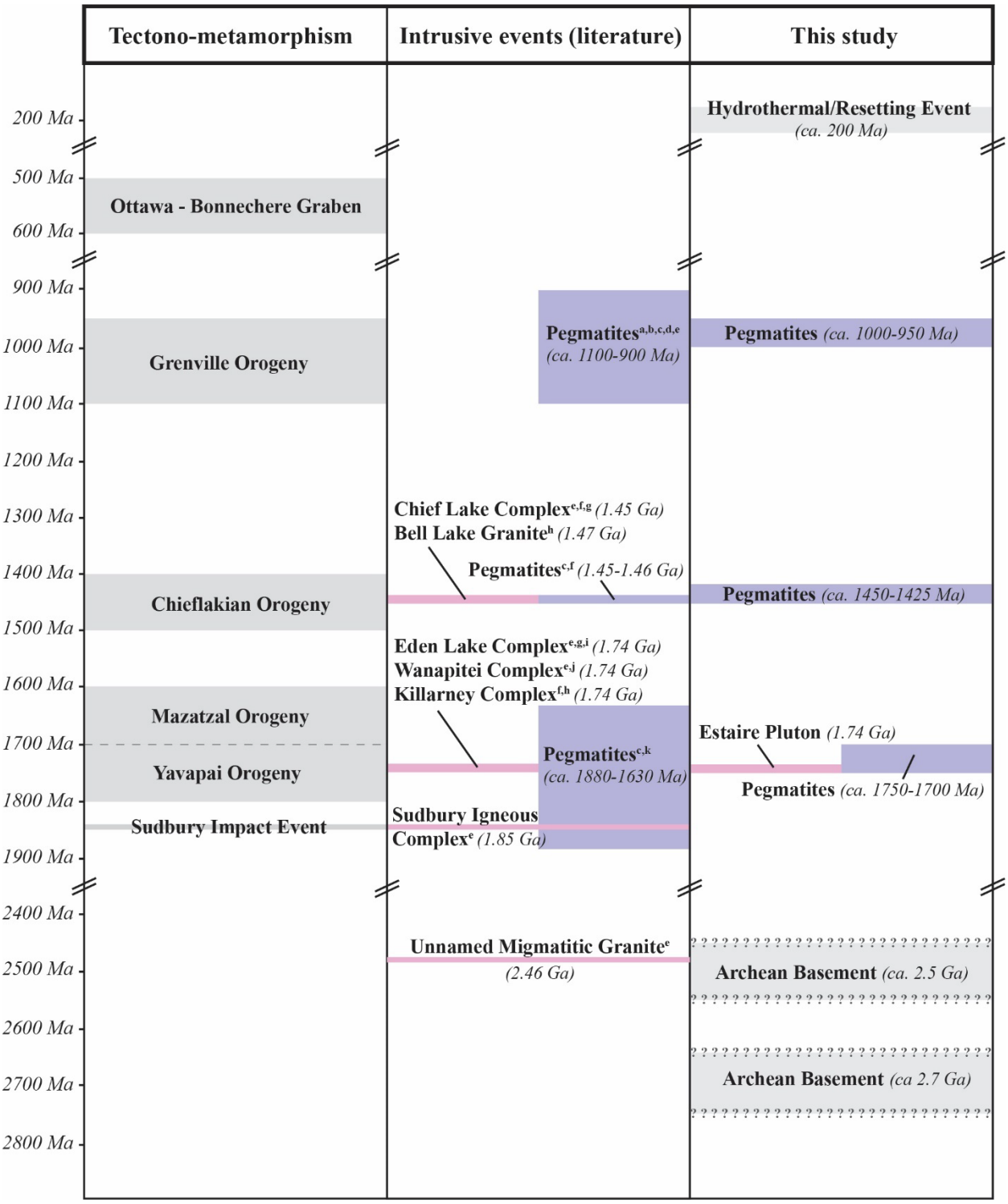

Fig. 13. Summary of the tectono-magmatic-metamorphic events which affected the study area based on a summary of data in the literature and this work. References: [a] Cumming et al. (1955), [b] Shilliberg and Cumming (1956), [c] Krogh (1994), [d] Easton et al. (1999), [e] Ames et al. (2008), [f] Raharimahefa et al. (2014),

[g] Davidson (2001), [h] Van Breemen and Davidson (1986), [i] Sullivan and Davidson (1993), [j] Prevec (1995), and [k] Davis et al. (1970).

Chapter 5

ORIGIN AND EVOLUTION OF THE POLYGENERATIONAL HIGHWAY 69 PEGMATITE GROUP (SUDBURY, CANADA)

Jérémie D. Pfister [a,] , Daniel J. Kontak [a], Ramon Lorenzo [a] Lee A. Groat [b], Mostafa Fayek [c]

[a] *Harquail School of Earth Sciences, Laurentian University, Sudbury, Ontario P3E 2C6, Canada*

[b] *Department of Earth, Ocean and Atmospheric Sciences, University of British Columbia, Vancouver, British Columbia V6T 1Z4, Canada*

[c] *Department of Geological Sciences, University of Manitoba, Winnipeg, Manitoba R3B 2E9, Canada*

To be further developed, separated and submitted as two publications

5.1 Abstract

Situated about 12 km south of Sudbury (Ontario, Canada) in the Grenville Front Tectonic Zone (GFTZ), the well-exposed yet poorly-studied Proterozoic Highway 69 pegmatite group is a polygenerational pegmatite swarm composed of three generations of pegmatites emplaced over 800 Ma (*ca*. 1.74, 1.45 and 0.98 Ga) that exhibit a mild Nb-Y-F (NYF) signature and hosts sub-economic rare-metal (*i.e.*, Nb, Y, REE, U) mineralization.

This study, using an integrated approach of field observations, detailed mapping, structural measurements, textural (BSE, SEM-CL), geochemical (ICP-MS, ICP-AES), mineralogical (SEM-EDS, LA-ICP-MS) and stable isotope (O) (SIMS) studies, aims to investigate the origin, nature and evolution of the pegmatites with a focus on the younger and more abundant Neoproterozoic pegmatites. Collectively, our results suggest that; (1) the Neoproterozoic pegmatites are likely of anatectic origin and were emplaced asynchronously; (2) the pegmatite-forming melt(s) were of relatively primitive composition with a mild NYF affinity; (3) the pegmatites formed at T of 500-600°C, which resulted in the development of various undercooling-related pegmatitic texture; (4) the pegmatites underwent significant fluid:rock interactions during their sub-solidus evolution, including an early sodic metasomatic stage and a late potassic, ferric stage; (5) the late potassic and ferric stage, responsible for the intense hematization of the pegmatites, re-mobilized significant rare-metal mineralization; and (6) the pegmatites evolved as a partially open system displaying pegmatite-wallrock exchange during both magmatic and metasomatic stages.

5.2 Introduction

Granitic pegmatites are an important source of rare metals (*i.e.*, Li, Nb, Ta, Sn, REE and U) that are critical for the global green energy transition. They are generally divided into two main families based on their geochemical signatures: Li-Cs-Ta (LCT) pegmatites and Nb-Y-F (NYF) pegmatites (Černý, 1991; Černý & Ercit, 2005; Martin & De Vito, 2005; London, 2008). Despite recent advances in our understanding of pegmatite formation, which have been fueled by the demand for these metals, several aspects of the formation and evolution of pegmatites to their present-day composition remain controversial. These include: (1) origin of these highly fractionated and in some cases very unusual melts (*i.e.*, fractional crystallization *versus* partial melting) (*e.g.*, Černý, 1991; London, 2008; Simmons & Webber, 2008; Simmons *et al.*, 2016; Knoll *et al*. 2018; Vignola *et al*., 2018; Webber *et al*., 2019); (2) nature of pegmatitic textures, such as their anisotropy, locally abundant graphic intergrowth, and magmatic versus metasomatic features, and the role of undercooling as it relates to their formation (*e.g.*, London 2005, 2008, 2018; Maneta & Baker, 2014; London & Morgan, 2017; Sirbescu *et al.,* 2017); (3) role of metasomatism during their evolution, particularly in regards to the rare-metal mineralization associated with the later stage units, such as aplitic albites (e.g., Černý, 1989; Kontak et al., 2002; Sweetapple & Collin, 2002; Kontak, 2006; Van Lichtervelde et al., 2007; London & Morgan, 2017; Fuchsloch et al., 2019; Pfister et al., 2023b); and (4) open-system *versus* closed-system behaviour (*e.g.*, Jahns, 1969; Kontak & Kyser, 2009; Martin & De Vito, 2014; Burns, 2019; London & Morgan, 2017; Ashworth et al., 2020; Pfister et al., 2023b).

Because Li commonly represents the most highly-prized commodity in pegmatites, the majority of the aforementioned studies have been focused on highly evolved pegmatites of the LCT family to the exclusion of other more simple types. We present here a detailed study of the poorly-understood yet well-exposed Highway 69 pegmatite group (*i.e*., locally named by the authors; see Van Walraven (2011) and Lorenzo (2017)), a relatively primitive NYF-type pegmatite field situated near Sudbury, Ontario, Canada. The study integrates field observations, detailed mapping, structural measurements, petrography (transmitted light microscopy, back-scattered electron (BSE) imaging, cathodoluminescence (CL) imaging), mineralogy (energy-dispersive spectroscopy (EDS)), trace elements (inductively coupled plasma

mass spectrometry (ICP-MS)), whole-rock (inductively coupled plasma atomic emission spectroscopy (ICP-AES)) and in situ $\delta^{18}O$ analyses (secondary ion mass spectrometry (SIMS)) to document the textural, mineralogical and geochemical evolution of the pegmatite swarm from time of dike emplacement to their current composition and address: (1) the nature of the pegmatite-forming melt; (2) origin of pegmatitic textures; (3) role of metasomatism; and (4) open- *versus* closed-system behaviour.

5.3 Regional geological setting and tectonic history

The study area is located about 12 km south of Sudbury (Ontario, Canada) within the Grenville Front Tectonic Zone (GFTZ) near the northwest end of the Grenville Province; Fig. 1). The Grenville Front, located about 5 km north of the study area and extending laterally for over 1900 km, marks the orogenic boundary between the Archean Superior Province to the north and the younger Grenville Province to the south. Additionally, two other tectonic domains also converge in this part of the GFTZ: the Southern Province and the Yavapai(-Mazatzal) Province.

The rock of the older Superior Province in this area consist of the Neoarchean Abitibi greenstone belt and granitic intrusions (ca. 2750-2675 Ma; Ayer *et al.*, 2002), and the high-grade tonalitic Levack gneisses (2711 ± 7 Ma; Petrus *et al.*, 2015). The younger Southern Province contains Paleoproterozoic (*i.e.*, 2452 Ma; Petrus *et al.*, 2015) metavolcanic rocks and metasedimentary rocks of the Huronian Supergroup, which were deposited along the southern margin of the older Superior craton as it transitioned from a rifted to passive continental margin (Craddock *et al.*, 2013). Around ca. 1.74-1.70 Ga, the Yavapai-Mazatzal orogeny initiated widespread magmatism resulting in numerous granitic intrusions (*e.g.*, the *ca*. 1.74 Ga Eden Lake complex, Killarney complex, Estaire pluton, Daisy Lake pluton, etc., see Fig. 2; Van Breemen and Davidson, 1988; Davidson and Van Breemen, 1994; Raharimahefa *et al.*, 2014; Pfister *et al.*,

2023), which were either emplaced or accreted along the southern margin of the Southern Province.

Rocks of the Grenville Province in the study area comprise of various packages of upper-amphibolite grade rocks consisting mostly of amphibole-rich orthogneisses and biotite-rich paragneisses, both locally migmatitic, as well as gneissic granite and minor quartzite (Thomson, 1959; Lumbers, 1976a; Ames *et al.*, 2008). The lithological contacts and dominant fabric in these rocks are generally oriented SW-NE, that is parallel to the trend of the Grenville Front (Fig. 2). This reflects the dominance of the youngest penetrative deformation in the area which is temporally constrained to between ca. 990 and 960 Ma based on U-Pb dating of pegmatite-hosted zircon, xenotime and monazite (see summary in Pfister *et al.*, 2023). The latter structural features, these being the NE-trending fold axes and related penetrative fabric, increase in intensity towards the NW as the Grenville Front is approached (Fig. 2).

5.4 Historical background, local geology and previous work

The northwesternmost part of the GTFZ hosts many pegmatite swarms (*e.g.*, Hewitt, 1952; Lumbers, 1976a, 1976b; Easton and Murphy, 2000; Easton and TerMeer, 2004), but pegmatitic dikes seem to be particularly common in the vicinity of the settlements of Wanup and Estaire (Figs. 2, 3). These were quarried intermittently through the first half of the century for quartz (~750,000 tons as fluxing component for the Sudbury Ni-Cu-PGE smelter), feldspar (~18,000 tons for the ceramic industry) and minor quantities of garnet and mica (Spencer, 1932; Hewitt, 1952; Lumbers, 1976a). Additionally, their relative enrichment in U(±Th), Nb(±Ta) and REEs has been of interest for the last century, first by academia and geological surveys (*e.g.,* discovery of the now-

discredited U-Nb mineral “toddite” (Ellsworth, 1926)), then followed by the mining industry during the uranium boom of the 1950s and 1960s (Lumbers, 1976a) without ever reaching commercial production.

The extension of a major highway (highway 69) in 2009 provided new and exceptional exposures of numerous pegmatites along roadcuts. Due to a particularly high concentration of pegmatites and the convenient perpendicular orientation of the roadcuts relative to the various host rocks which provides an optimal transect to address pegmatite-host rock interaction, a 12 km section of the highway was selected for detailed field and petrological studies.

Previous work on the highway 69 pegmatite swarm include B.Sc. theses by Van Walraven (2011) and Lorenzo (2017), as well as a detailed geochronology study of the pegmatites by Pfister *et al.* (2023). Together, these studies suggest the following: (1) the pegmatite swarm consists of three different dike generations emplaced at *ca.* 1740 Ma, *ca.* 1450-1430 Ma and *ca*. 1000-970 Ma; (2) widespread sub-solidus fluid:rock interaction occurred through the evolution of the pegmatites that locally remobilized rare-metals (RM; *i.e.*, Nb, Ta, REEs, U, Th); and (3) the youngest and more abundant Neoproterozoic pegmatites exhibit a remarkably large spectrum of primary features, such as disequilibrium textures, internal zoning and other anisotropic features, which range from completely absent to abundant from dike to dike, thus at odds with the current more uniform models for formation of pegmatitic textures (*e.g.,* London, 2008, 2016; Maneta & Baker, 2014; London & Morgan, 2017; Sirbescu *et al.,* 2017).

The three distinct pegmatite-forming events, spanning about 800 Ma, consist of the Yavapai orogeny (late Paleoproterozoic; *ca*. 1740 Ma), the Chieflakian event (Mesoproterozoic; *ca*. 1450-1430 Ma), and the Rigolet phase of the Grenville orogeny (early Neoproterozoic; *ca*. 1000-970 Ma). As discussed in Pfister *et al.* (2023), the presence of age-appropriate potential

progenitors (i.e., intrusions) near their contemporaneous pegmatites (Fig. 2) and lack of evidence for age-appropriate high T regional metamorphism in the study area suggest the pegmatites are associated with magmatism related to the Yavapai orogeny and the Chieflakian event and an origin likely related to fractional crystallization of a parental felsic magma. Contrarily, Neoproterozoic pegmatites associated with the Rigolet phase of the Grenville orogeny are presumably anatectic based on: (1) lack of age-appropriate potential progenitor intrusions in this part of the GTFZ; (2) widespread presence of leucosomes and anatectic sweats of similar age in the host rocks throughout the study area which indicates requisite PT conditions for partial melting were attained during peak regional metamorphism; and (3) presence of similar and contemporaneous anatectic pegmatite fields in other parts of the Grenville and Sveconorwegian provinces in Canada and Scandinavia (*e.g.,* Marsh *et al.*, 2012; Müller *et al.*, 2017). A summary of the geochronology of the pegmatites from Pfister *et al.* (2023) is presented in Figure 3.

5.5 Methods

Fieldwork, which included mapping of all roadcuts along the highway 69 transect shown in Figure 3, detailed mapping of important outcrops, sampling (K-feldspar, quartz, garnet, whole-rock and relevant samples for polished thin sections), structural measurements and field observations, were conducted by the authors from 2016 to 2021.

Sample preparation, which included cutting, making polished thin sections, crushing, hand-picking high-quality quartz and garnet fragments, and making epoxy mounds, was done at the Harquail School of Earth Sciences facilities (Sudbury, ON).

All of the polished thin sections were imaged and analyzed using a scanning electron microscope (SEM) coupled to energy-dispersive spectroscope (EDS) with cathodoluminescence (CL) and back-scattered electron (BSE) imaging capability. The latter utilized a Tescan Vega 3 SEM with an integrated CL detector coupled with a Bruker EDS system with 60 mm^2 X-ray detector housed in the Harquail School of Earth Sciences. The semi-quantitative EDS analyses were done using a 20 kV accelerating voltage, 1.2 nA beam current, working distance ranging from 15 to 18 mm and acquisition time from 3 to 15 s depending on whether data was collected for mineral identification or for chemical comparison. BSE and CL imaging were done using a 15 kV accelerating voltage and a 1.0 nA beam current. Data were processed using a combination of Oxford Instrumentation software AZtec and INCA.

Major and trace elements analyses of K-feldspar and whole-rock samples were done by the Australian Laboratory Services (ALS; Sudbury, ON). The samples were first crushed and pulverized, then underwent Li borate fusion and four acids digestion before analysis *via* Inductively Coupled Plasma Atomic Emission Spectroscopy (ICP-AES) for major elements and Inductively Coupled Mass Spectrometer (LA-ICP-MS) for trace elements. Internal lab standards were analyzed at the beginning and end of each session, while duplicates and blanks were analyzed every five samples.

A selection of high-quality hand-picked quartz fragments were mounted in epoxy pucks and, following grinding and polishing, prepared for in-situ isotopic (O) analysis with Secondary Ion Mass Spectrometry (SIMS) at the University of Manitoba using a Cameca 7F secondary ion mass spectrometer. The following parameters were used: (1) 4 nA primary ion beam of Cs+ accelerated at 10 kV; (2) spot size = 20 µm; (3) entrance slit = 250 µm; (4) deadtime = 27 ns; (5) 70 cycles over 10 minutes; (6) one cycle = 1 s of detection on ^{16}O and 5 s on ^{18}O; and (7) counts

= $1*10^6$ for ^{16}O and $2*10^3$ for ^{18}O. Reference materials consist of UWQ1 Quartz from Kelly *et al.* (2007). Analytical reproducibility for $\delta^{18}O$ on quartz standard is ± 0.8‰. Isotopic values ($\delta^{18}O$) are reported using the δ notation relative to Vienna Standard Mean Ocean Water (V–SMOW).

The trace element contents of the mounted quartz, as well as a selection of high-quality hand-picked garnet fragments, were analyzed using Laser Ablation Inductively Coupled Mass Spectrometer (LA-ICP-MS) at the Laurentian University. The laser ablation system consists of a 193 nm ArF excimer laser (Resonetic Resolution M-50 193 nm probe) coupled to a quadrupole ICP-MS Thermo Electron X Series II. The following parameters were used: (1) laser spot size = 75 µm; (2) pulse duration = 20 ns; (3) repetition rate = 8 Hz; (4) fluence = 5 J/cm2; (5) carrier gas = He; and (6) nebulizer gas = Ar. Each spot consisted of 30 s of background followed by 30 s of ablation. Reference material used consist of NIST 610 for garnet and 612 for quartz (Jochum *et al.*, 2011) and BHVO2G (Jochum *et al.*, 2005). The trace-element data was processed using the Internal Standard DRS method within the software Iolite v.4 (Paton *et al.*, 2011).

Finally, trace element data for a large populations of zircon, monazite and xenotime grains used in a previous geochronological study of the HWY 69 pegmatite swarm (Pfister *et al.*, 2023) were also obtained using LA-ICP-MS at Laurentian University. The system comprised a Photon Machine Analyte G2 ArF excimer laser coupled with a Thermo Scientific iCap-TQ ICP-MS. The data was also processed using the Internal Standard DRS method within the software Iolite v.4 using NIST 610 as reference material and Zr, Ce and Y as internal standards. Note that the theoretical xenotime formula $(Y_{0.75}HREE_{0.25})PO_4$ was used instead of the idealized YPO_4 formula to address the significant atomic mass difference between Y (88.9 amu) and HREE (159 – 175 amu).

5.6 Results

5.6.1 General observations and characteristics

5.6.1.1 Host rocks

The distribution of host rocks is depicted in Figure 3. While highly diverse, the host rocks are grouped in four main categories for the purpose of this study: (1) amphibole-rich rocks (*e.g.,* amphibolite and amphibole-rich gneisses differentiated based on quartz content and presence/absence of banding) (Fig. 4B), biotite-rich paragneisses (Fig. 4C), granite (Fig. 4D) and quartzite (Fig. 4E). The various host rocks are interlayered on the scale of decameter to hectometer (Fig. 5A) and contacts between them are usually sharp (Fig. 5B, C). Overall, there is a higher concentration of biotite gneisses to the north and amphibole-rich rocks and granite to the south (Fig. 4A).

The various packages of biotite gneisses are usually banded (Figs. 4C, 5C), albeit not always (Fig. 5D), and consist mostly of biotite, quartz and plagioclase with highly variable amounts of K-feldspar, amphibole and garnet. Accessory phases include pyrite, titanite, thorite, zircon and monazite (Fig. 5E-I). Kyanite, while not observed by the present authors, has previously been reported in multiple outcrops of the biotite-rich gneisses about 500 m west of pegmatites 1-5 (Fig. 3 A) (Lumbers 1976).

Amphibole-dominated rocks occur either as homogeneous amphibolite (Fig. 4B), occasionally containing plagioclase and garnet (Fig. 5J) or as banded amphibole-dominated orthogneisses (Fig. 5K) containing amphibole, plagioclase and minor quartz with highly variable amounts of garnet and biotite. Accessory phases include pyrite, chalcopyrite, ilmenite and titanite (Fig. 5L-N).

The granite, which is restricted to the southern part of the study area, is often interlayered with amphibolite and amphibole gneisses (Fig. 5A) and usually exhibits foliation (Fig. 5O), albeit not always present (Fig. 4D). It consists of K-feldspar, plagioclase, quartz, biotite and minor amphibole. Accessory phases include zircon, magnetite, ilmenite, titanite, xenotime, rutile, apatite, allanite and secondary REE fluorocarbonate (Fig. 5P, Q, R). Accessory zircon (<30 μm) is particularly abundant with up to 100+ zircon observed per thin section (*e.g.,* Fig. 5Q).

The quartzite, which was only observed in one roadcut (Fig. 4A, E), is putatively composed mostly of quartz (Fig. 5S) with secondary muscovite (Fig. 5T) and accessory rutile (Fig. 5U). Finally, sporadic diabase and lamprophyre dikes were also observed in the study area (Fig. 5V).

5.6.1.2 Leucosomes

Leucosomes are common through the entire field area and occur both in the amphibole-dominated rocks and biotite gneisses and their coalescence is observed in several outcrops (Fig. 6A). Plagioclase (commonly andesine) is always present and is typically the most abundant phase. It occurs as crystals up to 30 cm (Fig. 6B) and many amphibolite-hosted leucosomes consist mostly of plagioclase (Fig. 6C). Quartz also occurs in most leucosomes, albeit in highly variable abundance (*e.g.,* Fig. 6C *versus* 6D). Coarse (0.5 – 4 cm) amphibole is very common in amphibolite-hosted leucosomes (Fig. 6 E). Garnet is commonly observed, but is more common in leucosome in amphibolite (Fig. 6F, G). K-feldspar is common in paragneiss-hosted leucosomes (Fig. 6 H), but scarce where hosted in amphibolite. Biotite is usually found in K-feldspar-free leucosomes (*e.g.,* amphibolite-hosted) and can be locally abundant (Fig. 6 I). The leucosomes are locally pegmatitic with both very coarse grain size (up to 30 cm; Fig. 6B) and disequilibrium

textures such as graphic-like garnet – quartz intergrowth (Fig. 6G). Multiple leucosomes exhibit reaction rims consisting of garnet (Fig. 6J) or biotite (Fig. 6K).

Important accessory phases in amphibolite-hosted leucosomes include titanite (Fig. 6L), blue apatite (Fig. 6M) and sulfides (Fig. 6N). Note that blue apatite is exclusively found in amphibolite-hosted leucosomes and is mutually exclusive with garnet. Biotite gneiss-hosted leucosomes tend to contain less accessory phases than amphibolite-hosted ones and include sporadic allanite-(Ce) (Fig. 6O), molybdenite (Fig. 6P), zircon (Fig. 6Q), titanite (Fig. 6R) and monazite (Fig. 6S).

5.6.1.3 Pegmatites

About 50 pegmatites are exposed along the roadcuts of highway 69 in the study area, and consist mostly of high aspect-ratio dikes ranging from 5 cm to 5 m in width and up to 50 m in length. The pegmatites are remarkably diverse and exhibit a large range of both textural and mineralogical features.

Typical exposures of the various pegmatites are illustrated in Figure 7. Paleoproterozoic pegmatites (Fig. 7 A-C) are typically highly deformed, almost entirely recrystallized with the exception of the more competent quartz core (Fig. 7A), and are aligned parallel to the fabric of the enveloping host rock (Fig. 7C). Mesoproterozoic pegmatites (Fig. 7D-G) are moderately deformed, commonly exhibit low degree of boudinage (Fig. 7E, G), are aligned parallel to the fabric of the host rock (Fig. 7 D, F), and are partially recrystallized, although relict K-feldspar and quartz megacrysts are often present (Fig. 7E, G). Neither Paleoproterozoic nor Mesoproterozoic pegmatites contain coarse primary mica, either biotite or muscovite. In marked contrast, the

Neoproterozoic pegmatites (Fig. 7H-L) are mostly undeformed and their internal zoning ranges from well-developed (Fig. 7H) to completely isotropic (Fig. 7I, J). While some are oriented parallel to the fabric of the host rock, most are discordant to the fabric (*e.g.*, Fig. 7I), including earlier leucosomes (Fig. 7 K, L).

Zoned Neoproterozoic pegmatites (*e.g.,* Fig. 8A) exhibit a large range of mineralogical and textural features. Their border zone commonly consists of medium- to coarse-grained irregular albite-quartz intergrowth (*e.g.,* Fig. 8B); additionally they often contain muscovite, biotite and/or garnet (Fig. 8C, D, E) at their wallrock contact. Feldspar in the border zone sometimes exhibits a funnel-shaped morphology (*i.e.*, inward broadening) and are generally oriented perpendicular to the pegmatite-wallrock contact (Fig. 8F). In contrast, large K-feldspar megacrysts in the inner zone are often irregularly shaped (Fig. 8G) and exhibit graphic texture (Fig. 8H). Quartz sometimes exhibits dendritic morphologies (Fig. 8I, J, K). Coarse-grained intergrowths of muscovite-quartz (Fig. 8 L) are locally abundant and are spatially associated with K-feldspar near the core zones of some pegmatites. Notably, muscovite is more abundant than quartz in these intergrowth which argues against a hydrothermal reaction (breakdown of K-feldspar to quartz-muscovite: $3\ KAlSi_3O_8 + 2H^+$ (*i.e.,* acidic fluid) $= 6\ SiO_2 + KAl_3Si_3O_{10}(OH)_2 + 2\ K^+$). Graphic intergrowth of spessartine-quartz (Fig. 8M, N) is present in a few of the largest pegmatites in the northern part of the study area where it is mostly found along the edges of euhedral K-feldspar megacrysts (Fig. 8M). A similar graphic garnet-quartz intergrowth was also observed in a couple of leucosomes (*e.g.,* Fig. 8 G), although the garnet is almandine rather than spessartine. Although these graphic garnet-quartz intergrowths are rarely reported in pegmatites, it is similar to features Zhang *et al.* (2001) documented in Italian pegmatites. Additionally, garnet commonly occurs as layers (Fig. 8O-R) in the Neoproterozoic pegmatites where they are found at the boundary between the inner and outer

zones (Fig. 8O), or at the edges of K-feldspar megacrysts (Fig. 8P, Q, R). When garnet rims bulbous-shaped K-feldspar megacrysts (a common morphology in large pegmatites near Wanup; *e.g.,* Fig. 8G, Q), they form what we have coined to be "cauliflower" garnet (Fig. 8Q, R). Pegmatitic quartz cores are generally monomineralic, although megacrystic (to 2 m) euhedral crystal of K-feldspar are sometimes observed (Fig. 8S). Sporadic accessory phases in quartz cores include garnet (Fig. 8T), muscovite (Fig. 8U), pyrite (Fig. 8V), and biotite, which is sometimes rimmed by muscovite (Fig. 8W).

On the smaller scale, micro-graphic K-feldspar-quartz intergrowths (Fig. 9A, B) and vermicular albite-quartz intergrowth (Fig. 9C) are common in all Neoproterozoic pegmatites, whether zoned or homogeneous. Perthitic textured K-feldspar (Fig. 9D) is present in all but the most recrystallized Paleoproterozoic pegmatites. Four main types of feldspars are noted in the pegmatites: (1) primitive K-feldspar, ranging from Ab_{25} to Ab_{9}, and often exhibiting perthitic texture; (2) end-member K-feldspar ($Ab_{<2}$); (3) low-Ca albite ($An_{<8}$); and (4) oligoclase (An_{12-22}). Four types of feldspars and their textural relationships are seen in Figure 9E-H. End-member K-feldspar is invariably the last phase and replaces both oligoclase (Fig. 9E, F) and low-Ca albite (Fig. 9G, H). Low-Ca albite is generally observed replacing primitive K-feldspar (Fig. 9H), but never end-member K-feldspar. Neither oligoclase nor primitive K-feldspar are observed replacing any earlier phase. Figure 9H shows primitive K-feldspar (in a primary K-feldspar-quartz intergrowth) being partially replaced by low-Ca albite, itself being replaced by end-member K-feldspar along fractures and within pits. Of particular interest here is the development of porosity and abundant hematite deposition associated with the replacement of plagioclase (*i.e.,* oligoclase and low-Ca albite) by end-member K-feldspar (Fig. 9F, G). One of the striking features of the Highway 69 pegmatites is the intense hematization of feldspars, particularly plagioclase (*e.g.,* Fig.

8F), which seems to be associated with their K-feldspathization, and thus suggest the presence of a K-, Fe-rich fluid during the sub-solidus evolution of the pegmatites.

Common accessory phases in Neoproterozoic pegmatites include zircon, xenotime, uraninite, thorite, columbite-(Fe), monazite, and apatite (Fig. 9I-L). Late-stage phases (other than hematite) in fractures and pits include galena, chalcopyrite, pyrite, xenotime, zircon, various Nb-Ta-Ti-U(±Ca, Pb, REEs, Fe) oxides, and Cu-Zn carbonate (Fig. 9M-U). It is worth noting that many of these late-stage (*i.e.*, re-mobilized) phases include elements that are traditionally considered immobile, such as REEs, Nb, Ta, Zr, Ti, Th and U.

The most common accessory phases in Mesoproterozoic pegmatites include zircon, monazite and xenotime (Fig. 10A, B). Late-stage phases include uraninite, magnetite, various Nb-Ta-Ti-U(±Ca, Pb, REEs, Fe) oxides, quartz veinlets and zircon (Fig. 10C-I). Allanite-(Ce), which is observed in Neoproterozoic (locally abundant; see Fig. 13) and Mesoproterozoic pegmatites in addition to the Paleoproterozoic Estaire granite, is often partially or entirely replaced by bastnäsite (LREE fluorocarbonate) (see Fig. 10J, K. Large (cm to dm) masses of an unidentified phase exhibiting intense radiation haloes was noted in a few pegmatites, but are now entirely replaced by a mixture of chlorite, thorite, allanite-(Ce), zircon, and other HFSE phases (Fig. 10L-N).

Heavy mineral concentrates of 32 pegmatites produced by Pfister *et al.* (2023) for a geochronology study of the Highway 69 pegmatites contained some textures and minerals that are relevant to the present study and are therefore described here. A selection of grains showing features that were not otherwise observed in polished thin section is presented in Figure 11 and include: (1) abundant fragments of zoned rutile hosted in calcite (Fig. 11A), where the zoning is due to Nb (4.5 wt% Nb_2O_5; Fig. 11B); (2) pseudomorphs of bladed hematite after unidentified euhedral precursors (Fig. 11C, D), which are sometimes associated with μm-sized grains of

monazite-(La) (Fig. 11E); (3) magnetite-rutile intergrowths (Fig. 11F); (4) pyrite rimmed by magnetite in chalcopyrite (Fig. 11G); (5) xenotime rimming and crosscutting uraninite (Fig. 11H); and (6) intensely altered zircon exhibiting porosity development via CDP. Also note that rutile and/or ilmenite was found in all but 3 of the concentrates, which is relevant for Ti-based geothermometry presented below.

CL imaging of pegmatitic quartz (Fig. 12) reveals complex textures with multiple generations of quartz and abundant CDP features.

5.6.1.4 Pegmatite #6

Pegmatite 6 is an exceptionally well exposed example of a zoned Neoproterozoic K-feldspar-rich pegmatite associated with a chemically-distinct apatite-rich pegmatitic leucosome and a fine- to medium-grained allanite-rich border zone (Fig. 13A, B). The K-feldspar-rich pegmatite, which is notable reddened, is zoned with a well-developed quartz core (Fig. 13 B, C), an inner zone and a fine- to medium-grained border zone. The inner zone, which represent the bulk of the pegmatite, has a similar mineralogy than other Neoproterozoic pegmatites and consists mostly of very coarse-grained primitive K-feldspar (~Ab_{20}), oligoclase (~An_{13}) and quartz, as well as minor biotite. The finer-grained border zone contains the highest concentration of allanite-(Ce) (Fig. 13F, G, H) observed in the study area with single crystals up to 10 cm long, as well as locally abundant apatite up to 5 mm (Fig. 13F), which is otherwise lacking in other pegmatites (where scarce isolated apatite crystal rarely exceed 50 μm; *e.g.,* Fig. 9L). The pegmatitic leucosome to the left consists mostly of megacrystic plagioclase ranging from oligoclase (An_{22}) to andesine (An_{39}), with minor quartz, annite (Fig. 13D) and widespread prismatic accessory blue apatite (Fig. 13E)

up to 4 cm. This assemblage is typical of leucosomes observed across the study area (see above) and differs from the K-feldspar-bearing pegmatites with a lack of K-feldspar, more calcic plagioclase and abundant blue apatite. Pfister *et al.* (2023) dated zircon from both the pegmatitic leucosome and the Kf-rich pegmatite which yielded overlapping ages of 981.7 ± 1.6 Ma (n = 38) and 977.3 ± 2.4 Ma (n = 13), respectively.

5.6.1.5 Pegmatite #9W

Pegmatite #9W is a zoned Neoproterozoic pegmatite situated in the northern part of the study area (Fig. 3). It is one of the larger pegmatites exposed along the highway and one of the few Neoproterozoic pegmatites exhibiting some degree of deformation. That the pegmatite is exposed as a large, accessible, flattish, glacially polished surface provided an opportunity to see in detail its intricate internal feature which was captured with a detailed map (Fig. 14). It consists mostly of irregular-shaped megacrystic (50-150 cm) K-feldspar (Fig. 8G) in a matrix of albite/oligoclase, quartz, muscovite and minor K-feldspar. The K-feldspar megacrysts often exhibit graphic texture (Fig. 8H) and are sometimes rimmed by garnet (*i.e.*, "cauliflower garnet"; Figs. 8Q, R), although not always (Fig. 8G). The detailed outcrop map (Fig. 14) reveals a quartz core, as well as a distribution of garnet and muscovite-quartz intergrowth (Fig. 8L) concentrated around the core of the pegmatite. Importantly the graphic texture is noted to vary considerably in term of the development of its abundance and the scaling (*i.e.*, feature per unit area). Additionally, this pegmatite is seen to extend eastwards across highway 69 where development of graphic texture continues and is even more irregular in its development. (*i.e.*, grain size).

5.6.2 Structural data

Close to 500 strike and dip measurements of fabrics in the hosts, leucosomes and pegmatites in the study area are shown in Figure 15. The fabrics in the leucosomes and the host rocks are generally oriented along the SW-NE axis, which is parallel to the Grenville Front. The pegmatites do not exhibit any obvious trend, although slightly more of them are oriented along the SSE-NNW and ESE-WNW axes, which are roughly orthogonal to the fabric of the host rocks.

Additional structural features and observations are summarized in Figure 16. These include: (1) local shear zones (Fig. 16A) ; (2) en echelon leucosomes (Fig. 16B) and pegmatites (Fig. 16C, D) ; (3) intensely deformed Paleo- and Mesoproterozoic pegmatites exhibiting dynamic recrystallization of the original K-feldspar megacrysts (Fig. 16E) and relic quartz core (Fig. 7A); (4) gneissic fabric of the ca. 1740 Ma Estaire Pluton (Fig. 16F); (5) undeformed pegmatite crosscutting the host rock fabric (Fig. 16G) and leucosomes (Fig. 7K, L); (6) folding of the pegmatites (Fig. 16H); (7) ductile deformation of wallrock fragments and ribbons in pegmatites (Fig. 16I, J, K); (8) weak boudinage of Paleo- and Mesoproterozoic pegmatites (Fig. 7D-E); and (9) deformation twinning of pegmatitic plagioclase (Fig. 16L). Overall, the pegmatites exhibit a large range of deformation intensity, even within the Neoproterozoic generation.

Finally, crosscutting relationships between pegmatites are rare, but pegmatite 38, an undeformed Neoproterozoic pegmatite, crosscuts pegmatite 39 and undated fine-grained granitic dikes (Fig. 17).

5.6.3 Whole-rock and mineral chemistry

5.6.3.1 Whole-rock

Whole-rock analyses of the host rocks (amphibolite, biotite gneiss), leucosomes, the Estaire Pluton (Fig. 3) and the fine-grained granitic dikes seen in Figure 17 are reported in Table 1. The chemistry of the fine-grained granitic dikes (# 72-77) is distinct from the Estaire Pluton (# 70-71) that is enriched in REEs, HFSE (*e.g.,* Nb, Ta, Zr, Ti), as well as FeO and MgO, whereas the fine-grained granitic dikes contain higher SiO_2, Ba and Sr.

Garnet-bearing and garnet-free amphibolite (#81-82), as well as garnet-bearing and garnet-free biotite gneiss (#83-84) were also analyzed. As expected, the amphibolite contains higher MgO, FeO and CaO whereas the biotite gneiss contains higher K_2O and SiO_2. Na_2O and Al_2O_3 contents are similar in both host rock types. As for trace elements, the biotite gneiss contains more HFSE (Zr, Hf, U, Th, REEs), whereas the amphibolite contains slightly more mafic elements (*e.g.,* V, Cr) and volatiles. There is no significant differences in composition between garnet-bearing versus garnet-free amphibolite samples.

A sample of garnet-bearing leucosome (#78) was analyzed but did not reveal any significant geochemical features and is compositionally similar to the fine-grained granitic dikes (# 72-77) with the exception of lower LREEs. Whole-rock analysis of a lamprophyre (#79) dike reveals, as expected, high MgO, K_2O, P_2O_5, Ti, Ba, Sr and volatiles.

5.6.3.2 K-feldspar

Fresh K-feldspar megacrysts from selected pegmatites were analyzed for both major and trace elements, which are summarized in Table 2. Most of the pegmatites are Neoproterozoic (*ca.*

990-960 Ma), with the exception of pegmatite 24 which is Mesoproterozoic (*ca*. 1450 Ma) and pegmatite 48 which is indeterminate, but either Neoproterozoic or Mesoproterozoic (see discussion in Pfister *et al.* 2023). The bulk chemistry of the K-feldspars are overall uniform and show limited variation, which suggest primary signatures will show little subsolidus modification. Overall, the chemistry of the K-feldspar (*e.g*., K/Rb, K/Cs; Cerny *et al*., 1985; London, 2022) suggest the pegmatite-forming melts were relatively primitive. The K-feldspar from pegmatite 24, the only unequivocally Mesoproterozoic pegmatite included in this dataset, exhibits significantly higher Fe than the Neoproterozoic pegmatites, as well as moderately elevated Ba, Sr contents. While these elements typically reflect sub-solidus fluid:rock interaction, it is worth noting that pegmatite 24 contains abundant primary magnetite. The chemistry of K-feldspar from pegmatite 48, whose age is indeterminate, exhibits no distinctive compositional difference from the other pegmatites of this dataset. The rest of this dataset (Neoproterozoic pegmatites only) was georeferenced and plotted on the map of the study area to investigate potential regional zoning, as is often observed in pegmatite fields (*e.g.,* Cerny, 1991; London, 2008), but revealed no regional zoning in terms of K-feldspar chemistry.

5.6.3.3 Garnet

Fresh garnet samples (n = 72) from various pegmatitic zones (*e.g.,* border zone, outer zone, inner zone, core zone) and assemblages (*e.g.,* quartz-garnet graphic intergrowth (Fig. 8M, N), garnet-bearing quartz-muscovite intergrowth (Fig. 8L)), as well as garnets from the wallrock and their leucosomes, were analyzed for both major and trace elements. The major elements data are summarized in Table 3 and Figure 18, while the detailed results of the trace elements are presented

in supplementary File 1. Note that Cr, La and Th were also analyzed, but not reported as they were consistently below the limit of detection (LOD). Conversion of garnet composition into end-member components was done using the method of Locock (2008).

Pegmatitic garnets belong to the spessartine-almandine series with minor (<5%) pyrope and grossular components. As for trace elements, the pegmatitic garnets are enriched (1000s ppm) in (H)REE and HFSE. There is a direct correlation between the composition of the garnets and their location within the pegmatites (*e.g.,* border zone, inner zone, core, etc.), as shown in Figure 18, which is noted to be independent of their spatial context. With few exceptions (*e.g.,* garnet from the core of the pegmatites), the Mn-, HFSE- and REE-content of the garnets increases away from the wallrock contact towards the core zones. Figure 19 shows weak to moderate positive correlation between Mn and various trace elements (*i.e.,* Ga, Ge, Hf, Nb, Ta, Ti, Zn, Zr), which again depends on which zone or assemblage the garnet come from.

Garnets from the host rocks are all almandine with significant (< 30%) grossular component, lesser pyrope (< 15%) and minor spessartine (< 5%) components. Biotite-gneiss-hosted garnets are richer in Ca than amphibolite-hosted ones, and garnets from leucosomes exhibit higher Fe content, while Mn and Mg contents are relatively constant across all garnets from the various host rocks (Table 3, Fig. 18).

A traverse across a euhedral gem-quality garnet from the "cauliflower" garnet texture in Peg. 9W (Fig. 8Q, R) was done to address potential zoning and investigate the nature and origin of this texture. While there is no significant variation in major elements, the trace elements, in particular REEs, showed some considerable changes from core to rim (Fig. 20). Elements that are compatible in garnet (*i.e.*, Y, HREEs, Sc) increase in concentration from core to rim, whereas incompatible elements (*i.e.,* LREEs, Ta, Nb, Zr, Hf, U) decrease from core to rim and moderately

compatible elements (*i.e.*, MREEs) do not exhibit any particular trend and are relatively constant from core to rim.

5.6.3.4 Quartz chemistry and geothermometry

Fresh quartz samples from selected pegmatites were analyzed for a variety of trace elements (*i.e.*, Li, Be, B, Na, Al, P, K, Ca, Ti, V, Cr, Mn, Ge, As, Rb, Sr, Y, Sn, Cs, Ba, REEs). Of these, only Al, P, Ti and Ge were present in meaningful quantities and are reported in Table 4. For others such as Na, K, Sr, Sn, Ba, and the REEs, they were detected in most samples, but yielded values too close to the limited of detection (LOD) and analytical uncertainty to be meaningfully interpreted here. Suspiciously high (up to 590 ppm) and constant Ca values, also reported by Lorenzo (2017), are here interpreted as the result polyatomic interferences (*i.e.,* $^{44}Ca = {}^{28}Si^{16}O^{+}$). Other elements (*i.e.*, Li, Be, B, V, Cr, Mn, As, Rb, Cs) were not detected.

Al content is highly variable and ranges from 15 to 394 ppm with a mean of 67 ppm and a standard deviation of ±77 ppm, which indicates that the data do not follow a normal distribution. The P content is the most constant of all elements analyzed and ranges from 16.0 to 27.2 ppm with a mean of 20.9 ppm and a standard deviation of ±2.9 ppm. The Ti content is variable and ranges from 3.0 to 30.4 ppm with a mean of 7.8 ppm and a standard deviation of ±5.6 ppm. The Ge content is also variable and ranges from 0.50 to 3.67 ppm with a mean of 1.0 ppm and a standard deviation of ±0.6 ppm. There is no apparent correlation among the Al, P, Ti and Ge contents for the quartz. The Ge/Ti ratio of quartz, a reliable index of magmatic evolution (*e.g.*, Jacamon and Larsen, 2009) ranges from 0.03 to 0.88 with a mean of 0.29.

Overall, the trace elements in quartz do not exhibit any correlation with the ages of the pegmatites (*i.e.*, Paleo- Meso- and Neoproterozoic) or the host rocks (see Fig. 4). Additionally, the data do not show any type of regional zoning when georeferenced and plotted spatially.

The Ti-in-quartz geothermometer "TitaniQ" (Wark and Watson, 2006; Thomas *et al.*, 2010; Huang and Audétat, 2012), which has been previously applied to granitic pegmatites (*e.g.,* Müller *et al.*, 2015; Ashworth *et al.*, 2020; Pfister *et al.*, 2023b), is used to estimate the temperature of quartz formation. Correct application of this method requires several parameters to be addressed, such as Ti diffusion in quartz, pressure and αTiO_2. These are inferred to be about 90 μm (Cherniak *et al.*, 2007), 6 kbar (Lumbers, 1976), and 0.5 (presence of ilmenite), respectively. However, these factors do not affect the calculated temperatures by more than ± 50 °C in the range of temperatures expected for pegmatite formation (*i.e.*, 500-600 °C) (see discussion in Pfister *et al.*, 2023b). Therefore, all calculated temperatures are reported here with a ± 50 °C uncertainty to avoid any ambiguity regarding the estimation of the aforementioned parameters.

Overall, the calculated temperatures (summarized in Fig. 21) are in good agreement with temperature of pegmatite formation (*i.e.*, 450-600 °C; London, 2008; Simmons *et al.*, 2008) with 94% of the data overlapping with the 500-600 °C range. The calculated temperature of quartz formation in an amphibole-hosted leucosome of haplogranitic composition is 601 ± 50 °C, which is higher than 88% of the calculated temperature of pegmatitic quartz formation.

5.6.3.5 Trace element chemistry of zircon, monazite and xenotime, geothermometry and oxybarometry

Large populations of zircon (n = 774), monazite (n = 230) and xenotime (n = 295) from 33 different pegmatites covering the entire study area and all ages of pegmatites (*i.e.,* Paleo-, Meso- and Neoproterozoic) were analyzed for trace elements (supplementary File 2), in addition to U-Pb geochronology (Pfister *et al.,* 2023).

Overall, these accessory phases are U-rich: 93% of the zircon contain >1000 ppm U, 75% of the monazite contain >1000 ppm U, and 100% of the xenotime contain >1000 ppm U (with 38% having >10,000 ppm U). This caused widespread metamictization, which in turn affected trace element content during subsequent fluid:rock interaction and mobilization. For example, Sr, Ca, Fe and LREE are effective at identifying disturbed U-Pb systematics in zircon (Fig. 22) and thus metamictization, as these elements do not fit in the crystalline structure of zircon (*e.g.*, Geisler *et al.*, 2003). Additionally, the trace elements often help distinguish among the different generations of zircon, monazite and xenotime on the local scale (Pfister *et al.,* 2023). However, they do not exhibit any apparent spatial or temporal trend on the regional scale (Fig. 23).

Despite significant overlap, the chondrite-normalized (McDonough and Sun, 1995) REE profiles for zircon, monazite and xenotime (Fig. 23) reveal the following: (1) discordant zircon are strongly enriched in REE, particularly LREE (up to 50-fold increase); (2) concordant zircon exhibit subtle positive Ce and negative Eu anomalies; (3) concordant REE phosphates exhibit a strong negative Eu anomaly; (4) discordant xenotime are slightly enriched in LREE (mostly La and Ce); (5) discordant and concordant monazite share the same REE profile, which is partially due to monazite's resistance to radiation damage (*i.e.,* metamictization) (*e.g.,* Meldrum *et al.,* 1997; Meldrum *et al.*, 1998); (6) concordant Mesoproterozoic zircon are slightly enriched in LREE compared to concordant Neoproterozoic zircon (note that not enough concordant Paleoproterozoic and older zircon were found and analyzed by Pfister *et al.*, (2023) to draw similar conclusions,

although they do show different profiles; see Fig. 23 A); and (7) REE phosphates from pegmatite 52B formed under more oxidized conditions than other pegmatites.

Ti-in-zircon geothermometry (Watson *et al.,* 2006; Fu *et al.*, 2008) was attempted using the same parameters as for the Ti-in-quartz geothermometry discussed above. However, 22% of the zircon contain below LOD Ti content or have too great an analytical uncertainty whereas the rest cover most of the temperature range for terrestrial magmas from ~600 to ~1400°C (Fig. 24). Concordant zircon (U-Pb) cover a smaller yet still large range from ~600 to ~1000°C (with a few outliers >1000°C), which do not represent a reasonable temperature for pegmatite formation.

Similarly, the Trail *et al.* (2012) and the Loucks *et al.* (2020) zircon oxybarometers were used with moderate success, as shown in Figure 25. The data from low-T concordant zircon suggest that they formed under slightly reduced conditions ($\log(fO_{2(sample)}) - \log(fO_{2(FMQ)}) = -2$ to 0), although extrapolating the oxybarometers (calibrated for >800°C) to temperature of pegmatite formation (*i.e.,* 500 - 600°C) yields some degree of uncertainty. The large spread in both T and fO_2 for the rest of the zircon can be attributed to sub-solidus fluid:rock interaction and attest to how widespread this process was.

5.6.4 Oxygen isotopes

$\delta^{18}O_{quartz}$ values for 29 measurements for quartz from 21 localities range from 8.0 to 14.0‰ and there is intra-locality variation outside of that expected from analytical reproducibility (Table 5). When plotted on a map of the study area (Fig. 26), the data reveal no clear regional trend, although the six values above 12.0 ‰ are all located in the northern part of the study area, thus away from the Estaire Pluton. All samples originating from the granite-rich part of the study area

(Fig. 26) yielded values below 11.1‰. It is noted that plotting $\delta^{18}O_{quartz}$ values *versus* calculated Ti-in-quartz temperatures does not yield any apparent correlation.

5.7 Discussion

5.7.1 Nature of the pegmatites

5.7.1.1 Pegmatite and melt signatures

The high K/Rb (*i.e.,* 164 - 809) and K/Cs (*i.e.,* 8,975 – 128,302) ratios of the K-feldspars (Table 2) indicate that the pegmatite-forming melt(s) were not highly evolved (*e.g.,* Shaw, 1968; Shearer *et al*., 1985). This is consistent with the relatively primitive mineralogy observed in the pegmatites and lack of notable enrichment of LILE and HFSE that might otherwise be expected.

Using the K/Rb-Ga discrimination diagram from Wise (2013), the chemistry of primary K-feldspar suggest the pegmatites have an NYF (Nb-Y-F) geochemical signature, which again is consistent with the mineralogy observed (*e.g*. locally abundant Nb(±Ta)-, U(±Th)-, Y+REE-accessory phases; see Figs. 9, 10).

5.7.1.2 Temperature of pegmatite formation

The Ti-in-quartz geothermometer (Huang and Audétat, 2012) suggests that the pegmatites formed around 500 to 600°C (Fig. 21), which is in good agreement with empirical and experimental data on T of pegmatite formation available in the literature, in particular for simple pegmatites (Webber *et al.*, 1999; London, 2005, 2008; Simmons & Webber, 2008). It is further supported by the abundance of disequilibrium-related (*i.e.*, undercooling) textures presented in

Figure 8, which would be favoured by higher initial melt temperatures and less evolved magmas not enriched in flux elements (*e.g.,* F, B. Li).

The Ti-in-zircon geothermometer (Watson *et al*., 2006) yielded less robust data, which we attribute to the fact that it is not calibrated for the low temperatures relevant to the present study. For example, 2 ppm Ti (the LOD for Ti in the present LA-ICP-MS analyses), yields a temperature of formation of 602°C, which is why all calculated values plot above 600°C (Fig. 24). However, the calculated values using this calibration qualitatively indicate the zircon formed at relatively low temperature (Fig. 24).

5.7.1.3 Oxidation state

The trace-elements-in-zircon oxybarometer of Loucks *et al*. (2020) yielded a large spread of values (Fig. 25) with the majority of data concentrated between $\log(fO_{2(\text{sample})})$ - $\log(fO_{2(\text{FMQ})})$ values of -2 to 0 (Fig. 25B), suggesting that the melt was slightly reduced. However, all concordant zircon have positive Ce anomalies (Ce/Ce* > 1.5; see Sup. File 2), as is seen in the chondrite-normalized REE patterns (Fig. 23A, B), indicating that they were formed under relative oxidizing conditions. Moreover, the absence of fayalite but presence of both primary quartz and magnetite (*e.g*., Peg 24) confirm that the pegmatites formed under more oxidizing conditions than the FMQ buffer, and not more reduced as the Loucks *et al*. (2020) oxybarometer suggests.

5.7.1.4 Regional zoning

Various georeferenced maps of trace elements in quartz, K-feldspar, garnet, zircon, monazite and xenotime were produced to investigate potential zoning across the Highway 69 pegmatite swarm. These plots did not however yield any meaningful regional spatial trend. A map of $\delta^{18}O_{quartz}$ values shows that all pegmatites hosted in the southern granite-rich area (*i.e.*, Estaire Pluton) have values below 11.1‰ and six of the pegmatites hosted in gneiss packages in the northern part of the study area have values above 12.0‰. This reflects pegmatite:WR interaction, which are further discussed below in section 5.3.

5.7.1.5 Structural controls on pegmatite emplacement

A comparison of the rose diagrams for the host rocks, leucosomes and pegmatites (Fig. 15) reveals that the host rocks and leucosomes share a preferred orientation along a NE-SW axis, that is parallel to the Grenville Front, while the granitic pegmatites have no apparent preferred orientation. This is in part due to the fact that older generations of pegmatites were overprinted by the main deformation event during the Grenville Orogeny and consequently share the same orientation as the fabric of the host rocks (*e.g.*, Fig. 7C, D, F), whereas the Neoproterozoic pegmatites are generally crosscutting the fabric of the host rock (*e.g.*, Fig. 7I, K, L). However, even the Neoproterozoic pegmatites exhibit a wide range of orientations, although slightly more of them are oriented along the SSE-NNW and ESE-WNW axes, which are roughly orthogonal to fabric of the host rocks.

The main controls on the morphology and orientation of pegmatites at the time of their emplacement involved some combination of fluid pressure, lithostatic and directed stresses, host rocks rheology, strength and ductility anisotropies, as well as dilational directions (Brisbin, 1986).

The large range of morphologies, ranging from irregular bulbous (*e.g.*, Fig. 7H) to straight thin dikes (*e.g.*, Fig. 5A), and seemingly random orientations (Fig. 15) of the Neoproterozoic pegmatites suggest a complex interplay between these controls. This, in turn, suggests that the Neoproterozoic pegmatites were emplaced under different conditions (*i.e.*, variable deviatoric stress) and thus not emplaced simultaneously. For example, irregular bulbous pegmatites are typical of ductile/transitional conditions and thin straight dikes are typical of brittle conditions (Brisbin, 1986). Additionally, the abundance of disequilibrium-related textures and well-developed internal zoning in some Neoproterozoic pegmatites but not others, which is directly correlated to the degree of undercooling (Lofgren, 1974; London, 2008; Maneta & Baker, 2014; London & Morgan, 2017; Sirbescu *et al.*, 2017), suggest different host rock temperatures during emplacement, which further support asynchronous emplacement of the Neoproterozoic pegmatites. Finally, it is worth noting that the U-Pb dating of the pegmatites by Pfister *et al.* (2023) yielded variable ages ranging from 956.2 ± 7.7 Ma to 996.2 ± 6.5 Ma for the Neoproterozoic pegmatites, although higher-precision dating would be required to further address this question.

5.7.2 Evolution of the pegmatites

The textural and mineralogical information presented in the result section has been used to construct a paragenesis of the Neoproterozoic pegmatites (Fig. 28), which forms in part the basis of the following discussion on the evolution of the pegmatites. Note that the mineralogy varies from one pegmatite to another as they were likely asynchronous, thus this represent a generic paragenesis of the Neoproterozoic pegmatites.

5.7.2.1 Magmatic stage

5.7.2.1.1 Primary mineralogy

The primary mineral assemblage (see Fig. 28) of the pegmatites consist of quartz (*e.g.*, Fig. 7, 8) K-feldspar of relatively primitive composition (Ab_{9-25}) (*e.g.,* Fig. 9, Table 2) and oligoclase (An_{12-22}) (*e.g.,* Fig. 9), with minor muscovite (*e.g.*, Fig. 8), biotite (*e.g.*, Fig. 8), and garnet of the almandine-spessartine series (*e.g.*, Figs. 8, 18, Table 3). Common accessory magmatic phases include allanite, zircon, xenotime, monazite, and various Nb-, Y(±HREE)-, Ti-, U- oxides, such as euxenite and columbite (*e.g.*, Figs. 8, 9, 10), which are all common in NYF pegmatites (Ercit, 2005; London, 2008), including many pegmatite fields associated with the Grenville and Sveconorwegian Orogens (*e.g.*, Ercit, 1994, 2005; Müller *et al.*, 2017, Turlin *et al.*, 2017).

The Ge/Ti ratio in quartz, a reliable indicator of magmatic differentiation (*e.g.*, Larsen *et al.*, 2004; Jacamon & Larsen, 2009; Breiter *et al.*, 2017) that is particularly robust during sub-solidus processes (Larsen *et al.*, 2004), ranges from 0.03 to 0.75 with a mean of 0.29 (Table 4). These values are similar to contemporaneous anatectic NYF pegmatites of the Sveconorwegian Orogeny (*i.e.*, extension of the Grenville Orogeny in Scandinavia), such as the Evje pegmatite field (Larsen *et al.*, 2004), and indicate a low degree of magmatic fractionation. This is further supported by the relatively high K/Rb and K/Cs ratios in fresh perthitic K-feldspar megacrysts (Table 2), which range from 164 to 809 and 8,975 to 128,302, respectively, and which also indicate a low degree of magmatic fractionation.

The chemistry of fresh primary garnets (Table 3, Sup. File 1 and Fig. 18), all part of the almandine-spessartine series, exhibit a strong positive correlation between their Mn-content and spatial location relative to the pegmatite-wallrock contact (Fig. 18). The closer the garnets are to

the wallrock contact, the higher their Fe content (and conversely for Mn), which reflects wallrock interaction. Since garnets exhibit very few CDP features (*i.e.*, robust to sub-solidus processes), no apparent zoning under BSE (*e.g.*, Fig. 20A), invariably euhedral morphologies, and an absence of Mn-bearing secondary mineral assemblages in the study area, we interpret this pegmatite-wallrock interaction to be associated with the magmatic stage. Thus, the concentration of Mn in garnet reflects a geochemical coupling with the wallrock which indicates the pegmatites behaved as a partially open system during their emplacement and subsequent magmatic evolution. Such open-system behaviour in pegmatites has been repeatedly documented in the literature (*e.g*., Taylor *et al.*, 1979; Lentz, 1996; Kontak, 2006; Martin & De Vito, 2015; Fuchsloch *et al.*, 2018; Pfister *et al.*, 2023b), despite multiple experimental models of pegmatite formation arguing for a strictly closed-system behaviour (*e.g.*, Jahns & Burnham, 1969; Černý, 1991 and references therein; London & Morgan, 2017).

Trace elements in garnet (Sup. File 1) reveal high concentrations of HSFE and HREE (*e.g*., up to 6,500 ppm Y; Fig. 20), as expected in REE-enriched NYF pegmatites (*e.g.*, Müller *et al.*, 2012). Figure 19, which compares the Mn-content of the garnets against several trace elements (*i.e.,* Ga, Ge, Hf, Nb, Ta, Ti, Zn, Zr), exhibits weak to moderate positive correlations which indicates these elements are internally derived, with the possible exception of Ti, which is abundant in wallrock-hosted garnets. A rim-to-rim traverse in a garnet from the "cauliflower" garnet texture domain (*e.g.,* Fig. 8Q) shows that compatible elements (*e.g.,* Y, HREE) decrease from core to rim, whereas the incompatible elements increase (Fig. 20). These trends are typical of Rayleigh fractionation, which implies a locally closed system, such as a pocket of residual melt or a boundary layer (Webber *et al*., 1997, London, 2008, 2018).

Thus, garnet chemistry supports a partially open-system behaviour at the dike scale during emplacement, while the rim-to-rim trace elements profiles indicate a locally closed-system behaviour.

5.7.2.1.2 Primary textures

The Highway 69 pegmatite group exhibits a very large range of textures (see Figs. 8 to 12). Some are restricted to a few dikes - *e.g.*, dendritic quartz (Fig. 8I, J, K), graphic garnet-quartz intergrowth (Fig. 8M, N), coarse muscovite-quartz intergrowth (Fig. 8L) – whereas others are present in most or all undeformed pegmatites (*e.g.*, graphic texture (Fig. 8H, 9A, B) and irregular albite/oligoclase-quartz intergrowth (Fig. 8B, 9C)).

Many of these textures, such as dendritic morphologies, (micro-)graphic texture and high aspect-ratio crystals oriented perpendicular to the wallrock contact, are indicative of disequilibrium conditions promoted by undercooling (Lofgren, 1974; Maneta & Baker, 2014; London & Morgan, 2017; Sirbescu *et al.,* 2017). Experiments by London (2008), Maneta & Baker (2014) and Sirbescu *et al.* (2017) showed that irregular bimineralic intergrowth, graphic texture and high aspect-ratio crystals form under a moderate degree of undercooling (*e.g.*, 50 to 150°C), whereas skeletal and dendritic crystal morphologies form under higher degrees of undercooling (*e.g.*, 100 to 290°C). The latter textures were only observed in pegmatites exhibiting the most well-developed internal zoning (*e.g.*, pegmatites 5, 19, 44), which also exhibits the sharpest decrease in grain size in their border zones (Fig. 8B); all of this supports a large degree of undercooling. The high aspect-ratio crystals, irregular bimineralic intergrowth and coarse graphic texture were mostly observed in pegmatites exhibiting weak to moderately developed internal zoning (*e.g.*, pegmatites

5, 6, 7, 8, 9, 22, 27, 39, 45, 46, 52) and a less significant grain size decrease in their border zones, which supports a moderate degree of undercooling. Finally, where homogenous and weakly internally zoned (*e.g.*, Fig. 7I, J, L), the pegmatites lack most of these textures, with the exception of microscopic to fine-grained graphic texture; these observations suggest a low degree of undercooling and a small temperature differential between the pegmatites and host rocks.

Besides these well-documented disequilibrium-related textures, two other textures observed in the Neoproterozoic pegmatites remain more ambiguous: (1) "cauliflower" garnet (Fig. 8Q); and (2) coarse muscovite-quartz intergrowth (Fig. 8L).

The "cauliflower" garnet and garnet layers (Fig. 8O) have a very similar chemistry (Table 3, Fig. 18) that overlaps with that of isolated garnets found in the inner zone (Fig. 18) where both layered and "cauliflower" garnets are found (Fig. 14). Garnet layers are found in a variety of pegmatites ranging from weakly internal (*e.g.,* pegmatite 18) to strongly zoned (*e.g.*, pegmatite 5), while "cauliflower" garnet is only found in moderately to strongly internally zoned pegmatites (*e.g*., pegmatites 9, 44). Because of their Mn-rich chemistry (Fig. 18) and distribution (*i.e.*, edges of megacrysts (Fig. 8P) or between inner and outer zones (Fig. 8O)), it is most likely that the garnet layers represent crystallization of excluded components along the crystallization front (*cf*., London, 2008; London & Morgan, 2017), as has been documented in many other pegmatites (*e.g*., Webber *et al.,* 1997; Morgan & London, 1999; Felch, 2014; Felch *et al.*, 2016). The similar compositions, euhedral morphologies, and distribution of "cauliflower" garnet around K-feldspar megacrysts (Figs. 8Q, 14) suggest they formed in the same way as the garnet layers. Additionally, the trace element traverses of a select "cauliflower" garnet, indicative of locally closed system as discussed above, further supports their formation from a boundary layer at the edge of a rapidly growing K-feldspar megacryst. However, the bulbous morphology of the K-feldspar megacryst,

which in turn is responsible for the so-called “cauliflower” texture, remains enigmatic and needs further study.

Similarly to “cauliflower” garnet, the coarse muscovite-quartz intergrowth (Fig. 8L) is restricted to moderately-to-strongly internally zoned pegmatites (*e.g.*, pegmatites 8, 9, 44). This texture, rarely reported in the literature, was also observed by the first author in the pegmatites of the West Mount Apatite mining district (Maine, USA) and in the pegmatites of the White Picacho mining district (Arizona, USA). Two aspects of this texture are noted: (1) it is invariably found with K-feldspar, which has a broadly similar chemistry; and (2) the muscovite consists of coarse (cm to dm) books. Breakdown of K-feldspar to a muscovite-quartz intergrowth ($3\ KAlSi_3O_8 + 2H^+ = 6\ SiO_2 + KAl_3Si_3O_{10}(OH)_2 + 2\ K^+$) is very common in felsic rocks and is also observed in other pegmatites in the study area (*e.g.*, pegmatite 29). However, such replacement texture is usually observed as a fine-grained intergrowth of muscovite and quartz, commonly accompanied by porosity development. Here, the muscovite consists of coarse books, and porosity development is not observed. Additionally, replacement of K-feldspar by a fine-grained muscovite-quartz intergrowth is observed in both the outter and inner zones of the pegmatites, whereas this coarse intergrowth is spatially restricted to the inner zone, usually in the vicinity of the quartz core, as illustrated in Figure 14. Finally, accessory garnet occurring in the coarse muscovite-quartz intergrowth has a very evolved composition (*i.e.,* high Mn, HFSE and REE contents; Figs. 18, 19), suggesting a primary magmatic origin.

Note that primary textures in Meso- and Paleoproterozoic pegmatites are harder to address as they were deformed during the Grenville orogeny and are partially to entirely re-crystallized. However, micro-graphic texture is observed in megacrystic K-feldspar remnants in Mesoproterozoic pegmatites in the southernmost part of the study area (Fig. 3).

5.7.2.2 Metasomatic stage

While most of the macroscopic textures visible in the Neoproterozoic pegmatites are primary, there is also a profusion of secondary features seen of both textural and mineralogical nature on the microscopic scale. Such microscopic features are often overlooked in pegmatites in favor of the more exotic staple pegmatitic textures, which have captured geologists' attention for well over a century (*e.g.*, Hunt, 1871). This is an observation common to many pegmatites world-wide (*e.g*. Kontak, 2006; Martin & De Vito, 2014; Pfister *et al*., 2023b), which has greatly contributed to the common misconception that pegmatites are purely magmatic vessels and that metasomatism is basically absent in all but the most evolved pegmatites (*e.g*., London, 2008, 2018; London & Morgan, 2017). We present here evidence for multiple stages of metasomatism from the earlier primitive magmatic stage to the subsequent modification of the Highway 69 pegmatite group.

5.7.2.2.1 Early metasomatism

5.7.2.2.2 Perthite

The first generation of K-feldspar crystals (Fig. 28), which were originally formed as homogeneous sanidine (*e.g*., Parsons & Lee, 2005) are now present as perthitic microcline (*e.g*., Fig. 9D) with a primitive composition ranging from Ab_{15} to Ab_{23}, as seen in our analyses of large (>500 g) hand samples (see Table 2). Perthitic texture is an exsolution-related phenomenon which occurs under subsolidus conditions and thus is a unequivocally secondary feature. Furthermore,

the development and coarsening of perthitic (*i.e.*, film through flame to bead; see Parsons & Lee, 2005) is accompanied by porosity development, a fundamental feature of CDP processes indicative of fluid-mediated reactions (Worden *et al.* 1990, Putnis 2002, Parsons & Lee 2005, Plumper & Putnis 2009, Maneta & Anderson 2018). The presence of K-feldspar exhibiting macroscopic perthitic texture across the study area attest to widespread fluid:rock interactions (*i.e.*, metasomatism).

5.7.2.2.3 Albitization

Besides the development and coarsening of perthitic texture, the first generation of K-feldspar is often partially replaced by albite (*i.e.*, $Ab_{<8}$) (Fig. 9H), which is also accompanied by secondary quartz (dark under CL, see Fig. 12), and minor muscovite (Fig. 28); the latter represents a local sink for excess K released during albitization of K-feldspar, as is often observed with late-stage albitic units in more evolved pegmatites (*e.g.*, Černý, 1991; Kontak *et al.,* 2002; Kontak, 2006; Kontak & Kyser, 2009; Pfister *et al.*, 2023b).

The albitization of K-feldspar is widespread, yet not pervasive. It can be found in most pegmatites along Highway 69, but is usually observed as a minor feature in most dikes, which likely reflects a preservation bias. Secondary albite was subsequently replaced by end-member K-feldspar during later stages of metasomatism, as discussed below. It is therefore likely that this feature was more abundant than its current distribution suggests. In some dikes, albitization of K-feldspar is associated with sporadic accessory phases such as xenotime (Fig. 9P) and various Nb-bearing oxides (*e.g.,* Fig. 9R). Additionally, grains of ilmenite found in or near secondary albite are being replaced by a rutile-magnetite intergrowth.

Albitization of K-feldspar, often associated with rare-metal mineralization, is a particularly common feature in evolved pegmatites (Černý 1982a, Černý 1989, Suwimonprecha *et al.* 1995, Fuertes-Fuente & Martin-Izard 1998, Lumpkin 1998, Sweetapple & Collins 2002, Kontak 2006, Kontak & Kyser 2009, Wise & Brown 2011, Kaeter *et al.* 2018, Fuchsloch *et al.* 2019), but is less commonly reported in more primitive pegmatites, such as the Highway 69 pegmatite group.

Finally, we note that such albitization of K-feldspar is seldom observed in the K-feldspar - bearing host rocks and leucosomes, and thus likely related to a pegmatite-derived sodic fluid, as is commonly documented in pegmatites (*e.g.*, Jahns, 1955; Jahns and Burnham, 1969; Černý, 1989; London, 2008; Kontak & Kyser, 2009; Kaeter *et al.* 2018; Pfister *et al.*, 2023b).

5.7.2.2.4 Late metasomatism

One of the salient features of the Highway 69 pegmatite group is their intense hematization (*e.g.*, Figs. 7, 8, 9; Van Walraven, 2011; Lorenzo, 2017), which reflects significant pegmatite-wallrock interaction, as the Neoproterozoic pegmatites are generally Fe-poor (*e.g.*, garnet chemistry), whereas the host rocks contain 6.9 – 17.5 wt % Fe_2O_3 (Table 1). A distinguishing feature of this process in the pegmatites is that plagioclase (*i.e.*, both primary oligoclase and secondary albite) are commonly more intensely hematized than K-feldspar (*e.g.*, Figs. 7H, I, 8F). Transmitted light microscopy shows that plagioclase is often more porous than K-feldspar, and BSE imaging of the samples reveals various degrees of K-feldspathization of plagioclase associated with porosity development and hematization (*e.g.,* Fig. 9 E-H). This suggest fluid-mediated CDP processes related to a K-, Fe- bearing fluid, which is further supported by the presence of secondary biotite associated with this assemblage. Accessory phases associated with

this metasomatic stage include abundant rare-metal oxides (Figs. 9R, S, T), zircon (Fig. 9Q), monazite (Fig. 10F) and uraninite (Fig. 10C), as well as various sulphides (*e.g.*, Fig. 9M, N, O). These features are all found within pores rimmed by near-end-member K-feldspar in oligoclase and/or albite, as indicated by the brighter color under BSE (Figs. 9, 10). Note that monazite associated with hematization is La-dominant, as Ce becomes quadrivalent under oxidizing conditions.

Interestingly, K-feldspathization and hematization of plagioclase are absent in the leucosomes (Fig. 6), despite abundant plagioclase, albeit of slightly different composition (*i.e.*, andesine). This is particularly evident near pegmatite 6 (Fig. 3), where the younger pegmatite is directly adjacent to the slightly older (Pfister *et al*., 2023) leucosome (Fig. 13), yet only the feldspars in the pegmatite are hematized and those in the leucosome relatively fresh and not hematized (*i.e*., quite glassy). The same is observed adjacent to other pegmatites that crosscut leucosomes (*e.g*., Fig, 7K, L). Nonetheless, intense hematization of plagioclase, and to a lesser extent K-feldspar, is observed in pegmatites of all ages. This suggests that either the fluid was internally-derived, which is at odds with the large amount of Fe associated with this stage of metasomatism, or that the fluid simply did not react with the more Ca-rich plagioclase present in the host rocks and leucosomes.

5.7.3 Rare-metal mineralization

Rare-metal (*i.e.,* Nb, Ta, Y, REE and U) mineralization occurs through the entire evolution of the pegmatites. Primary mineralization usually occurs as inclusions and μm- to mm-sized euhedral crystals of columbite, various Nb-Y(±REE, U) oxides, monazite, xenotime, allanite and

uraninite (Figs. 9I-K, 10A, B), although cm- to dm-sized crystals of allanite-(Ce) (*e.g.*, Fig. 13) and unidentified radioactive phase(s) (*i.e.*, presence of radiation halo), now replaced by a mixture of chlorite, thorite, allanite and zircon (Fig. 10L, M) were observed. Note that the highest concentration of allanite is observed in the border zone (*e.g.*, Fig. 13), suggesting that some of the elements (*i.e.*, Ca, Fe) might have been externally-derived, and local pegmatite-wallrock interaction might have triggered allanite crystallization during the magmatic stage. Similar processes in pegmatites have been experimentally and empirically documented in the literature (*i.e.*, London *et al.*, 1996; Van Lichtervelede *et al*., 2007; Linnen *et al*., 2019).

Metasomatic-related rare-metal mineralization is abundant and seems to be mostly associated with K-feldspathization and hematization of feldspars, as also noted by Lorenzo (2017). These consist mostly of Nb(±Ta) - Y(±REE) - U(±Th) - Ti oxides of highly variable chemistry, sometimes present as mixtures. Note that the primary oxides generally have Fe>Ca, whereas the secondary oxides are more often Ca- or Pb- dominant (Fig. 9R, S). Whereas some might argue that metasomatism should produce fewer phases (*e.g.* Van Lichtervelede *et al*., 2007; Linnen *et al.*, 2019) and that these rare-metals are considered immobile (*e.g.*, Taylor *et al.,* 2005, Wood, 2005; Van Lichtervelde *et al.,* 2007), their morphologies and distribution (*i.e.*, irregular masses filling pores and fractures associated with K-, Fe- metasomatism; see Figs. 9, 10) indicate beyond reasonable doubt that these are secondary. Of relevance to the above are experiments by Timofeev *et al.* (2015, 2017) and Anderson *et al.* (2019), which demonstrate that Nb and Ta can be re-mobilized by acidic, F-bearing fluids. Additionally, Harlaux *et al.* (2017) and Fredriksson (2017) recently documented Ta- and Nb-enrichment in fluid inclusions from pegmatites. Furthermore, the widespread presence of late-stage bastnäsite in the pegmatites (*e.g*., Fig. 10J, K, N) suggest the

presence of an acidic, CO_2-, F-bearing fluid which is particularly efficient at re-mobilizing REE and other HFSE (*e.g.*, Sheard *et al.*, 2012; Gysi & Williams-Jones, 2013).

Finally, the presence of these secondary rare-metals-bearing phases being restricted to the pegmatites and absent in the host rocks suggest that the REE and HFSE elements were internally-derived from the pegmatites and subsequently remobilized on the local scale.

5.8 Summary and conclusions

The Highway 69 pegmatite group represent a rare example of a polygenerational pegmatite swarm that was emplaced over a period spanning >800 Ma. Even the younger and more abundant Neoproterozoic pegmatites, which are interpreted to be of anatectic origin, were likely asynchronously emplaced, as suggested by the different degrees of undercooling, structural controls, and textural and mineralogical variations between the dikes.

The pegmatites exhibit a relatively primitive chemistry with a mild NYF signature associated with minor, yet widespread Nb(±Ta) - Y(±REE) - U(±Th) mineralization, much of which has been re-mobilized during metasomatism.

Whereas the vast majority of the macroscopic textures are primary, there is an overwhelming abundance of secondary features (both textural and chemical) on the microscopic scale, suggesting that the pegmatites underwent significant sub-solidus fluid:rock interaction during their evolution. This shows that, contrarily to popular belief, metasomatism is not limited to the most evolved pegmatites, but is in fact common even in primitive ones.

This study also documents significant pegmatite-wallrock interaction, during both the magmatic stage (*i.e.*, magmatic garnet chemistry) and the prolonged metasomatic stage (*i.e.*, intense hematization), and demonstrates that pegmatites evolve as partially open systems, contrarily to what popular models of pegmatite formation suggest (*e.g.*, Jahns & Burnham, 1969; Černý, 1991; London & Morgan, 2017).

5.9 Future Work

Several aspects of the Highway 69 pegmatite group deserve further work (*e.g.*, mica chemistry, detailed structural study, detailed study of the rare-metals oxides, etc.), but of particular interest to the topics discussed above is the secondary mineralogy associated with the various metasomatic stages (*e.g.,* secondary zircon, xenotime, monazite, RM oxides, allanite and bastnäsite), which could potentially be dated to accurately constrain the timing of metasomatism.

5.10 Acknowledgements

The authors would like to thank Drs. Jeffrey Marsh, Joe Petrus and Longbo Yang for their help with LA-ICP-MS analyses, as well as Drs. William Zhe and Kirk Ross for their assistance regarding the calibration and usage of the SEM-EDS and SEM-CL at the Laurentian University. This study was supported financially by an NSERC Discovery Grant to Dr. Daniel Kontak and a GTA fellowship to Jérémie Pfister from the Laurentian University.

5.11 References

Ames D. E., Davidson A. and Wodicka N. (2008) Geology of the Giant Sudbury Polymetallic Mining Camp, Ontario, Canada. *Econ. Geol.* **103**, 1057–1077.

Anderson A. J., Mayanovic R. A. and Lee T. (2019) The local structure of Ta(V) aqua ions in high temperature fluoride and chloride-bearing solutions: Implications for Ta transport in granite-related postmagmatic fluids. *Can. Mineral.* **57**, 1–19.

Ashworth L., Kinnaird J. A., Nex P. A. M., Harris C. and Müller A. B. (2020) Origin of rare-element-mineralized Damara Belt pegmatites: A geochemical and light stable isotope study. *Lithos* **372**–**373**, 105-155.

Ayer J., Amelin Y., Corfu F., Kamo S., Ketchum J., Kwok K. and Trowell N. (2002) Evolution of the southern Abitibi greenstone belt based on U-Pb geochronology: Autochthonous volcanic construction followed by plutonism, regional deformation and sedimentation. *Precambrian Res.* **115**, 63–95.

Van Breemen O. and Davidson A. (1989) Northeast extension of Proterozoic terranes of mid-continental North America: Discussion. *Bull. Geol. Soc. Am.* **101**, 755–756.

Breiter K., Ďurišová J., Hrstka T., Korbelová Z., Hložková Vaňková M., Vašinová Galiová M., Kanický V., Rambousek P., Knésl I., Dobeš P. and Dosbaba M. (2017) Assessment of magmatic vs. metasomatic processes in rare-metal granites: A case study of the Cínovec/Zinnwald Sn–W–Li deposit, Central Europe. *Lithos* **292**–**293**, 198–217.

Brisbin W. C. (1986) Mechanics of pegmatite intrusion. *Am. Mineral.* **71**, 644–651.

Burns M. G. (2019) A fluid inclusion study of the Little Nahanni LCT-type pegmatite group, NWT Canada: Implications for the nature and origin of fluids in LCT-type pegmatites and pegmatite evolution. Laurentian University.

Černý P. (1982a) Anatomy and classification of granitic pegmatites. *Mineral. Assoc. Canada, Short Course Handb.* **8**, 1–39.

Černý P. (1982b) The Tanco pegmatite at Bernic Lake, southeastern Manitoba. *Mineral. Assoc. Canada, Short Course Handb.* **8**, 527–543.

Černý P. (1989) Characteristics of pegmatite deposits of tantalum. In *Lanthanides, Tantalum and Niobium* Berlin. pp. 195–239.

Černý P. (1991) Rare-element Granitic pegmatite:Anatomy and internal evolution of pegmatite deposits. *Geosci. Canada* **18(2)**, 49–67.

Černý P. and Ercit T. S. (2005) The classification of granitic pegmatites revisited. **43**, 2005–2026.

Černý P., Meintzer R. E. and Anderson A. J. (1985) Extreme fractionation in rare-element granitic pegmatites: selected examples of data and mechanisms. *Can. Mineral.* **23**, 381–421.

Cherniak D. J., Watson E. B. and Wark D. A. (2007) Ti diffusion in quartz. *Chem. Geol.* **236**, 65–74.

Craddock J. P., Rainbird R. H., Davis W. J., Davidson C., Vervoort J. D., Konstantinou A., Boerboom T., Vorhies S., Kerber L. and Lundquist B. (2013) Detrital zircon geochronology and provenance of the Paleoproterozoic Huron (~2.4-2.2 Ga) and Animikie (~2.2-1.8 Ga) basins, southern Superior province. *J. Geol.* **121**, 623–644.

Davidson A. and Van Breemen O. (1994) *U-Pb ages of granites near the Grenville Front, Ontario*.,

Easton R. M. and Murphy E. I. (2000) Map 3427 - Geology of the Street Township. *Ontario Geol. Surv.*

Easton R. M. and TerMeer M. (2004) Map 3535 - Geology of the Henry and Loughrin Townships. *Ontario Geol. Surv*.

Ellsworth H. V. (1926) Toddite - A new Uranium mineral from Sudbury District, Ontario. *Am. Mineral.* **11**, 332–334.

Ercit T. S. (2005) REE-Enriched Granitic Pegmatites. *Rare-element geochemistry Miner. Depos.*, 175–199.

Ercit T. S. (1994) The geochemistry and crystal chemistry of columbite-group minerals from granitic pegmatites, southwestern Grenville Province, Canadian Shield. *Can. Mineral.* **32**, 421–438.

Felch M., Falster A. U. and Simmons W. B. (2016) Iron-bearing pollucite and tourmaline replacement of garnet in the garnet line in the Mt. Mica and havey pegmatites, western Maine. *Can. Mineral.* **54**, 1071–1086.

Felch M. M. (2014) The Garnet Line in Oxford County , Maine Pegmatites . University of New Orleans.

Fredriksson J. R. (2017) Fluid inclusion and trace-element analysis of the rare- element pegmatite bodies Altim and Tamanduá from the Borborema Province, Brazil. University of Helsinki.

Fu B., Page F. Z., Cavosie A. J., Fournelle J., Kita N. T., Lackey J. S., Wilde S. A. and Valley J. W. (2008) Ti-in-zircon thermometry: Applications and limitations. *Contrib. to Mineral. Petrol.* **156**, 197–215.

Fuchsloch W. C., Nex P. A. M. and Kinnaird J. A. (2018) Classification, mineralogical and geochemical variations in pegmatites of the Cape Cross-Uis pegmatite belt, Namibia. *Lithos* **296**–**299**, 79–95.

Fuchsloch W. C., Nex P. A. M. and Kinnaird J. A. (2019) The geochemical evolution of Nb–Ta–Sn oxides from pegmatites of the Cape Cross–Uis pegmatite belt, Namibia. *Mineral. Mag.* **83**, 161–179.

Fuertes-Fuente M. and Martin-Izard A. (1998) The Forcarei Sur rare-element granitic pegmatite field and associated mineralization, Galicia, Spain. *Can. Mineral.* **36**, 303–325.

Gysi A. P. and Williams-Jones A. E. (2013) Hydrothermal mobilization of pegmatite-hosted REE and Zr at Strange Lake, Canada: A reaction path model. *Geochim. Cosmochim. Acta* **122**, 324–352.

Harlaux M., Mercadier J., Bonzi W. M. E., Kremer V., Marignac C. and Cuney M. (2017) Geochemical Signature of Magmatic-Hydrothermal Fluids Exsolved from the Beauvoir Rare-Metal Granite (Massif Central, France): Insights from LA-ICPMS Analysis of Primary Fluid Inclusions. *Geofluids*.

Harley S. L. and Kelly N. M. (2007) Zircon: Tiny but timely. *Elements* **3**, 13–18.

Hewitt D. F. (1952) *Feldspar in Ontario*.,

Huang R. and Audétat A. (2012) The titanium-in-quartz (TitaniQ) thermobarometer: A critical examination and re-calibration. *Geochim. Cosmochim. Acta* **84**, 75–89.

Hunt, T. S. (1871). Notes on granitic rocks. *American Journal of Science*, (3), 182-191

Jacamon F. and Larsen R. B. (2009) Trace element evolution of quartz in the charnockitic Kleivan granite, SW-Norway: The Ge/Ti ratio of quartz as an index of igneous differentiation. *Lithos* **107**, 281–291.

Jahns R. H. (1955) The study of pegmatites. *Econ. Geol.* **50th Anniv**, 1025–1130.

Jahns R. H. and Burnham C. W. (1969) Experimental studies of pegmatite genesis: I. A model for the

derivation and crystallization of granitic pegmatites. *Econ. Geol.* **64**, 843–864.

Jochum K. P., Weis U., Stoll B., Kuzmin D., Yang Q., Raczek I., Jacob D. E., Stracke A., Birbaum K., Frick D. A., Günther D. and Enzweiler J. (2011) Determination of reference values for NIST SRM 610-617 glasses following ISO guidelines. *Geostand. Geoanalytical Res.* **35**, 397–429.

Jochum K. P., Willbold M., Raczek I., Stoll B. and Herwig K. (2005) Chemical characterisation of the USGS reference glasses GSA-1G, GSC-1G, GSD-1G, GSE-1G, BCR-2G, BHVO-2G and BIR-1G using EPMA, ID-TIMS, ID-ICP-MS and LA-ICP-MS. *Geostand. Geoanalytical Res.* **29**, 285–302.

Kaeter D., Barros R., Menuge J. F. and Chew D. M. (2018) The magmatic–hydrothermal transition in rare-element pegmatites from southeast Ireland: LA-ICP-MS chemical mapping of muscovite and columbite–tantalite. *Geochim. Cosmochim. Acta* **240**, 98–130.

Knoll T., Schuster R., Huet B., Mali H., Onuk P., Horschinegg M., Ertl A. and Giester G. (2018) Spodumene pegmatites and related leucogranites from the austroalpine unit (eastern alps, central europe): Field relations, petrography, geochemistry, and geochronology. *Can. Mineral.* **56**, 489–528.

Kontak D. J. (2006) Nature and origin of an LCT-suite pegmatite with late-stage sodium enrichment, Brazil Lake, Yarmouth County, Nova Scotia. I. Geological setting and petrology. *Can. Mineral.* **44**, 563–598.

Kontak D. J., Dostal J., Kyser K. and Archibald D. A. (2002) A petrological, geochemical, isotopic and fluid-inclusion study of 370Ma pegmatite-aplite sheets, Peggys Cive, Nova Scotia, Canada. *Can. Mineral.* **40**, 1249–1286.

Kontak D.J., Groat L., & Barnes E.M. (2004) A visit to the Little Nahanni rare-element pegmatites, N.W.T., and other curiosities along the way. *Newsletter of the Mineralogical Association of Canada* **42(5)**, p. 1, 4, 5, 20, 21

Kontak D. J. and Kyser T. K. (2009) Nature and origin of an LCT-suite pegmatite with late-stage sodium enrichment, Brazil Lake, yarmouth county, Nova Scotia. II. Implications of stable isotopes (δ18o, δd) for magma source, internal crystallization and nature of sodium metasomatism. *Can. Mineral.* **47**, 745–764.

Larsen R. B., Henderson I., Ihlen P. M. and Jacamon F. (2004) Distribution and petrogenetic behaviour of trace elements in granitic pegmatite quartz form South Norway. *Contrib. to Mineral. Petrol.* **147**, 615–628.

Lentz D. (1996) U, Mo, and REE mineralization in late-tectonic granitic pegmatites, southwestern Grenville Province, Canada. *Ore Geol. Rev.* **11**, 197–227.

Van Lichtervelde M., Salvi S., Beziat D. and Linnen R. L. (2007) Textural features and chemical evolution in tantalum oxides: Magmatic versus hydrothermal origins for Ta mineralization in the Tanco Lower pegmatite, Manitoba, Canada. *Econ. Geol.* **102**, 257–276.

Linnen R., McNeil A. and Flemming R. (2019) Some Thoughts On Metasomatism in Pegmatites. *Can. Mineral.* **57**, 765–766.

Locock A. J. (2008) An Excel spreadsheet to recast analyses of garnet into end-member components, and a synopsis of the crystal chemistry of natural silicate garnets. *Comput. Geosci.* **34**, 1769–1780.

Lofgren G. (1974) An experimental study of plagioclase crystal morphology; isothermal crystallization. *Am. J. Sci.* **274**, 243–273.

London D. (2022) A Rayleigh model of cesium fractionation in granite-pegmatite systems. *Am. Mineral.*

107, 82–91.

London D. (2005) Granitic pegmatites: An assessment of current concepts and directions for the future. *Lithos* **80**, 281–303.

London D. (2018) Ore-forming processes within granitic pegmatites. *Ore Geol. Rev.* **101**, 349–383.

London D. (2008) *Pegmatites*., The Canadian Mineralogist, Special Publication 10, Quebec.

London D. and Morgan G. B. (2017) Experimental crystallization of the Macusani Obsidian, with applications to lithium-rich granitic pegmatites. *J. Petrol.* **58**, 1005–1030.

London D., Morgan G. B. and Wolf M. B. (1996) Boron in granitic rocks and their contact aureoles. *Rev. Mineral. Geochemistry* **33**, 299–330.

Lorenzo R. I. (2017) Relevance of fluid:rock interaction in Proterozoic pegmatites near Sudbury, Ontario to mineralization in rare-metal pegmatite settings. Laurentian University.

Loucks R. R., Fiorentini M. L. and Henriquez G. J. (2020) New magmatic oxybarometer using trace elements in zircon. *J. Petrol.* **61**.

Lumbers S. B. (1976a) Geology of the Burwash Area Districts of Nipissing, Parry Sound, and Sudbury. *Ontario Geol. Surv.*

Lumbers S. B. (1976b) Map 1196 - Mattawa-Deep River area (western half), District of Nipissing. *Ontario Geol. Surv.*

Lumpkin G. R. (1998) Rare-element mineralogy and internal evolution of the Rutherford #2 pegmatite, Amelia County, Virginia:A classic locality revisited. *Can. Mineral.* **36**, 339–353.

Maneta V. and Anderson A. J. (2018) Monitoring the crystallization of water-saturated granitic melts in real time using the hydrothermal diamond anvil cell. *Contrib. to Mineral. Petrol.* **173**, 1–18.

Maneta V. and Baker D. R. (2014) Exploring the effect of lithium on pegmatitic textures: An experimental study. *Am. Mineral.* **99**, 1383–1403.

Marsh J. H., Gerbi C. C., Culshaw N. G., Johnson S. E., Wooden J. L. and Clark C. (2012) Using zircon U-Pb ages and trace element chemistry to constrain the timing of metamorphic events, pegmatite dike emplacement, and shearing in the southern Parry Sound domain, Grenville Province, Canada. *Precambrian Res.* **192**–**195**, 142–165.

Martin R. F. and De Vito C. (2014) The late-stage miniflood of Ca in granitic pegmatites: An open-system acid-reflux model involving plagioclase in the exocontact. *Can. Mineral.* **52**, 165–181.

Martin R. F. and De Vito C. (2005) The patterns of enrichment in felsic pegmatites ultimately depend on tectonic setting. *Can. Mineral.* **43**, 2027–2048.

Mcdonough W. F. and Sun S. S. (1995) The composition of the Earth. *Chemical* **120**, 223–253.

Meldrum A. and Boatner L. (1997) Displacive radiation effects in the monazite- and zircon-structure orthophosphates. *Phys. Rev. B - Condens. Matter Mater. Phys.* **56**, 13805–13814.

Meldrum A., Boatner L. A., Weber W. J. and Ewing R. C. (1998) Radiation damage in zircon and monazite. *Geochim. Cosmochim. Acta* **62**, 2509–2520.

Morgan VI G. B. and London D. (1999) Crystallization of the Little Three layered pegmatite-aplite dike, Ramona District, California. *Contrib. to Mineral. Petrol.* **136**, 310–330.

Müller A., Ihlen P. M., Snook B., Larsen R. B., Flem B., Bingen B. and Williamson B. J. (2015) The chemistry of quartz in granitic pegmatites of southern Norway: Petrogenetic and economic implications. *Econ. Geol.* **110**, 1737–1757.

Müller A., Kearsley A., Spratt J. and Seltmann R. (2012) Petrogenetic implications of magmatic garnet in granitic pegmatites from Southern Norway. *Can. Mineral.* **50**, 1095–1115.

Müller A., Romer R. L. and Pedersen R. B. (2017) The sveconorwegian pegmatite province -thousands of pegmatites without parental granites. *Can. Mineral.* **55**, 283–315.

Parsons I. and Lee M. R. (2005) Minerals are not just chemical compounds. *Can. Mineral.* **43**, 1959–1992.

Paton C., Hellstrom J., Paul B., Woodhead J. and Hergt J. (2011) Iolite: Freeware for the visualisation and processing of mass spectrometric data. *J. Anal. At. Spectrom.* **26**, 2508–2518.

Petrus J. A., Kenny G. G., Ayer J. A., Lightfoot P. C. and Kamber B. S. (2016) Uranium-lead zircon systematics in the Sudbury impact crater-fill: Implications for target lithologies and crater evolution. *J. Geol. Soc. London.* **173**, 59–75.

Pfister J. D., Kontak D. J. and Groat L. (2023) Textural and mineralogical evolution of the Little Nahanni Pegmatite Group (NWT, Canada) with implications for metasomatism, rare-metal mineralization and pegmatite-wall rock interaction. *Can. Mineral.* Accepted with revisions.

Pfister J. D., Kontak D. J. and Marsh J. (2023b) Unraveling 800 Ma of pegmatite formation in the western Grenville Front Tectonic Zone near Sudbury, Canada. *Precambrian Research.* Accepted with revisions.

Plümper O. and Putnis A. (2009) The complex hydrothermal history of granitic rocks: Multiple feldspar replacement reactions under subsolidus conditions. *J. Petrol.* **50**, 967–987.

Putnis A. (2002) Mineral replacement reactions: from macroscopic observations to microscopic mechanisms. *Mineral. Mag.* **66**, 689–708.

Raharimahefa T., Lafrance B. and Tinkham D. K. (2014) New structural, metamorphic, and U–Pb geochronological constraints on the Blezardian Orogeny and Yavapai Orogeny in the Southern Province, Sudbury, Canada. *Can. J. Earth Sci.* **51**, 750–774.

Shaw D. M. (1968) A review of K-Rb fractionation trends by covariance analysis. *Geochim. Cosmochim. Acta* **32**, 573–601.

Sheard E. R., Williams-Jones A. E., Heiligmann M., Pederson C. and Trueman D. L. (2012) Controls on the concentration of Zr, Nb and Rare Earth Elements in the Thor Lake Rare Metal Deposit Canada. *Econ. Geol.* **107**, 81–104. Available at:

Shearer C. K., Papike J. J. and Laul J. C. (1985) Chemistry of potassium feldspars from three zoned pegmatites, Black Hills, South Dakota: Implications concerning pegmatite evolution. *Geochim. Cosmochim. Acta* **49**, 663–673.

Simmons W. B. S. and Webber K. L. (2008) Pegmatite genesis: state of the art. *Eur. J. Mineral.* **20**, 421–438.

Simmons W., Falster A., Webber K., Roda-Robles E., Boudreaux A. P., Grassi L. R. and Freeman G. (2016) Bulk composition of MT. Mica Pegmatite, Maine, USA: Implications for the Origin of An LCT Type Pegmatite by Anatexis. *Can. Mineral.* **54**, 1053–1070.

Sirbescu M. L. C., Schmidt C., Veksler I. V., Whittington A. G. and Wilke M. (2017) Experimental crystallization of undercooled felsic liquids: Generation of pegmatitic texture. *J. Petrol.* **58**, 539–568.

Spence H.S. (1932) Feldspar. Canada Dept. Mines, Mines Br. **731**, 145.

Suwimonprecha P., Cerny P. and Friedrich G. (1995) Rare metal mineralization related to granites and pegmatites, Phuket, Thailand. *Econ. Geol.* **90**, 603–615.

Sweetapple M. T. and Collins P. L. F. (2002) Genetic framework for the classification and distribution of Archean rare metal pegmatites in the North Pilbara Craton, Western Australia. *Econ. Geol.* **97**, 873–895.

Taylor B. E., Foord E. E. and Friedrichsen H. (1979) Stable isotope and fluid inclusion studies of gem-bearing granitic pegmatite-aplite dikes, San Diego Co., California. *Contrib. to Mineral. Petrol.* **68**, 187–205.

Taylor R. P., Pedersen J. C., Bubar D. S., Campbell I. C., Rees K., Morgan J. A. and Barclay W. A. (2005) The nature and distribution of tantalum mineralization in pegmatite dikes, Lilypad Lakes property, Fort Hope, Northwestern Ontario. *Explor. Min. Geol.* **14**, 31–44.

Thomas J. B., Watson E. B., Spear F. S., Shemella P. T., Nayak S. K. and Lanzirotti A. (2010) TitaniQ under pressure: The effect of pressure and temperature on the solubility of Ti in quartz. *Contrib. to Mineral. Petrol.* **160**, 743–759.

Thomson J. E. (1959) Map 2017 - Broder, Dill, Neelon and Dryden Townships. *Ontario Geol. Surv.*

Timofeev A., Migdisov A. A. and Williams-Jones A. E. (2015) An experimental study of the solubility and speciation of tantalum in fluoride-bearing aqueous solutions at elevated temperature. *Geochim. Cosmochim. Acta* **158**, 103–111.

Timofeev A., Migdisov A. A. and Williams-Jones A. E. (2017) An experimental study of the solubility and speciation of tantalum in fluoride-bearing aqueous solutions at elevated temperature. *Geochim. Cosmochim. Acta* **197**, 294–304.

Trail D., Bruce Watson E. and Tailby N. D. (2012) Ce and Eu anomalies in zircon as proxies for the oxidation state of magmas. *Geochim. Cosmochim. Acta* **97**, 70–87.

Turlin F., André-Mayer A. S., Moukhsil A., Vanderhaeghe O., Gervais F., Solgadi F., Groulier P. A. and Poujol M. (2017) Unusual LREE-rich, peraluminous, monazite- or allanite-bearing pegmatitic granite in the central Grenville Province, Québec. *Ore Geol. Rev.* **89**, 627–667.

Van Walraven P. (2011) A textural and mineralogical study of pegmatites on Highway 69, Sudbury, Ontario, with implications for the London model. Laurentian University.

Vignola, P., Zucali, M., Rotiroti, N., Marotta, G., Risplendente, A., Pavese, A., & Bertoldi, G. (2018) The chrysoberyl-and phosphate-bearing albite pegmatite of Malga Garbella, Val Di Rabbi, Trento province, Italy. *The Canadian Mineralogist*, **56**, 411-424.

Wark D. A. and Watson E. B. (2006) TitaniQ: A titanium-in-quartz geothermometer. *Contrib. to Mineral. Petrol.* **152**, 743–754.

Watson E. B., Wark D. A. and Thomas J. B. (2006) Crystallization thermometers for zircon and rutile. *Contrib. to Mineral. Petrol.* **151**, 413–433.

Webber K. L., Falster A. U., Simmons W. B. and Foord E. E. (1997) The role of diffusion-controlled oscillatory nucleation in the formation of line rock in pegmatite-aplite dikes. *J. Petrol.* **38**, 1777–1791.

Webber K. L., Simmons W. B., Falster A. U. and Foord E. E. (1999) Cooling rates and crystallization dynamics of shallow level pegmatite-aplite dikes, San Diego County, California. *Am. Mineral.* **84**, 708–717.

Webber K. L., Simmons W. B., Falster A. U. and Hanson S. L. (2019) Anatectic pegmatites of the Oxford County pegmatite field, Maine, USA. *Can. Mineral.* **57**, 811–815.

Wise M. A. and Brown C. D. (2011) Chemical composition of coexisting columbite-group minerals and cassiterite from the Black Mountain pegmatite, Maine. *Eur. J. Mineral.* **23**, 817–828.

Wise, M. A., Simmons, W. B., Webber, K. L., Falster, A. U., Roda-Robles, E., Hanson, S. L., and Galliski, M. A. (2013). The discrimination of LCT and NYF granitic pegmatites using mineral chemistry: A pilot study. In *Contributions to the 6th International Symposium on Granitic Pegmatites PEG2013,* pp. 156-157.

Wood S. A. (2005) The aqueous geochemistry of zirconium, hafnium, niobium and tantalum. In *Rare-element geochemistry and mineral deposits* (eds. R. L. Linnen and I. M. Samson). GAC Short Course Notes 17, Ontario. pp. 217–268.

Worden R. H., Walker F. D. L., Parsons I. and Brown W. L. (1990) Development of microporosity, diffusion channels and deuteric coarsening in perthitic alkali feldspars. *Contrib. to Mineral. Petrol.* **104**, 507–515.

Zhang C., Giere R., Stiinitz H., Brack P. and Ulmer P. (2001) Quartz-garnet intergrowths in granitic pegmatites from Bergell and Adamello, Italy. *Schweizer Mineral. und Petrogr. Mitteilungen* **81**, 89–113.

5.12 Tables and figures

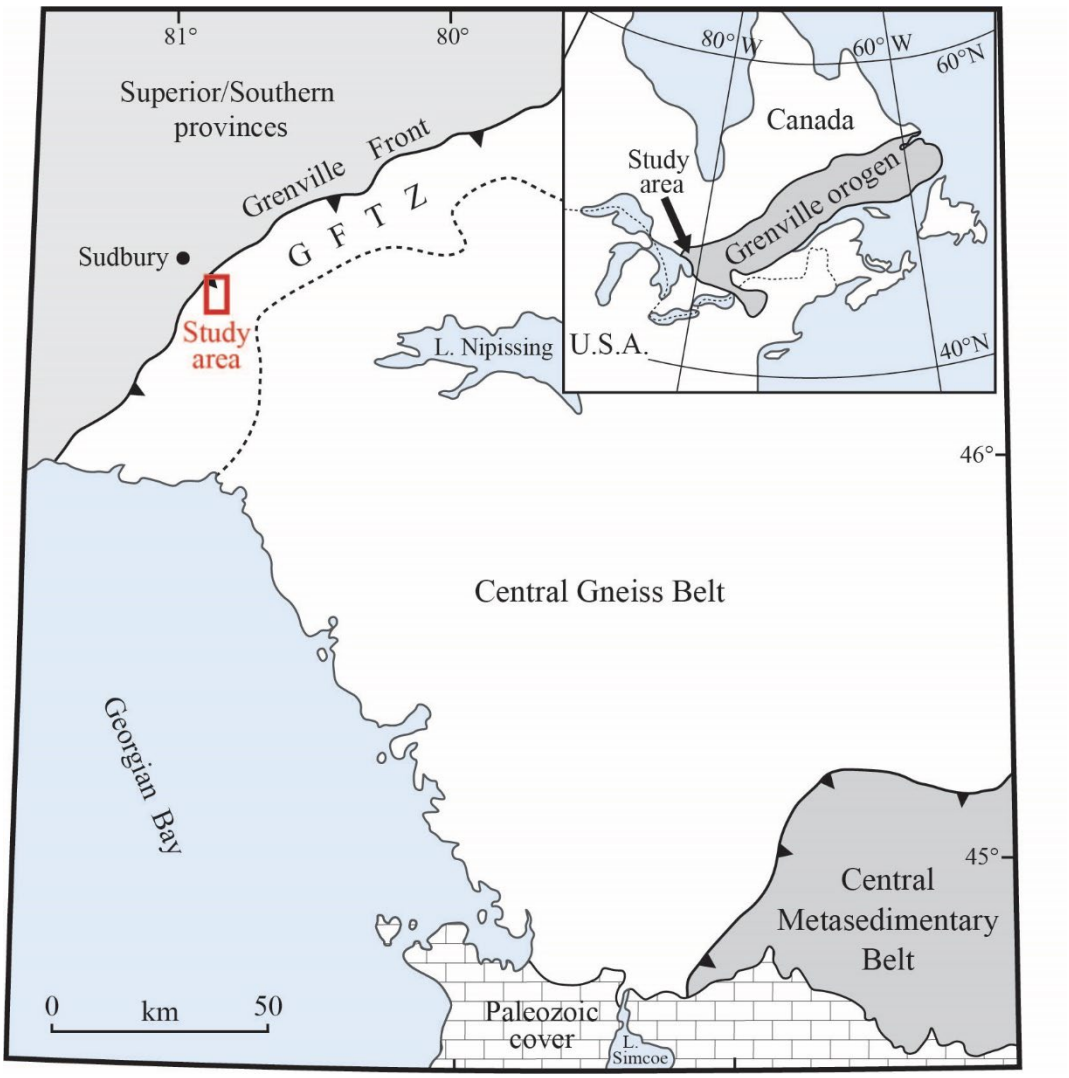

Fig. 1. Simplified geological map of southern Ontario, Canada, showing the extent of the Grenville Province and location of the study area (in red) south of Sudbury (modified after Marsh *et al.*, 2012). GFTZ = Grenville Front Tectonic Zone.

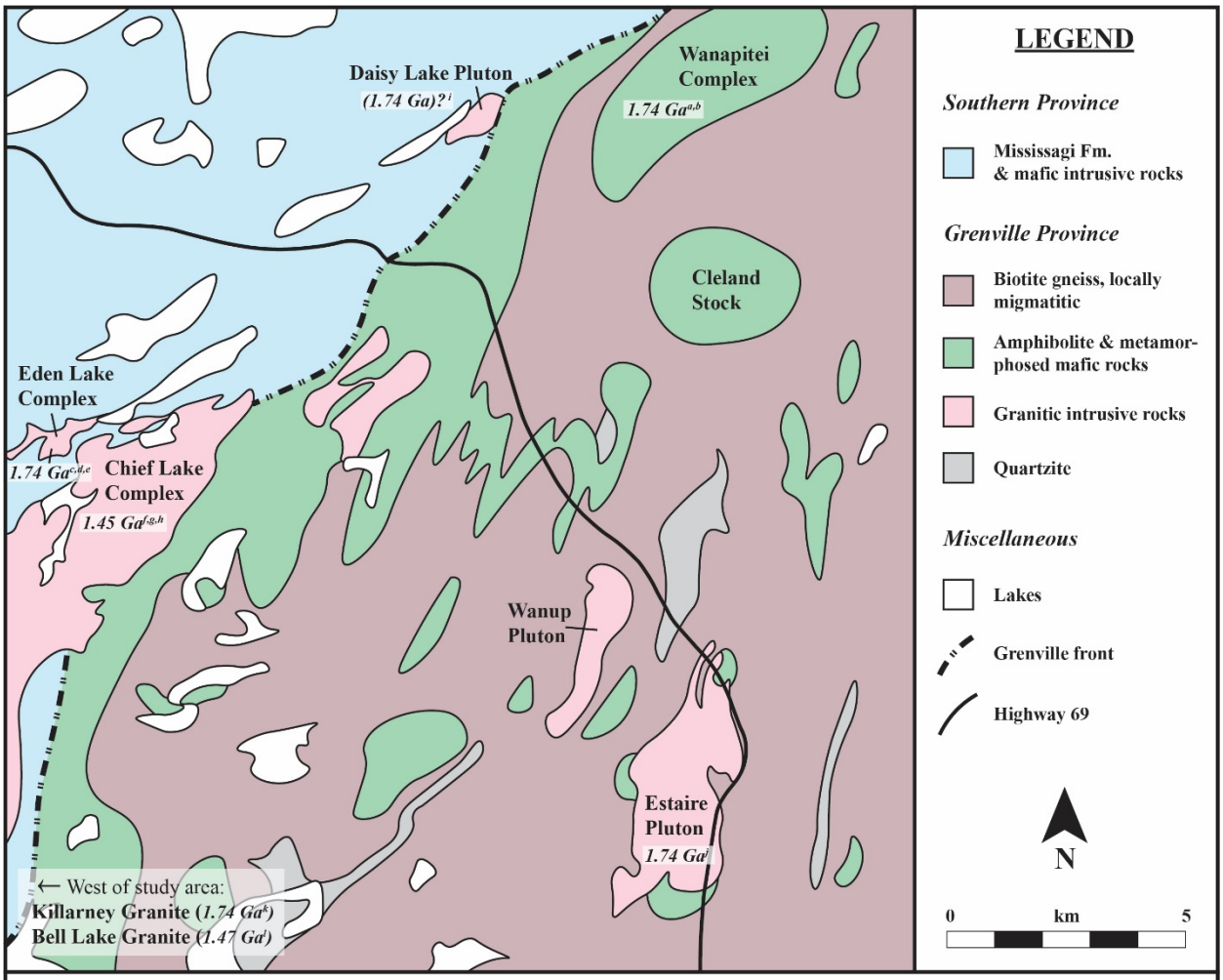

	Intrusion	Method	Reference
a	Wanapitei Complex	U-Pb zircon	Prevec (1995)
b	Wanapitei Complex	U-Pb zircon	Ames et al. (2005)
c	Eden Lake Complex	U-Pb zircon	Ames et al. (2005)
d	Eden Lake Complex	U-Pb zircon & monazite	Sullivan & Davidson (1993)
e	Eden Lake Complex	U-Pb zircon	Raharimahefa et al. (2014)
f	Chief Lake Complex	U-Pb zircon	Raharimahefa et al. (2014)
g	Chief Lake Complex	U-Pb zircon	Davidson & Van Breemen (1994)
h	Chief Lake Complex	U-Pb zircon	Ames et al. (2005)
i	Daisy Lake Granodiorite	N/A; *See discussion in Davidson (1992) and Davidson & Van Breemen (1994)*	
j	Estaire Pluton	U-Pb zircon	Pfister et al. (2023)
k	Killarney Granite	U-Pb zircon	Van Breemen & Davidson (1988)
l	Bell Lake Granite	U-Pb zircon	Van Breemen & Davidson (1988)

Fig. 2. Simplified regional geological map of the study area (modified after Lumbers, 1976a) south of Sudbury, Ontario showing the locations and ages of major intrusions, along with the respective dating methods used and relevant references.

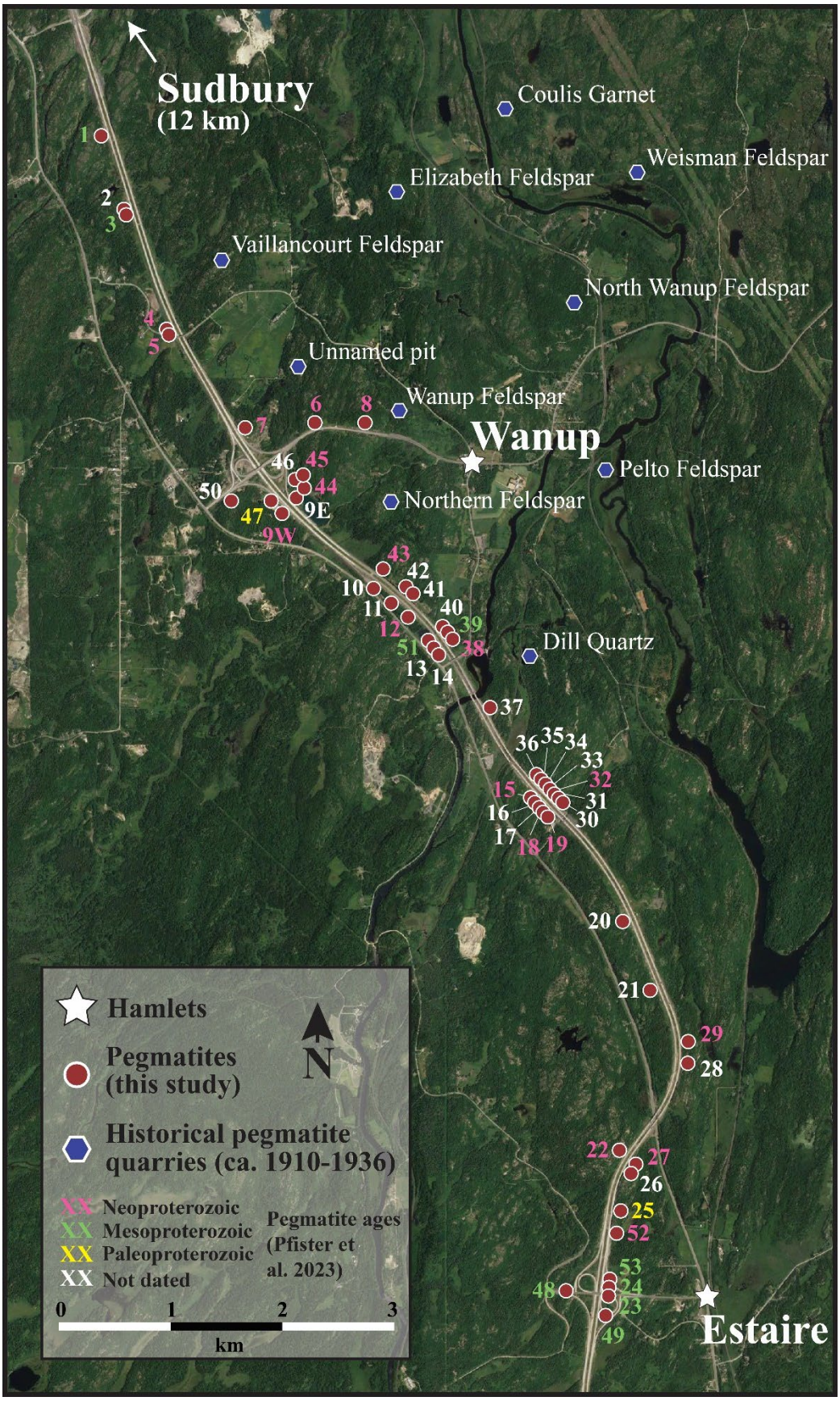
Sudbury
(12 km)
Coulis Garnet
Weisman Feldspar
Elizabeth Feldspar
Vaillancourt Feldspar
North Wanup Feldspar
Unnamed pit
Wanup Feldspar
Wanup
Pelto Feldspar
Northern Feldspar
Dill Quartz
Estaire
1
2
3
4
5
6
7
8
9E
9W
10
11
12
13
14
15
16
17
18
19
20
21
22
23
24
25
26
27
28
29
30
31
32
33
34
35
36
37
38
39
40
41
42
43
44
45
46
47
48
49
50
51
52
53
Hamlets
Pegmatites (this study)
Historical pegmatite quarries (ca. 1910-1936)
N
XX Neoproterozoic
XX Mesoproterozoic
XX Paleoproterozoic
XX Not dated
Pegmatite ages (Pfister et al. 2023)
0
1
2
3
km

Fig. 3. Satellite image (© Google Earth 2021) of the study area along provincial Highway 69 south of Sudbury, Ontario showing the location of historical K-feldspar-rich pegmatite quarries (blue hexagons) and the pegmatites discussed in this study (red circles). The ages of the pegmatites are from Pfister *et al.* (2023) based on U-Pb dating of zircon, monazite and xenotime. Note that the numbers assigned to pegmatites have no meaning other than in the context of this study (*e.g.*, sample locations).

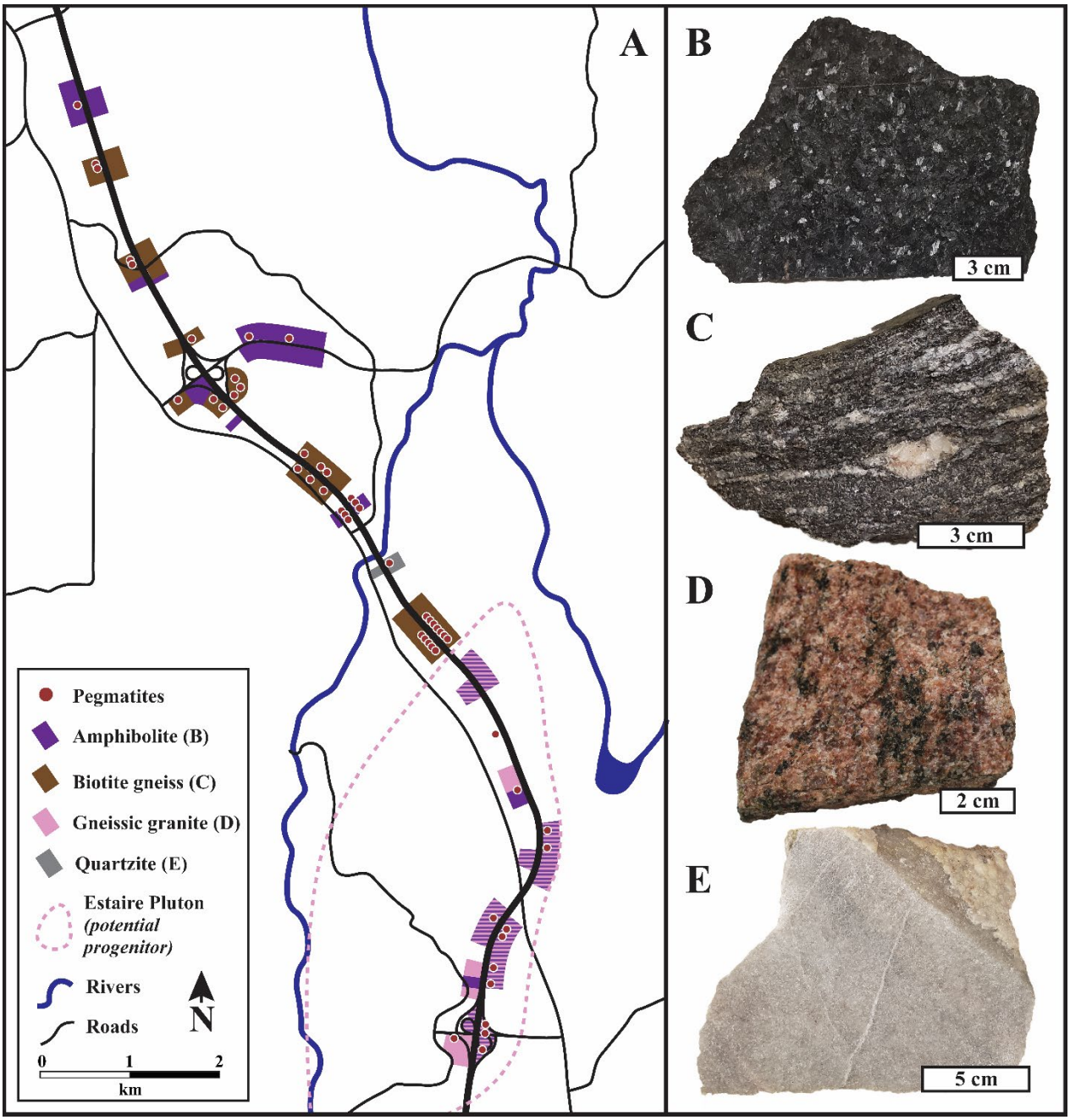

Fig. 4. A) Simplified map showing the distribution of the various host rocks to pegmatites along roadcuts of Highway 69. B-E) Typical hand samples of the four types of host rocks: B) Amphibolite; C) Biotite gneiss; D) Granite (*ca.* 1.74 Ga Estaire pluton; Pfister *et al.*, 2023); and E) Quartzite.

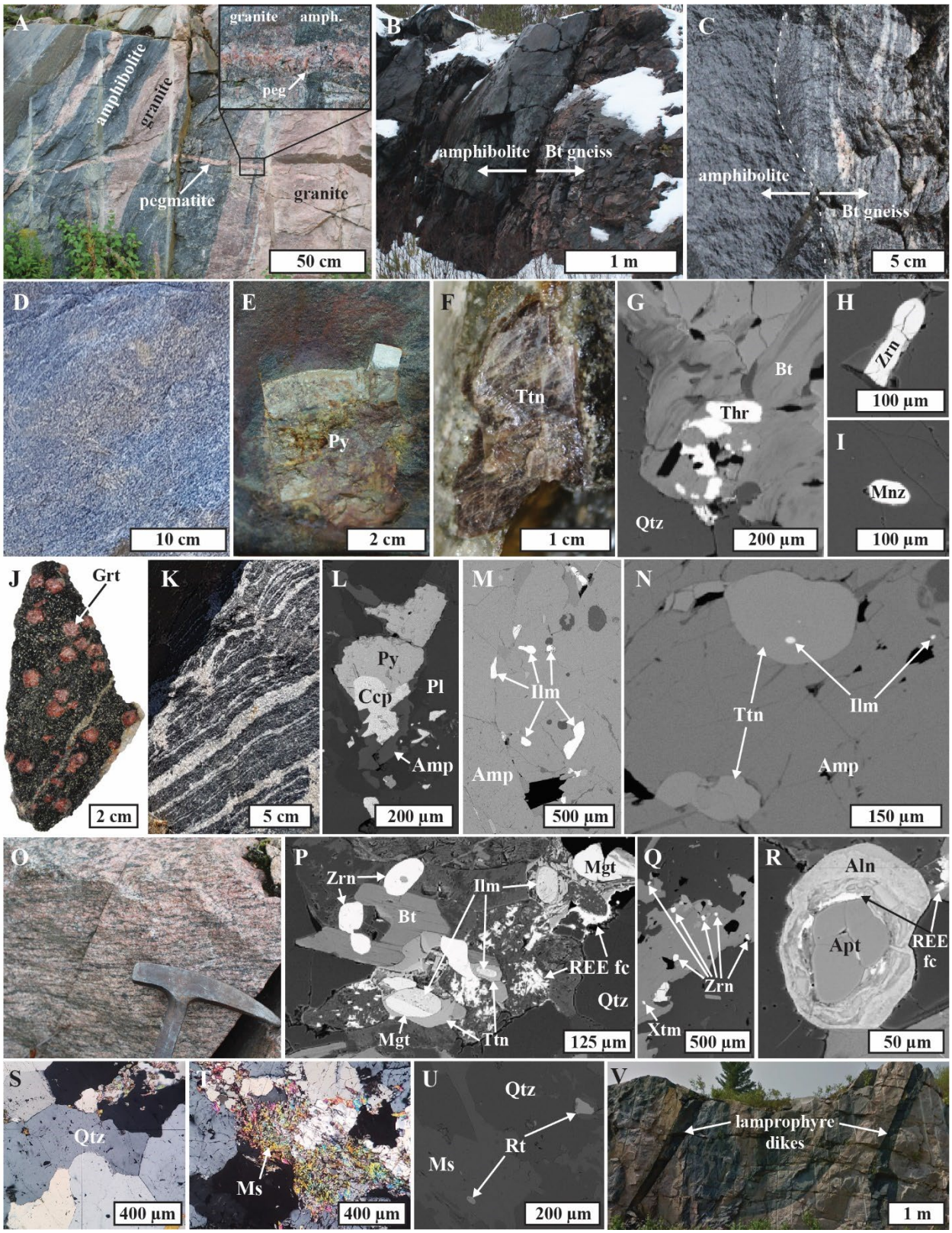
A
amphibolite
granite
pegmatite
granite
granite amph.
peg
50 cm
B
amphibolite Bt gneiss
1 m
C
amphibolite
Bt gneiss
5 cm
D
10 cm
E
Py
2 cm
F
Ttn
1 cm
G
Bt
Thr
Qtz
200 µm
H
Zrn
100 µm
I
Mnz
100 µm
J
Grt
2 cm
K
5 cm
L
Py
Ccp
Pl
Amp
200 µm
M
Ilm
Amp
500 µm
N
Ttn
Ilm
Amp
150 µm
O
P
Zrn
Ilm
Mgt
Bt
REE fc
Qtz
Mgt
Ttn
125 µm
Q
Zrn
Xtm
500 µm
R
Aln
Apt
REE fc
50 µm
S
Qtz
400 µm
T
Ms
400 µm
U
Qtz
Rt
Ms
200 µm
V
lamprophyre dikes
1 m

Fig. 5. Outcrop photos along with photomicrographs and BSE images of host rocks (outcrops and hand samples). Mineral abbreviations: Ab = albite; Aln = allanite-(Ce); Amp = amphibole; Bt = biotie; Apt = apatite; Ccp = chalcopyrite; Ilm = ilmenite; Mgt = magnetite; Mnz = monazite; Ms = muscovite; Pl = plagioclase; Py = pyrite; Qtz = quartz; REE fc. = (L)REE fluorocarbonate; Rt = rutile; Thr = thorite; Ttn = titanite; Urn = uraninite; Xtm = xenotime; Zrn = zircon. Order: A-C) Contacts and crosscutting relationships; D-I) Biotite gneiss; J-N) Amphibolite; O-R) Granite; S-U) Quartzite; V) Lamprophyre dikes.

A) Outcrop near Estaire (see Fig. 3) showing interlayered amphibolite and granite (*ca.* 1740 Ma Estaire granite pluton) crosscut by a thin (<10 cm) pegmatite dike. B, C) Sharp contact between biotite gneiss and amphibolite. D) Homogeneous garnet-free, leucosome-free biotite gneiss. E) Large euhedral pyrite in biotite gneiss. F) Large titanite in biotite gneiss. G) Thorite hosted biotite gneiss. H) Zircon hosted in quartz from biotite gneiss. I) Monazite hosted in quartz from biotite gneiss. J) Garnet-bearing amphibolite. K) Banded amphibolite; note how the leucosomes locally coalesce. L) Late-stage pyrite and chalcopyrite in amphibolite. M) Ilmenite in amphibolite. N) Titanite and ilmenite in amphibolite. O) *ca*. 1740 Ma Estaire granite; note the gneissic fabric. P) Accessory phases hosted in the Estaire pluton: magnetite, ilmenite, titanite, zircon and secondary LREE fluorocarbonate. Note how the titanite rims ilmenite (±magnetite). Q) Zircon and xenotime hosted in the Estaire pluton. Note the abundance of zircon crystals (up to 150 per polished thin section). R) Apatite rimmed by allanite-(Ce); note the bright secondary LREE fluorocarbonate. S) Quartzite with 120° triple points indicative of recrystallization. T) Muscovite hosted in quartzite. U) Accessory rutile in quartzite. V) Lamprophyric dikes crosscutting an amphibolite-granite package near Estaire.

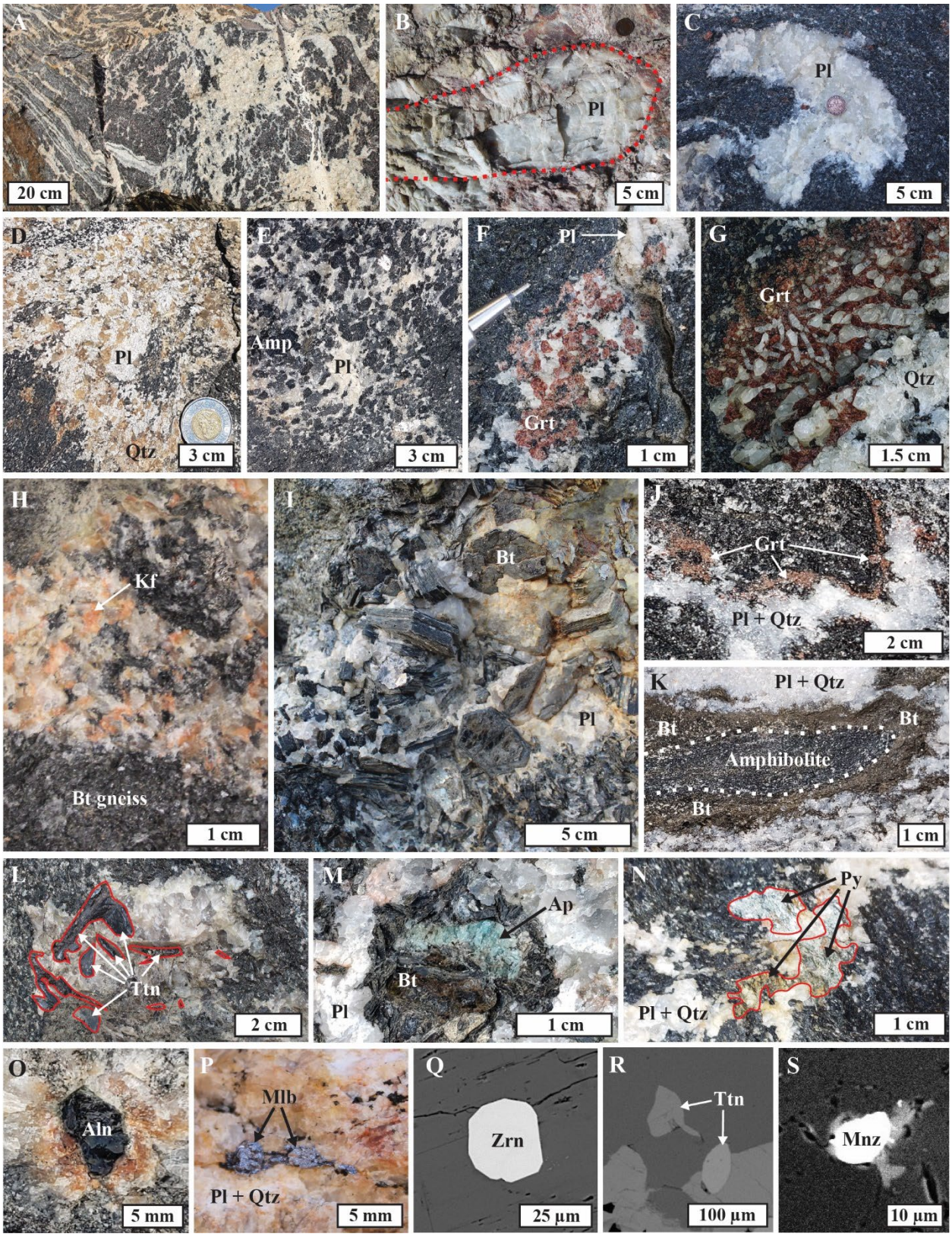
A
20 cm
B
Pl
5 cm
C
Pl
5 cm
D
Pl
Qtz
3 cm
E
Amp
Pl
3 cm
F
Pl
Grt
1 cm
G
Grt
Qtz
1.5 cm
H
Kf
Bt gneiss
1 cm
I
Bt
Pl
5 cm
J
Grt
Pl + Qtz
2 cm
K
Pl + Qtz
Bt
Bt
Amphibolite
Bt
1 cm
L
Ttn
2 cm
M
Ap
Bt
Pl
1 cm
N
Py
Pl + Qtz
1 cm
O
Aln
5 mm
P
Mlb
Pl + Qtz
5 mm
Q
Zrn
25 µm
R
Ttn
100 µm
S
Mnz
10 µm

Fig. 6. Outcrop photos along with photomicrographs and BSE images of leucosomes (outcrops and hand samples) hosted in amphibolite and biotite gneiss. Mineral abbreviations as above. A) Amphibolite-hosted leucosomes coalescing together. B) Megacrystic plagioclase in a pegmatitic leucosome near pegmatite #6 (see Fig. 3). C) Amphibolite-hosted plagioclase-rich (with minor/accessory quartz) leucosome. D) Amphibolite-hosted plagioclase-quartz leucosome. E) Amphibolite-hosted plagioclase-amphibolite leucosome. F) Amphibolite-hosted plagioclase-garnet leucosome. G) Graphic-like garnet-quartz intergrowth, indicative of undercooling and disequilibrium conditions. H) Biotite-gneiss-hosted leucosome consisting of K-feldspar, quartz and plagioclase. I) Pegmatitic plagioclase-biotite leucosome (with accessory blue apatite) hosted in amphibolite. J) Garnet rimming an amphibolite-hosted plagioclase-quartz leucosome. K) Biotite rimming an amphibolite-hosted plagioclase-quartz leucosome. L) Coarse titanite in a amphibolite-hosted plagioclase-rich leucosome. M) Coarse apatite and biotite in a plagioclase-rich leucosome. N) Coarse pyrite in plagioclase-rich leucosome. O) Allanite-(Ce) in a fine-grained plagioclase-quartz leucosome. P) Molybdenite in a fine-grained plagioclase-quartz leucosome. Q, R, S) Zircon, titanite and monazite in biotite-gneiss-hosted leucosomes.

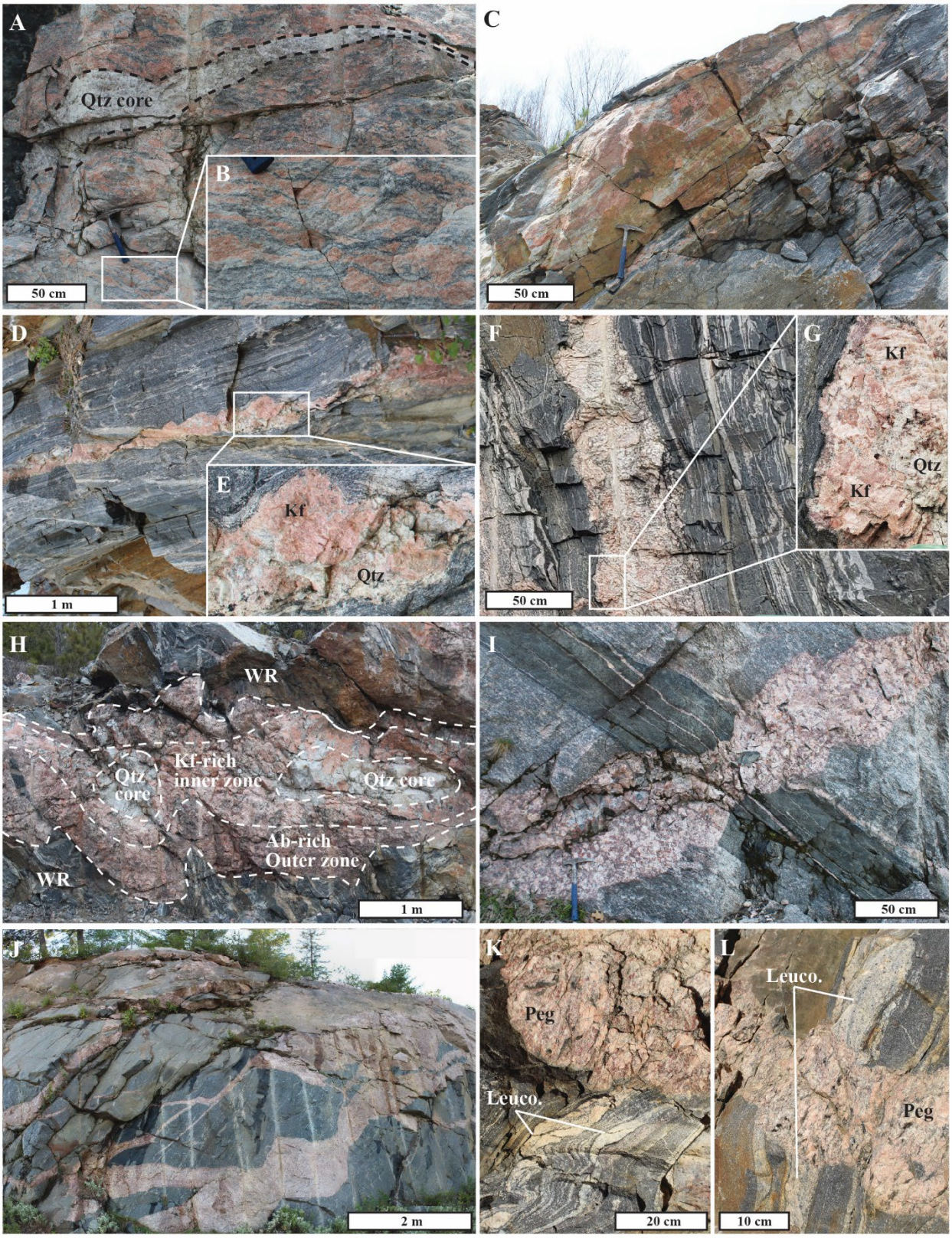
A
Qtz core
B
50 cm
C
50 cm
D
1 m
E
Kf
Qtz
F
50 cm
G
Kf
Qtz
Kf
H
WR
Qtz core
Kf-rich inner zone
Qtz core
Ab-rich Outer zone
WR
1 m
I
50 cm
J
2 m
K
Peg
Leuco.
20 cm
L
Leuco.
Peg
10 cm

Fig. 7. Typical examples of pegmatite outcrops along Highway 69, ordered from older to younger. Abbreviations as follows: Ab = albite; Kf = K-feldspar; Leuco = leucosome; Peg = pegmatite; Qtz = quartz. A, B, C) Paleoproterozoic pegmatites (*ca*. 1740 Ma; Pfister *et al.,* 2023). These are highly deformed, almost entirely recrystallized with the exception of remnant quartz core (A), and oriented parallel to the host rocks fabric (C). Note the deformed K-feldspar megacrysts (B), which underwent complete dynamic recrystallization. D- G) Mesoproterozoic pegmatites (*ca*. 1430-1450 Ma; Pfister *et al.,* 2023). These are moderately deformed, sometimes exhibit light boudinage (D), are aligned parallel to the host rocks fabric (D,F) and exhibit various degrees of recrystallization (E,G) with notably more remnant K-feldspar, quartz and albite megacrysts (E,G) than the Paleozoic pegmatites. Note that both Paleo- and Mesoproterozoic pegmatites lack coarse primary micas. H-L) Neoproterozoic pegmatites (*ca*. 950-990 Ma; Pfister et al 2023) which are highly diverse in terms of morphology, textures, mineralogy and deformation. The pegmatites range from mildly deformed to undeformed, from a few meters wide to <10 cm wide, from convoluted bulbous dikes to straight thin dikes, from strongly zoned (H) to internally homogeneous (I-L), from crosscutting the host rock fabric (including leucosomes; I, K, L) to being aligned with it, and from exhibiting abundant disequilibrium textures (see Fig. 8) to containing none.

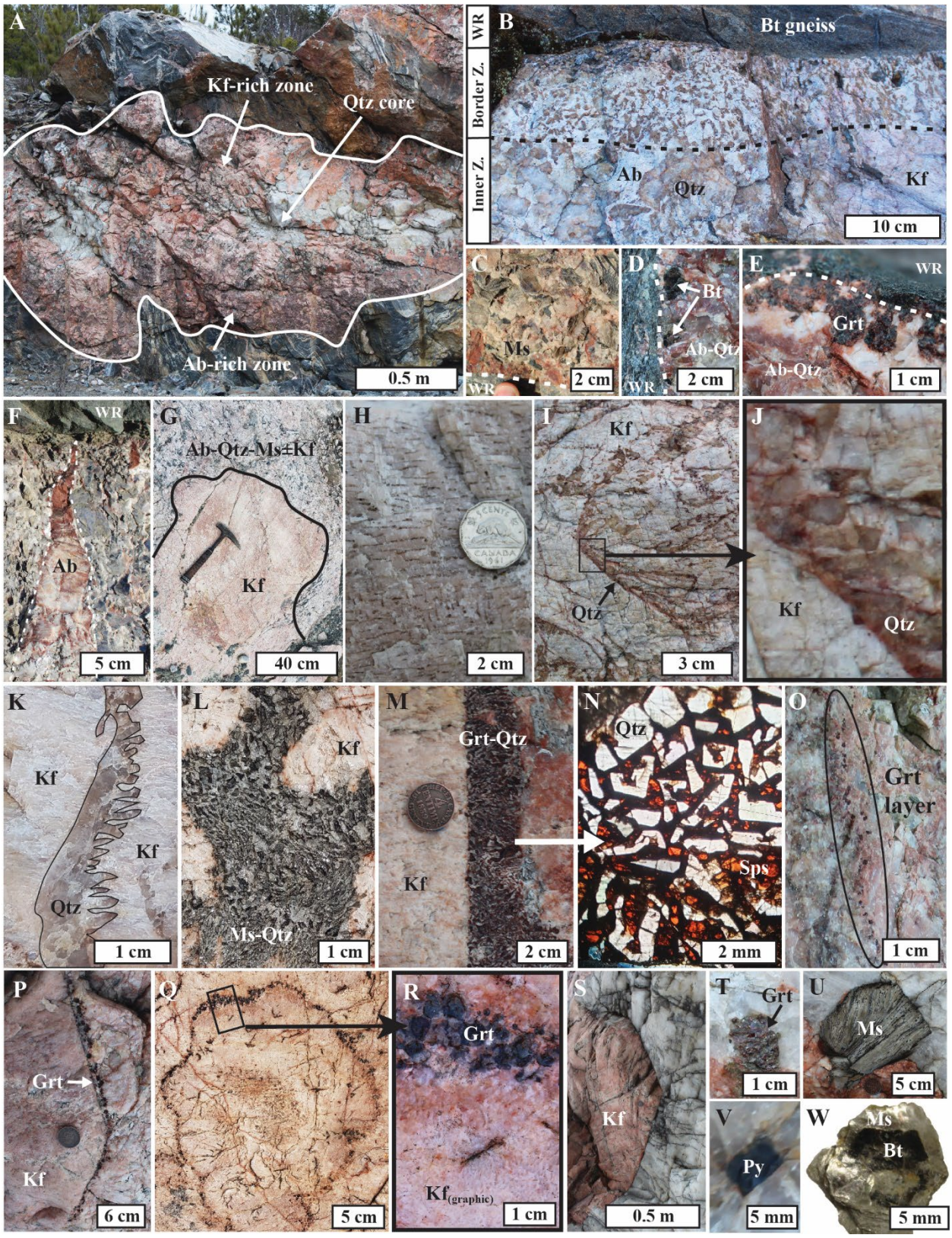
A
Kf-rich zone
Qtz core
Ab-rich zone
0.5 m
B
WR
Border Z.
Inner Z.
Bt gneiss
Ab
Qtz
Kf
10 cm
C
Ms
2 cm
WR
D
Bt
Ab-Qtz
2 cm
WR
E
WR
Grt
Ab-Qtz
1 cm
F
WR
Ab
5 cm
G
Ab-Qtz-Ms±Kf
Kf
40 cm
H
2 cm
I
Kf
Qtz
3 cm
J
Kf
Qtz
K
Kf
Kf
Qtz
1 cm
L
Kf
Ms-Qtz
1 cm
M
Grt-Qtz
Kf
2 cm
N
Qtz
Sps
2 mm
O
Grt
layer
1 cm
P
Grt
Kf
6 cm
Q
5 cm
R
Grt
Kf(graphic)
1 cm
S
Kf
0.5 m
T
Grt
1 cm
U
Ms
5 cm
V
Py
5 mm
W
Ms
Bt
5 mm

Fig. 8. Primary zoning and textures in pegmatites. Mineral abbreviations: Ab = albite; Bt = biotite; Grt = garnet; Kf = K-feldspar; Ms = muscovite; Py = pyrite; Qtz = quartz; Sps = spessartine; WR = wallrock. A) Pegmatite #7 exhibits strong internal zoning with a Kf-rich zone, Ab-rich (up to An_{11}) zone and a well-developed quartz core. Note its irregular bulbous morphology. B) Pegmatite(#5)-wallrock contact showing a border zone consisting of medium to coarse albite-quartz intergrowth and an inner zone consisting of very coarse albite-quartz intergrowth with megacrystic K-feldspar and quartz. C, D, E) Coarse crystals of muscovite, biotite and garnet at the pegmatite-wallrock contact. Note that garnet in picture E was analyzed and yielded the least manganiferous pegmatitic garnet ($Alm_{60\text{-}70}$ $Sps_{25\text{-}30}$ $\Sigma(Prp+Grs)_{5\text{-}10}$ $\Sigma(other)_{<5}$). F) Funnel-shaped megacrystic albite (An_7) growing inwards from the pegmatite-wallrock contact. Note the hematization of the albite, which is more intense close to the WR contact. G) Megacrystic K-feldspar surrounded by a matrix of albite, quartz, muscovite and minor K-feldspar. H) Close-up of the graphic texture in a K-feldspar megacryst from the same pegmatite (#9W) than image G. I, J, K) Examples of dendritic quartz crystals hosted in K-feldspar megacrysts. L) Irregular mass of coarse muscovite-quartz (± spessartine) intergrowth. Note the orientation of the muscovite books. M, N) Graphic quartz-garnet intergrowth. Note that such intergrowths are mostly observed at the edge of K-feldspar megacrysts (see sharp boundary in image M). The garnet in image N was analyzed and yielded some of the most manganiferous composition ($Sps_{55\text{-}65}$ $Alm_{35\text{-}40}$ $\Sigma(Prp+Grs)_{<5}$ $\Sigma(other)_{<5}$). O, P) Garnet layers in pegmatites. These layers are either found between internal zones (*e.g.* picture O with Kf-rich zone on the right and Ab-rich to the right), or at the edges of early K-feldspar (rarely quartz) megacrystics (*e.g.* picture P). Crystals from garnet layers were analyzed and yielded the following composition: $Sps_{40\text{-}50}$ $Alm_{40\text{-}50}$ $\Sigma(Prp+Grs)_{5\text{-}10}$ $\Sigma(other)_{<5}$. Q, R) "Cauliflower garnet" in pegmatite #9W consisting of a layer of euhedral garnet (spessartine)

± quartz surrounding a bulbous-shaped K-feldspar megacryst (similar to image G, also from pegmatite #9W). Note that the K-feldspar exhibit graphic texture that is coarsening outwards up until the garnet layer. Multiple euhedral crystals from the "cauliflower" garnet were analyzed and yielded the following composition: Sps_{50-60} Alm_{35-45} $\Sigma(Prp+Grs)_{\sim 5}$ $\Sigma(other)_{<5}$. S-W) Various coarse euhedral minerals found in the quartz core of pegmatites, including megacrystic K-feldspar, garnet, pyrite, muscovite and biotite. Note that biotite books from the quartz core occasionally exhibit rims of muscovite such as in picture W (from pegmatite #5). The garnet in image T was analyzed and yielded the following composition: Alm_{55-65} Sps_{30-35} $\Sigma(Prp+Grs)_{5-10}$ $\Sigma(other)_{<5}$.

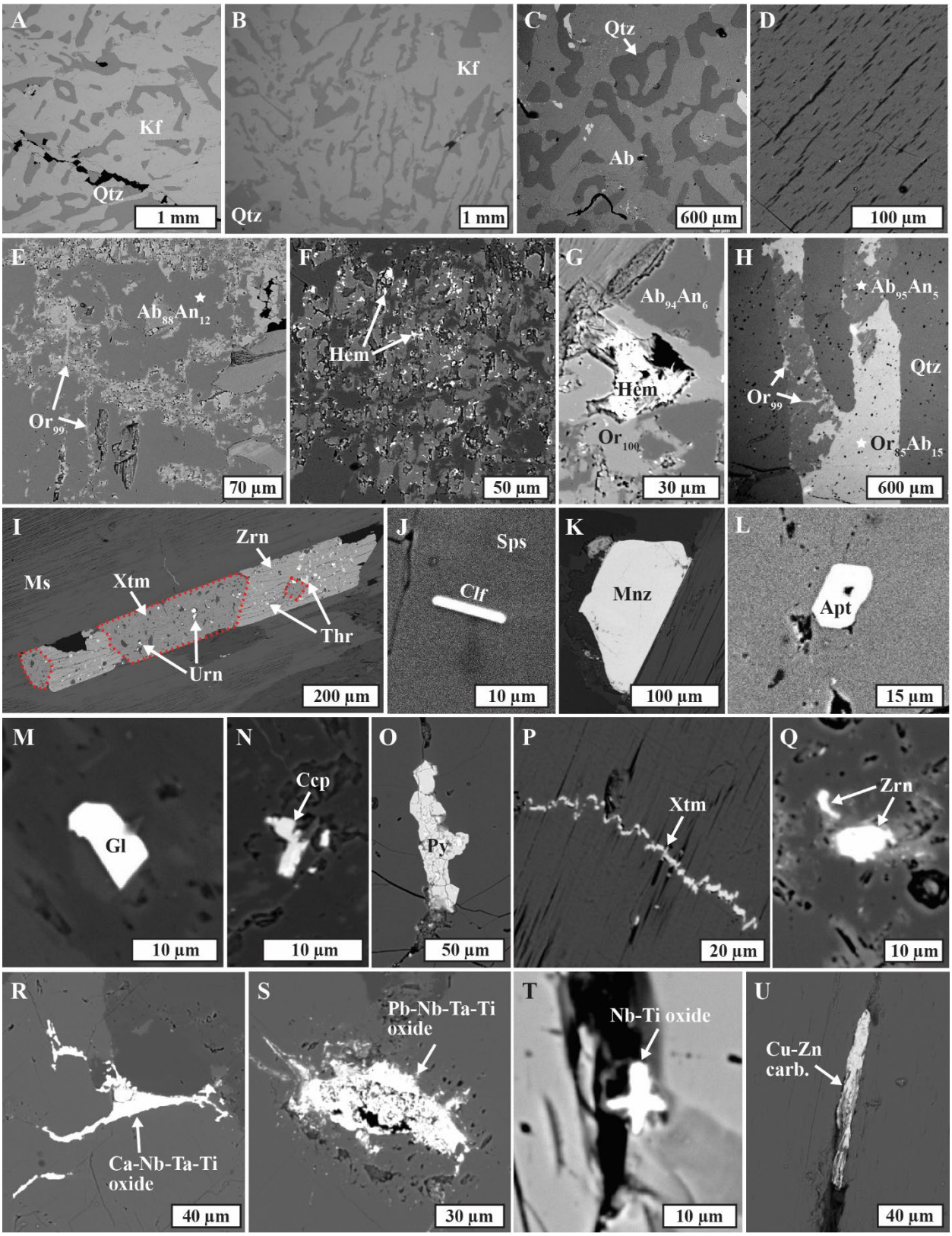
A
Kf
Qtz
1 mm
B
Kf
Qtz
1 mm
C
Qtz
Ab
600 µm
D
100 µm
E
Ab88An12
Or99
70 µm
F
Hem
50 µm
G
Ab94An6
Hem
Or100
30 µm
H
Ab95An5
Qtz
Or99
Or85Ab15
600 µm
I
Zrn
Ms
Xtm
Thr
Urn
200 µm
J
Sps
Clf
10 µm
K
Mnz
100 µm
L
Apt
15 µm
M
Gl
10 µm
N
Ccp
10 µm
O
Py
50 µm
P
Xtm
20 µm
Q
Zrn
10 µm
R
Ca-Nb-Ta-Ti oxide
40 µm
S
Pb-Nb-Ta-Ti oxide
30 µm
T
Nb-Ti oxide
10 µm
U
Cu-Zn carb.
40 µm

Fig. 9. BSE pictures of textures and accessory phases from the Neoproterozoic pegmatites. Mineral abbreviations: Ab = albite; An = anorthite; Apt = apatite; carb. = carbonates; Ccp = chalcopyrite; Clf = columbite-(Fe); Gl = galena; Grt = garnet; Hem = hematite; Kf = K-feldspar; Mnz = monazite; Ms = muscovite; Py = pyrite; Qtz = quartz; Sps = spessartine; Thr = thorite; Urn = uraninite; Xtm = xenotime; Zrn = zircon. A, B) K-feldspar-quartz graphic intergrowth. C) Ca-bearing albite (An_{15}) – quartz myrmekitic-like texture D) Perthitic texture in K-feldspar E) End-member K-feldspar replacing oligoclase (An_{12}) Note the development of porosity, typical of CDP. F, G) Secondary hematite in pits associated with the replacement of albite by K-feldspar and associated porosity development. This is why the feldspars, in particular Ca-bearing albite, exhibit an intense red color in outcrops. H) Primary K-feldspar ($Or_{85}Ab_{15}$) (in quartz) being replaced by albite ($Ab_{95}An_5$), itself being replaced by end-member K-feldspar. I) Xenotime-zircon intergrowth with thorite and uraninite inclusions hosted in muscovite. Note that the bright inclusions in zircon consist almost entirely of thorite, where the bright inclusions in xenotime consist almost entirely of uraninite. J) Primary columbite-(Fe) inclusions in spessartine. K) Monazite in quartz-muscovite assemblage. L) Euhedral apatite in quartz. M) Galena inclusion in feldspar. N-U) Late-stage chalcopyrite, pyrite, xenotime, zircon, unidentified Nb-Ti (±Ca, Pb, Ta) oxides and Cu-Zn carbonate in pits and fractures.

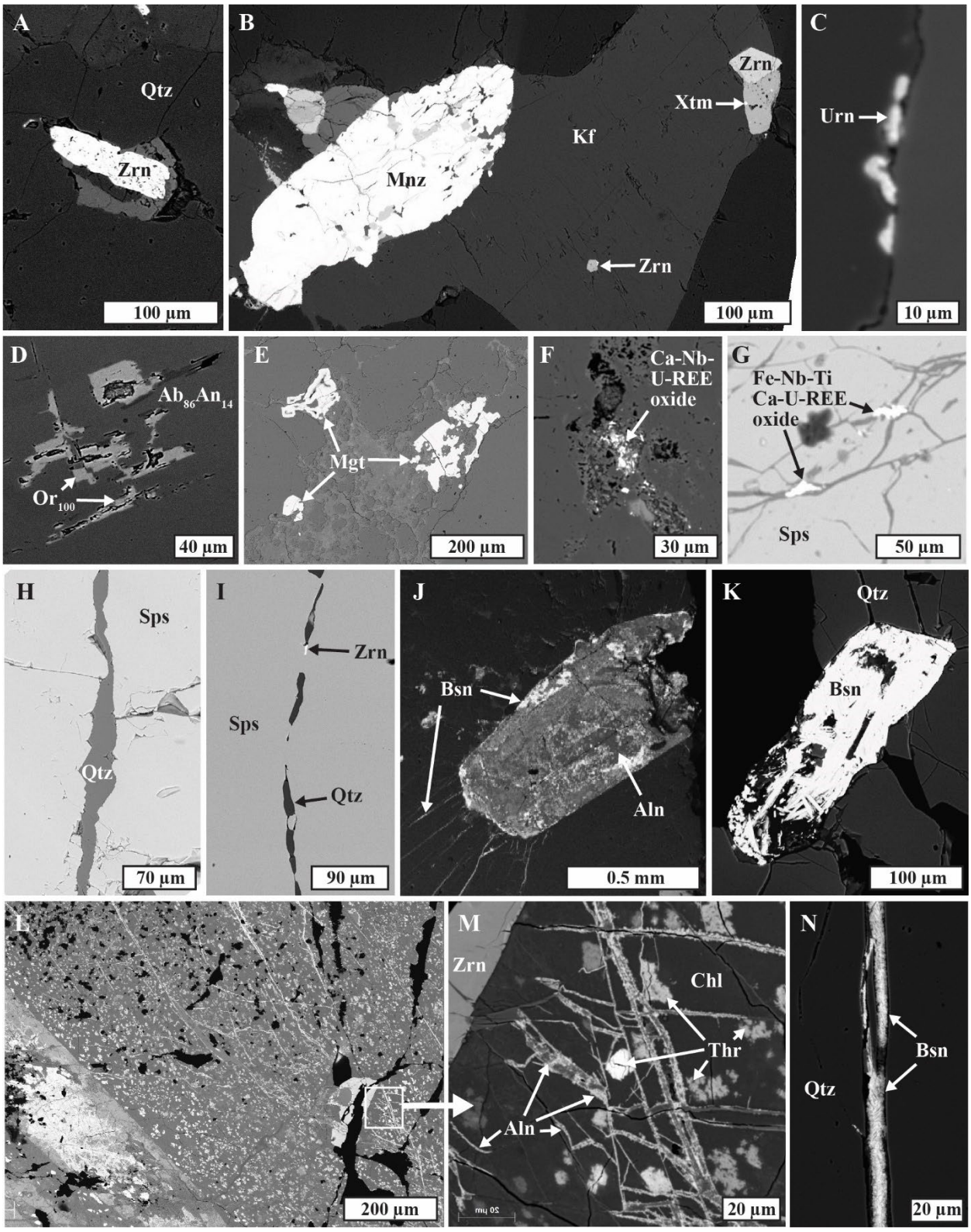
A
Qtz
Zrn
100 µm
B
Zrn
Xtm
Kf
Mnz
Zrn
100 µm
C
Urn
10 µm
D
Ab86An14
Or100
40 µm
E
Mgt
200 µm
F
Ca-Nb-U-REE oxide
30 µm
G
Fe-Nb-Ti Ca-U-REE oxide
Sps
50 µm
H
Sps
Qtz
70 µm
I
Zrn
Sps
Qtz
90 µm
J
Bsn
Aln
0.5 mm
K
Qtz
Bsn
100 µm
L
200 µm
M
Zrn
Chl
Thr
Aln
20 µm
N
Bsn
Qtz
20 µm

Fig. 10. Additional BSE pictures of textures and accessory phases from the Mesoproterozoic and Neoproterozoic pegmatites. Mineral abbreviations: Ab = albite; Aln = Allanite-(Ce); An = anorthite; Bsn = bastnäsite; Chl = chlorite; Kf = K-feldspar; Mnz = monazite; Mgt = magnetite; Qtz = quartz; Sps = spessartine; Thr = thorite; Urn = uraninite; Xtm = xenotime; Zrn = zircon. A) Zircon in quartz. B) Monazite, zircon and xenotime in K-feldspar. C) Late-stage uraninite along fracture. D) K-feldspathization of oligoclase along fluid pathway. E) Late-stage magnetite. F, G) Late-stage Ca-U-Nb-REE (±Fe, Ti) oxides in pits and fractures. H, I) Quartz veinlets with accessory zircon crosscutting spessartine. Note the healing of the spessartine in picture I. J, K) Bastnäsite replacing allanite-(Ce). Note the presence of allanite-(Ce) remnants in picture J, while allanite-(Ce) is completely replaced in picture K. L,M) Pseudomorph after an unidentified megacrystic phase, now consisting of chlorite with patches and veinlets of thorite and allanite. N) Late-stage bastnäsite in a fracture in quartz.

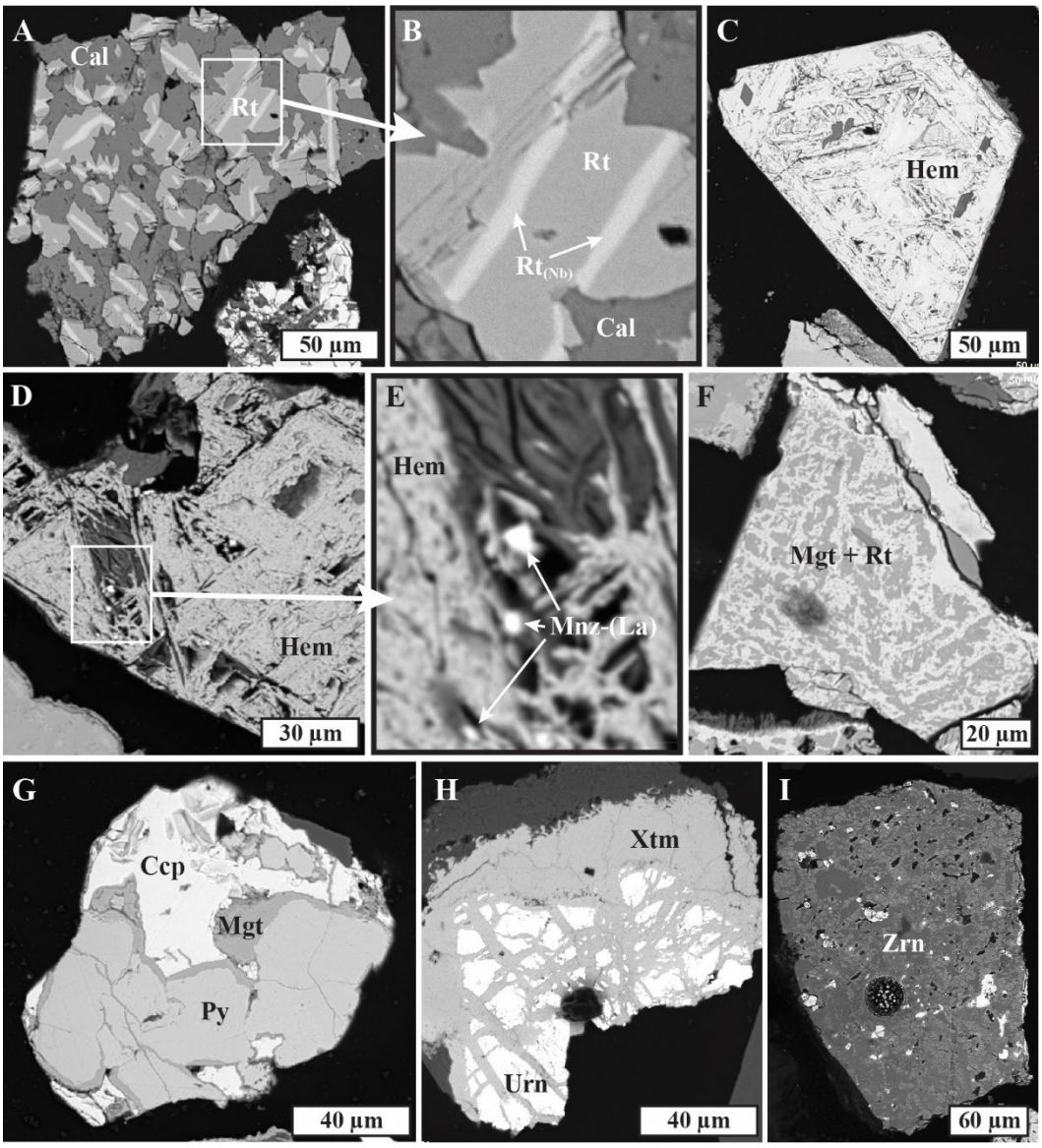

Fig. 11. SEM pictures of secondary features in selected grains from the heavy mineral concentrates used for the geochronoloical study of the Highway 69 pegmatites by Pfister *et al.* (2023). Minera abbreviations: Cal = calcite; Ccp = chalcopyrite; Hem = hematite; Mgt = magnetite; Mnz-(La) = monazite-(La); Py = pyrite; Rt = rutile ($Rt_{(Nb)}$ = niobian rutile); Urn = uraninite ; Xtm = xenotime; Zrn = zircon. A, B) Rutile remnants and secondary calcite assemblage. Note the bright Nb-rich (up to 4.5 wt% Nb_2O_5) zoning in the rutile remnants. C, D) Hematite pseudomorphs after unknown phases. E) Close-up of the secondary hematite in picture D with late-stage La-dominant monazite

in pits. F) Magnetite-rutile intergrowth. G) Pyrite rimmed by magnetite in chalcopyrite. H) Uraninite crosscut by xenotime. I) A highly altered grain of zircon. Note the porosity development, typical of CDP. The circular feature is a laser ablation pit.

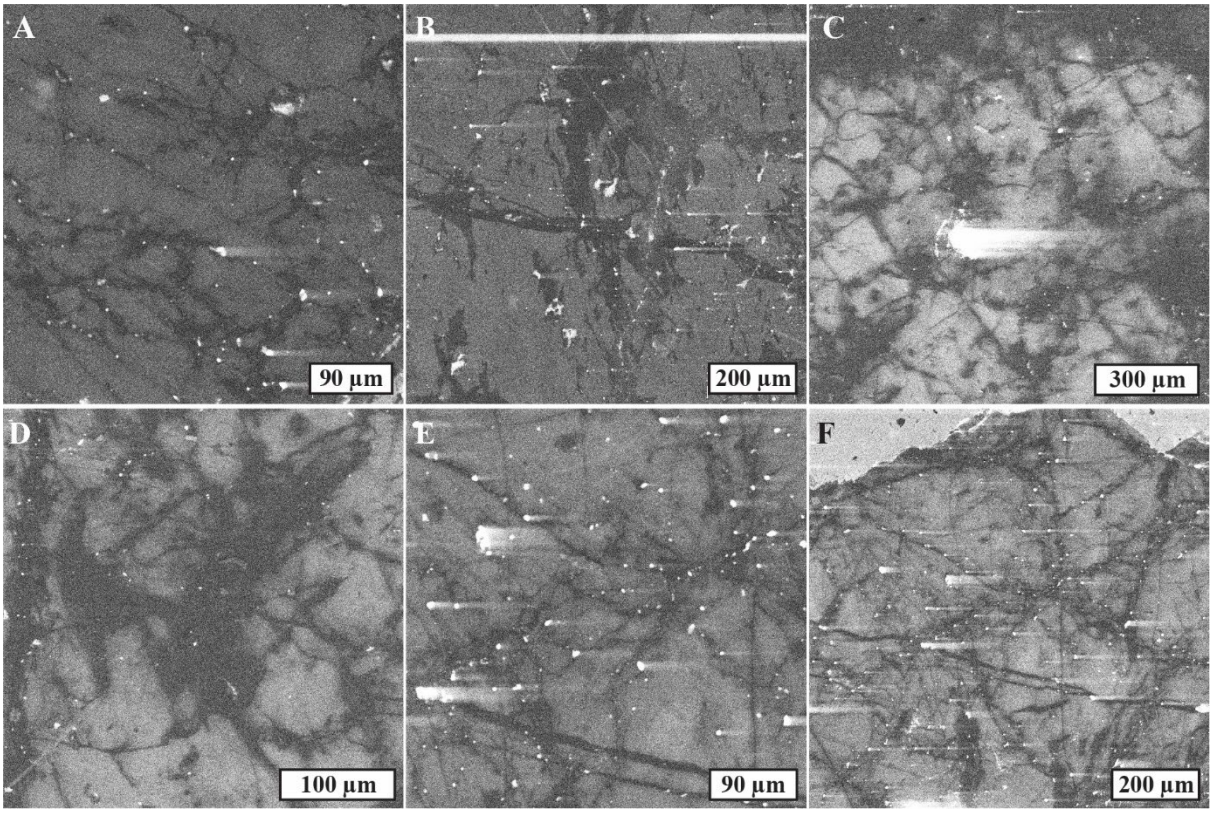

Fig. 12. CL imaging of quartz samples from the Neoproterozoic pegmatites. Note the abundance of secondary quartz (dark grey), which is not otherwise visible in thin section observations. Bright spots are mostly pits and fractures lined with polishing powder and rarely apatite inclusions (*e.g.* large bright spot in picture C).

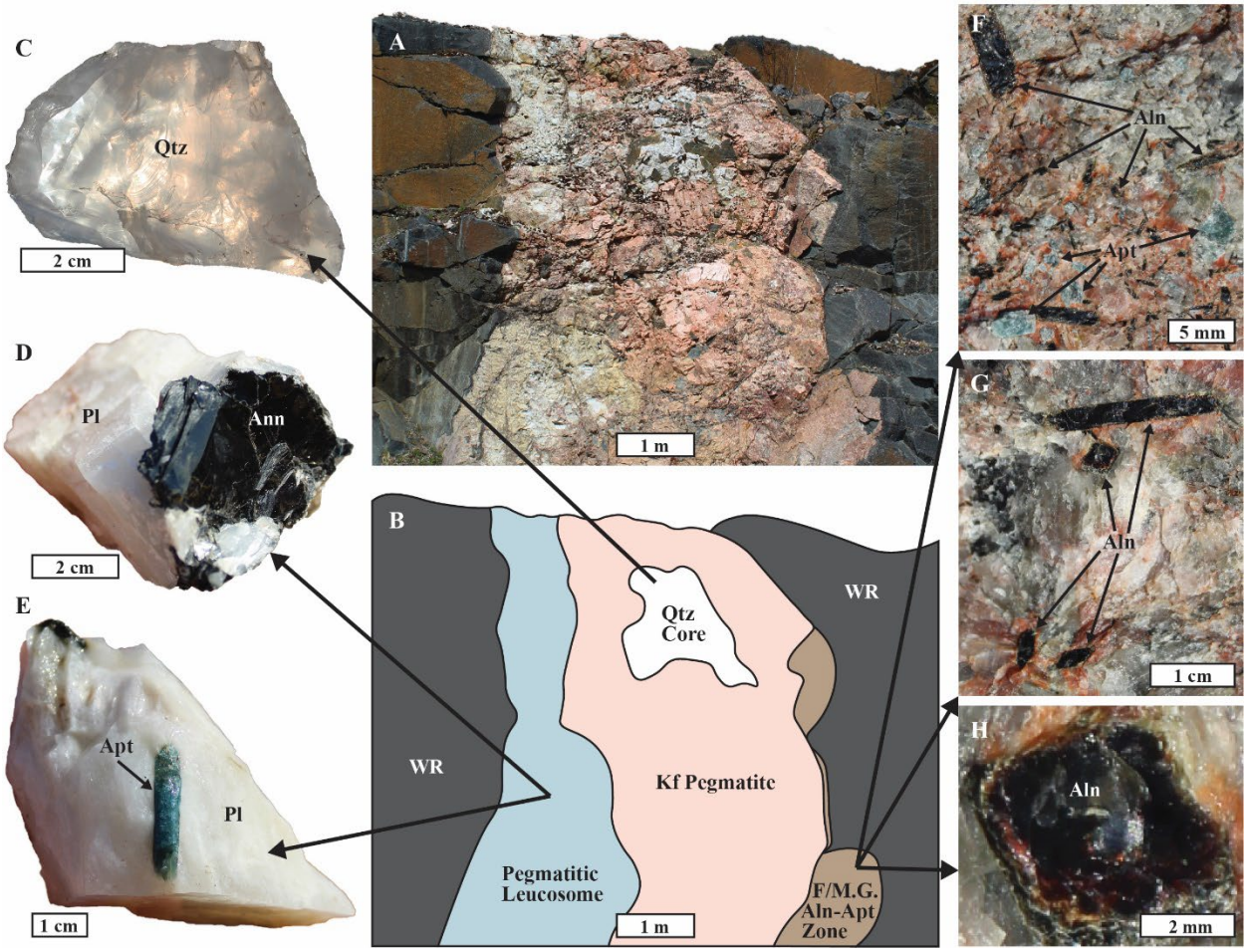

Fig. 13. Pegmatite #6 (see Fig. 3 for location). Mineral abbreviations: Aln = allanite-(Ce); Ann = annite; Apt = apatite; Pl = plagioclase; Qtz = quartz. A, B) Photograph and simplified map of pegmatite #6. Note the quartz core, the allanite-rich border zone and the chemically distinct pegmatitic leucosome to the left. C) Hand sample of fresh, gemmy quartz from the core. D, E) Hand samples from the pegmatitic leucosome, including coarse annite and blue fluorapatite in megacrystic plagioclase (oligoclase-andesine). F, G, H) Hand samples from the border zone of the K-feldspar-rich pegmatite showing abundant allanite-(Ce). Note how glassy and fresh the allanite is image H.

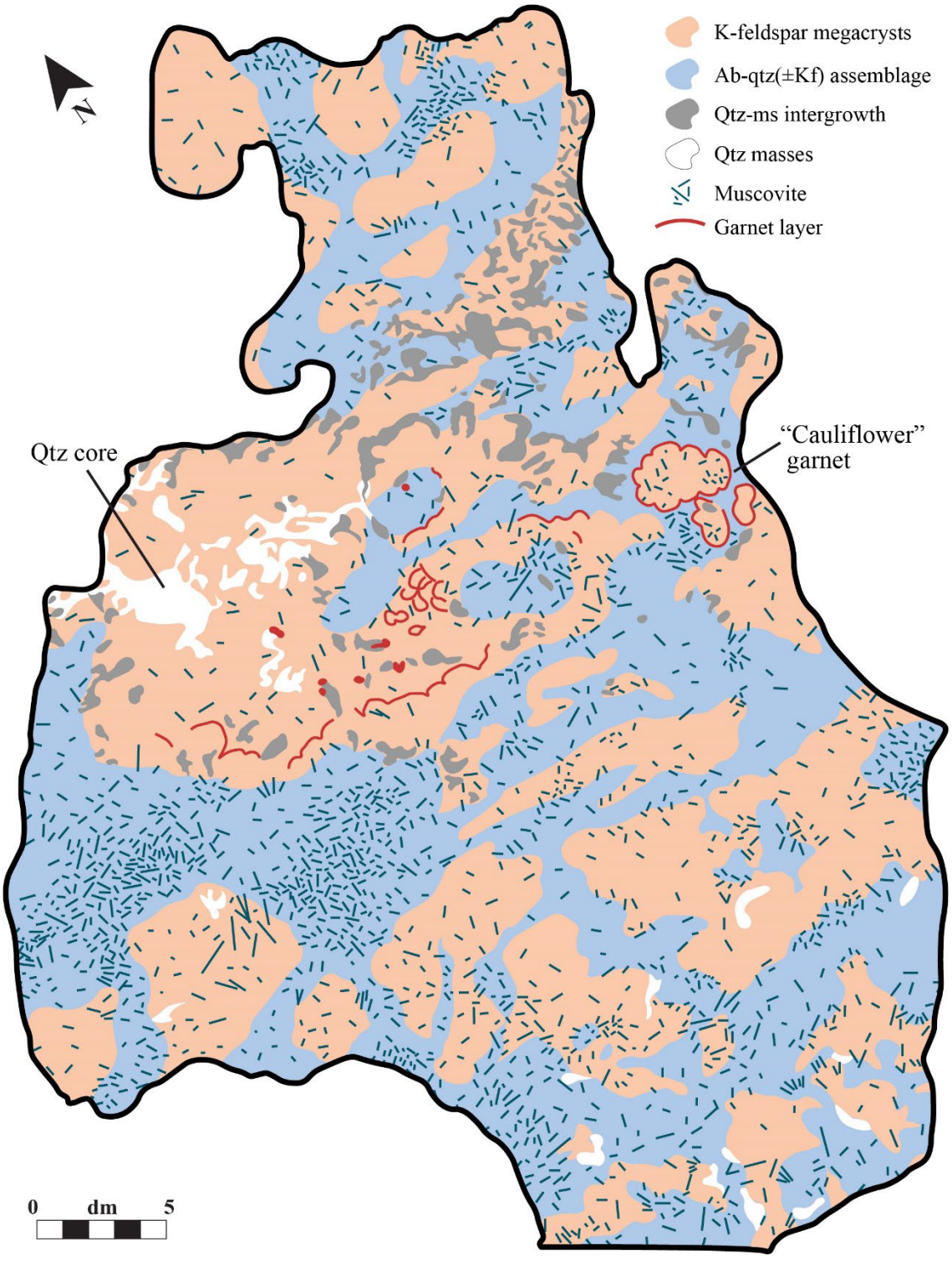

Fig. 14. Detailed outcrop map of pegmatite #9W. Ab = albite; Kf = K-feldspar; Ms = muscovite; Qtz = quartz. Note the quartz core and surrounding distribution of garnet layers/cauliflower garnet

(Fig. 8Q, R), and muscovite-quartz intergrowth (Fig. 8L). The K-feldspar megacrysts (Fig. 8G) are anhedral, variably deformed and commonly host graphic texture (Fig. 8M).

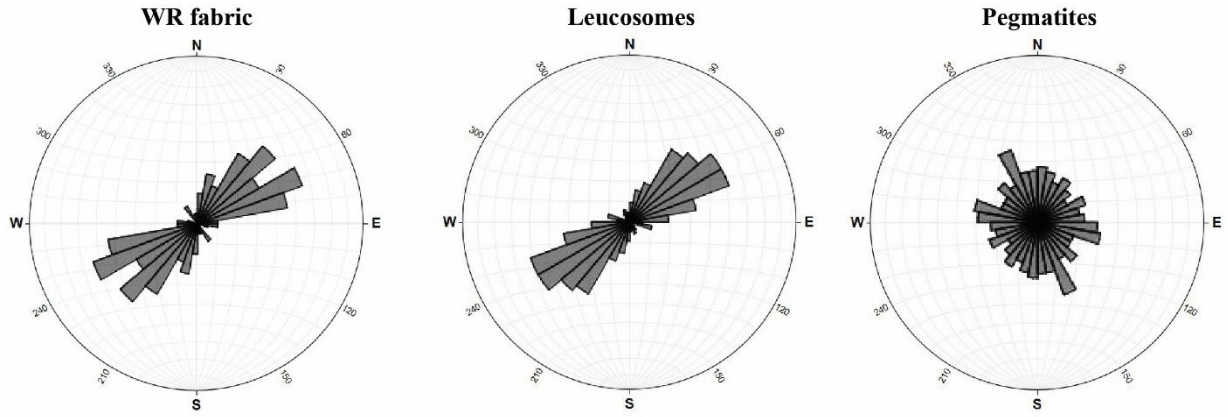

Fig. 15. Rose diagrams of structural measurements for the host rocks, biotite gneiss-hosted leucosomes, and pegmatites.

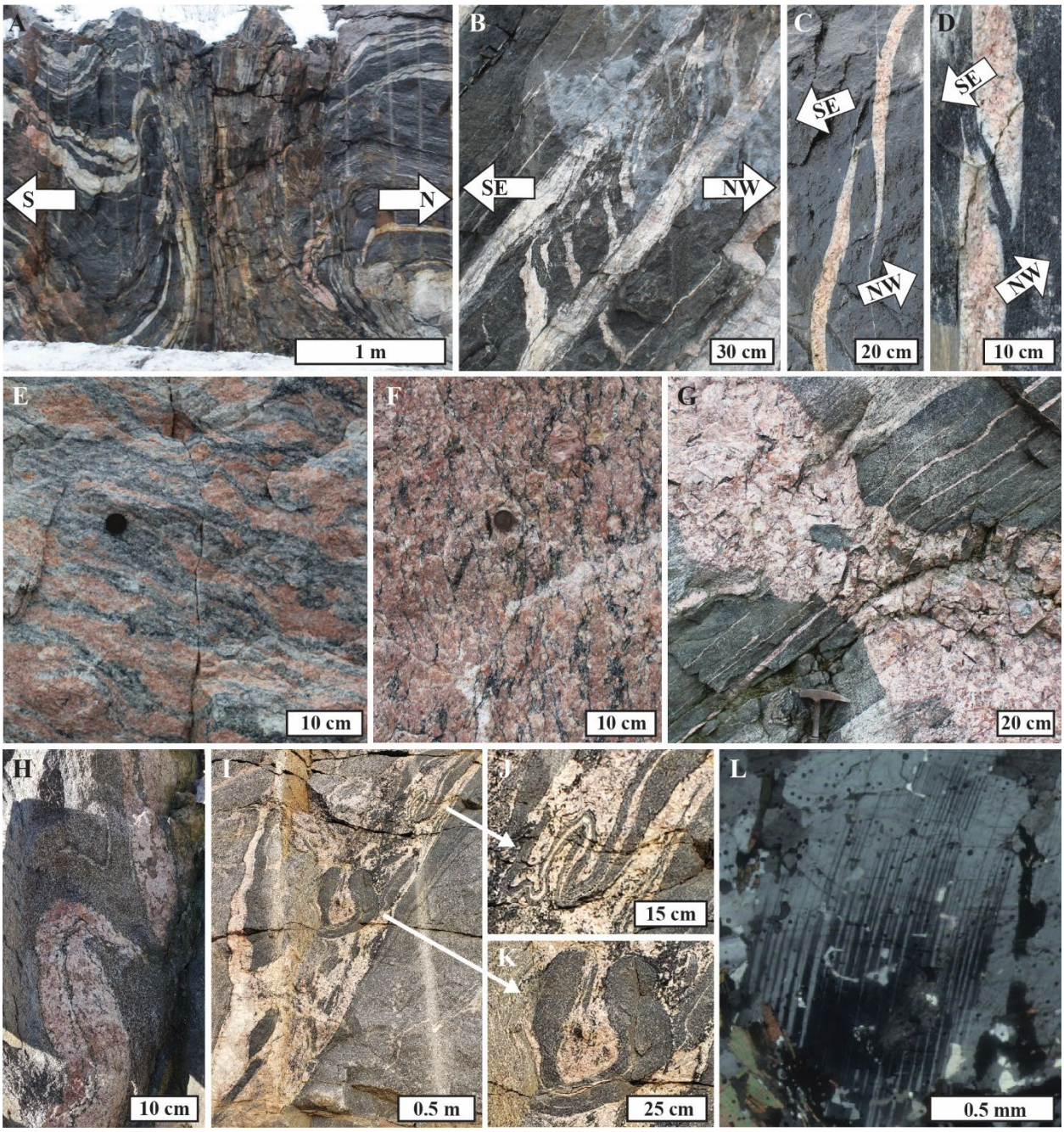

Fig. 16. Structural features and observations. A) Local shear zone across the highway from pegmatite #7 (see Fig. 3). B, C, D) En echelon leucosomes and pegmatites. E) Intensely deformed Paleoproterozoic pegmatite 47 exhibiting dynamic recrystallization of the original K-feldspar megacrysts. F) Gneissic fabric of the Estaire Pluton. G) Undeformed Neoproterozoic pegmatite 12 crosscutting the host rock fabric. Note how the pegmatite locally branched off the main dike to

follow the fabric of the host amphibolite layer. H) Folding of a pegmatite near Estaire. I, J, K) Ductile deformed wallrock fragments and ribbons in pegmatite #52. L) Pegmatite-hosted plagioclase exhibiting deformation twinning.

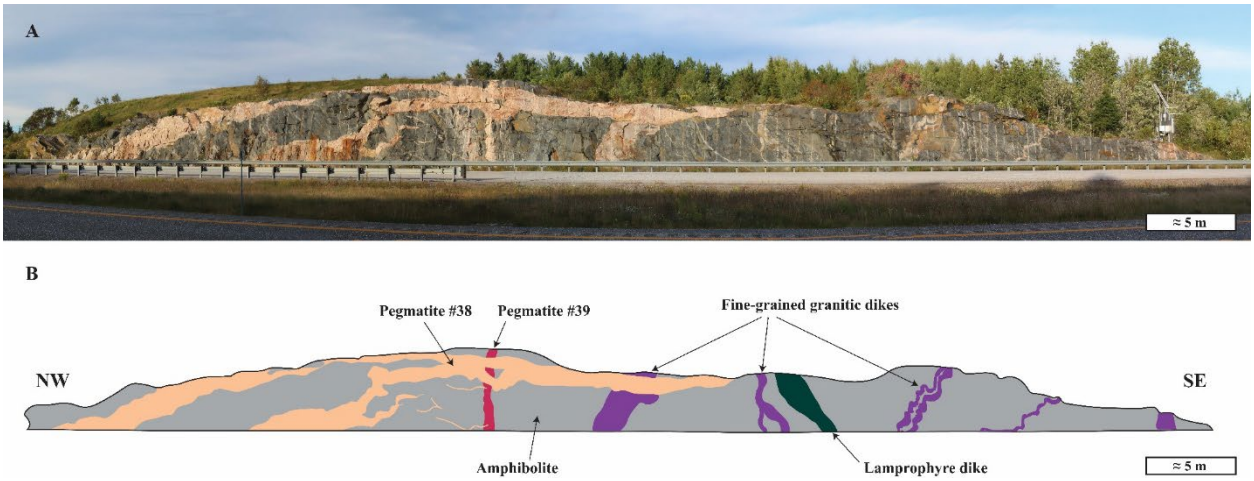

Fig. 17. Road cut showing crosscutting relationships with the subhorizontal pegmatite #38 (Neoproterozoic) crosscutting subvertical pegmatite #39 and fine-grained granitic dikes. Note that the alteration halo around the lamprophyre dike to the right overprints the fine-grained granitic dike to its left.

	70	**71**	**72**	**73**	**74**	**75**	**76**	**77**	**78**	**79**	**80**	**81**	**82**	**83**	**84**
	EP	*EP*	*FGD*	*FGD*	*FGD*	*FGD*	*FGD*	*FGD*	*Leuco*	*Lamp*	*Mafic*	*Bt gn*	*Bt gn*	*Amp*	*Amp*
SiO_2	72.7	71.9	75.5	75.5	75.6	72.5	73.1	73.9	75.2	51	64.7	69.8	67.4	46.9	43.4
Al_2O_3	13.7	13.85	12.8	13.8	13.3	12.95	13.3	12.9	12.5	12.7	15.05	12.85	13.55	16.4	13.65
Fe_2O_3	2.74	2.84	1.83	1.96	1.61	1.81	1.37	1.7	1.98	7.23	8.78	6.91	7.43	13.75	17.5
CaO	1.07	1.03	1.18	1.99	0.93	0.73	1.2	1.18	1.18	6.86	3.82	2.63	2.4	10.3	11.15
MgO	0.47	0.59	0.34	0.33	0.35	0.38	0.2	0.28	0.19	8.05	1.45	1.41	1.24	6.27	8.49
Na_2O	2.73	2.65	2.12	2.88	2.04	1.74	2.01	1.92	2.09	1.08	3.51	2.29	2.69	2.58	1.78
K_2O	6.21	6.48	5.44	3.86	6.37	6.89	6.44	6.59	5.55	7.16	2.91	3.04	3.85	1.02	0.77
Cr_2O_3	0.002	0.002	--	0.003	0.002	--	--	0.002	0.005	0.045	0.006	0.008	0.007	0.019	0.021
TiO_2	0.34	0.36	0.08	0.08	0.17	0.16	0.09	0.12	0.09	1.75	1	0.7	0.86	0.9	1.02
MnO	0.03	0.03	0.01	0.01	0.01	0.01	0.01	0.02	0.05	0.1	0.18	0.11	0.11	0.19	0.24
P_2O_5	0.07	0.07	0.03	0.02	0.02	0.02	0.03	0.03	0.01	1.17	0.34	0.19	0.2	0.09	0.08
SrO	0.01	0.01	0.03	0.04	0.03	0.03	0.03	0.03	0.01	0.33	0.04	0.02	0.02	0.02	0.01
BaO	0.1	0.1	0.25	0.14	0.44	0.47	0.36	0.32	0.08	0.88	0.17	0.11	0.11	0.02	0.02
LOI	0.31	0.43	0.6	0.56	0.26	0.33	0.47	0.38	0.15	1.07	0.01	0.41	0.23	0.9	0.88
Total	*100.48*	*100.34*	*100.21*	*101.17*	*101.13*	*98.02*	*98.61*	*99.37*	*99.09*	*99.43*	*101.97*	*100.48*	*100.1*	*99.36*	*99.01*
Ba	921	869	2260	1450	3910	4470	3350	3100	678	7820	1480	931	952	147	134.5
Ce	119.5	128	120.5	155.5	82.8	89.2	108	171	16.4	413	76.1	100	90.5	15.5	21.6
Cr	20	20	20	20	20	20	10	10	20	300	20	40	30	120	140
Cs	2.38	2.25	1.66	1.39	2.29	2.81	0.86	1.02	0.86	1.96	1.4	3.83	1.47	1.55	0.65
Dy	5.53	5.24	1.05	1.31	0.99	0.84	0.79	1.09	3.86	5.12	7.39	6.96	5.86	3.45	4.51
Er	3.46	3.26	0.59	0.76	0.46	0.53	0.24	0.57	3.38	1.76	4.1	3.98	3.31	2.37	2.82
Eu	1.07	1.26	0.84	0.99	0.99	1.06	0.9	1.06	1.08	5.23	3.38	1.74	1.92	0.83	0.97
Ga	17.9	18.3	13.8	17.5	13.3	13.8	12.9	13	13.5	20.6	22.9	19.8	22.2	18	19.3
Gd	6.46	5.96	2.44	2.84	1.69	1.45	1.84	2.66	2	11.3	8.54	7.6	6.74	2.9	3.46
Hf	9.1	8.8	5.2	6.1	3.8	3.6	3.5	3.7	4.2	16.2	14.6	8.1	7.2	1.7	2.1
Ho	1.17	1.11	0.17	0.22	0.14	0.13	0.12	0.17	0.95	0.77	1.29	1.25	1.1	0.7	0.85
La	61.6	64.3	72.2	91.6	50.5	52.1	68.3	106	8.8	192.5	35.5	47.8	43.3	6.8	10
Lu	0.46	0.46	0.09	0.1	0.08	0.05	0.07	0.08	0.58	0.15	0.54	0.5	0.43	0.27	0.34
Nb	21.7	22.3	3.7	3.2	5.1	5	2.1	2.8	2.1	18.1	29.5	12.4	13.1	5.3	4.4
Nd	48.6	52.1	35.7	44.3	25	25.2	30.8	49.4	6.7	162	42.8	46.3	42.5	9.6	11.8
Pr	12.95	14.15	10.9	13.85	7.54	7.86	9.7	15.75	1.73	42.3	9.89	11.55	10.55	2.01	2.7
Rb	181.5	181.5	136	90.6	169.5	190.5	155.5	146	139.5	132	63.8	131	145	19.9	14.1
Sm	7.83	8.62	3.92	5.16	3.19	2.94	3.55	5.32	1.41	21.7	9.21	9.23	8.18	2.37	3.11
Sn	2	2	1	1	1	1	--	1	--	2	4	2	2	3	1
Sr	118.5	112.5	230	362	261	271	297	256	113.5	2650	350	191.5	211	163.5	76.9
Ta	1.1	1.1	0.5	0.3	0.6	0.6	0.2	0.3	0.1	0.8	1.2	0.6	0.9	2.8	1.1
Tb	0.91	0.91	0.22	0.27	0.2	0.16	0.21	0.29	0.46	1.18	1.16	1.15	1.01	0.49	0.59
Th	19	21.3	37.7	36.6	23.7	24.2	35.1	47.1	27.9	31.2	3.55	13.05	10.05	1.5	4.15
Tm	0.54	0.44	0.09	0.11	0.06	0.05	0.04	0.07	0.48	0.19	0.51	0.52	0.46	0.29	0.33
U	5.28	5.74	4.48	3.21	3.43	3.11	3.04	3.8	9.73	5.13	1.89	2.9	2.88	1.21	1.53
V	31	25	25	22	7	9	10	7	--	131	50	50	80	285	332
W	7	3	1	1	1	1	1	1	1	1	1	1	1	1	1
Y	29.8	29.8	6	6.8	4.4	4.8	3.6	5	27.6	18.8	35.1	34.6	30.8	18.2	23.9
Yb	2.95	3.19	0.73	0.63	0.45	0.58	0.31	0.42	3.48	1.21	3.65	3.77	3.2	1.91	2.31
Zr	339	339	169	221	121	104	130	131	115	729	709	299	274	62	57

Table 1. Major and trace elements from whole-rock analyses of various rocks. Major elements are reported in wt% oxides and trace elements in ppm. Note that the leucosome (sample #78) was

hosted in biotite gneiss. Amp = amphibolite ; Bt gn = biotite gneiss EP = Estaire Pluton ; FGD = fine-grained granitic dikes ; Lamp = lamprophyre ; Leuco = leucosome ; Mafic = mafic wallrock.

Peg #	**5**	**6**	**7**	**8**	**9E**	**10**	**14**	**17**	**19**	**21**	**22**	**24**	**32**	**38**	**43**	**44**	**48**
Age[*]	*Np*	*Np*	*Np*	*Np*	*Np*	*Np*	*Np*	*Np*	*Np*	*Np*	*Np*	*Mp*	*Np*	*Np*	*Np*	*Np*	*Mp/Np?*
SiO_2	66.8	66.7	66.8	66.4	66.4	66.4	66.5	66.4	66.4	66.6	65.8	65.2	68.6	66.3	70.7	66.9	66.2
Al_2O_3	18.05	18.9	18.5	18.6	18.7	18.75	18.55	18.95	18.25	18.6	18.9	18	17.65	18.9	15.7	18.85	19
Fe_2O_3	0.35	0.33	0.21	0.32	0.26	0.41	0.72	0.36	0.35	1.32	0.46	2.33	0.59	0.36	0.27	0.51	0.23
CaO	0.07	0.08	0.08	0.08	0.09	0.1	0.13	0.13	0.11	0.17	0.09	0.2	0.13	0.19	0.06	0.07	0.13
MgO	--	--	--	--	--	--	--	--	0.04	0.05	--	0.04	0.03	0.04	--	--	--
Na_2O	1.62	2.02	2.11	2.28	1.86	1.98	1.64	2.05	1.63	2.37	1.83	1.74	1.95	1.88	1.64	2.52	1.89
K_2O	13.3	13.7	13.2	13.05	13.5	13.3	13.75	13.25	13.05	12.45	13.65	12.8	12.25	13.05	11.55	12.85	13.45
TiO_2	--	--	--	--	--	--	--	--	--	--	--	--	--	--	--	--	--
MnO	--	--	--	0.02	--	--	--	--	--	0.02	--	0.02	--	--	--	--	--
P_2O_5	0.02	--	0.03	0.03	0.03	--	0.02	0.02	0.02	0.02	--	--	0.02		--	0.02	--
LOI	0.23	0.11	0.17	0.2	0.24	0.31	0.05	0.31	0.27	0.26	0.31	0.13	0.23	0.31	0.21	0.14	0.21
Total	*100.4*	*101.8*	*101.1*	*101.0*	*101.1*	*101.3*	*101.4*	*101.5*	*100.1*	*101.9*	*101.0*	*100.5*	*101.5*	*101.0*	*100.1*	*101.9*	*101.1*
Ba	133.5	308	193	51.9	12.6	38.9	476	92.3	2080	69	71.7	2090	78.1	5790	57.9	114	2280
Ce	3.3	1.3	1	1.1	1.7	0.8	1	2.4	1	1.6	2.7	2.8	1.2	4.7	3.9	1.3	1.9
Cs	20.3	6.57	4.09	7.21	14.05	20.7	3.93	3.26	5.57	23.4	9.2	5.78	5.59	2.87	10.3	40.4	16.25
Cu	3	--	--	2	6	2	7	10	--	2	4	9	3	3	2	--	--
Dy	0.15	0.14	0.14	0.25	0.12	0.27	0.52	0.56	0.5	0.35	0.28	0.11	0.83	0.1	0.51	0.05	0.06
Er	0.19	0.06	0.09	0.19	0.06	0.15	0.36	0.32	0.53	0.16	0.16	0.08	0.56	0.07	0.24	0.03	0.05
Eu	0.16	0.69	0.61	0.27	0.19	0.09	0.84	0.73	0.43	0.11	0.33	0.77	0.6	1.16	0.3	0.13	0.22
Ga	22.2	17.1	14.7	17	23	27.3	18.2	17.3	12.6	42.5	23.6	15.3	18	13.5	20.7	27.7	16.5
Gd	0.19	0.13	--	0.15	0.17	0.08	0.16	0.49	0.31	0.26	0.25	0.19	0.56	0.32	0.39	0.09	0.1
Hf	--	--	--	--	--	--	--	0.2	0.4	--	--	--	0.3	--	--	--	--
Ho	0.03	0.02	0.03	0.07	0.01	0.05	0.09	0.13	0.18	0.06	0.05	0.01	0.17	0.02	0.09		0.01
La	4	1	0.8	0.8	1	0.6	0.9	1.6	0.5	1.2	3.7	2	0.8	3.5	2.4	0.8	0.7
Lu	0.02	0.02	0.02	0.05	0.02	--	0.03	0.07	0.11	--	0.02	0.01	0.09	--	--	--	--
Nb	0.2	--	--	0.8	--	1.3	0.3	0.6	2	0.8	0.5	0.2	1.2	--	0.6	--	--
Nd	1.5	0.4	0.5	0.4	0.7	0.3	0.4	1	0.4	0.5	1.2	0.8	0.4	1.7	1.8	0.4	0.6
Pb	169	174	196	210	206	155	159	183	85	119	149	60	172	79	151	129	77
Pr	0.34	0.15	0.1	0.1	0.18	0.09	0.11	0.26	0.07	0.16	0.3	0.23	0.09	0.47	0.42	0.12	0.14
Rb	685	611	492	966	1025	1250	523	630	495	1170	804	429	709	293	785	1420	543
Sm	0.3	--	0.14	--	0.14	0.12	0.08	0.29	0.15	0.26	0.22	0.24	0.2	0.32	0.42	0.11	--
Sr	41	116	111	25.7	14.2	23.6	149	75.5	504	30.4	36.9	356	60.8	509	31.7	24.8	202
Ta	0.3	--	--	0.4	--	0.5	--	0.3	0.3	0.3	0.2	--	0.6	--	0.3	0.2	--
Tb	0.03	0.02	0.02	0.05	--	0.02	0.04	0.08	0.09	0.05	0.04	--	0.12	0.03	0.07	--	--
Th	0.15	0.44	0.12	0.2	--	0.13	0.15	0.75	0.18	0.08	0.17	0.27	0.53	0.39	0.84	0.09	0.07
Tm	0.02	--	--	0.05	--	--	0.05	0.05	0.07	0.02	0.02	--	0.08	--	0.03	--	--
U	0.24	0.47	0.43	2.89	0.55	0.46	0.94	2.56	2.35	3.65	0.48	0.36	1.13	0.21	0.91	0.1	0.34
V	193	8	18	--	--	--	6	--	7	5	90	10	5	--	7	--	9
W	22	--	--	--	--	--	--	--	--	2	2	--	--	--	--	--	--
Y	1.5	0.8	0.8	2.1	0.8	1.1	3.4	3.7	4.2	1.9	2.1	0.6	5.7	0.9	3.2	0.5	0.3
Yb	0.05	0.1	0.05	0.43	0.08	0.12	0.39	0.23	0.58	0.11	0.13	0.04	0.52	--	0.27	0.07	--
Zr	2	--	--	--	--	2	3	3	4	2	4	2	3	2	2	--	--
ΣREE	11.78	5.18	3.81	8.37	11.91	9.12	6.75	11.5	4.19	9.81	7.9	11.92	14.05	3.6	6.11	4.94	4.31

An	0.4	0.4	0.4	0.4	0.5	0.5	0.7	0.7	0.6	0.9	0.5	1.1	0.7	1.0	0.4	0.4	0.7
Ab	15.6	18.2	19.5	20.9	17.2	18.4	15.2	18.9	15.9	22.2	16.8	16.9	19.3	17.8	17.7	22.9	17.5
Or	84.1	81.4	80.1	78.7	82.3	81.1	84.1	80.4	83.5	76.9	82.7	82.0	79.9	81.2	82.0	76.8	81.9
K/Rb	352	164	479	267	407	487	245	239	193	477	382	308	450	542	314	809	193
K/Cs	18487	8975	66109	31641	58838	91065	51071	27112	18129	98722	114684	41865	23355	62486	61834	128302	15013

Table 2. Major and trace elements of K-feldspar from selected pegmatites. Major elements are reported in wt. %, trace elements are reported in ppm, feldspar components (An, Ab, Or) are reported in % and elemental ratios (K/Rb, K/Cs) are unitless.*Ages (U-Pb zircon, monazite and xenotime) from Pfister *et al.* (2023). Np = Neoproterozoic (*ca.* 990-960 Ma) ; Mp = Mesoproterozoic (*ca.* 1450 Ma).

	WR contact (n = 10)		Border zone (n = 86)		Inner zone (n = 30)		Core zone (n = 5)		"Cauliflower" garnet (n = 12)		Garnet layer (n = 6)		Graphic grt-qtz (n = 17)		Ms-qtz intergrowth (n = 5)	
	Mean	*1σ*	*Mean*	*1σ*	*Mean*	*1σ*	*Mean*	*1σ*	*Mean*	*1σ*	*Mean*	*1σ*	*Mean*	*1σ*	*Mean*	*1σ*
SiO_2	37.30	±1.58	37.11	±1.00	37.00	±1.37	37.03	±1.20	36.96	±0.72	37.03	±0.67	36.71	±0.93	37.37	±1.50
TiO_2	0.20	±0.06	0.16	±0.05	0.19	±0.07	0.24	±0.09	0.20	±0.05	0.20	±0.05	0.19	±0.05	0.25	±0.06
Y_2O_3	0.33	±0.15	0.33	±0.24	0.43	±0.21	0.19	±0.03	0.47	±0.16	0.59	±0.08	0.28	±0.14	0.25	±0.14
Al_2O_3	21.56	±0.90	20.55	±0.71	20.67	±0.70	21.27	±0.62	20.92	±0.38	20.68	±0.33	20.53	±0.51	20.88	±0.69
FeO	25.79	±1.52	21.12	±1.64	16.75	±1.88	24.40	±1.36	17.34	±0.69	19.11	±1.14	15.21	±0.93	13.32	±0.95
MnO	11.78	±1.69	18.40	±1.86	22.23	±2.46	13.67	±1.00	21.58	±1.65	19.68	±1.19	25.00	±1.58	25.96	±1.90
MgO	1.18	±0.21	0.91	±0.23	0.60	±0.22	1.26	±0.04	0.46	±0.16	0.73	±0.08	0.37	±0.16	0.26	±0.14
CaO	0.96	±0.17	0.94	±0.50	1.09	±0.36	1.26	±0.13	1.09	±0.22	1.31	±0.11	0.83	±0.28	0.38	±0.16
Comments	*Garnet found directly at the WR contact (e.g. Fig. 8E).*		*Isolated euhedral garnet from the border zone or the inner zone, but <10 cm from the WR.*		*Isolated euhedral garnet from the inner zone (>10 cm from WR contact).*		*Euhedral garnet from the massive quartz core (e.g. Fig. 8T).*		*Euhedral garnets from the "cauliflower" garnet texture (e.g. Fig. 8Q,R).*		*Euhedral garnet from garnet layers (e.g. Fig. 8O).*		*Garnet from the graphic-like quartz-garnet intergrowth (e.g. Fig. 8M,N).*		*Garnet from muscovite-quartz intergrowth (e.g Fig. 8L)*	

	Biotite gneiss (n = 3)		Leucosome biotite gneiss (n = 5)		Amphibolite (n = 4)		Leucosome amphibolite (n = 5)	
	Mean	*1σ*	*Mean*	*1σ*	*Mean*	*1σ*	*Mean*	*1σ*
SiO_2	38.90	±0.40	37.49	±2.15	37.29	±0.61	38.48	±0.99
TiO_2	-	-	0.36	±0.00	0.18	±0.08	-	-
Y_2O_3	0.15	±0.00	0.33	±0.00	0.12	±0.00	0.17	±0.01
Al_2O_3	21.98	±0.26	22.77	±1.94	21.73	±0.78	21.57	±0.31
FeO	24.52	±0.82	31.39	±1.45	29.17	±1.05	25.79	±1.26
MnO	1.08	±0.15	1.42	±0.06	1.82	±0.35	1.72	±0.21
MgO	2.87	±0.10	3.15	±0.12	3.93	±0.35	3.68	±0.21
CaO	9.79	±0.37	2.83	±0.50	5.10	±0.82	7.64	±0.38
Comments	*Garnet from biotite gneiss.*		*Garnet from leucosome hosted in biotite gneiss.*		*Garnet from amphibolite (e.g. Fig. 5J).*		*Garnet from leucosome hosted in amphibolite (e.g. Fig. 6F).*	

Table 3. Composition (major elements only; SEM-EDS) of various garnets from the pegmatites and host rocks.

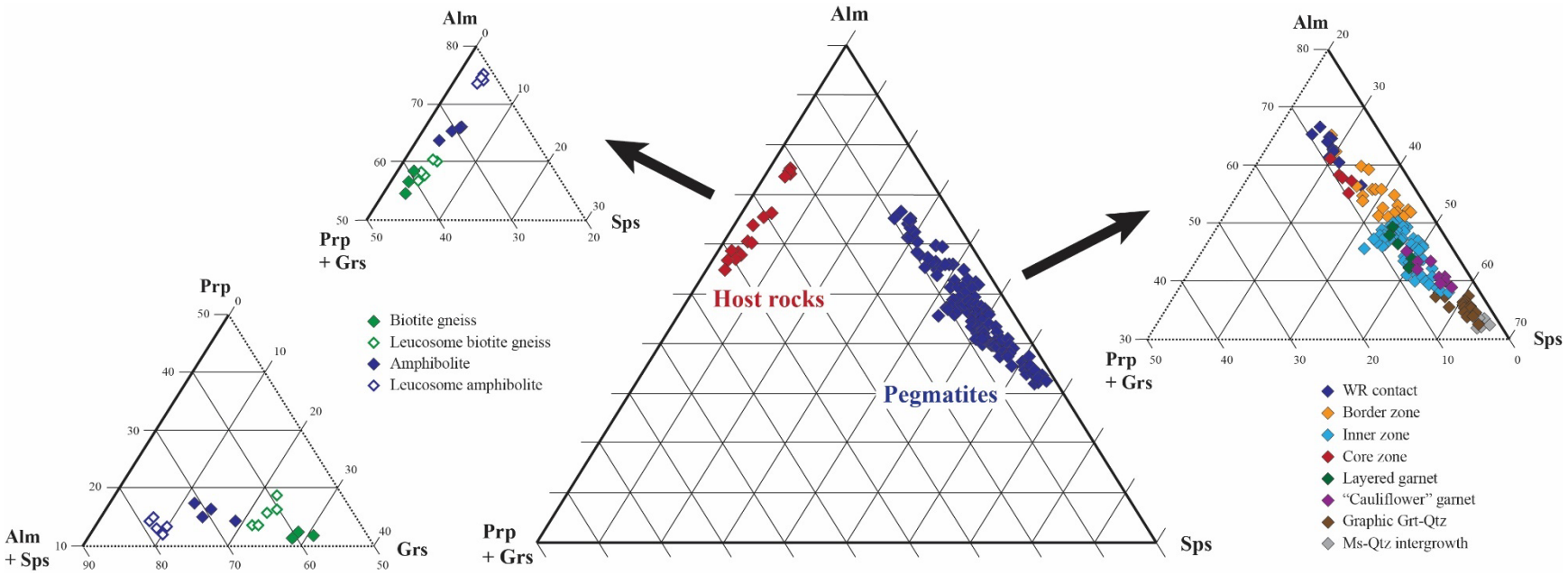

Fig. 18. Garnet compositions plotted in different ternary spaces. Alm = almandine; Grs = grossular; Prp = pyrope; Sps = spessartine.

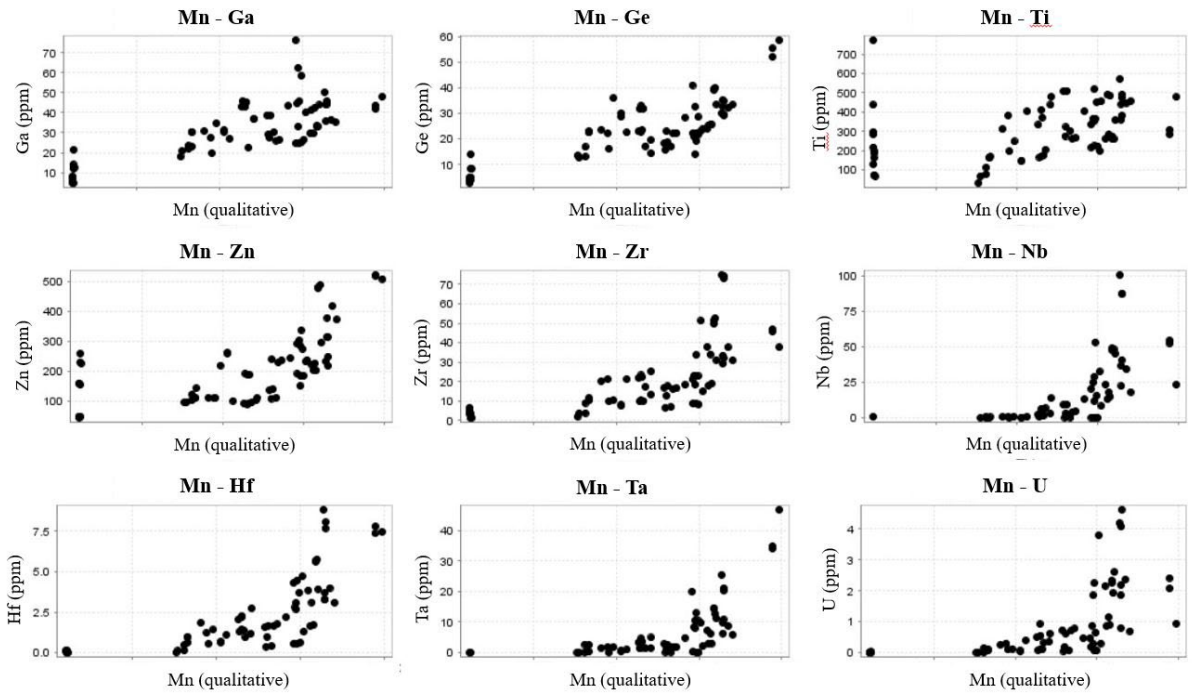

Fig. 19. Graphs of LA-ICP-MS data for garnet showing weak to moderate positive correlation between Mn content of the garnet (proxy for pegmatite-WR interaction) and various trace elements. Note that Mn scale is only qualitative as quantification was made difficult by the difference in Mn content between the reference material (NIST 610; 485 ppm Mn) and analyzed samples (up to 26 wt% MnO).

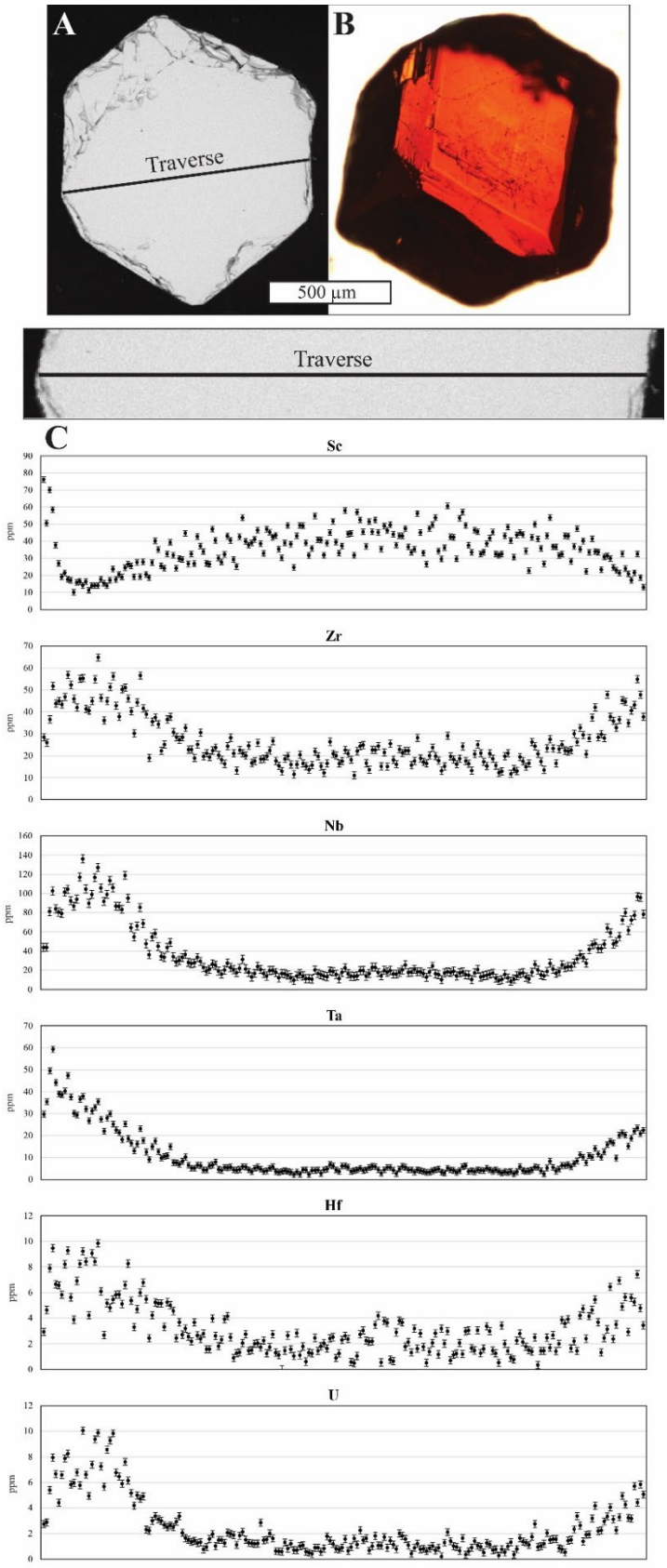
A
Traverse
500 µm
B
Traverse
C
Sc
Zr
Nb
Ta
Hf
U
ppm

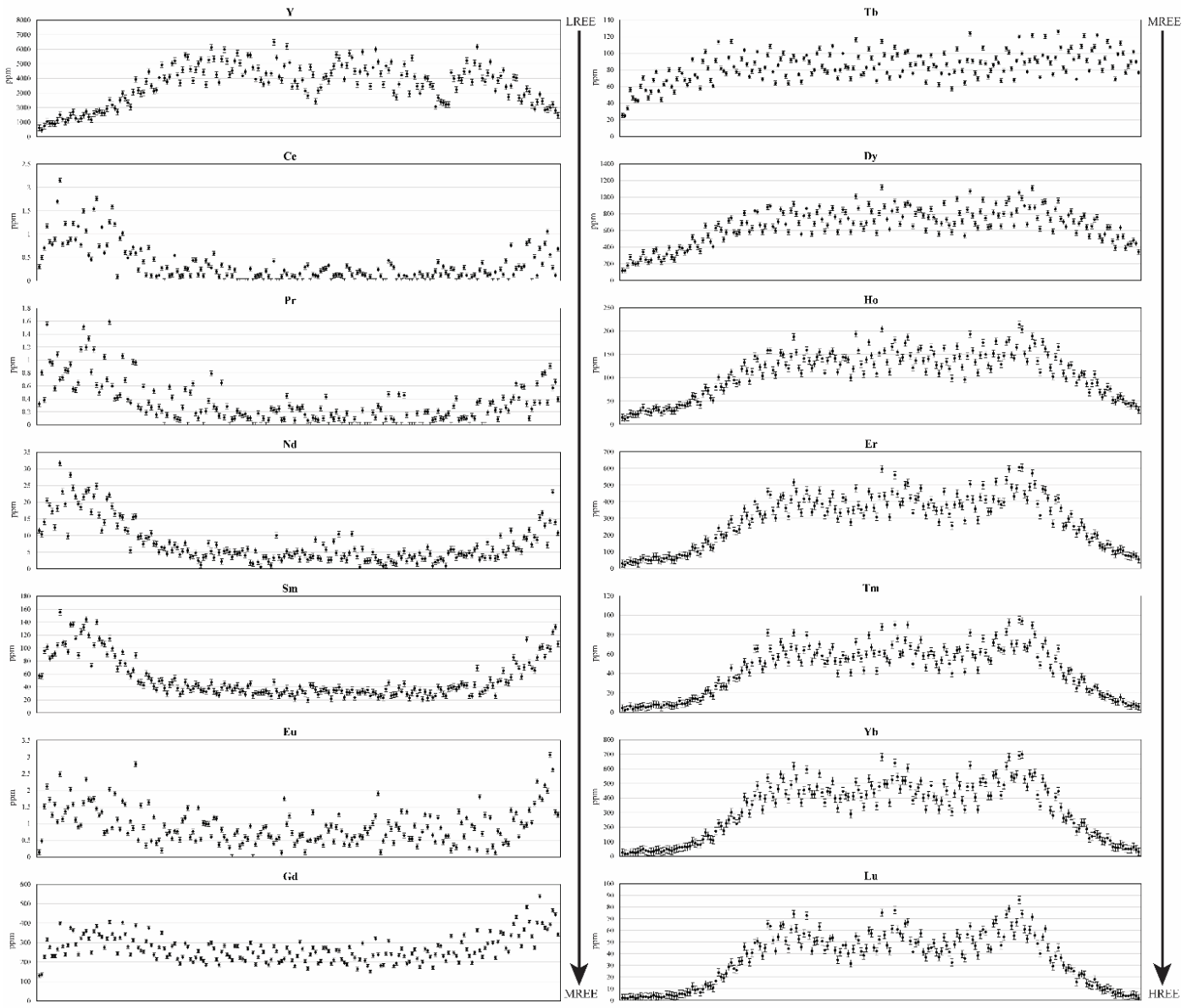

Fig. 20. Trace element data LA ICP-MS (with 2σ error bars) from a traverse across a gem-quality garnet crystal from the cauliflower garnet texture in Peg #9W. A) Back-scattered electron imaging of the garnet crystal. Note the lack of zoning. B) Picture of the garnet crystal under transmitted light. Note the lack of inclusions. C) Trace element profiles of the traverse (HFSE and REE). The REE profiles are ordered from lightest to heaviest.

Pegmatite and analysis #	Al (ppm)	Al Int2SE (ppm)	P (ppm)	P Int2SE (ppm)	Ti (ppm)	Ti Int2SE (ppm)	Ge (ppm)	Ge Int2SE (ppm)	Ge/Ti
5_A	41.9	±5.0	23.0	±3.5	5.5	±0.7	0.89	±0.19	0.25
5_B	73.9	±2.0	19.3	±2.9	30.4	±2.0	0.70	±0.19	0.03
6	58.9	±5.9	20.3	±3.2	7.7	±1.0	0.73	±0.19	0.14
7_A	40.6	±8.2	25.5	±4.4	5.5	±1.3	0.71	±0.17	0.20
7_B	58.5	±4.5	15.5	±3.8	5.1	±0.9	0.69	±0.18	0.20
9E_A	22.1	±1.6	17.1	±2.3	2.7	±0.7	0.98	±0.16	0.55
9E_B	27.2	±4.8	21.2	±3.6	3.7	±0.8	0.88	±0.19	0.36
9W	58.0	±3.7	18.6	±3.2	7.9	±1.1	3.67	±0.32	0.70
10	32.4	±2.0	20.8	±3.6	7.5	±1.3	0.79	±0.20	0.16
11	112.0	±13.0	20.4	±3.6	5.0	±0.8	0.99	±0.17	0.30
12	55.3	±5.6	22.8	±4.0	3.0	±0.9	1.72	±0.23	0.88
14	246.0	±19.0	18.8	±3.5	4.2	±0.8	1.50	±0.22	0.55
21	73.0	±25.0	19.9	±4.0	12.2	±1.6	0.56	±0.22	0.07
22	16.2	±1.9	18.8	±3.8	3.1	±0.8	1.52	±0.22	0.75
23	17.5	±1.8	20.6	±3.4	11.4	±1.3	1.04	±0.18	0.14
24	35.6	±2.5	23.2	±3.6	3.1	±1.2	1.21	±0.21	0.59
25	394.0	±88.0	23.3	±3.6	3.8	±0.9	1.14	±0.19	0.45
26	82.0	±21.0	18.1	±3.4	3.1	±0.8	0.94	±0.20	0.46
27	16.4	±2.8	23.7	±3.0	8.8	±1.2	0.58	±0.19	0.10
28	246.0	±80.0	24.6	±3.5	14.0	±1.5	0.83	±0.18	0.09
29_A	51.6	±2.3	20.7	±3.1	9.8	±1.2	0.50	±0.20	0.08
29_B	49.0	±2.2	20.1	±3.6	6.3	±0.8	0.86	±0.20	0.21
38	103.0	±18.0	20.6	±3.3	23.7	±1.8	1.95	±0.22	0.12
39	78.0	±12.0	27.2	±3.7	5.7	±1.1	0.88	±0.24	0.23
42	61.5	±6.5	22.0	±3.3	10.6	±1.3	1.04	±0.19	0.15
44_A	22.5	±1.6	23.8	±3.5	6.5	±1.0	1.22	±0.21	0.29
44_B	30.9	±1.9	25.2	±3.9	7.4	±0.9	1.10	±0.16	0.23
44_C	29.3	±5.3	19.5	±3.8	4.1	±0.9	0.87	±0.17	0.32
45_A	15.0	±2.1	17.7	±3.1	6.1	±1.1	0.52	±0.18	0.13
45_B	31.8	±1.6	20.5	±3.6	7.5	±0.9	0.65	±0.16	0.13
45_C	30.6	±8.0	16.9	±4.0	6.5	±0.9	0.70	±0.22	0.16
46_A	17.0	±2.2	18.2	±3.2	5.5	±0.8	-	-	-
46_B	51.0	±12.0	26.1	±3.7	7.6	±2.9	1.45	±0.26	0.29
46_C	29.2	±2.4	19.8	±4.0	5.8	±1.0	1.19	±0.23	0.31
Anatectic sweat†	25.0	±4.2	16.0	±3.7	10.9	±1.1	0.67	±0.15	0.09

Table 4. Trace elements of quartz from selected pegmatites. Int2SE = analytical uncertainty. LOD Al = 4.0 ppm; LOD P = 10.0 ppm; LOD Ti = 1.8 ppm; LOD Ge = 0.40 ppm. †Anatectic sweat is amphibolite-hosted.

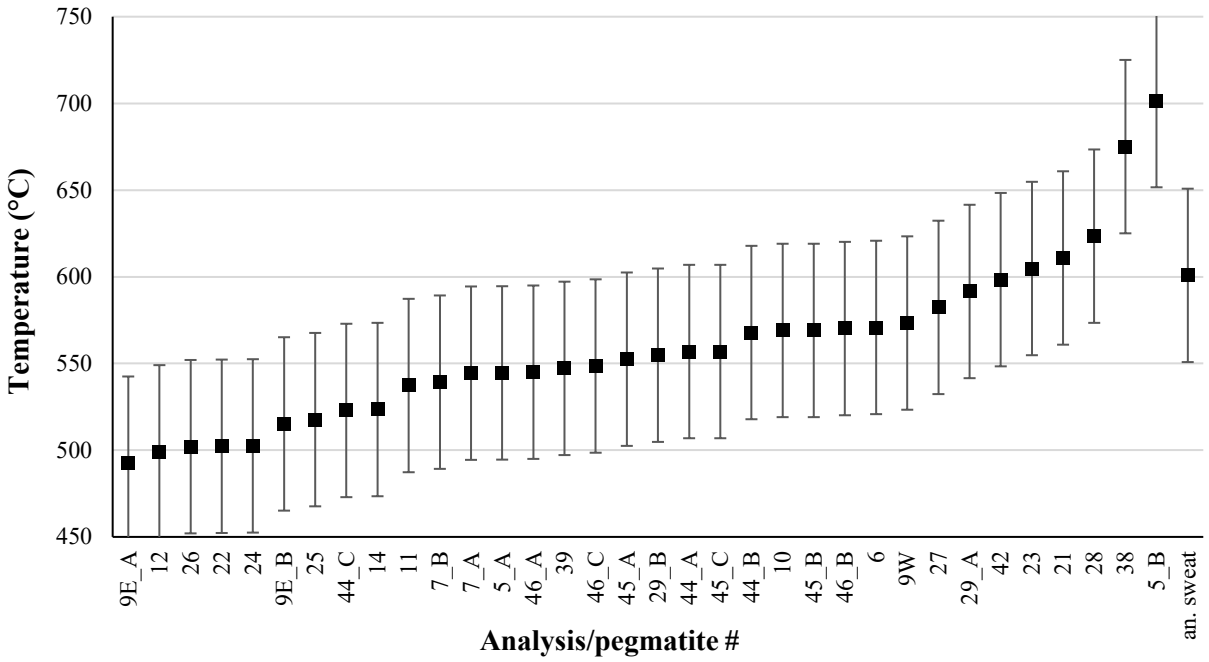

Fig. 21. Summary of the calculated TitaniQ values using equation of Huang and Audétat (2012) for each quartz sample; see Fig 3 for sample/pegmatite locations. Note that all error bars are set at ± 50°C due to the uncertainty of some parameters (see text for discussion).

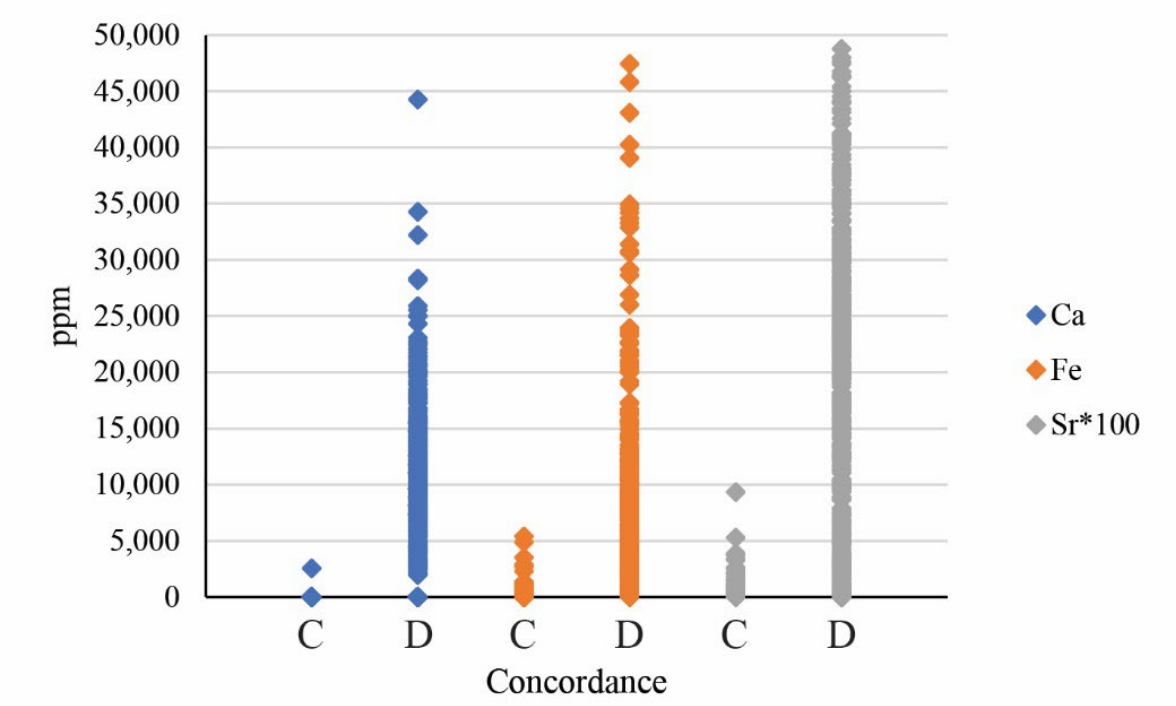

Fig. 22. Plot of Ca, Fe and Sr(*100) content of concordant (C) versus discordant (D) zircon.

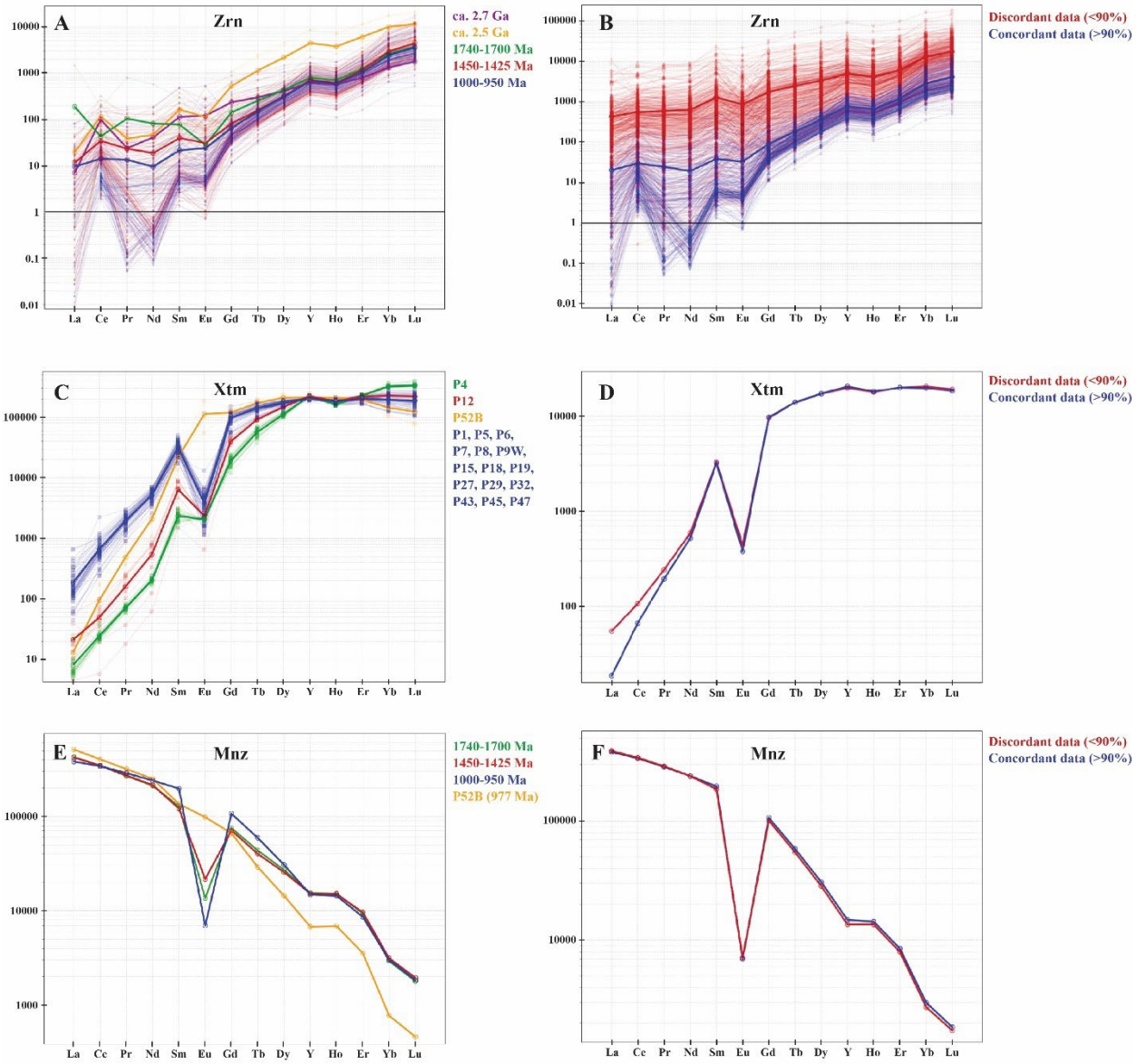

Fig. 23. Chondrite-normalized (McDonough and Sun, 1995) REE profiles for zircon (Zrn), monazite (Mnz) and xenotime (Xtm) in Highway 69 pegmatites. Note the minerals are color-coded for their age, except for xenotime which are invariably Grenvillian, and that the bold lines represent averages. A) Plot of concordant zircon only, color-coded for different zircon age generations. Note that n = 103 for concordant Neoproterozoic zircon, n = 135 for Mesoproterozoic, n = 8 for Paleoproterozoic and n = 13 for older concordant zircon. B) Plot of concordant (n = 159) versus discordant (n = 615) zircon. C) Plot of concordant xenotime only, color-coded for different REE

profiles (as all xenotime observed is Neoproterozoic; see Pfister *et al*., 2023). Note that all pegmatites but three have similar REE profile. D) Plot of concordant (n = 81) versus discordant (n = 214) xenotime. E) Plot of concordant monazite only, color-coded for different zircon age generations. Note that pegmatite #52B is plotted separately as it exhibits a distinctive REE profile from other Neoproterozoic pegmatites (also visible in xenotime; see graph C). F) Plot of concordant (n = 105) versus discordant (n = 125) monazite.

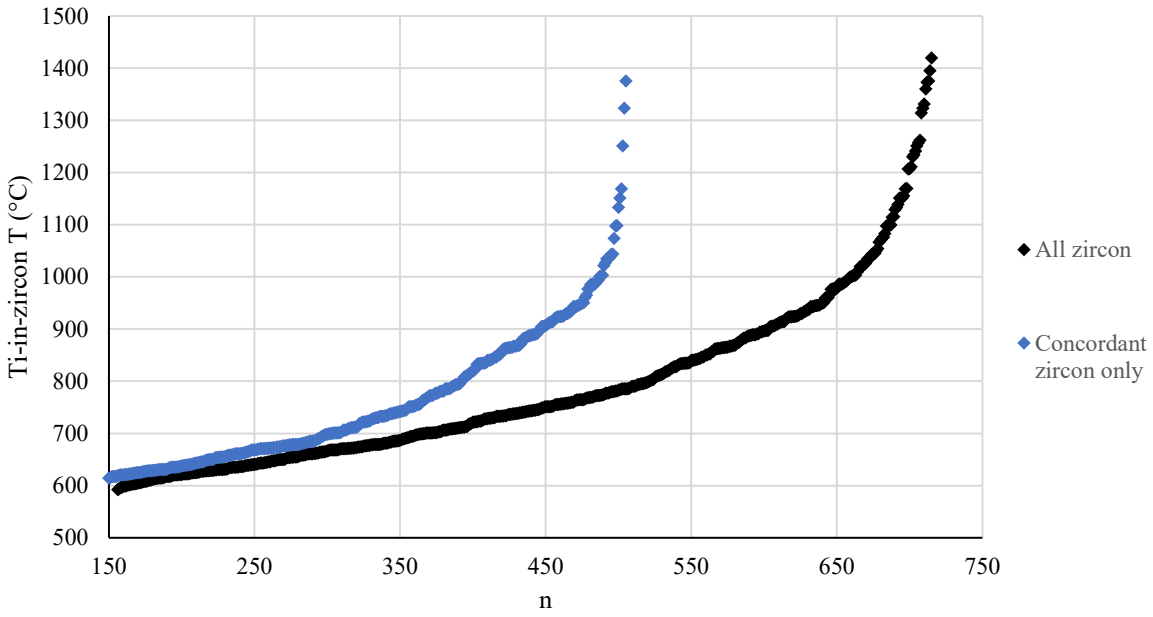

Fig. 24. A plot of Ti-in-zircon temperatures based on the geothermometer of Watson *et al.* (2006) versus cumulative frequency; n = number of zircon grains analyzed. Note that about 150 of the analyses yielded no values due low Ti contents (below LOD) and/or high analytical uncertainty, thus why the abscissa starts at 150.

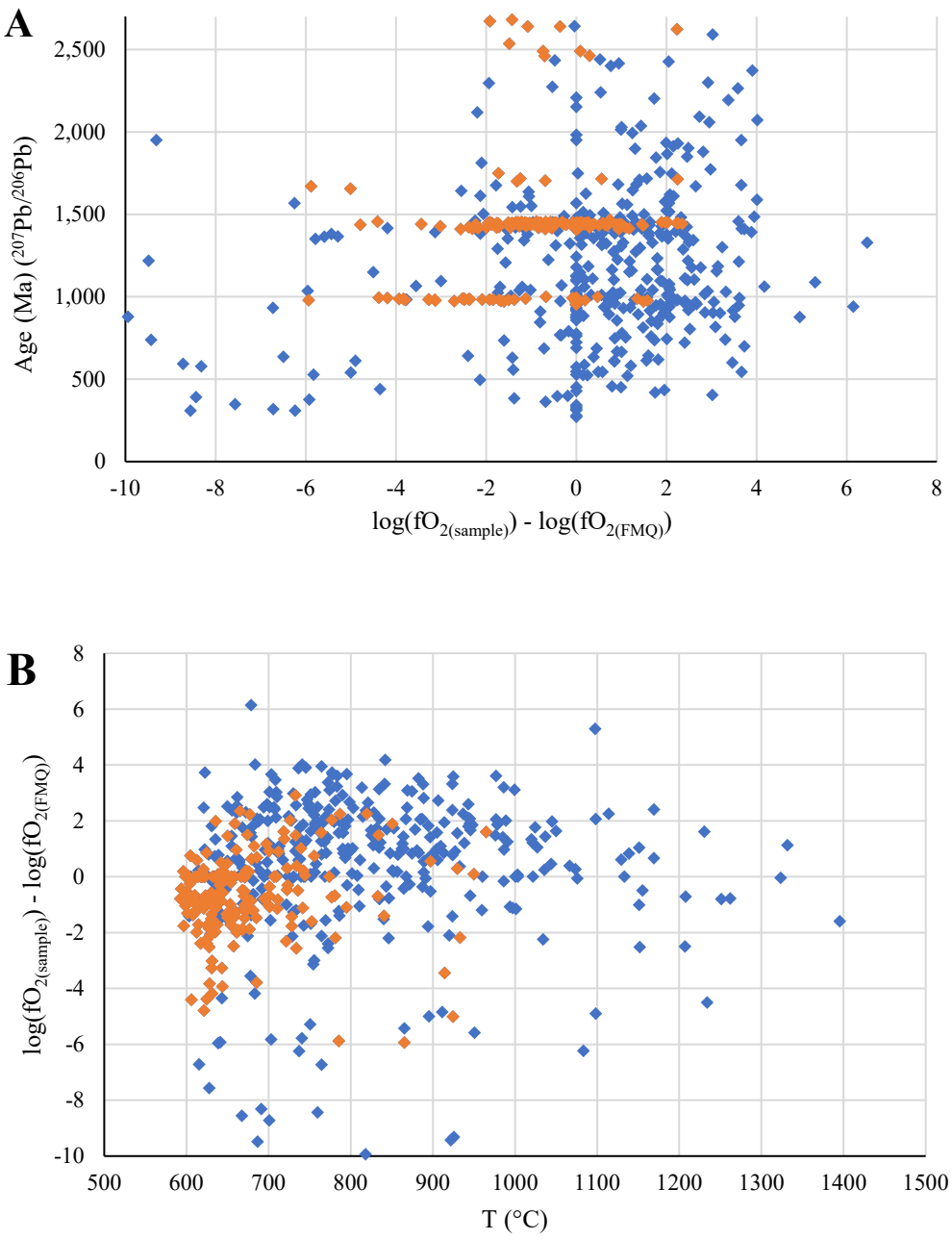

Fig. 25. Oxybarometry data (zircon) using the method of Loucks *et al.* (2020). Blue diamonds = all zircon; orange diamonds = concordant zircon only (Pfister *et al.*, 2023). A) Age ($^{207}Pb/^{206}Pb$)

versus $\log(_{fO2(sample)})$ - $\log(_{fO2(FMQ)})$. B) $\log(_{fO2(sample)})$ - $\log(_{fO2(FMQ)})$ versus T (using the Ti-in-zircon geothermometry method of Watson *et al.*, 2006). Note that concordant and discordant zircon with below LOD Ti, U and/or Ce are not shown in the figure.

Pegmatite and analysis #	**$\delta^{18}O$ (‰)**
5	10.7
6	12.2
7	11.9
8	*10.0**
9E_A	8.8
9E_B	9.2
9W	12.3
10	8.0
12	14.0
14	12.9
21	8.3
22	9.8
23	9.8
24	11.7
25	9.4
26	10.1
27	8.6
28	10.6
29	11.1
38	10.1
39	11.7
44_A	10.9
44_B	11.2
44_C	12.6
45_A	14.0
45_B	9.2
46_A	9.5
46_B	12.7
Leucosome	9.7

Table 5. $\delta^{18}O_{qtz}$ (‰; VSMOW) values of selected pegmatites. Analytical uncertainty is ± 0.8‰ (see methods section).*Average value (n = 21; 8.0‰ to 12.2‰). Note that the leucosome is amphibolite-hosted.

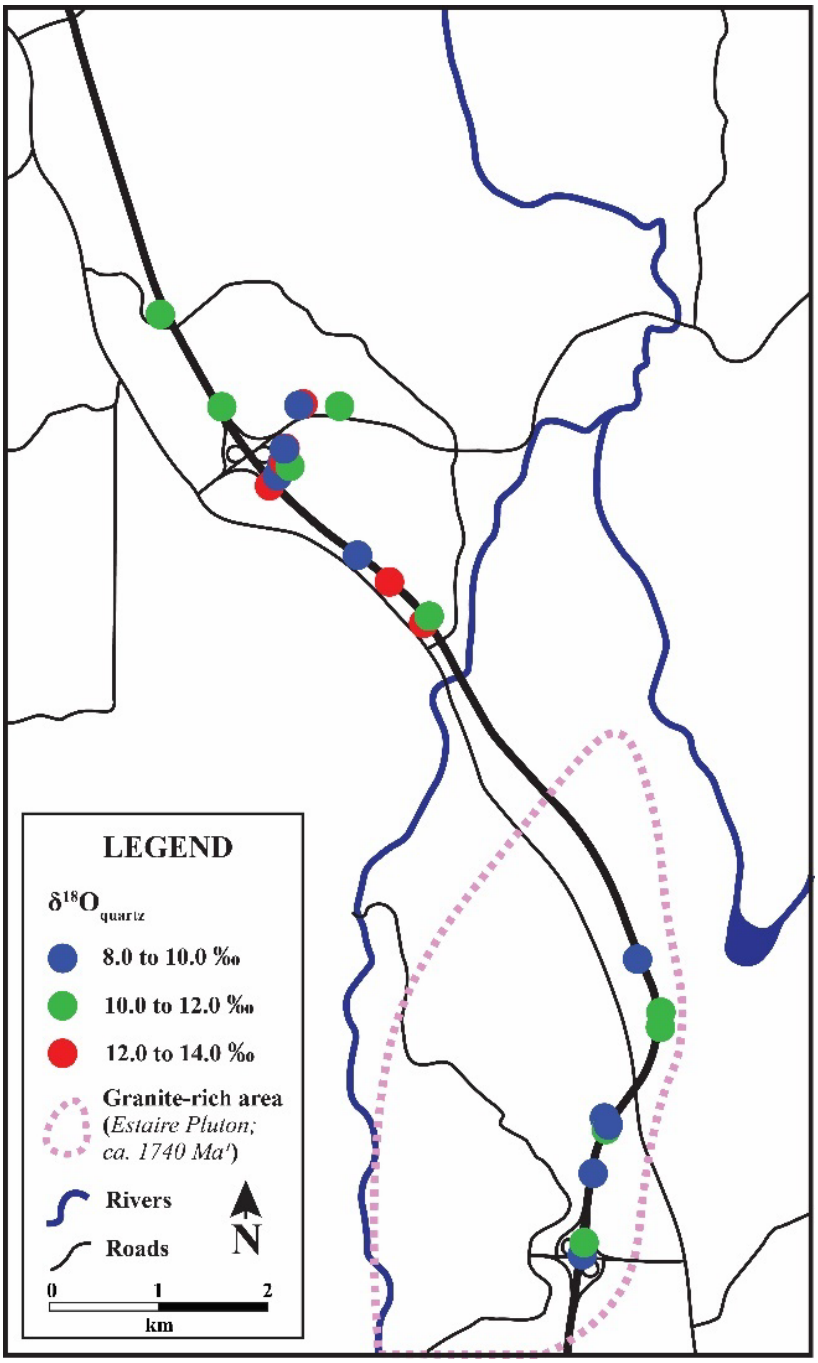

Fig. 26. Distribution of the $\delta^{18}O_{qtz}$ values. See text for discussion. [1]Pfister *et al.*, 2023

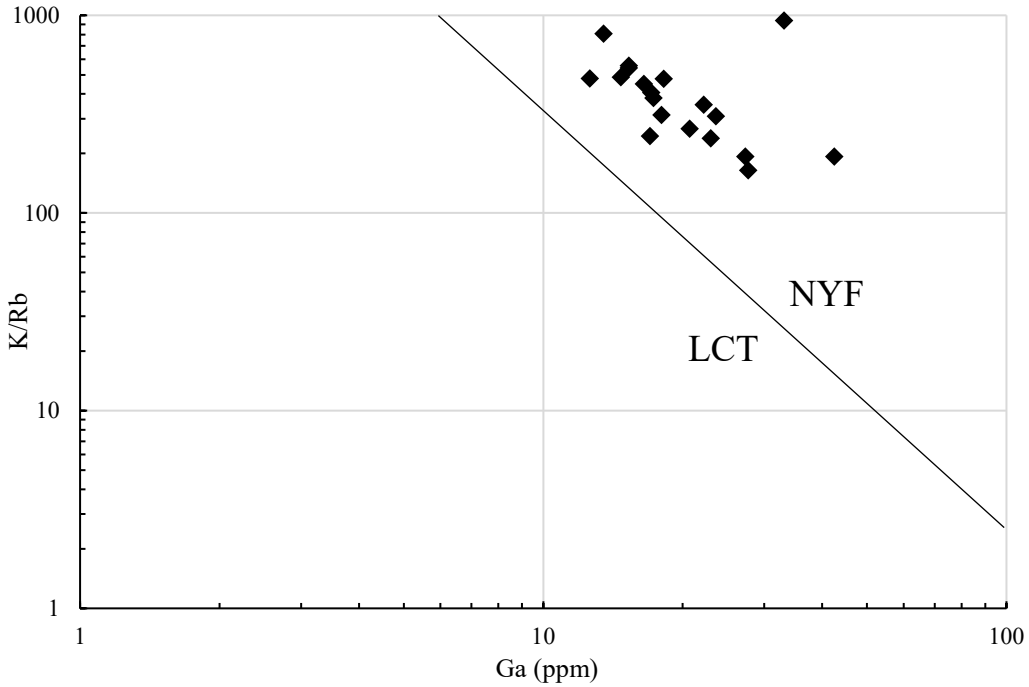

Fig. 27. K/Rb and Ga in primary K-feldspar: NYF versus LCT pegmatite discrimination diagram from Wise (2013).

		Magmatic stage	Early metasomatism	Late metasomatism
Quartz	Quartz I (bright CL)			
	Quartz II (dark CL)			
Feldspar	K-feldspar I (Ab_{9-25})			
	K-feldspar II (Or_{98-100})			
	Oligoclase (An_{12-22})			
	Albite ($An_{<8}$)			
Mica	Muscovite			
	Biotite			
Other silicates	Garnet (Alm-Sps series)			
	Zircon			
	Allanite-(Ce)			
	Thorite	?		
	Chlorite			
Phosphates	Monazite			
	Xenotime			
	Apatite			
Oxides	Columbite-(Fe)			
	Nb-Ti-Y-U-Ta-REE oxides			
	Uraninite			
	Hematite			
	Magnetite			
	Ilmenite			
	Rutile	?		
Sulfides	Pyrite			
	Chalcopyrite			
	Galena			
Carbonates	Calcite			
	Cu(±Zn) carbonates			
Fluorocarbonate	Bastnäsite			

Fig. 28. Summary of mineral paragenesis for the Neoproterozoic pegmatites. Major phases in dark grey, minor phases in grey and accessory phases in light grey. See text for discussion.